国際化推進共同研究概要

No.1

[採択番号]　24EA-1

タイトル： The development of the bulk ice crystal model in support of the EarthCARE mission

研究代表者： SAITO, Masanori

所内世話人： OKAMOTO Hajime

研究概要： EarthCARE衛星が2024年5月に打ち上げられ、搭載されている雲レーダとライダの情報から、氷粒子の微物理特性を抽出する事が期待されている。微物理特性抽出の精度は、使用される氷粒子モデルとそれらの後方散乱特性に依存している。本研究課題では、EarthCAREライダの後方散乱特性を中心に解析を進展させた。様々な氷粒子モデルを考慮すると、後方散乱特性は大きく変動することがわかった。偏光解消度は、0.3から0.6の間の値をとることがわかった。

The development of the bulk ice crystal model in support of the EarthCARE mission

Masanori Saito (University of Wyoming)

I. Abstract

Ice clouds involve various physical processes, which affect the microphysical properties of ice clouds, such as particle size distributions and ice water contents. The EarthCARE mission successfully launched a satellite in May 2024 and measures radiometric signals to obtain the global ice cloud properties. In particular, the EarthCARE satellite can profile the vertical distributions of the microphysical properties of ice clouds through a combination of lidar and radar observations. However, the accuracy and robustness of these retrievals primarily rely on the accuracy of the ice optical property model. This project develops lidar backscattering models for various ice crystal shapes (i.e., the lidar and depolarization ratios of ice crystals) for consideration of the implementation of the developed diagram into the EarthCARE operational algorithm. The results show the diversity of the backscattering properties among various ice crystals, but the depolarization ratios generally take values between 0.3 and 0.6.

II. Introduction

Ice clouds are distributed across the globe and modulate the global radiation budget through complex radiative and microphysical processes. Therefore, it is essential to monitor the optical and microphysical properties of ice clouds globally through spaceborne observations with remote sensing techniques. Spaceborne radar and lidar observations can profile the vertical structures of ice clouds using the radar-lidar algorithm that has been developed and improved over a couple of decades (e.g., Okamoto et al., 2003; Sato and Okamoto, 2011; Okamoto et al., 2019). This algorithm can infer ice cloud extinction and ice water content (or effective radius) profiles. The accuracy of these retrievals hinges primarily upon the assumption of the backscattering properties of ice crystals at both radar and lidar-relevant wavelengths. At lidar wavelengths, the reliable modeling studies of the backscattering properties of nonspherical ice crystals are still premature. In particular, some computational techniques based on geometric optics or physical optics principles are limited to simple nonspherical particle shapes, while ice crystals found in natural ice clouds show complex textures such as scall-scale surface roughness that can occur through the deposition-sublimation processes. Our light-scattering computational capabilities are applicable to such complex particle geometries (Saito and Yang, 2023). The primary goal of this study is to develop ice crystal optical property models for the EarthCARE mission, aiming at an incorporation of these models into the EarthCARE radar-lidar remote sensing algorithm.

III. Data and Method

We use the improved geometric optics method (Yang and Liou, 1996) and the CB correction method (Saito and Yang, 2023) to compute the backscattering properties of various ice crystals at 355 nm and 95 GHz, the wavelengths for the Atmospheric Lidar (ATLID) and Cloud Profiling Radar (CPR) aboard the EarthCARE satellite. Figure 1 illustrates the shapes of ice crystals considered in this study. We consider 63 hexagonal columns with various degrees of surface roughness and aspect ratios. We assume a gamma particle size distribution (PSD) consistent with Okamoto et al. (2019).

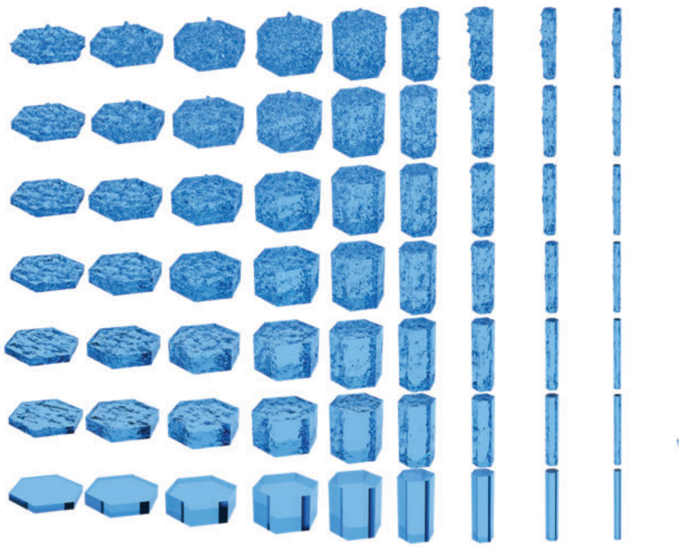

Figure 1. An illustration of ice crystal shapes considered in this study.

IV. Results

Figure 2 highlights the variations of the backscattering properties with the shape of ice crystals and effective radii for the case of single columns with various aspect ratios and surface roughness. The backscattering properties are sensitive to the small-scale surface texture. In particular, the results show substantial differences between smoothed particles and roughened particles as highlighted in dashed lines. The depolarization ratio typically ranges between 0.3 and 0.6, and the lidar ratio varies with the aspect ratio of ice crystals.

The radar reflectivity factors at 95 GHz are not sensitive to the particle morphologies but effective radius, as shown in Fig. 3.

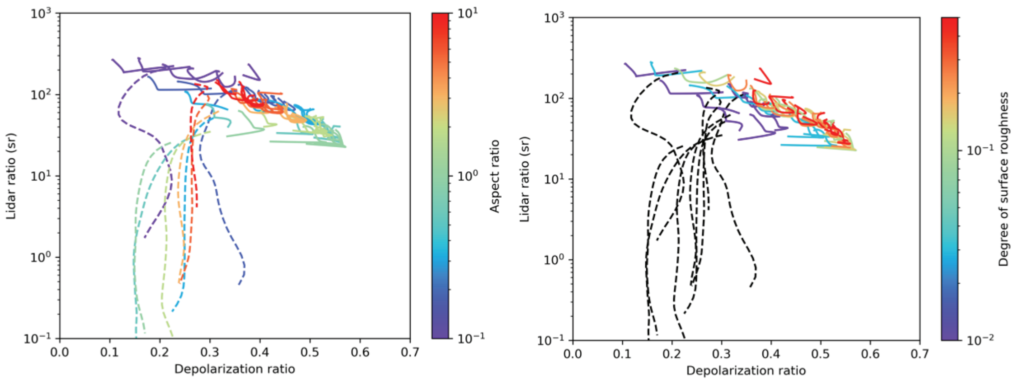

Figure 2. The backscattering properties of ice crystals with various effective radii and particle shapes at 355 nm.

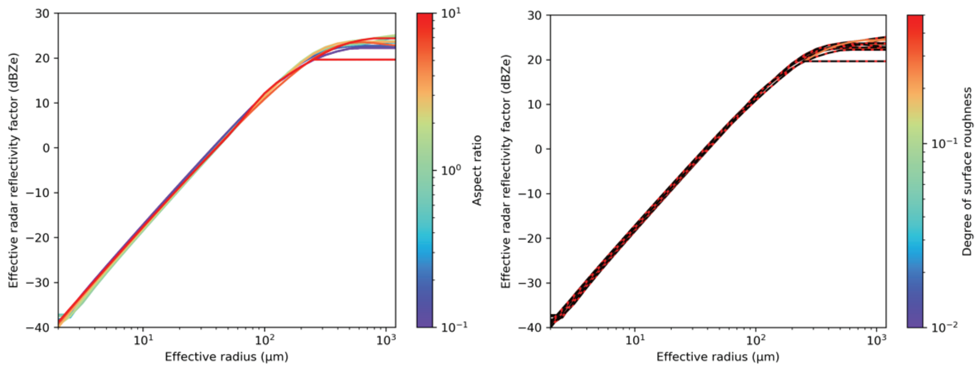

Figure 3. Same as Fig. 2 but at 95 GHz.

V. Discussion/Summary

In this study, we simulate the backscattering properties of various ice crystal shapes and effective radii. The particle shape is identified to be a critical factor in the backscattering properties. In particular, the aspect ratio of ice crystals has substantial impacts on the lidar ratio, and both characteristics (i.e., aspect ratio and surface roughness) affect the depolarization ratio. At 95 GHz, the radar reflectivity is essentially sensitive to the effective radius. A take-home message is that a combination of radar-lidar measurements can retrieve the effective radius and ice water content (IWC), but the ice crystal shape assumptions can contribute to potential biases in the retrievals. This implies that the radar-lidar algorithm needs to incorporate the uncertainty in backscattering associated with the ice crystal shape assumption.

VI. References

Okamoto, H., Iwasaki, S., Yasui, M., Horie, H., Kuroiwa, H., and Kumagai, H.: An algorithm for retrieval of cloud microphysics using 95-GHz cloud radar and lidar, J. Geophys. Res., 108, 4226– 4247, https://doi.org/10.1029/2001JD001225, 2003.

Okamoto, H., Sato, K., Borovoi, A., Ishimoto, H., Masuda, K., Konoshonkin, A., & Kustova, N. (2019). Interpretation of lidar ratio and depolarization ratio of ice clouds using spaceborne high-spectral-resolution polarization lidar. *Optics Express*, *27*(25), 36587-36600.

Sato, K., & Okamoto, H. (2011). Refinement of global ice microphysics using spaceborne active sensors. *Journal of Geophysical Research: Atmospheres*, *116*(D20).

Saito, M., & Yang, P. (2023). Quantifying the Impact of the Surface Roughness of Hexagonal Ice Crystals on Backscattering Properties for Lidar-Based Remote Sensing Applications. Geophysical Research Letters, 50(18), e2023GL104175.

Yang, P., and K. Liou (1996), Geometric-optics–integral-equation method for light scattering by nonspherical ice crystals, *Appl. Opt.*, *35*(33), 6568–6584.

VII. Research meeting and discussion

Masanori Saito visited the Research Institute for Applied Mechanics (RIAM) at Kyushu University, Japan between 16 and 20 December 2024 where he met with Dr. Hajime Okamoto and the group members for various research discussions. Saito gave a seminar at RIAM.

VIII. Other members of the joint research team

Hajime Okamoto   RIAM, Kyushu University

国際化推進共同研究概要

No.2

24EA-2

タイトル：　　Turbulent mixing in Asian Marginal Seas

研究代表者：　CHANG, Ming-Huei

所内世話人:　遠藤 貴洋

研究概要：
令和6年11月29日(金)に愛媛大学理学部総合研究棟1号館にて、国際ワークショップを開催した。台湾から6名の研究者、国内から12名の研究者と7名の学生が参加し、台湾から6件、国内から6件の研究成果発表があった。黒潮や潮汐流が地形の背後につくる乱流混合や、台風や海面冷却により発生する乱流混合について、その多様性や普遍性、生態系への影響に関する活発な議論があった。

Report on 2024 RIAM International Joint Research Project [#24EA-2]

Turbulent mixing in Asian Marginal Seas

CHANG, Ming-Huei

(Institute of Oceanography, National Taiwan University and Ocean Center, National Taiwan University)

Objective

Turbulent mixing plays an essential role in the ocean by smoothing (stirring & diffusion) the distribution of water properties and materials, consequently affecting the physical and biogeochemical environment. Understanding how mixing occurs and at what rates it proceeds is required to explore ocean variability. However, the phenomena that lead to turbulence have significant uncertainties in space and time because related measurements are sparse. As part of the international joint research project of RIAM (#18EA-2, #19EA-3, and #20EA-2), we carried out field experiments over the I-Lan Ridge between Taiwan and Yonaguni Island, Japan, where strong turbulent mixing is caused by the interaction of the Kuroshio current with steep bottom topography. The RIAM researchers also joined the field experiments to deploy their microstructure profiler. Through the intercomparison of the observed data in the research workshop held at RIAM, we quantified the turbulent dissipation and associated nutrient transport in the Kuroshio current over the I-Lan Ridge as well as their downstream extent, the results of which have been published in Q1 journals. Based on the success of our international joint research project of RIAM, we have decided to expand our scope to include various kinds of mixing processes in Asian marginal seas.

Primary members

The members involved in this collaborative research and their roles are:

- CHANG, Ming-Huei (National Taiwan University, Professor): Representative person
- ENDOH, Takahiro (RIAM, Associate Professor): RIAM advisor
- CHEN, Jia-Lin (National Cheng Kung University, Associate Professor): Numerical modeling
- CHENG, Yu-Hsin (National Taiwan Ocean University, Assistant Professor): Data analysis
- YANG, Yiing Jang (National Taiwan University, Professor): Data analysis
- JAN, Sen (National Taiwan University, Professor): Data analysis and numerical modeling (Note: He was a representative person of #18EA-2, #19EA-3, and #20EA-2)
- GUO, Xinyu (Ehime University, Professor): Numerical modelling
- NAGAI, Takeyoshi (Tokyo University of Marine Science and Technology, Associate Professor): Data analysis and numerical modeling
- HASEGAWA, Daisuke (Tohoku National Fisheries Research Institute, Senior Researcher): Data analysis
- INOUE, Ryuichiro (Japan Agency for Marine-Earth Science and Technology, Senior Researcher): Data analysis
- TSUTSUMI, Eisuke (Kagoshima University, Assistant Professor): Data analysis
- TAKAHASHI, Anne (AORI, The University of Tokyo, Postdoc Researcher): Data analysis and numerical modeling

Summary of our activities

We held the research workshop entitled “Workshop on turbulent mixing in Asian marginal seas” at Ehime University on November 29, 2024, after another workshop in Japanese held at the same place to invite as many Japanese researchers and students who study the turbulent mixing processes as possible. The abstract of the workshop theme was:

"Turbulent mixing plays several critical roles in the ocean, affecting key physical, biological, and chemical processes. For example, turbulent mixing distributes nutrients and larvae for biological productivity and fisheries, sustains abyssal stratification of the world's oceans, contributes to the global overturning circulation, redistributes heat and salt, and influences climate dynamics. This workshop encourages contributors to present recent findings of turbulent mixing obtained from field observations as well as theoretical, numerical, and laboratory studies. Through the detailed discussions, we would like to share our understanding of the turbulent mixing processes. The session encompasses a wide variety of aspects of turbulent mixing processes in Asian marginal seas; within the water column from the surface through the interior to the near boundary benthic mixing, the impact of turbulent mixing on the biogeochemical processes was also considered. Observational, theoretical, and numerical modeling studies are all welcome."

Six overseas researchers, 12 Japanese researchers, and 7 students attended the workshop. The research budget provided for this international joint research project has been used to support the travel expenses of the following 3 speakers:

- CHEN, Jia-Lin (National Cheng Kung University, Associate Professor)
- CHENG, Yu-Hsin (National Taiwan Ocean University, Assistant Professor)
- YANG, Kai-Chieh (National Taiwan University, Researcher)

We discussed diversity and universality in the turbulent mixing generated by currents interacting with various topographic features, typhoon, and surface cooling, as well as biogeochemical responses to these turbulent mixing. Finally, we agreed to continue our collaborative research and hold the workshop in the next fiscal year.

The agenda of the workshop is attached below.

Workshop on turbulent mixing in Asian marginal seas

Date: November 29 (Fri.), 2024

Venue: Meeting room on the 6th floor of No. 1 Building for comprehensive study in Faculty of Science in Johoku Campus, Ehime University
(URL of the map: https://www.ehime-u.ac.jp/en/about/access/)

Timetable (assuming 25 min. presentation and 5 min. discussion)

09:20-09:30 Opening remarks: Takahiro Endoh (RIAM)

(*Flow-topography interaction*)

09:30-10:00 Toshiyuki Hibiya (TUMSAT) and Yuki Tanaka (FPU)
Impacts of rough seafloor topography and tidal flow amplitude on benthic mixing hotspots

10:00-10:30 Kai-Chieh Yang (NTU) and Sen Jan (NTU)
Ongoing collaborative projects ARCTERX-KTEX

10:30-11:00 Yu-Hsin Cheng (NTOU)
Submesoscale features and turbulent mixing in the bay of southeastern Taiwan

11:00-11:30 Ming-Huei Chang (NTU)
Symmetric instability and turbulence within Green Island wake

11:30-13:00 Lunch break

13:00-13:30 Jia-Lin Chen (NCKU)
A numerical investigation of relative vorticity and potential vorticity under flow topography interaction

13:30-14:00 Yu-Yu Yeh (NTU)
Turbulence generation via nonlinear lee wave trailing edge instabilities in Kuroshio-seamount interactions

14:00-14:30 Eisuke Tsutsumi (KUFF), Ryuichiro Inoue (JAMSTEC), Takeyoshi Nagai (TUMSAT), Hirohiko Nakamura (KUFF), Ayako Nishina (KUFF), Takahiro Endoh (RIAM), Anne Takahashi (AORI), Ren-Chieh Lien (APL-UW), Eric Kunze (NWRA), Sachihiko Itoh (AORI), and Daisuke Hasegawa (FRA)
Seamount wake and turbulent mixing induced by geostrophic current and tides: an observational study at Hirase Seamount within the Kuroshio in Tokara Strait

14:30-15:00 Shuya Wang (WPI-AIMEC), Xinyu Guo (CMES), Shoichiro Kido (JAMSTEC), Hideharu Sasaki (JAMSTEC), and Yu-Xiang Qiao (TU)
Revisit the Kuroshio frontal eddies in the East China Sea: insight from eddy energy budget

15:00-15:20 Break

(*Surface layer mixing*)

15:20-15:50 Yiing Jang Yang (NTU)

Buoy observations of typhoon-induced turbulent mixing in the western North Pacific ocean

15:50-16:20 Yusuke Ushijima (CMES) and Yutaka Yoshikawa (KyotoU)

Nonlinearly interacting entrainment due to shear and convection in the surface ocean

(*Biogeochemical impact*)

16:20-16:50 Daisuke Hasegawa (FRA)

A detailed underwater glider observation of the Kuroshio front

16:50-17:20 Yingying Hu (CMES), Xinyu Guo (CMES), Yoshikazu Sasai (JAMSTEC), and Eisuke Tsutsumi (KUFF)

Nutrient supply to the euphotic zone by the vertical velocity and vertical mixing over the Kuroshio and Kuroshio Extension)

17:20-18:00 Closing remarks: Takahiro Endoh (RIAM)

国際化推進共同研究概要

No.3

[採択番号]　24EA-3

タイトル：A simulation study of the hotspot using the CALPUFF model for combining satellite observation and numerical model

研究代表者：Chultem BATBOLD

所内世話人：YUMIMOTO Keiya

研究概要：

　中国からモンゴルにかけて広がるゴビ砂漠に代表される砂漠地帯では、春や秋を中心に黄砂が発生し、日本列島に多大な影響を与えている。しかし、その発生メカニズムは未だに不明な部分が多い。黄砂は広大な砂漠地帯で一様に発生すると考えられ、数値モデルでもそのようにシミュレーションされてきた。しかし、近年の研究で、地形や地表面の状態によって、弱い風速でも大量の砂が舞い上げられる黄砂発生ホットスポットと呼ばれる地域があることがわかってきた。本研究では、静止気象衛星ひまわり８号および９号から得られたDust RGBデータを用い、黄砂発生ホットスポットの検出を行った。春季を中心にDust RGBデータを整備し、開発された黄砂発生ホットスポット検出アルゴリズムを用い、2017年から2023年の黄砂発生ホットスポットのデータベース化に成功した。さらに、黄砂発生時の気象データを収集し、GIS上でデータを統合することで、黄砂発生ホットスポットの総合的な解析を行うことが可能となった。このデータベースは今後、黄砂の発生メカニズムや年々変動の解明において重要なものである。

A simulation study of the hotspot using the CALPUFF model for combining satellite observation and numerical model

Department of Environment and Forest Engineering,

School of Engineering and Technology,

National University of Mongolia,

Doctor Chultem BATBOLD

The Content of the Result: ***Observed Dust Hotspots Over Mongolia: A Comparative Results of 2017 and 2023***

1. Introduction

Mongolia experiences significant wind storms in the spring and autumn associated with the formation and dissolution of the Siberian anticyclone. Particularly, southern Mongolia is a part of the Asian dust source region, which remains a critical issue in the East Asian region (Shin et al. 2021; Luo et al. 2022), posing major threats to surrounding environment and human health. This summary compares dust detection data over Mongolian territory during the spring months (March to May) in 2017 and 2023, using DustRGB from Japanese Himawari-8/9 geostationary satellite imagery overlaid on Google Earth. March, April, and May are spring months in Mongolia, characterized by transitional weather as temperatures gradually rise from winter to summer. The objective is to identify local dust hotspots and regional-scale dust storms, analyze their patterns, and determine trends over the given periods.

2. Materials

2.1. The region of interest

The region of interest is defined by the coordinates of the southwest (41°N, 87°E), northwest (52°N, 87°E), northeast (52°N, 120°E), and southeast (41°N, 120°E). Afterwards, we identified dust source spots and analyzed them by Increasing the scale.

2.2. Meteorological data

For selecting the time for data analysis, we relied on two meteorological factors: wind speed and cloud cover in the Gobi region, the main source of natural dust in Mongolia. The meteorological data were downloaded from the website ‘Visual Crossing,’ where weather history and forecasts are accessible (https://www.visualcrossing.com/). Hourly data can be obtained from the website (in some cases, three-hourly data for wind gusts and air pressure, although this is not always available).

2.3. Satellite image processing

Kyushu University provided the dust RGB retrieval code for Himawari-8/9, the Japanese geostationary satellite. The use of geostationary satellites plays an essential role in monitoring dust dispersion because these satellites can provide temporal coverage of when dust storm events evolve and spatial coverage of how wide the dust plume dispersed (Yamamoto, 2016). Himawari-8/9, a new-generation geostationary meteorological satellite, was launched on October 07, 2014, by the Japan Meteorological Agency (JMA) and put into operation on July 07, 2015. Himawari-8 remained operational until 2022, and its observational role was taken over by Himawari-9, the successor of Himawari-8. The Advanced Himawari Imager (AHI) onboard Himawari-8/9 has 16 spectral channels ranging from 0.47 to 13.3 μm wavelength, consisting of 3 visible, 3 near-infrared, 10 infrared channels. A high temporal resolution of 10-min to scan full disk observation enables Himawari-8/9 to observe continuously monitor specific regions for meteorological phenomena, including dust plumes (Bessho et al. 2016).

2.4. Google Earth base map

We identified the source areas by using Google Base Map as the background for the dust RGB images with a code extraction. Next, the National Atlas of Mongolia (Mongolian Academy of Science (MAS) 2009) was employed for detecting geographical objects that are potential dust hotspots.

3. Key findings

3.1. 2017 Observations

1. **Major Dust Hotspots:**
   - Frequent dust activity was observed near Shargiin Tsagaan Lake, Altai mountains slopes, and specific rangelands.
   - Mining areas, such as Bor-Undur flouride mine and Zuundalan coal mine contributed to localized hotspots.
2. **Geographic Features Influencing Dust Activity:**
   - Natural flood trenches, sandy plains, and dried lake beds served as primary dust sources.
   - Intermountain valleys and desert regions (e.g., Gobi) were significant source areas.
3. **Notable Dust Events:**
   - Large dust plumes originated from areas such as the Altai mountains range and southeastern Gobi regions.
   - Anthropogenic activities, including mining and agriculture, exacerbated soil vulnerability and dust generation.
4. **Sources:**
   - Dust originated from mountain slopes, intermountain areas, dry lake beds, and regions with significant natural flood trenches.
5. **Anthropogenic Influence**:

- Dust detected near Dashinchilen soum and the Tuul River indicated surface deterioration linked to human activities.

3.2. 2023 Observations

1. **Major Dust Hotspots**:
   - Frequent dust activity was observed near Khar, Durgun, Bayan, and Khar-Us lakes, located in the Great Lakes Depression.
   - The Tavan Tolgoi mining area and Erdenet mine tailings pond were notable dust sources.
   - Buuntsagaan Lake and Orog Lake in the Gobi region frequently generated dust events.
2. **Geographic Features Influencing Dust Activity**:
   - Sand dunes, dry lake beds, and natural floodwater trenches served as primary dust sources.
   - Intermountain valleys and steppe regions also contributed to dust dispersion.
3. **Notable Dust Events**:
   - Intense dust storms passed through Umnugovi Province and the southeastern Gobi region.
   - Dust plumes originated from the Great Lakes Valley and Lakes Depression.
   - Some dust events lasted for multiple days and shifted significantly over time.
4. **Sources of Dust**:
   - Dust primarily originated from the slopes of the Altai Mountains, intermountain areas, and dry lake regions.
   - Mining areas, including the Oyu Tolgoi and Tayan Nuur mines, contributed to localized dust emissions.
5. **Anthropogenic Influence**:
   - Mining activities, agriculture, and pasture degradation increased soil vulnerability to wind erosion.
   - Dust dispersion was detected from cultivated land near Ulaanbaatar and from burnt surfaces due to wildfires.
   - The Tuul River region exhibited signs of dust emissions, likely linked to intensive land use, leading to surface deterioration.

3.3. Comparison of 2017 and 2023

- **Temporal Patterns**: Both years exhibited peak dust activity in April, with consistent occurrences in known hotspots.
- **Spatial Distribution**: While many dust hotspots overlapped, 2023 showed increased dust activity in the Great Lakes Depression and mining regions.

- **Anthropogenic Factors**: Human-induced dust sources (e.g., mining and agriculture) appeared more prominent in 2023, reflecting expanding industrial activities.
- **Intensity**: Dust plumes in 2023 were more intense and widespread, likely influenced by climate change and land use changes.

4. Discussion & Recommendations

The comparative analysis reveals a rise in dust activity in Mongolia between 2017 and 2023, driven by both natural and anthropogenic factors. Climate change may be exacerbating conditions, such as increased aridity and soil erosion. Additionally, the intensification of dust storms in mining and agricultural areas underscores the need for sustainable land management.

In future research, we will compile the results from preliminary processing conducted, for example, between 2018 and 2022, and in 2024. Additionally, we plan to utilize other medium-orbit or geostationary satellites, such as the Chinese FY-4A (Luo et al. 2022) which offers a more direct viewing angle compared to Himawari-8/9 due to its geostationary position at 105°E, closer to Mongolia. AlNasser (2024) developed a comprehensive methodology to create a five-year (2018–2022) hourly dataset of dust plumes using data from the Spinning Enhanced Visible and InfraRed Imager (SEVIRI) aboard geostationary Meteosat satellites. This approach enabled detailed tracking and analysis of dust plume dynamics across major dust-producing regions. Our future research will focus on analyzing dust plume dynamics, facilitating studies into dust sources, transport mechanisms, and environmental impacts using similar methodologies within the field of dust research.

5. Conclusion

This study provides a comparative analysis of dust activity in Mongolia during the spring months of 2017 and 2023 using Himawari-8/9 DustRGB satellite imagery. The findings highlight key dust hotspots, sources, and dispersion patterns over time. While both years exhibited peak dust activity in April, notable differences emerged in the spatial distribution, intensity, and anthropogenic influence on dust emissions. Particularly, 2023 showed a wider extent of dust activity, with increased contributions from mining, agriculture, and land degradation in the Great Lakes Depression and other regions.

The observed increase in dust storm intensity and frequency suggests that climate change and land use changes may be exacerbating Mongolia's dust emissions. The expansion of mining operations, pasture degradation, and the desiccation of water bodies further contribute to dust dispersion.

Future research should extend the analysis to include additional years (2018–2022, 2024) to better understand long-term trends. Incorporating data from other geostationary and medium Earth orbit satellites, such as FY-4A and SEVIRI (Meteosat), could enhance dust detection accuracy and improve dust transport modeling. A multi-satellite approach will provide better spatial and temporal coverage, facilitating a more comprehensive understanding of Mongolia's evolving dust dynamics and their broader regional impacts.

6. References

Bessho, Kotaro, Kenji Date, Masahiro Hayashi, Akio Ikeda, Takahito Imai, Hidekazu Inoue, Yukihiro Kumagai, et al. 2016. "An Introduction to Himawari-8/9— Japan's New-

Generation Geostationary Meteorological Satellites." *Journal of the Meteorological Society of Japan. Ser. II* 94 (2): 151–83. https://doi.org/10.2151/jmsj.2016-009.

Luo, Jingning, Fuxiang Huang, Song Gao, Song Liu, Ruixia Liu, and Abhay Devasthale. 2022. "Satellite Monitoring of the Dust Storm over Northern China on 15 March 2021." *Atmosphere* 13 (January):157. https://doi.org/10.3390/atmos13020157.

Mongolian Academy of Science (MAS), The Institute of Geography. 2009. *Mongolian National Atlas*. Vol. II. Ulaanbaatar.

AlNasser, F., Entekhabi, D. DustSCAN: A Five Year (2018-2022) Hourly Dataset of Dust Plumes From SEVIRI. Sci Data 11, 607 (2024). https://doi.org/10.1038/s41597-024-03452-4

Shin, Yu-Rim, Eun-Ha Sohn, Ki-Hong Park, Geun-Hyeok Ryu, Soobong Lee, Seon-Young Lee, and Na-Yeon Park. 2021. "Improved Dust Detection over East Asia Using Geostationary Satellite Data." *Asia-Pacific Journal of Atmospheric Sciences* 57 (4): 787–98. https://doi.org/10.1007/s13143-021-00230-9.

K. Yamamoto, "Dust Detection Using IR Channels of Himawari-8," Universiy of Wisconsin-Madison, 206AD. [Online]. Available: https://www.aos.wisc.edu/aosjournal/Volume28/Yamamoto_MS.pdf

7. Appendices

7.1. Dust detection over Mongolian territory in 2017 (March to May)

<u>**Figure 1 – April 07, 2017**</u>

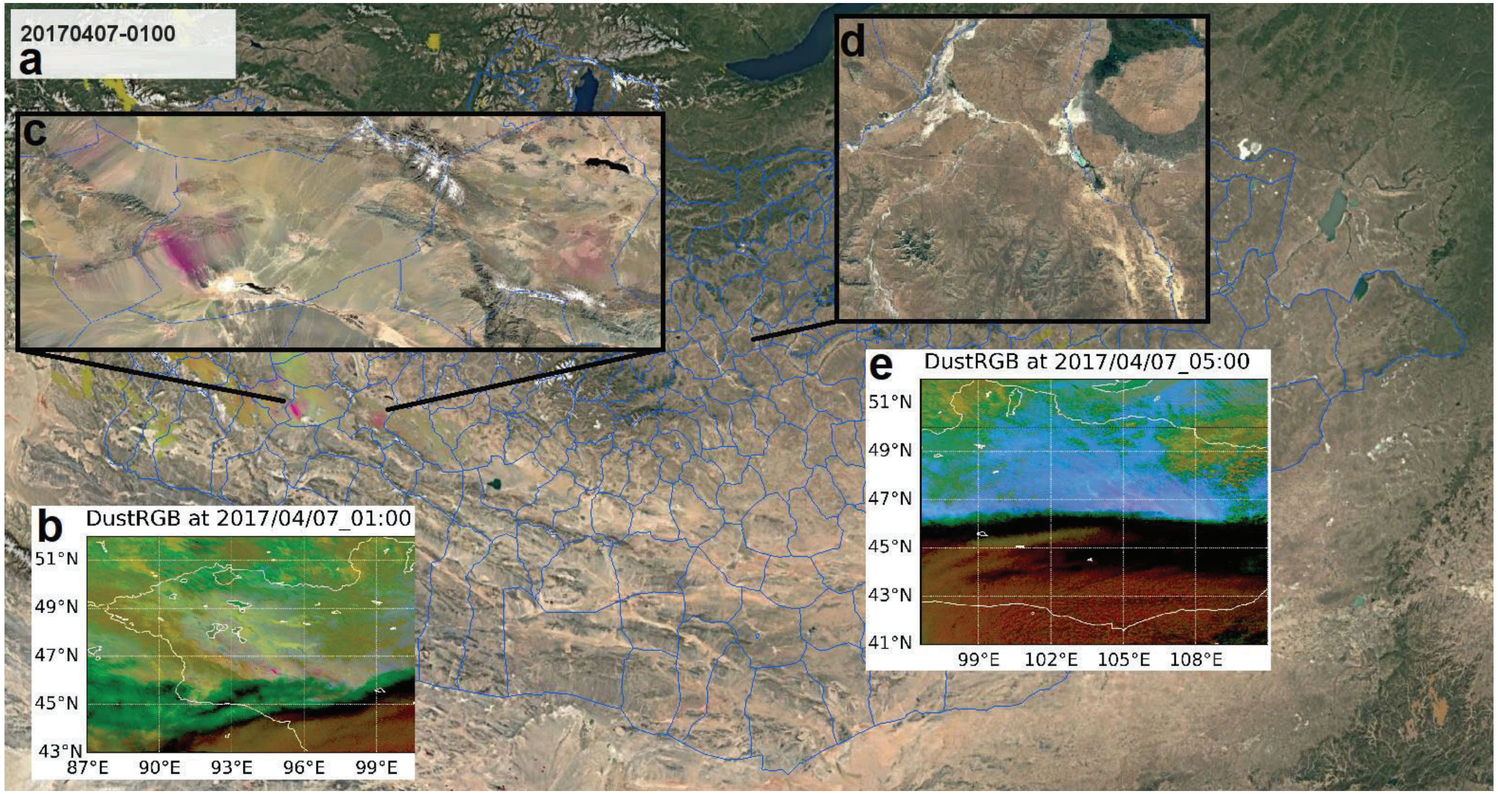

Introduction: Slight dust outbreaks were observed.

Figure 1a: The DustRGB map overlaid on Google Earth at 01:00 UTC on April 7, 2017.
Figure 1b: The DustRGB map at 01:00 UTC on April 7, 2017.
Figure 1c: A dust hotspot located north of Shargiin Tsagaan Lake (a regular dust hotspot). The hotspot is situated on the slope of a mountain with numerous natural flood trenches. Besides, as shown in the eastern part of the image, a sandy plain extends along the mountain valley. Dust is dispersed from this area.
Figure 1d: Dust detection near the Dashinchilen soum center in Bulgan province. Dust is dispersed from the area between the Khar Bukhiin River and the Tuul River. Since the source is near the local administrative center, anthropogenic impacts might have influenced surface deterioration. A very slight dust plume can be observed in Figure 1e.
Figure 1e: The DustRGB map overlaid on Google Earth at 05:00 UTC on April 07, 2017.

Figure 2 – April 16, 2017

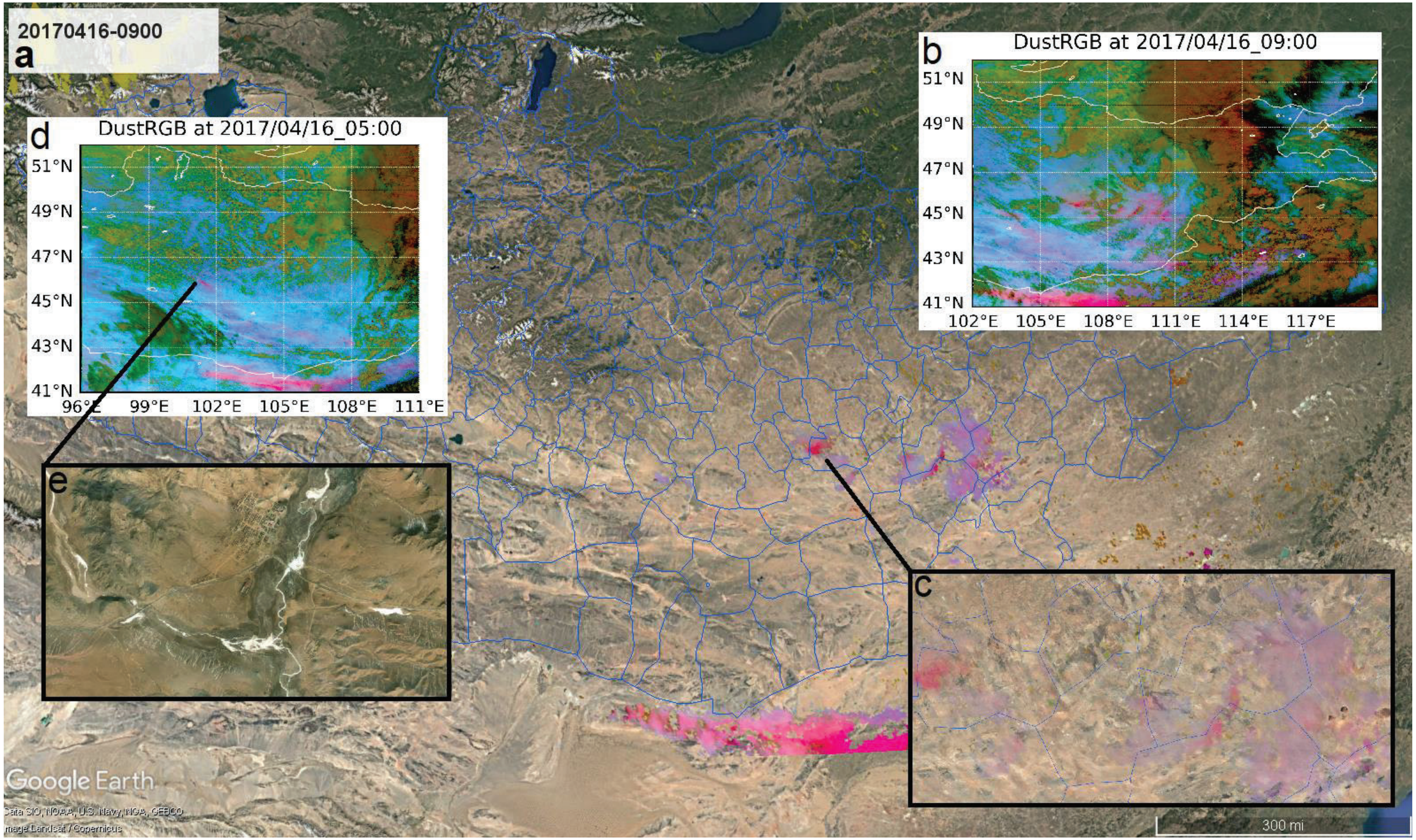

Figure 2a: The DustRGB map overlaid on Google Earth at 09:00 UTC on April 16, 2017.
Figure 2b: The DustRGB map at 09:00 UTC on April 16, 2017.
Figure 2c: Dust detection from a rangeland in a semi-desert region of Gurvansaikhan soum, Dundgovi province.
Figure 2d: The DustRGB map at 05:00 UTC on April 16, 2017.
Figure 2e: Dust hotspot near the Nariinteel soum center in Uvurkhangai province, along the Taats River.

Figure 3 – April 18, 2017

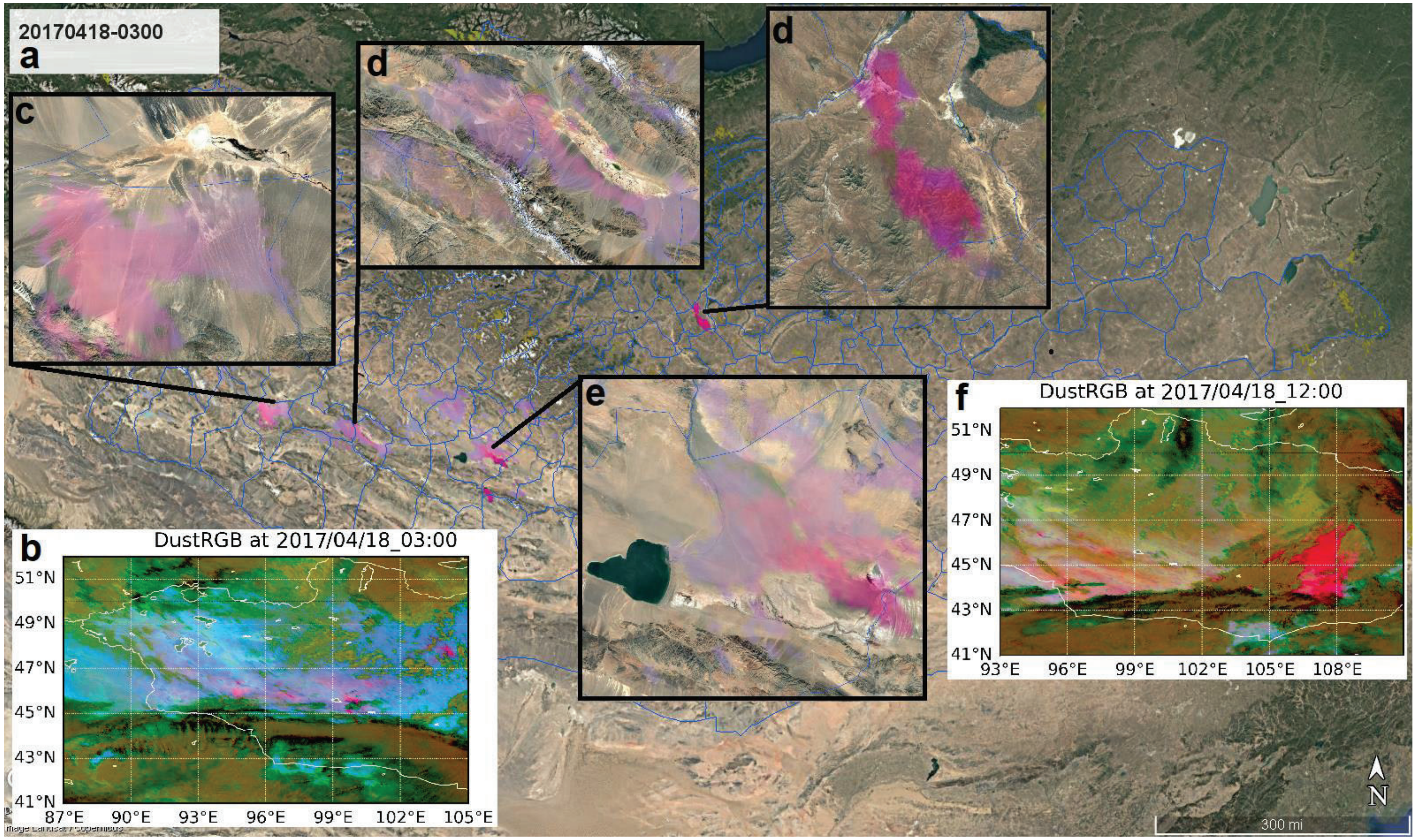

Introduction: Four observable dust hotspots and dust dispersions were detected at 03:00 UTC on Apr 18, 2017. Then the plume headed to east and southeast through Gobi region (as shown in **Figure 3f**).

Figure 3a: The DustRGB map overlaid on Google Earth at 03:00 UTC on April 18, 2017.
Figure 3b: The DustRGB map at 03:00 UTC on April 18, 2017.
Figure 3c: Dust dispersion south of Shargiin Tsagaan Lake (a regular dust hotspot). The hotspot is located on the slope of a mountain with numerous natural flood trenches.
Figure 3d: Dust dispersion from the intermountain area of the Altai mountains range.
Figure 3e: Dust detection around Buuntsagaan Lake, near the intersection of Buuntsagaan Lake and Baidrag River (a major tributary of the lake).
Figure 3f: The DustRGB map at 12:00 UTC on April 18, 2017.

Figure 4 – April 19, 2017

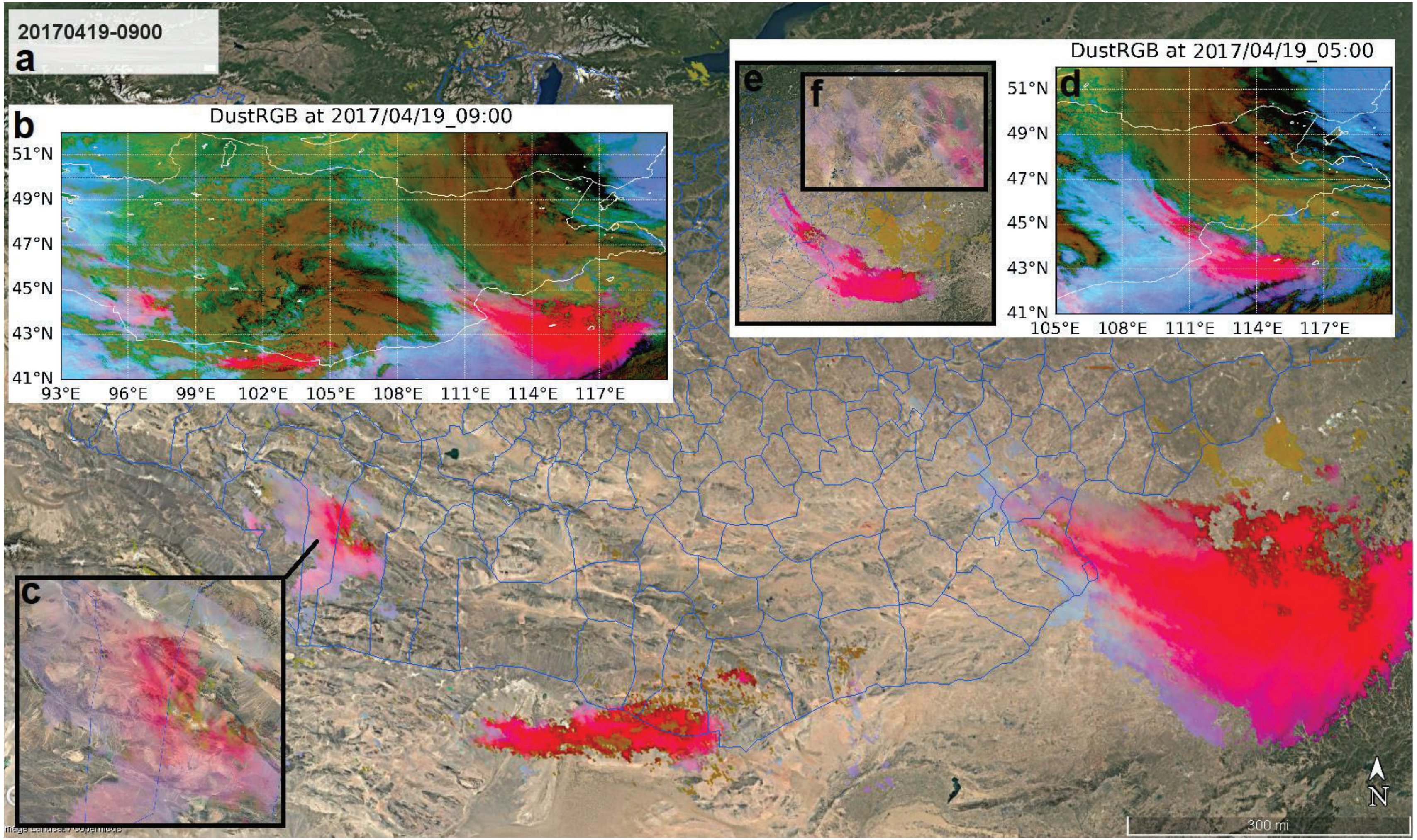

Introduction: Dust dispersed from the northwest and southeast regions in the Gobi.

Figure 4a: The DustRGB map overlaid on Google Earth at 09:00 UTC on April 19, 2017.
Figure 4b: The DustRGB map at 09:00 UTC on April 19, 2017.
Figure 4c: Dust dispersion from the intermountain area of the Altai mountains range.
Figure 4d: The DustRGB map at 05:00 UTC on April 19, 2017.
Figure 4e & f: Dust hotspots were detected from the Bor-Undur fluoride mine and the Zuundalan coal mine.

Figure 5 – April 21, 2017

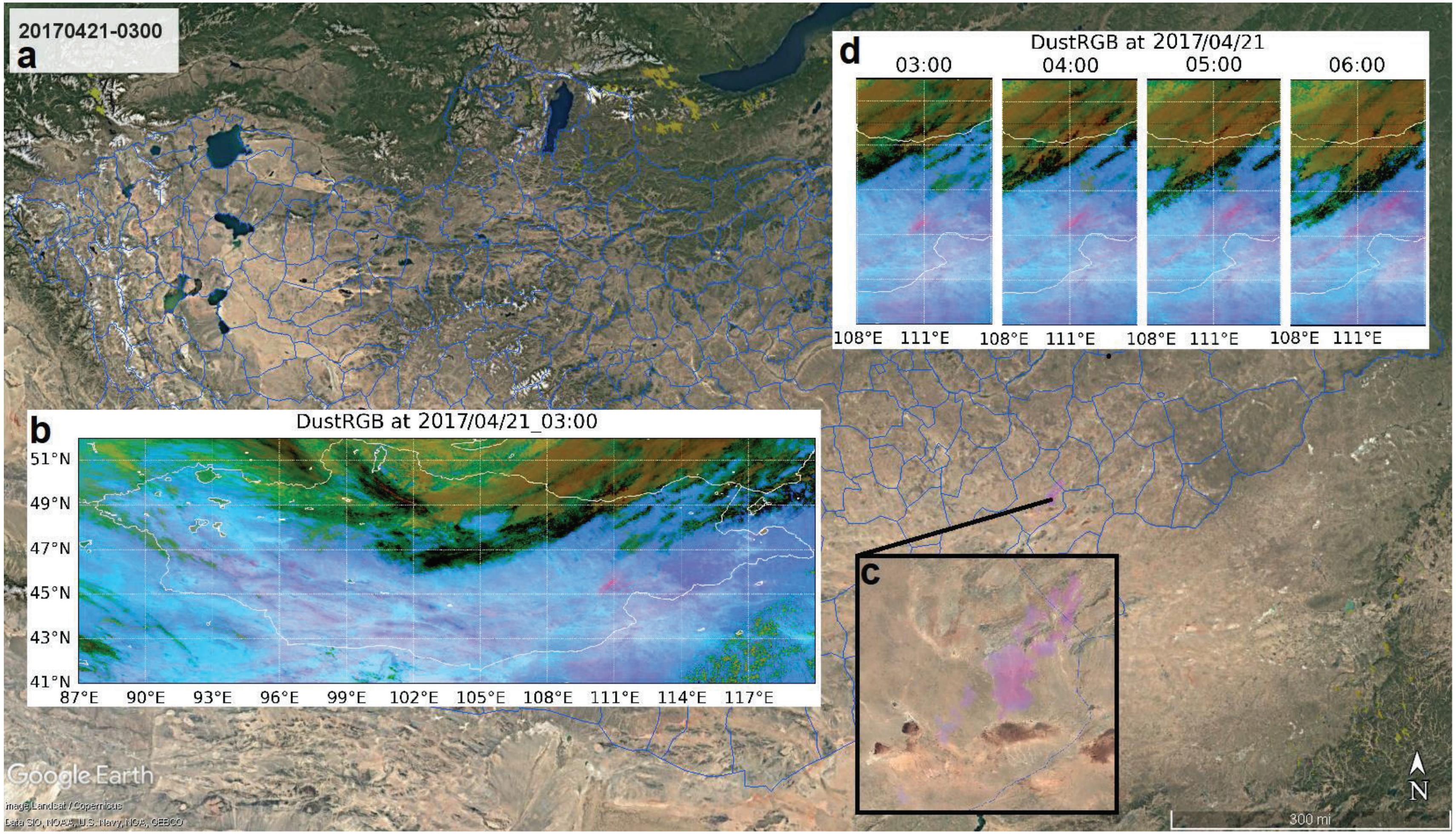

Introduction: A small dust plume was detected in the southeastern part of the country.

Figure 5a: The DustRGB map overlaid on Google Earth at 03:00 UTC on April 21, 2017.
Figure 5b: The DustRGB map at 03:00 UTC on April 21, 2017.
Figure 5c: The initial dust hotspot originated from the dry bed of Tsagaan Nuur Lake, a temporary lake fed by floodwaters in Altanshiree soum, Dornogovi province.
Figure 5d: The evolution of the dust plume over time at 03:00, 04:00, 05:00, and 06:00 UTC on April 21, 2017.

Figure 6 – May 02, 2017

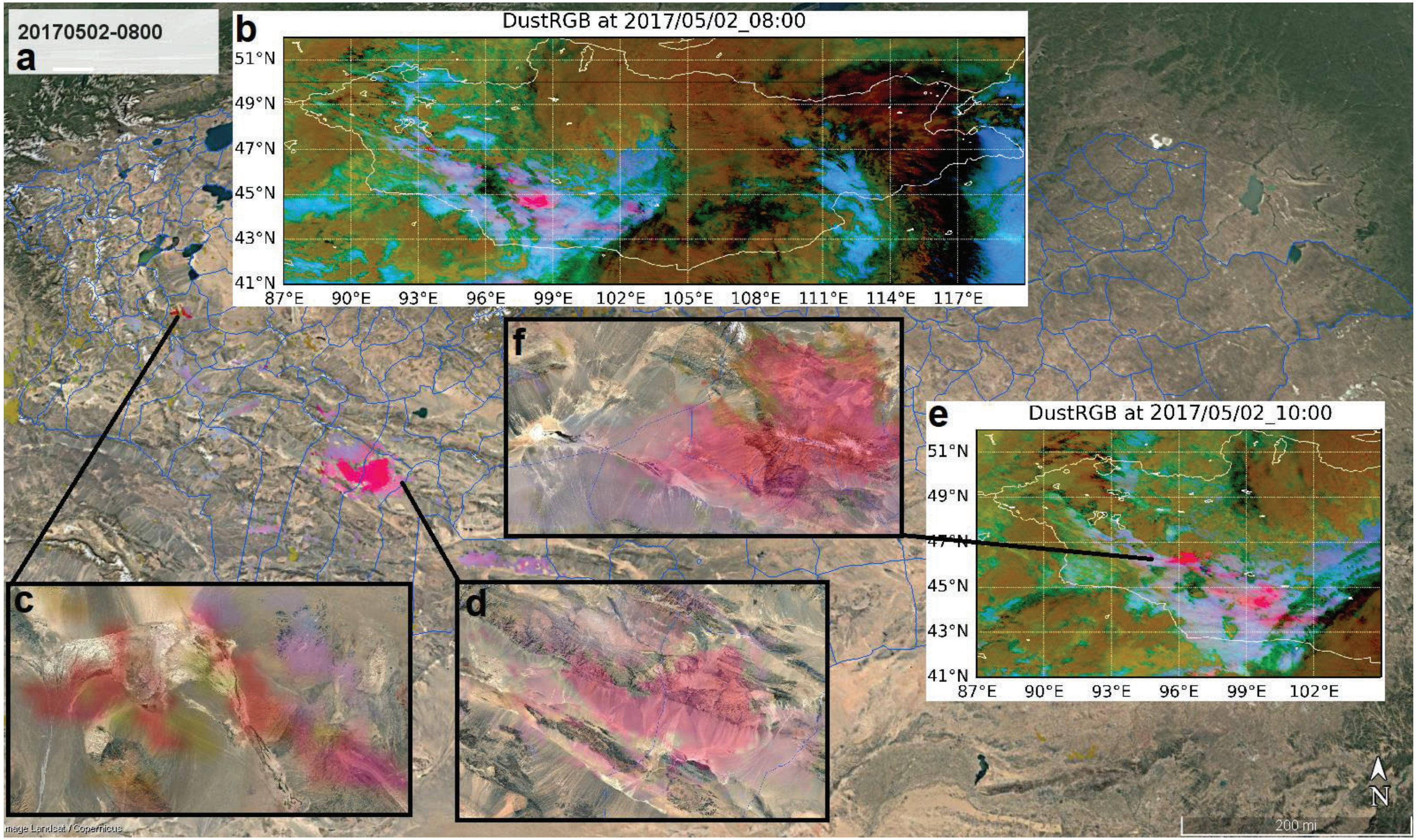

Figure 6a: The DustRGB map overlaid on Google Earth at 08:00 UTC on May 02, 2017.
Figure 6b: The DustRGB map at 08:00 UTC on May 02, 2017.
Figure 6c: A dust hotspot from the dry bed of Tsagaan Lake and its tributary river in Darvi soum, Khovd province.
Figure 6d: Dust dispersion from the intermountain area of the Altai mountains range.
Figure 6e: The DustRGB map at 10:00 UTC on May 02, 2017.
Figure 6f: A dust hotspot near Shargiin Tsagaan Lake and its supplying river.

Figure 7 – May 03, 2017

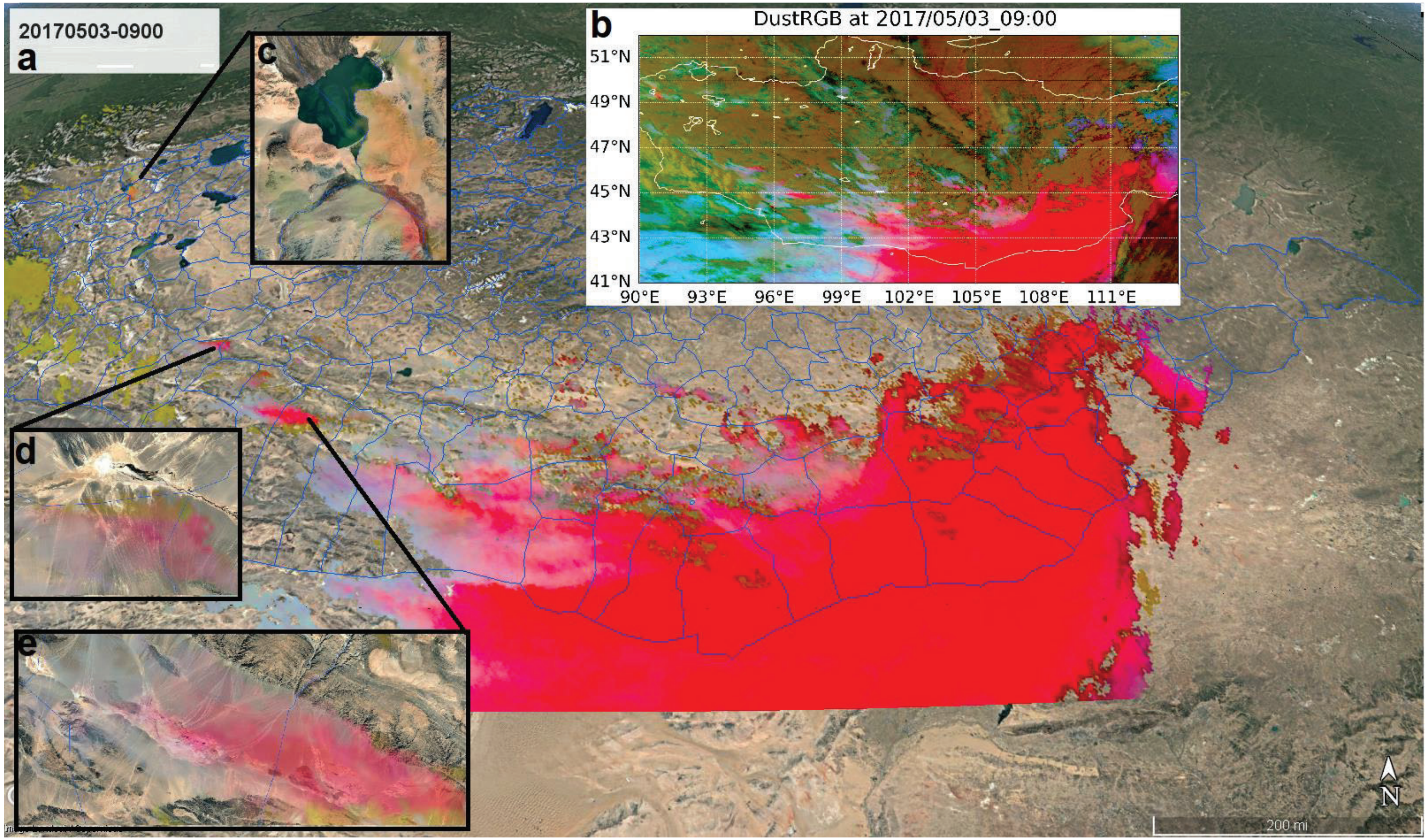

Introduction: Some dust hotspots in the Altain mountan region. Besides an intense regional scale dust storm occurred south and southeast part of the country.

Figure 7a: The DustRGB map overlaid on Google Earth at 09:00 UTC on May 03, 2017.
Figure 7b: The DustRGB map at 09:00 UTC on May 03, 2017.
Figure 7c: Dust dispersion along the shore of Achit Lake and its supplying river, the Khovd River, in the Great Lakes Depression.
Figure 7d: Dust dispersion north of Shargiin Tsagaan Lake (a regular dust hotspot). The hotspot is on the slope of a mountain with numerous natural flood trenches.
Figure 7e: A dust hotspot from the seasonal dry lake bed in the Altai mountains valley.

Figure 8 – May 04, 2017

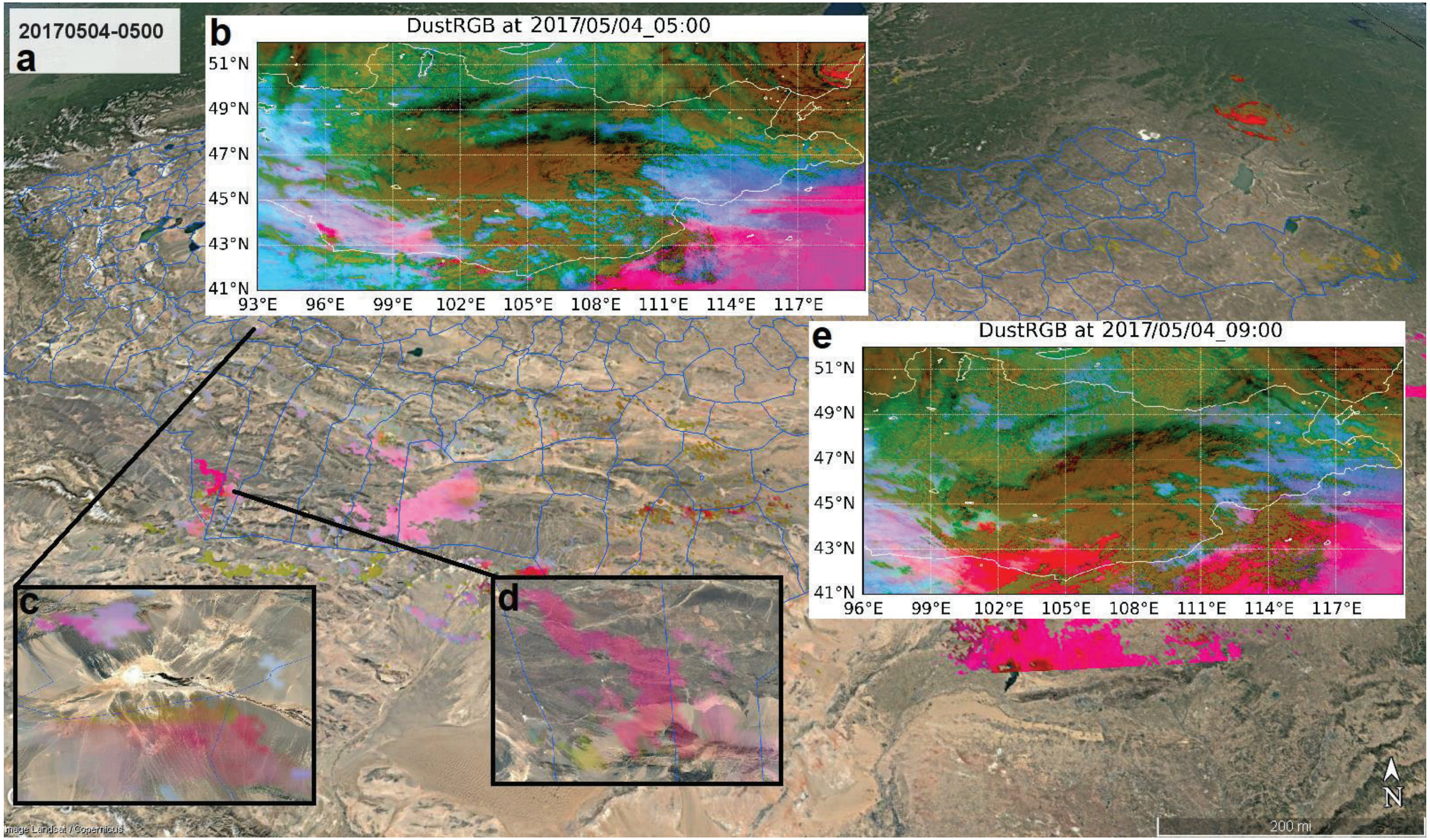

Figure 8a: The DustRGB map overlaid on Google Earth at 05:00 UTC on May 04, 2017.
Figure 8b: The DustRGB map at 05:00 UTC on May 04, 2017.
Figure 8c: Dust dispersion north of Shargiin Tsagaan Lake (a regular dust hotspot). The hotspot is located on the slope of a mountain with numerous natural flood trenches.
Figure 8d: A dust hotspot from the Altai Inner Gobi.
Figure 8e: The DustRGB map at 09:00 UTC on May 4, 2017. The dust hotspot in Figure **8d** evolved into a large dust plume.

Figure 9 – May 05, 2017

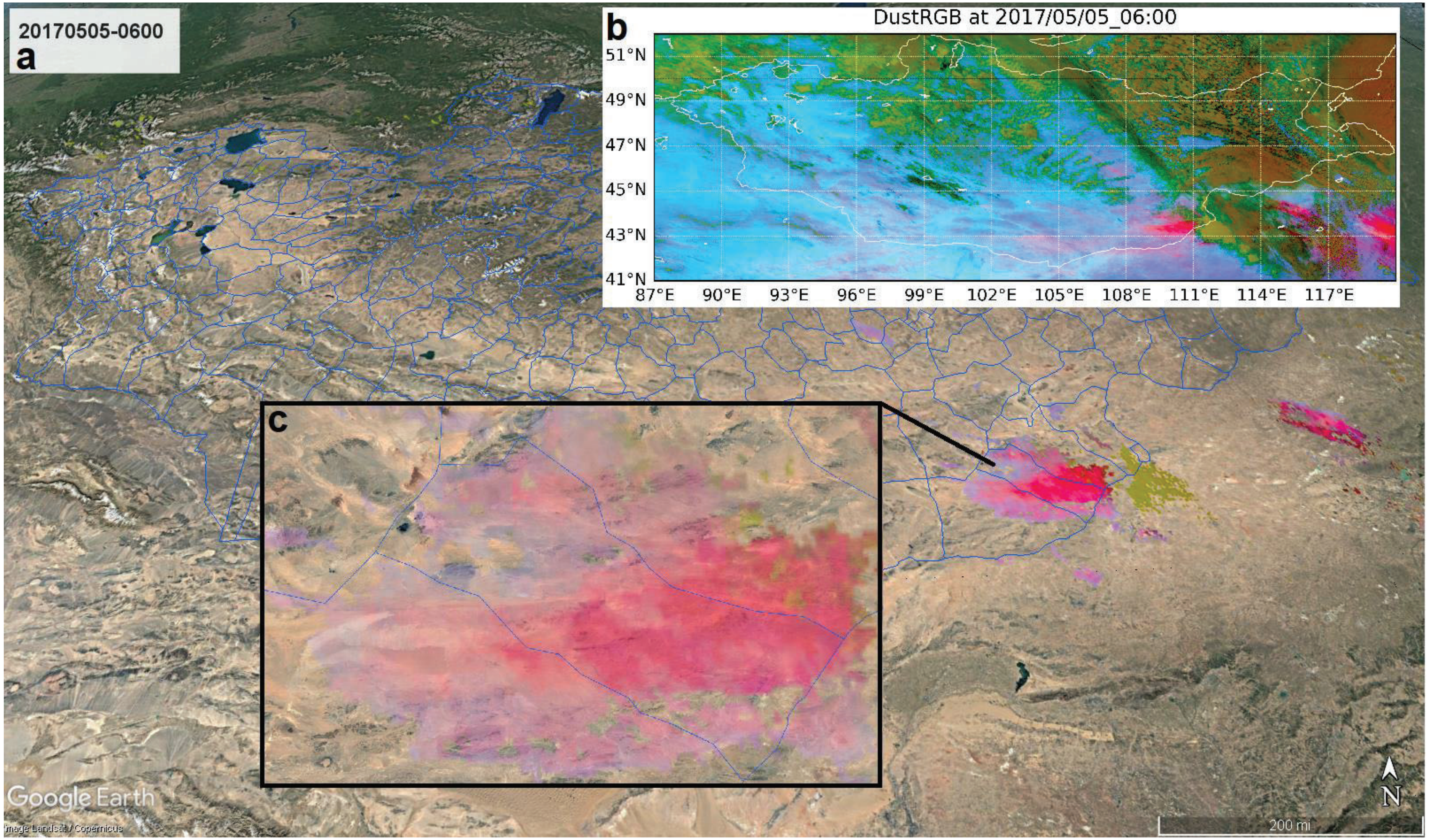

Figure 9a: The DustRGB map overlaid on Google Earth at 06:00 UTC on May 05, 2017.
Figure 9b: The DustRGB map at 06:00 UTC on May 05, 2017.
Figure 9c: A dust plume evolved from the southeastern part of the Gobi region in Dornogovi province.

Figure 10 – May 10, 2017

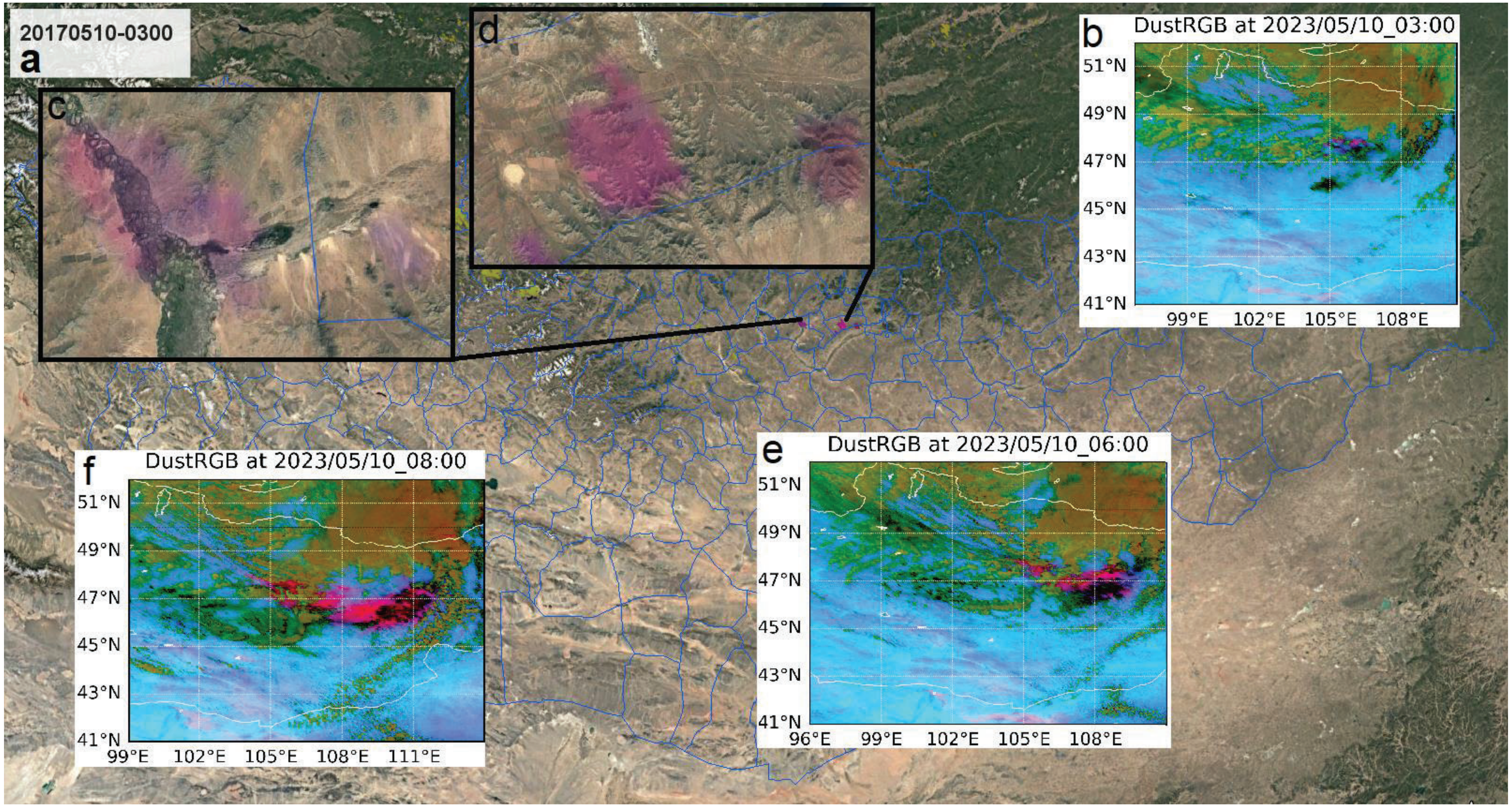

Introduction: Dust dispersion occurred from the center of the country, near Ulaanbaatar, the capital city of Mongolia. Two slight dust plumes evolved into a larger dust plume.

Figure 10a: The DustRGB map overlaid on Google Earth at 03:00 UTC on May 10, 2017.
Figure 10b: The DustRGB map at 03:00 UTC on May 10, 2017.
Figure 10c: A dust hotspot along the Tuul River in Lun soum, Tuv province.
Figure 10d: A dust hotspot from the cultivated area in Argalant soum, Tuv province.
Figure 10e: The DustRGB map at 06:00 UTC on May 10, 2017.
Figure 10f: The DustRGB map at 08:00 UTC on May 10, 2017.

7.2. Dust detection over Mongolian territory in 2023 (March to May)

Figure 11 – March 06, 2023

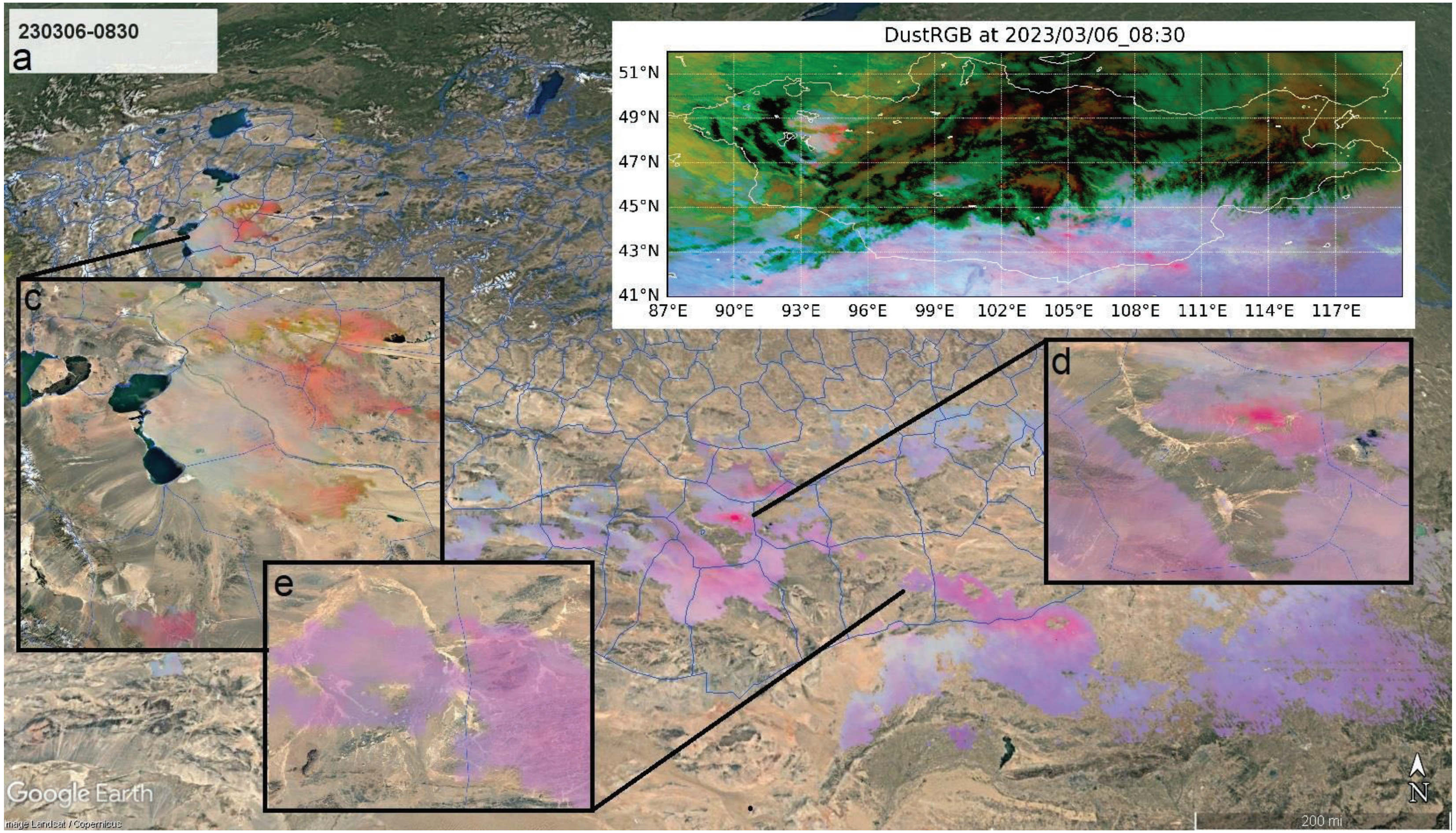

Introduction: Three observable dust hotspots were detected.

Figure 11a: The DustRGB map overlaid on Google Earth at 08:30 UTC on March 06, 2023.
Figure 11b: The DustRGB map at 08:30 UTC on March 06, 2023.
Figure 11c: Dust detection near Khar, Durgun, and Bayan lakes. This area is known as the Great Lakes Depression, where sand dunes exist.
Figure 11d: Dust detection near the "Tavan Tolgoi" mining area. There is a natural floodwater trench in this region. Additionally, mining activities contribute to soil vulnerability.
Figure 11e: Dust detection from a natural floodwater trench.

Figure 12 – March 09, 2023

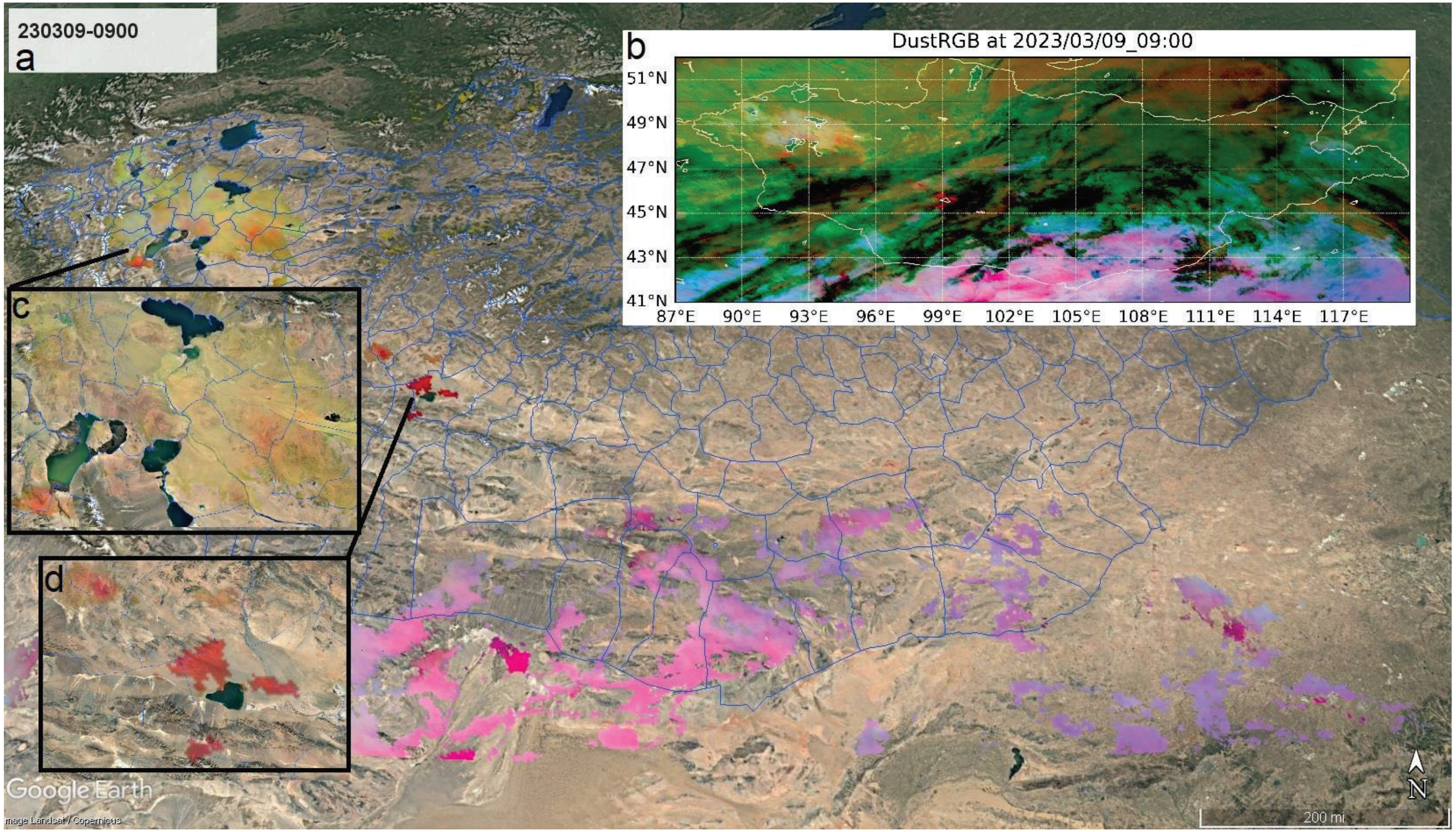

Figure 12a: The DustRGB map overlaid on Google Earth at 09:00 UTC on March 09, 2023.
Figure 12b: The DustRGB map at 09:00 UTC on March 09, 2023.
Figure 12c: Dust detection near Khar, Durgun, and Khar-Us lakes. This area is known as the Great Lakes Depression, where sand dunes exist.
Figure 12d: Dust detection around Buuntsagaan Lake. There is a natural floodwater trench.

Post script: It cannot be ruled out that other dust hotspots may exist beneath the cloud cover (see Figure 2a), especially the dust hotspot shown in Figure **12d**. An extensive dust storm passed through the Umnugovi Province (see Figures 2a and 2b).

Figure 13 – March 10, 2024

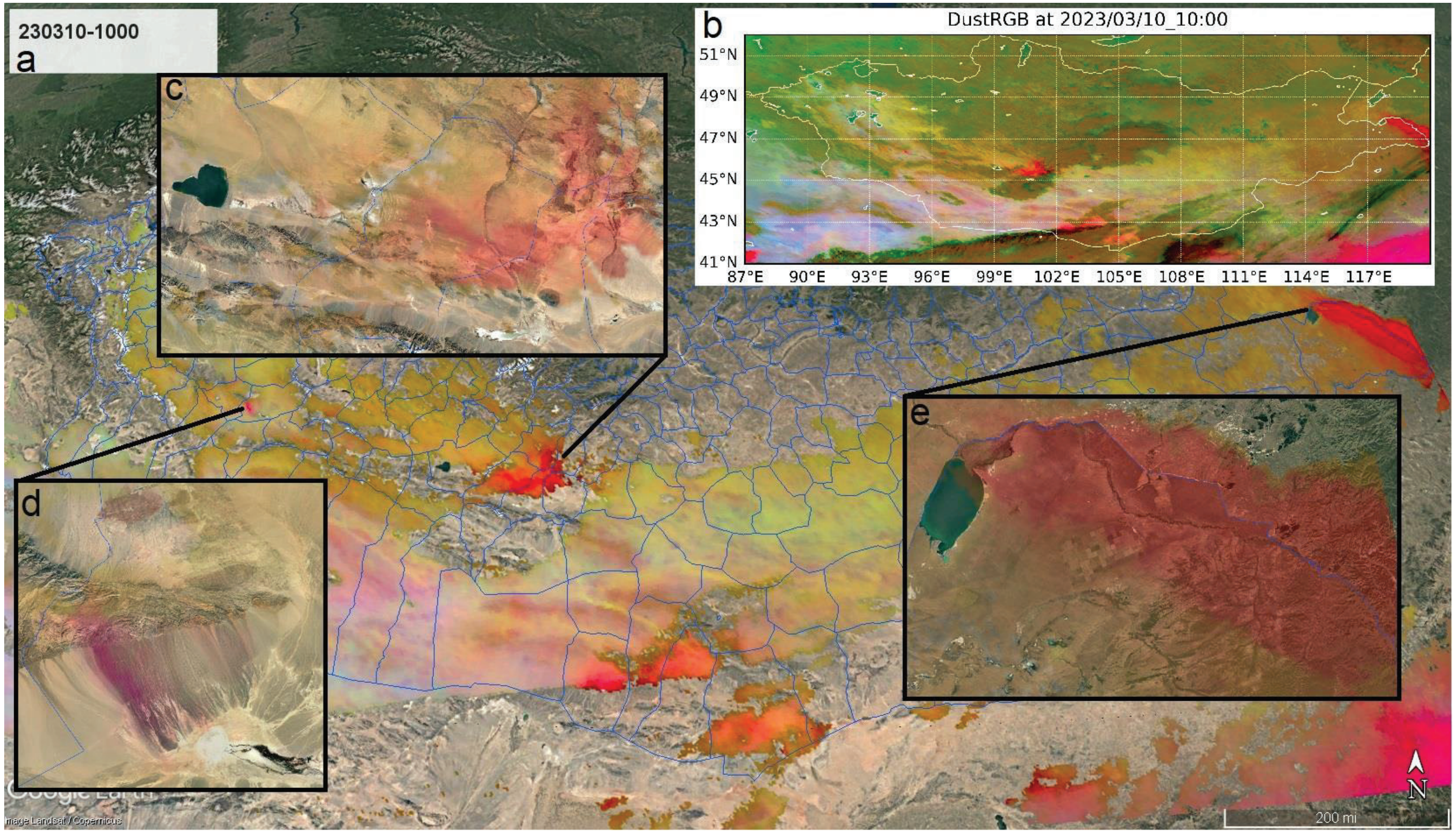

Introduction: Four observable dust hotspots and dust dispersion in the Gobi region were also detected (beneath cloud cover).

Figure 13a: The DustRGB map overlaid on Google Earth at 10:00 UTC on March 10, 2023.
Figure 13b: The DustRGB map at 10:00 UTC on March 10, 2023.
Figure 13c: Dust detection between Buuntsagaan Lake and Orog Lake, along the Tuin River (a tributary of Orog Lake). This area is called the Lakes Depression in the Gobi region.
Figure 13d: Dust dispersion from the north of Shargiin Tsagaan Lake (a regular dust hotspot). The hotspot is on the slope of a mountain with numerous natural flood trenches.
Figure 13e: Dust dispersion along the Khalkh River (a tributary of Buir Lake, which forms the water border between Mongolia and China).

Post script: It cannot be ruled out that other dust hotspots exist below the cloud cover. A dust storm passed through the Umnugovi Province (see Figures **13a** and **13b**).

Figure 14 – March 12, 2023

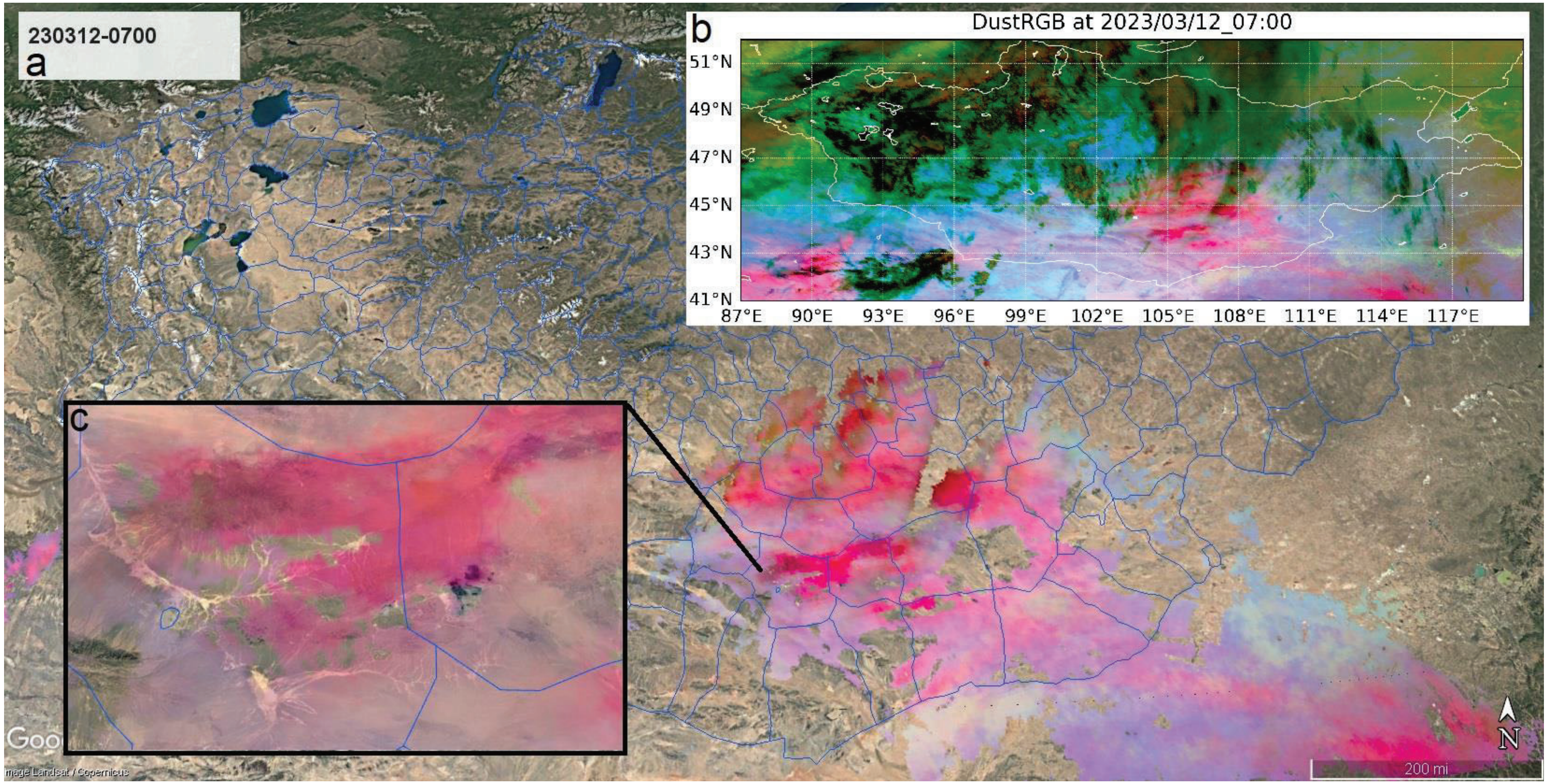

Introduction: Dust dispersed from the northern part of the Gobi region, and some intense dust plemes were observed.

Figure 14a: The DustRGB map overlaid on Google Earth at 07:00 UTC on March 12, 2023.
Figure 14b: The DustRGB map at 07:00 UTC on March 12, 2023.
Figure 14c: Dust detection near the "Tavan Tolgoi" mining area. There is a natural floodwater trench. Additionally, mining activities impact the vulnerability of the soil.

Figure 15 – March 14, 2023

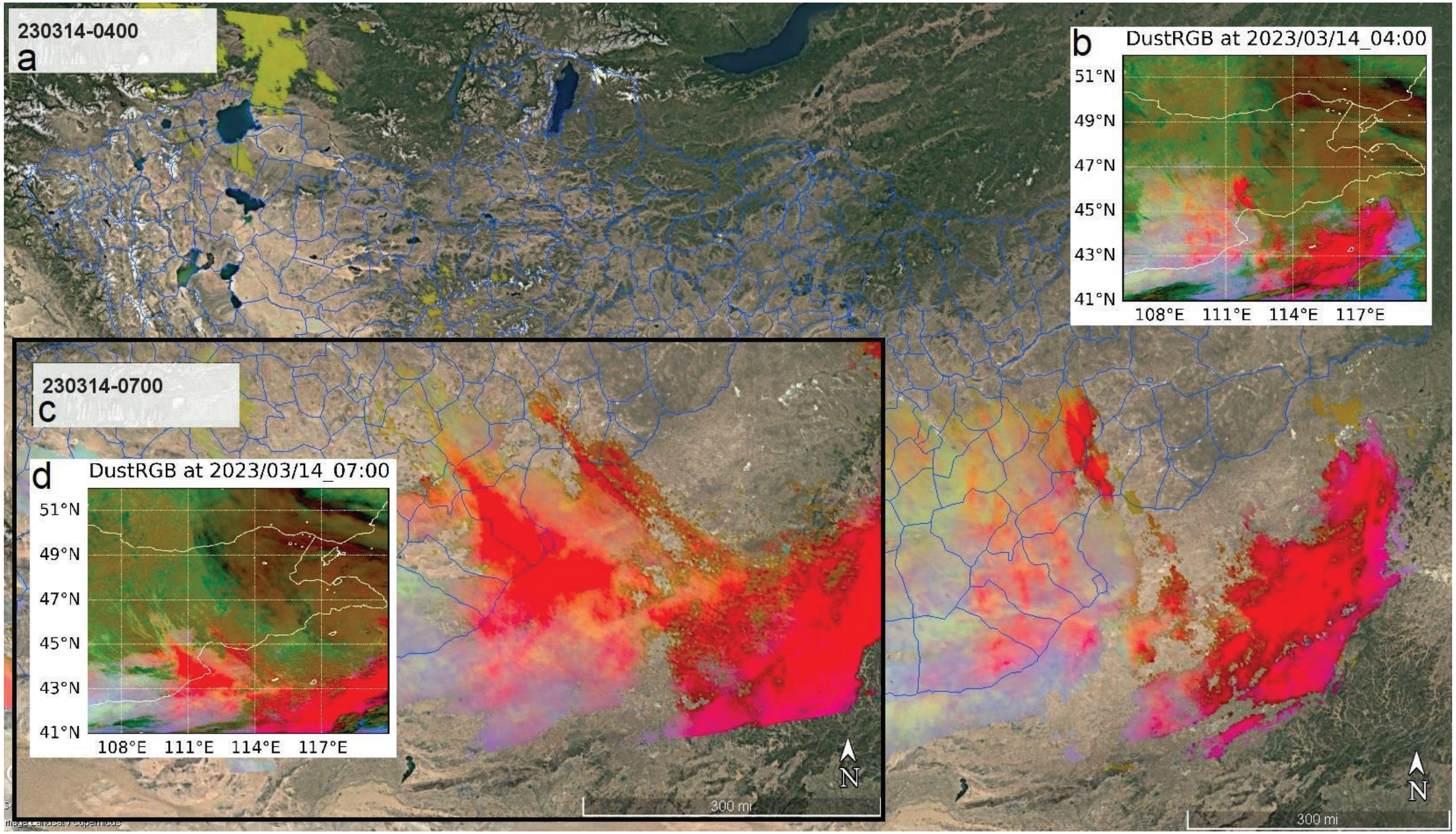

Introduction: Dust dispersed from the northeastern part of the Gobi region, and intense dust clouds were also observed.

Figure 15a: The DustRGB map overlaid on Google Earth at 04:00 UTC on March 14, 2023.
Figure 15b: The DustRGB map at 04:00 UTC on March 14, 2023.
Figure 15c: The DustRGB map overlaid on Google Earth at 07:00 UTC on March 14, 2023.
Figure 15d: The DustRGB map at 07:00 UTC on March 14, 2023.

<u>Figure 16 – March 21, 2023</u>

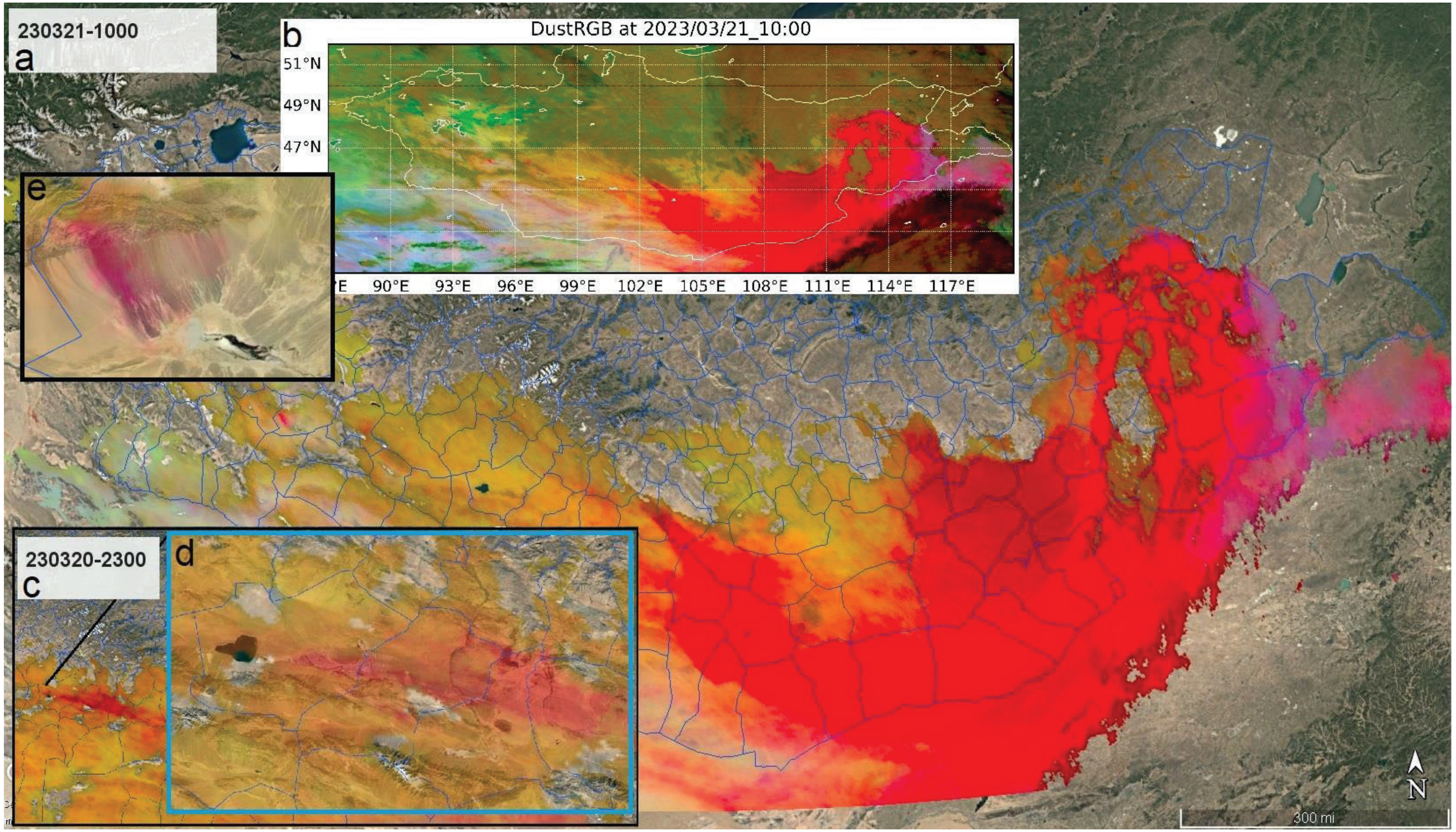

Introduction: In addition to an intense dust storm from the southern to the eastern part of Mongolian territory, two dust hotspots were detected.

Figure 16a: The DustRGB map overlaid on Google Earth at 10:00 UTC on March 21, 2023.
Figure 16b: The DustRGB map at 10:00 UTC on March 21, 2023.
Figure 16c: The DustRGB map overlaid on Google Earth at 23:00 UTC on March 20, 2023.
Figure 16d: Dust detection between Buuntsagaan Lake and Orog Lake. This area is called the Lakes Depression in the Gobi region.

Post script: A very intense dust storm occurred and lasted for an entire day. The dust hotspot shown in Figure 6d was the initial point.

Figure 17 – March 22, 2023

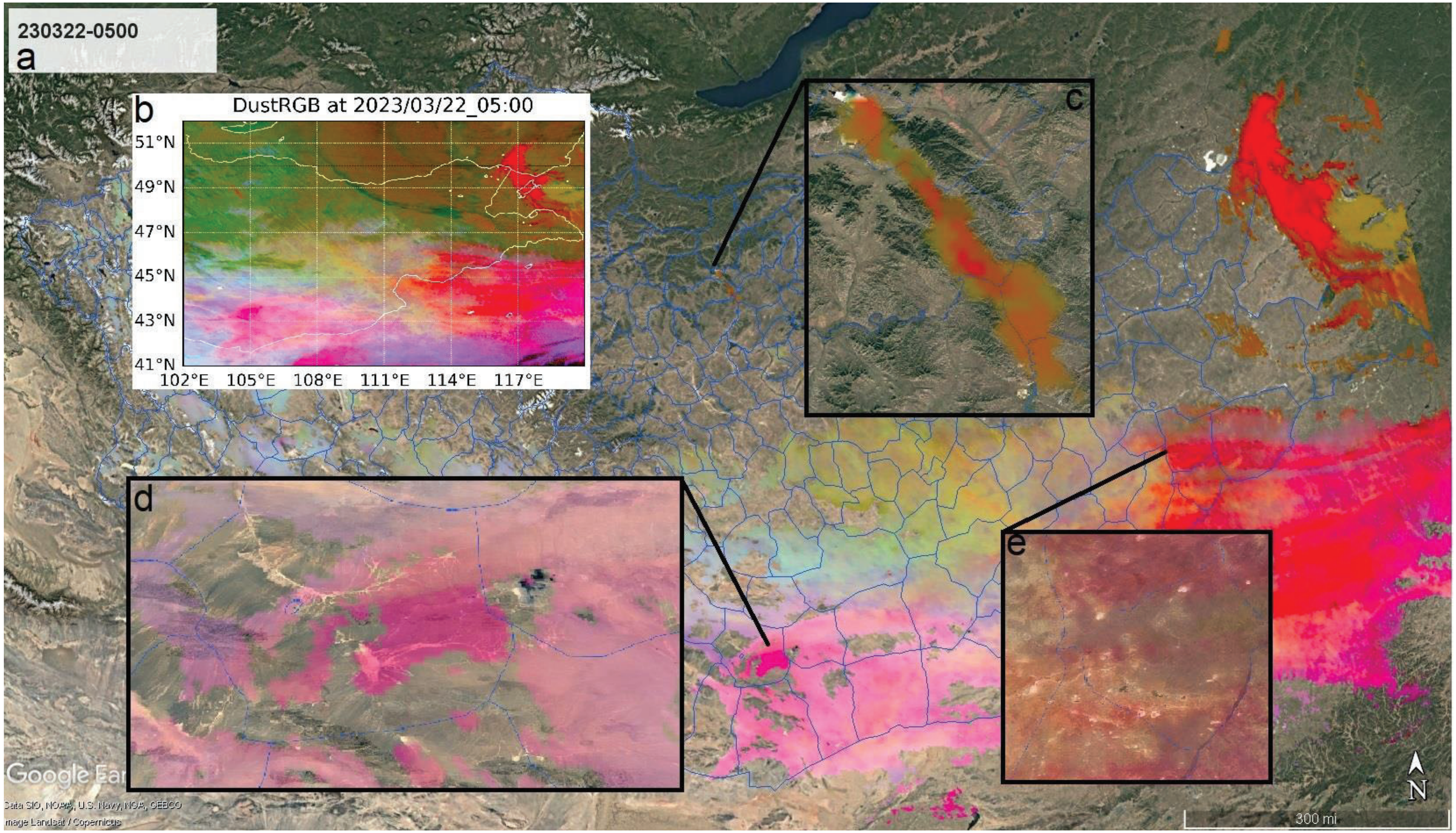

Introduction: Dust dispersion from the Erdenet mine tailings pond was detected. Additionally, the eastern and southern parts of Mongolia were affected by a dust storm.

Figure 17a: The DustRGB map overlaid on Google Earth at 05:00 UTC on March 22, 2023.
Figure 17b: The DustRGB map at 05:00 UTC on March 22, 2023.
Figure 17c: Dust dispersion from the Erdenet mine tailings pond.
Figure 17d: Dust detection near the "Tavan Tolgoi" mining area. There is a natural floodwater trench. Additionally, mining activities impact the vulnerability of the soil. Very intense dust was dispersed from the seasonal dry lake "Balgasiin Ulaan".
Figure 17e: At the edge of the intense dust cloud, there is a national protected area that includes several seasonal lakes.

Figure 18 – March 31, 2023

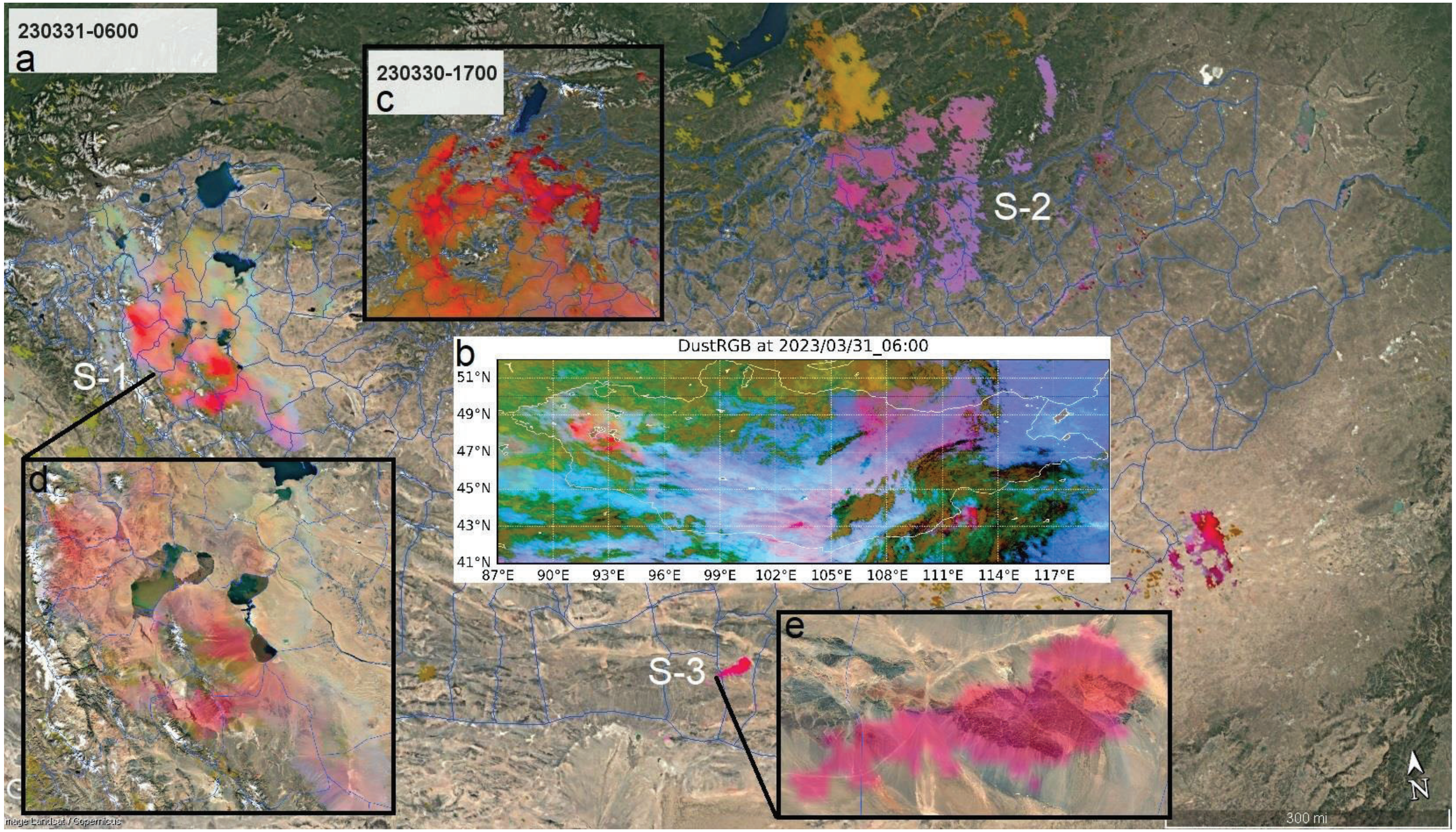

Introduction: Two dust hotspots were detected. A dust storm occurred from west to east in the northern part of the territory (Figure **18a** and **S-2** illustrate the shift from 17:00 to 06:00 UTC).

Figure 18a: The DustRGB map overlaid on Google Earth at 06:00 UTC on March 31, 2023.
Figure 8b: The DustRGB map at 06:00 UTC on March 31, 2023.
Figure 18c: Dust dispersion from the north side of Khangai mountains and south side of Khuvsgul mountains.
Figure 18d: Dust detection near Khar Lake, Durgun Lake, and Khar-Us Lake. This area is called the Great Lakes Depression, where sand dunes exist.
Figure 18e: Intense dust detection in a part of the Govi-Altai Mountains.

Post script: The northern part of Mongolia is a mountainous region with forests, where dust dispersion is very rare. Additionally, there is typically snow cover on during that period each year. However, due to increasing climate change, a dust storm occurred.

Figure 19 – April 09, 2023

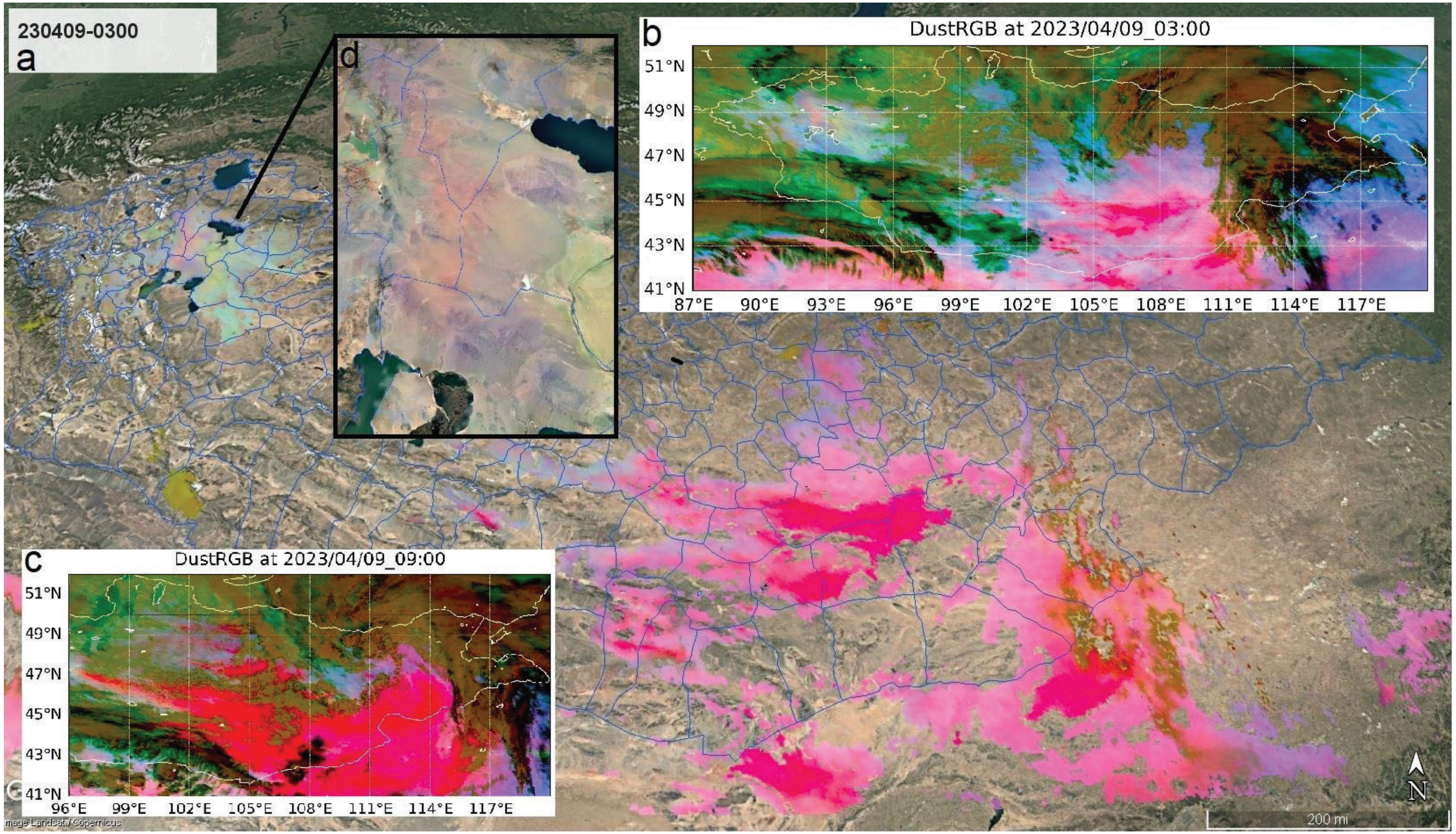

Introduction: An intense dust storm occurred over the central and southeastern parts of the territory.

Figure 19a: The DustRGB map overlaid on Google Earth at 03:00 UTC on April 09, 2023.
Figure 19b: The DustRGB map at 03:00 UTC on April 09, 2023.
Figure 19c: The DustRGB map at 09:00 UTC on April 09, 2023.
Figure 19d: Dust detection near Khargas Lake, Khar Lake, and Khar-Us Lake. This area is called the Great Lakes Depression, where sand dunes exist.

Figure 20 – April 10, 2023

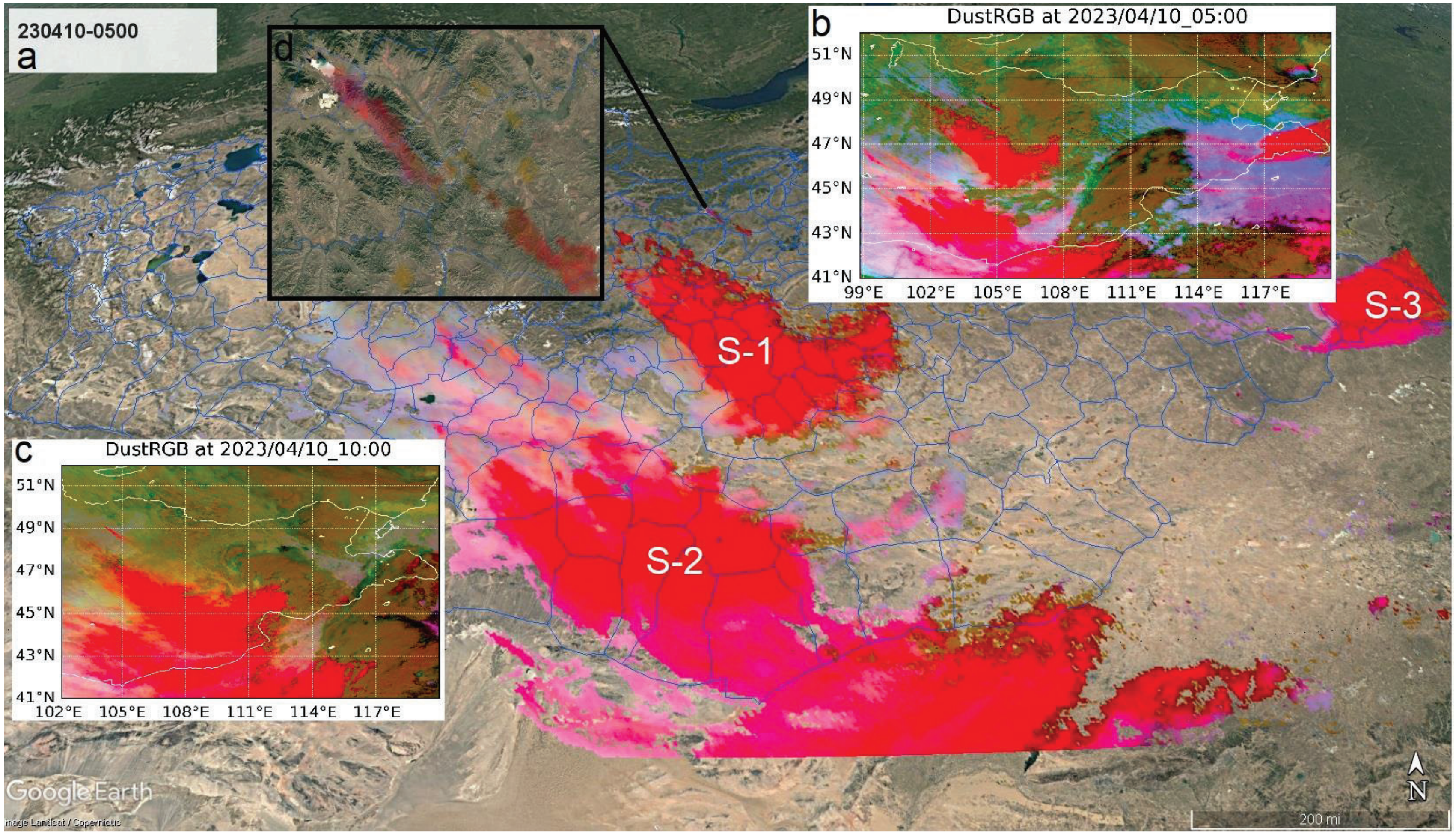

Introduction: Dust dispersion from the Erdenet mine tailings pond was detected. Additionally, three distinct dispersion areas are visible in Figure 20a (**S-1**, **S-2**, and **S-3**).

Figure 20a: The DustRGB map overlaid on Google Earth at 05:00 UTC on April 10, 2023.
Figure 20b: The DustRGB map at 05:00 UTC on April 10, 2023.
Figure 20c: The DustRGB map at 10:00 UTC on April 10, 2023.
Figure 20d: Dust dispersion from the Erdenet mine tailings pond.

Figure 21 – April 12, 2024

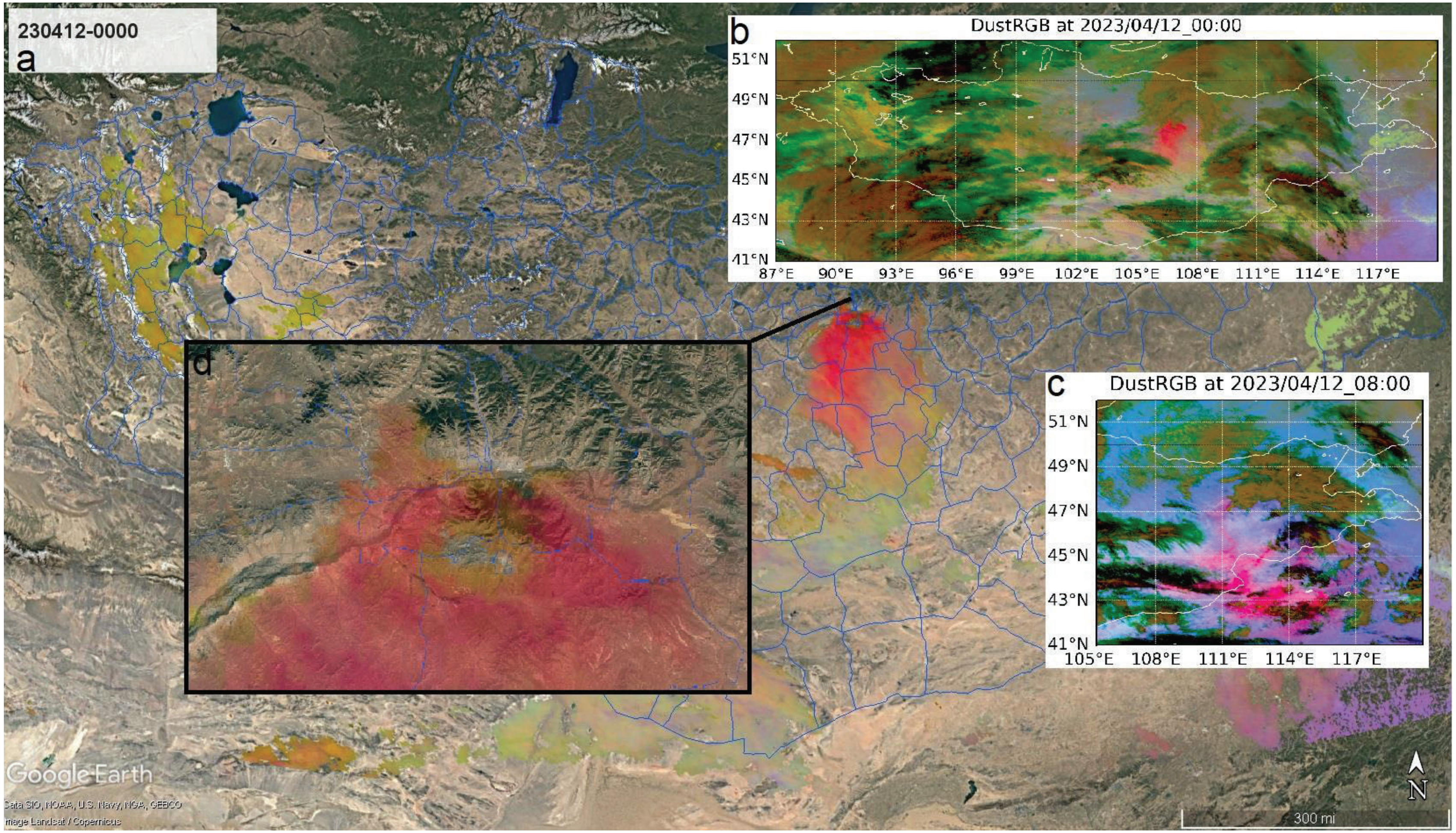

Introduction: A dust cloud moved from the northeast to the southeast. This shift can be seen in Figures **21b** and **21c**.

Figure 21a: The DustRGB map overlaid on Google Earth at 00:00 UTC on April 12, 2023.
Figure 21b: The DustRGB map at 00:00 UTC on April 12, 2023.
Figure 21c: The DustRGB map at 08:00 UTC on April 12, 2023.
Figure 21d: Dust dispersion near Ulaanbaatar, the capital city of Mongolia.

Figure 22 – April 13, 2023

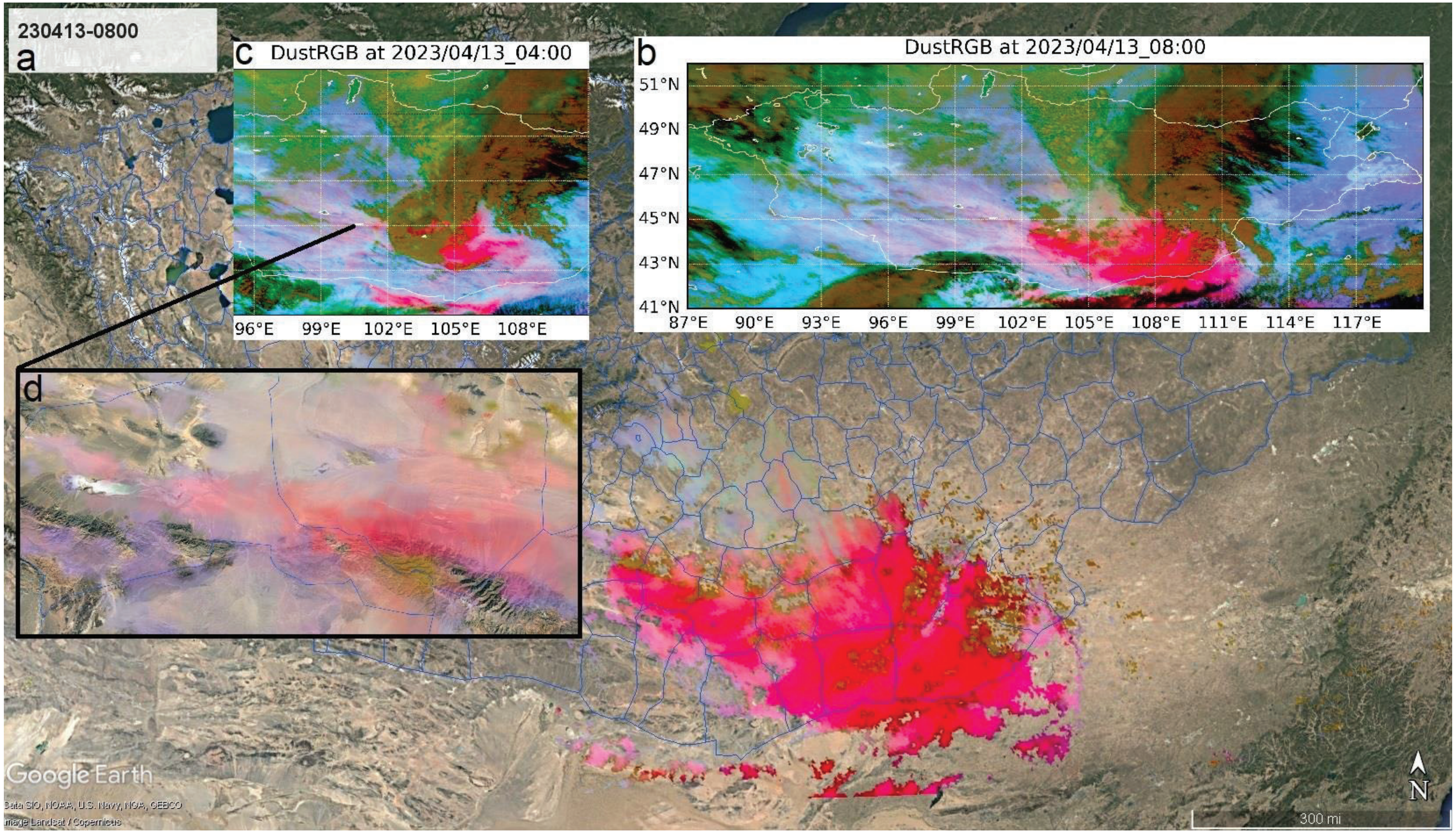

Introduction: Dust dispersion over the southeastern part of the territory.

Figure 22a: The DustRGB map overlaid on Google Earth at 08:00 UTC on April 13, 2023.
Figure 22b: The DustRGB map at 08:00 UTC on April 13, 2023.
Figure 22c: The DustRGB map at 04:00 UTC on April 13, 2023.
Figure 22d: The DustRGB map overlaid on Google Earth at 04:00 UTC on April 13, 2023. The initial point of dust dispersion was from Orog Lake.

Figure 23 – April 16, 2023

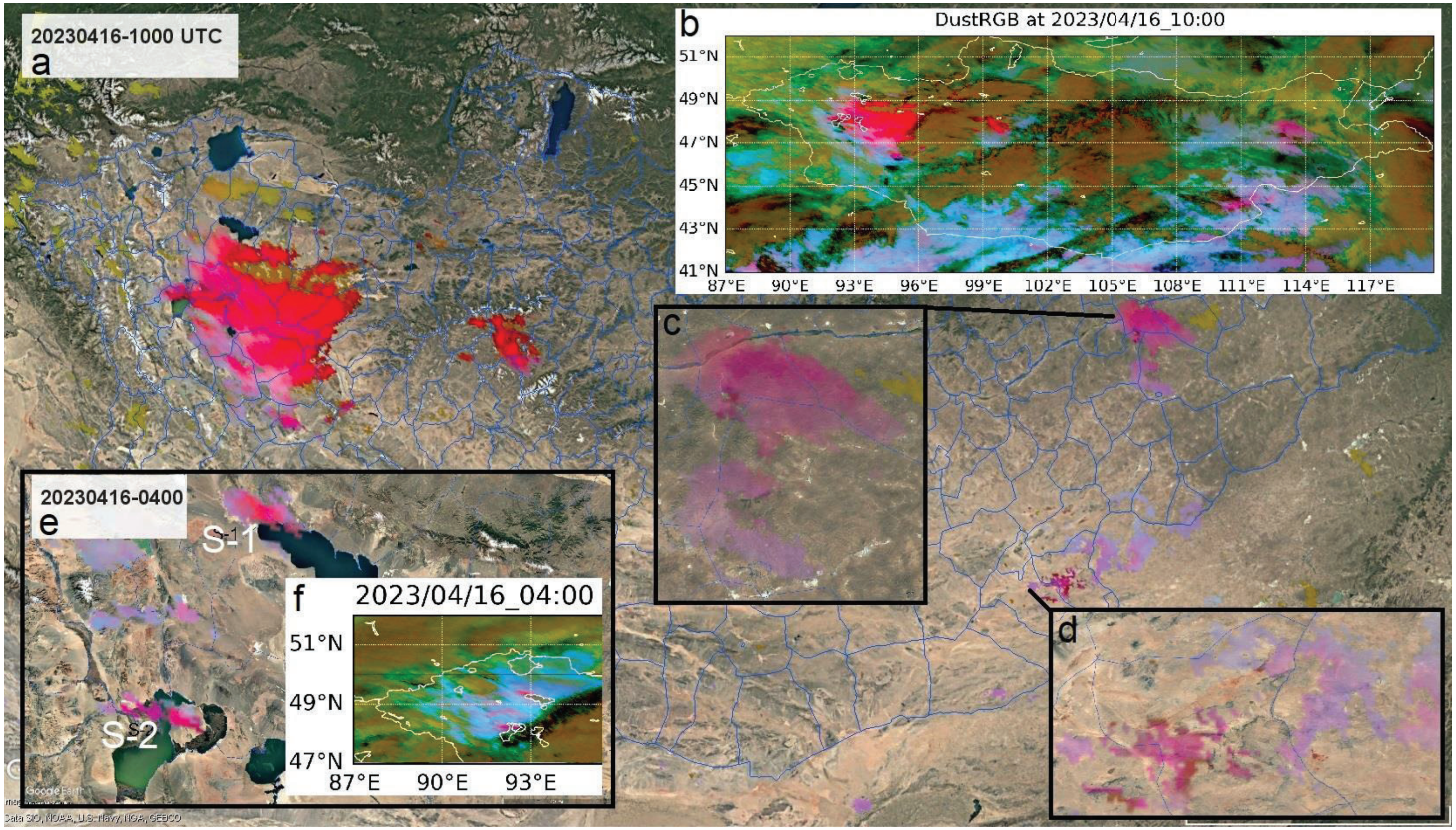

Introduction: A large dust plume originated from the Great Lakes Valley. The dust event lasted until the following day (see April 17, 2023). Additionally, two distinct mini dust plumes were detected.

Figure 23a: The DustRGB map overlaid on Google Earth at 10:00 UTC on April 16, 2023.
Figure 23b: The DustRGB map at 10:00 UTC on April 16, 2023.
Figure 23c: Dust plumes from the bank of the Kherlen River.
Figure 23d: Dust plume from the southeast of Dornogovi province.
Figure 23e: The DustRGB map overlaid on Google Earth at 04:00 UTC on April 16, 2023.
Figure 23f: The DustRGB map at 04:00 UTC on April 16, 2023. The initial point of the large dust plume was near Khyargas Lake (**S-1**) and Khar-Us Lake (**S-2**) at 04:00 UTC on April 16, 2023. This area is called the Great Lakes Depression, where sand dunes exist.

Post script: As shown in Figure **23a**, part of the plume was under cloud cover at 10:00 UTC on April 16, 2023.

Figure 24 – April 17, 2023

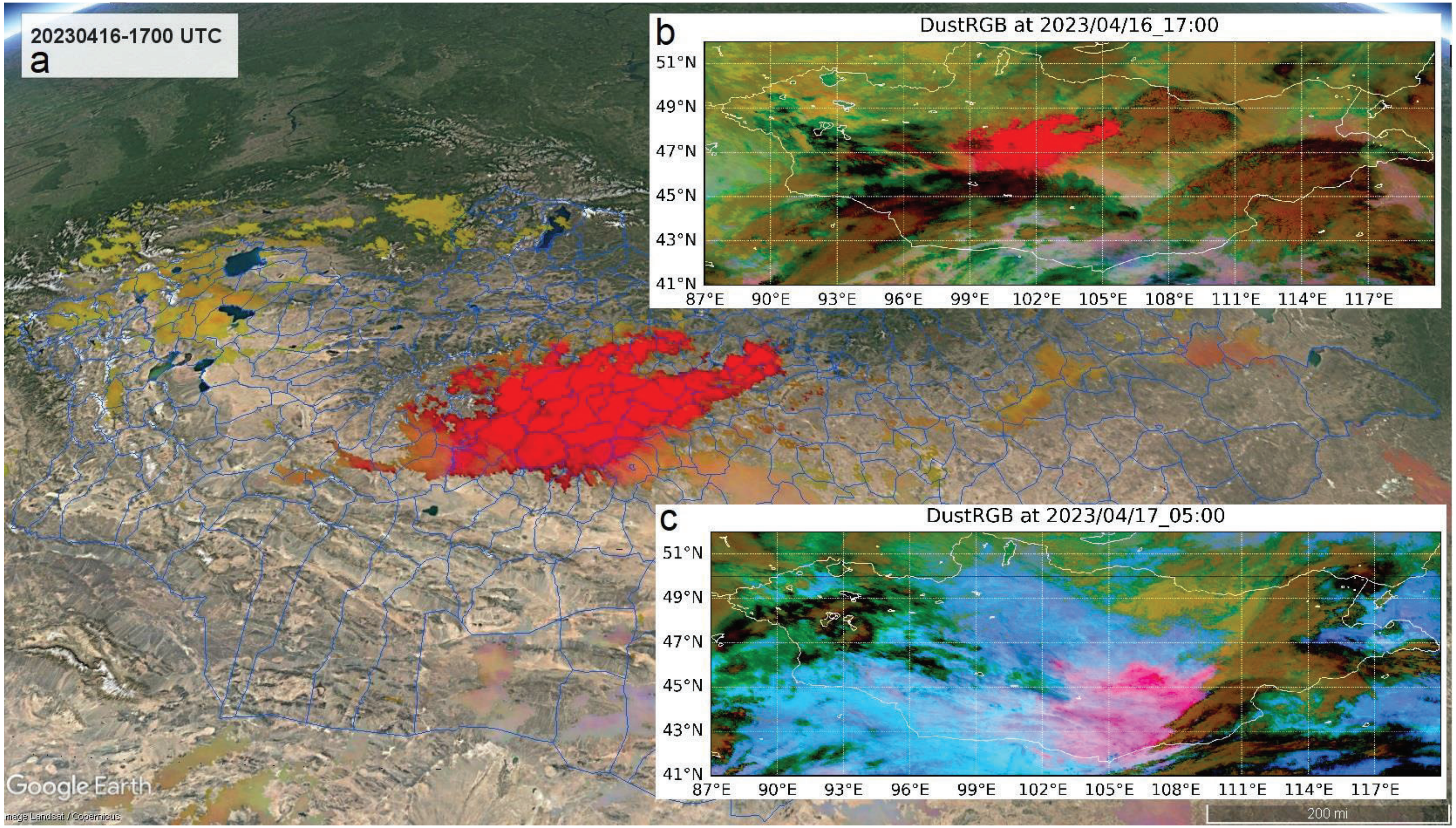

Introduction: The dust events on April 17, 2023, were a continuation of the previous storm on April 16, 2023. The shift from the northwest to the southeast between 17:00 UTC on April 16, 2023, and 05:00 UTC on April 17, 2023, can be seen in Figures **24b** and **24c**.

Figure 24a: The DustRGB map overlaid on Google Earth at 17:00 UTC on April 16, 2023.
Figure 24b: The DustRGB map at 17:00 UTC on April 16, 2023.
Figure 24c: The DustRGB map at 05:00 UTC on April 17, 2023.

Figure 25 – April 18, 2023

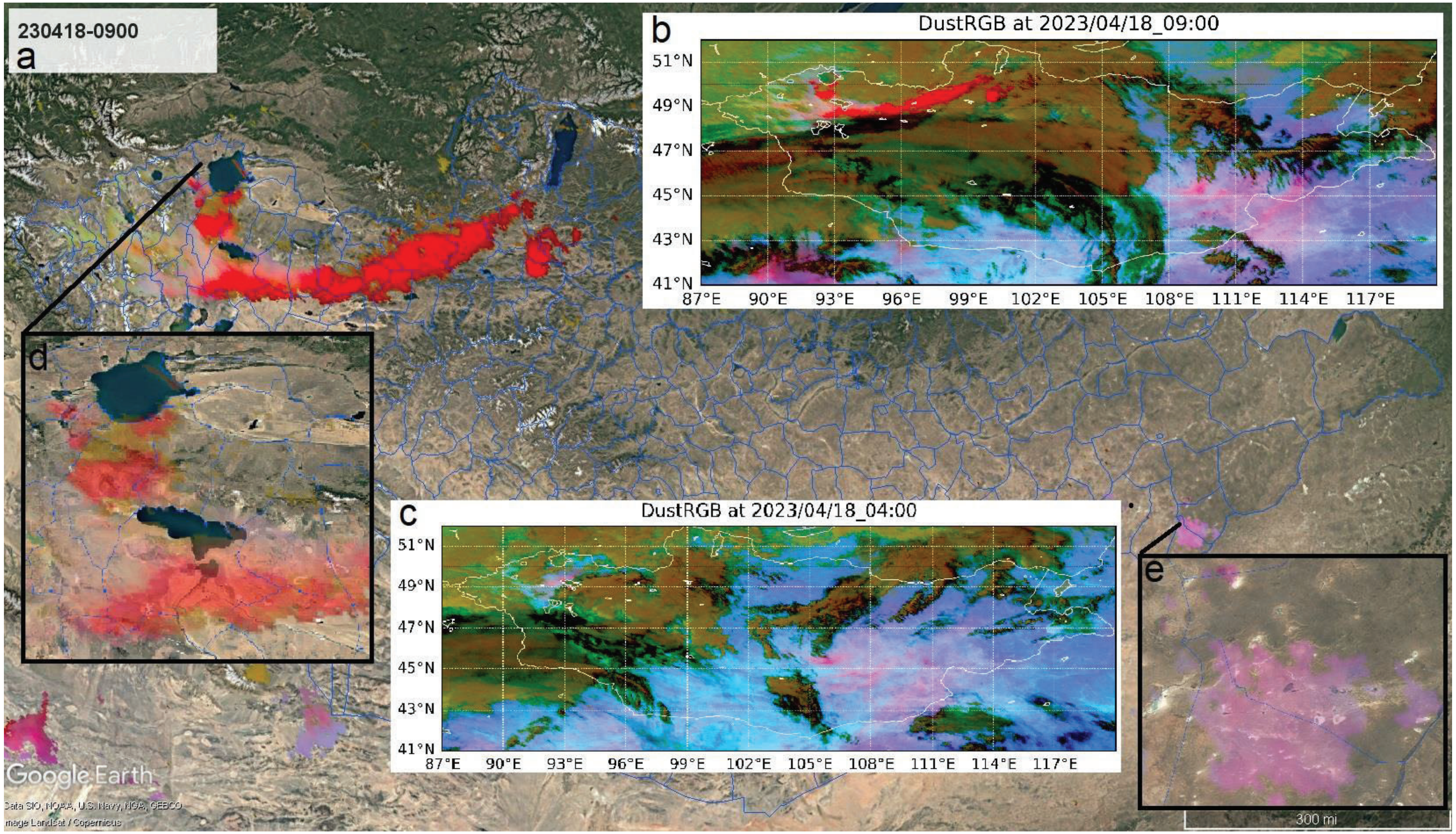

Introduction: A dust event was initiated from the Great Lakes Depression and the southeast of the territory (Figure **25c**). The further evolution of the dust plume is shown in Figures 25a and 25b.

Figure 25a: The DustRGB map overlaid on Google Earth at 09:00 UTC on April 18, 2023.
Figure 25b: The DustRGB map at 09:00 UTC on April 18, 2023.
Figure 25c: The DustRGB map at 04:00 UTC on April 18, 2023.
Figure 25d: Dust detection near Uvs, Khargas, and Airag lakes. This area is called the Great Lakes Depression, where sand dunes exist.
Figure 25e: There's a national protected area that includes several seasonal lakes.

Post script: It cannot be ruled out that there are other dust hotspots below the cloud cover (Figure **25b**)

Figure 26 – April 19, 2023

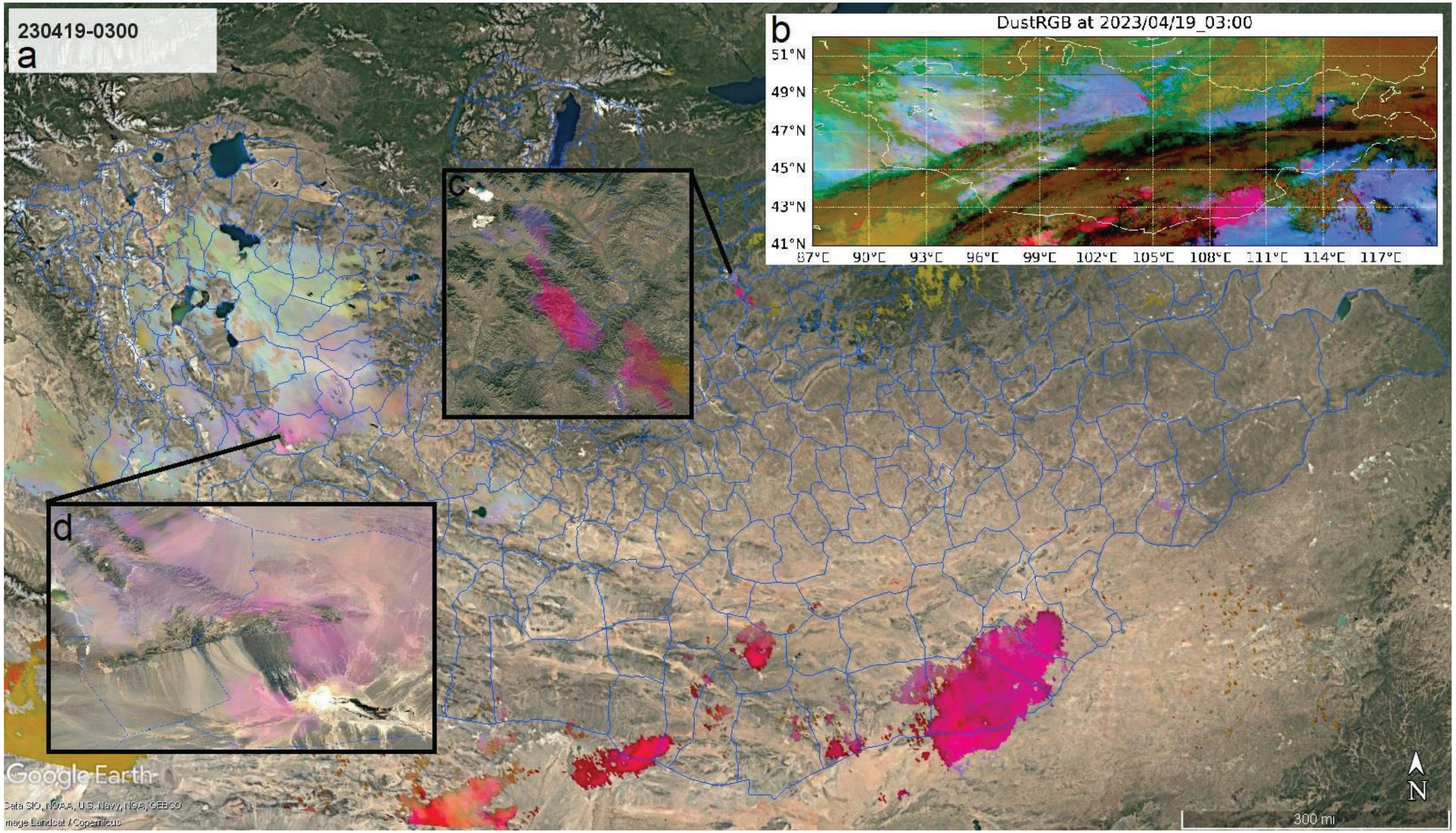

Introduction: There are two distinct dust hotspots, including the Erdenet mine tailings pond. Additionally, a dust storm occurred in the southern part of the territory.

Figure 26a: The DustRGB map overlaid on Google Earth at 03:00 UTC on April 19, 2023.
Figure 26b: The DustRGB map at 03:00 UTC on April 19, 2023.
Figure 26c: Dust dispersion from the Erdenet mine tailings pond.
Figure 26d: Dust dispersion from the north of Shargiin Tsagaan Lake (a regular dust hotspot). The hotspot is the slope of a mountain with many natural flood trenches.

Post script: It cannot be ruled out that there are other dust hotspots below the cloud cover, especially in the southern part of the territory (Figure 26b).

Figure 27 – April 25, 2023

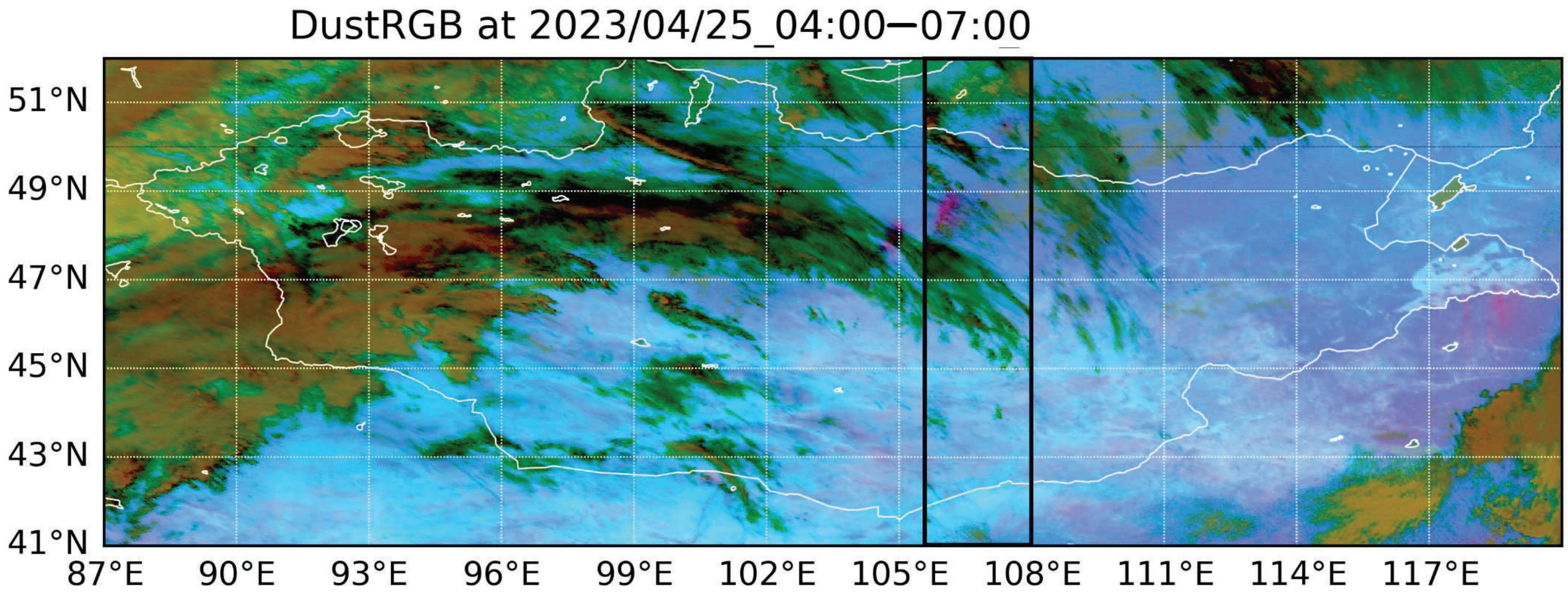

Introduction: A small dust plume was detected, moving from southwest to northeast (Figure 27). The DustRGB image at 07:00 UTC on April 25, 2023, includes a black-outlined rectangle highlighting the dust plume movement.

Figure 28 – April 26, 2023

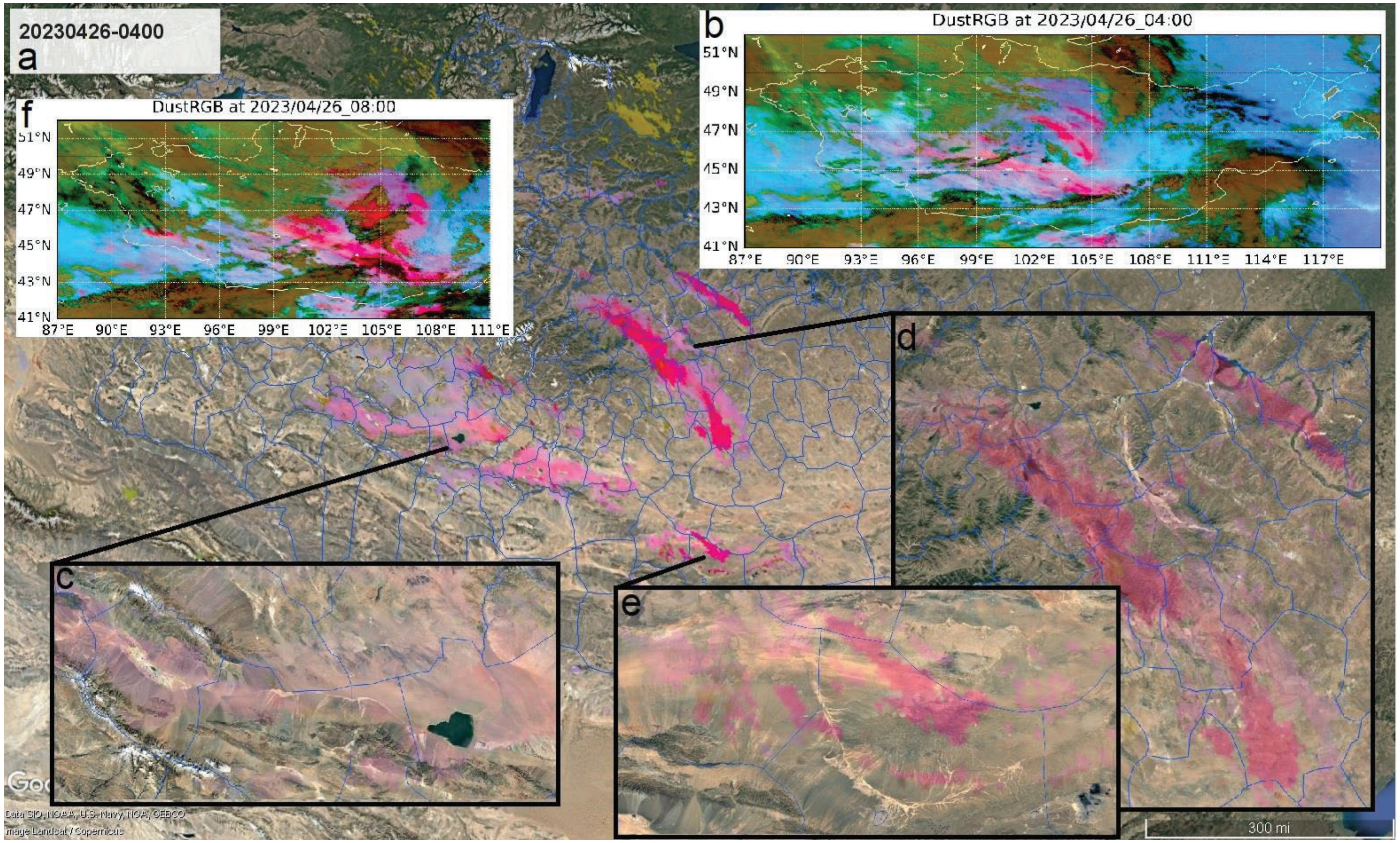

Introduction: Several distinct dust plumes were detected.

Figure 28a: The DustRGB map overlaid on Google Earth at 04:00 UTC on April 26, 2023.
Figure 28b: The DustRGB map at 04:00 UTC on April 26, 2023.
Figure 28c: Dust dispersion along the Lakes Depression between the Khangai and Gobi-Altai mountains. An intense plume was detected near Buuntsagaan Lake.
Figure 28d: Two distinct dust plumes heading southeast were detected.
Figure 28e: A dust plume was intense near Ulaan Lake, which has mostly been dry in recent decades.
Figure 28f: The DustRGB map at 08:00 UTC on April 26, 2023.

Post script: As shown in Figure **28b**, some dust plumes originated from the northern part of the territory. Geographically, this area is not very vulnerable to wind erosion, and dust storms are rare.

Figure 19 – April 27, 2023

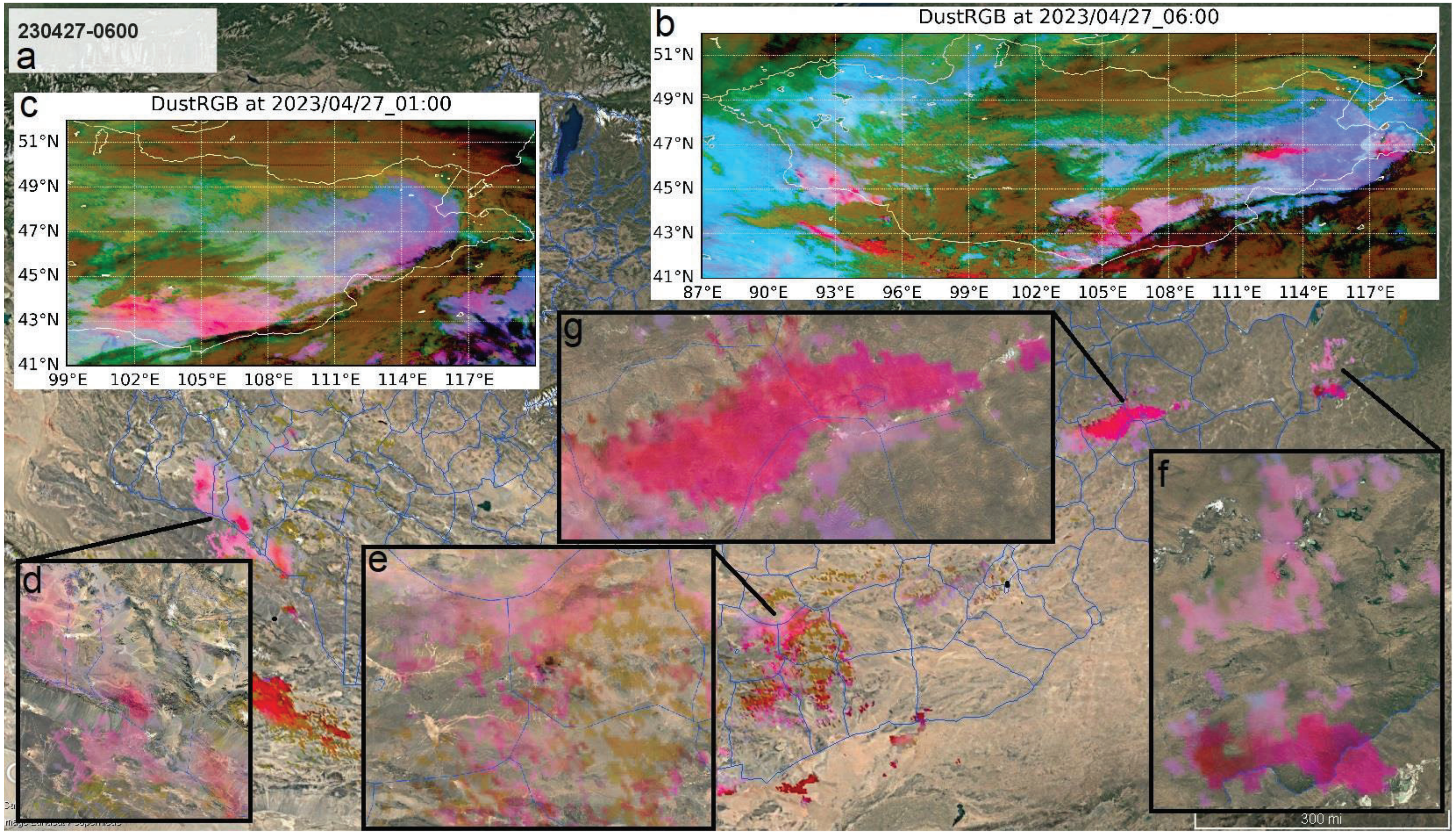

Introduction: Dust events occurred sporadically in some parts of the territory. Figure **29c** shows the beginning of dust dispersion.

Figure 29a: The DustRGB map overlaid on Google Earth at 06:00 UTC on April 27, 2023.
Figure 29b: The DustRGB map at 06:00 UTC on April 27, 2023.
Figure 29c: The DustRGB map at 01:00 UTC on April 27, 2023.
Figure 29d: Dust was dispersed from the southern part of the Altai Mountains.
Figure 29e: Dust detection near the "Tavan Tolgoi" mining area. There is a natural floodwater trench. Additionally, mining activities impact the vulnerability of the soil.
Figure 29f: Dust dispersion from a burnt surface. Wildfires occur in some places in Mongolia, especially in the eastern part of the territory.
Figure 29g: There are many successive seasonal lakes along the latitude.

Figure 30 – May 01, 2023

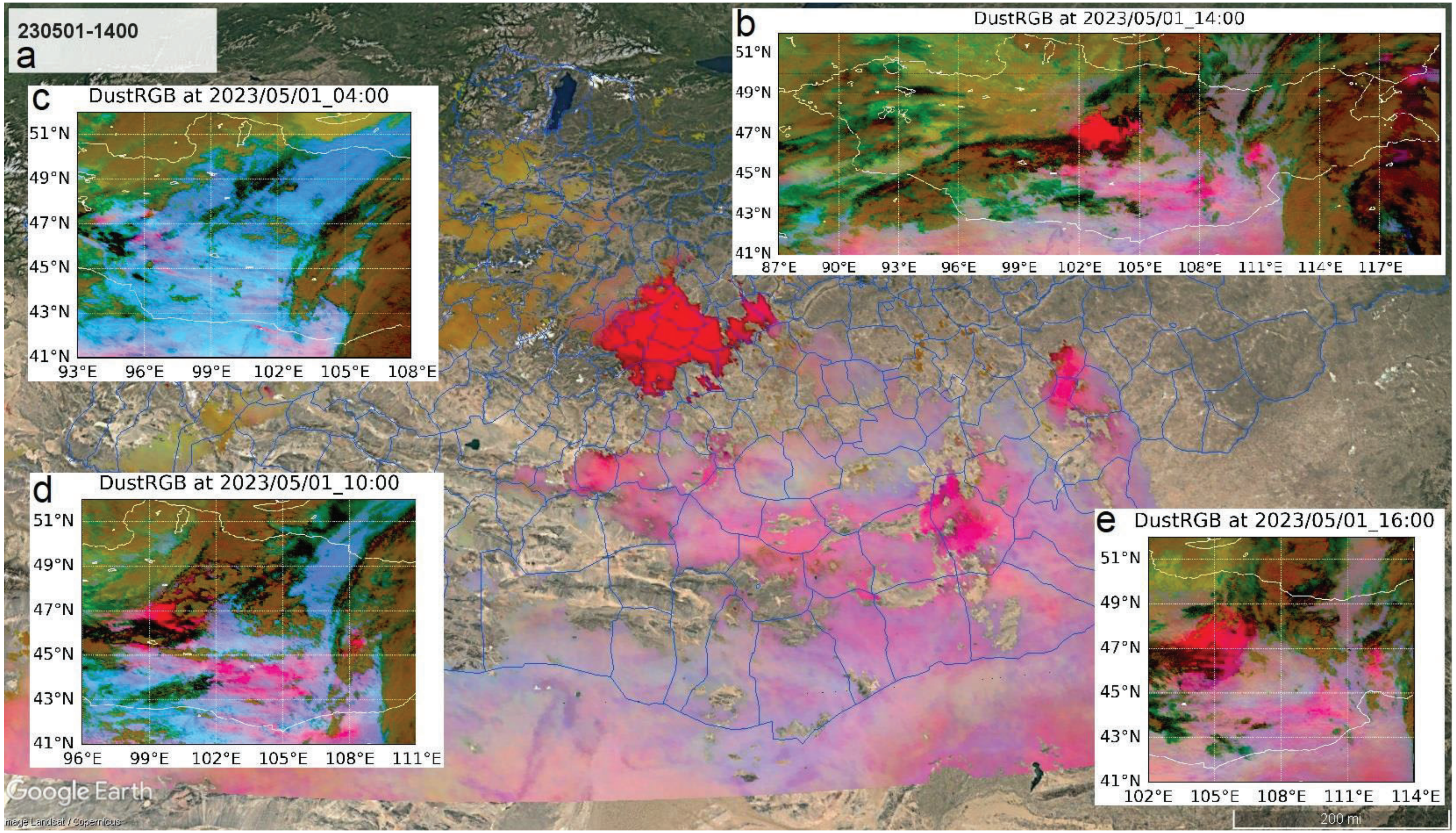

Introduction: Dust was dispersed from the western part of the territory around 04:00 UTC on April 26, 2023 (Figure **30c**). The plume headed in an eastern direction, and the dust event lasted until the following day.

Figure 30a: The DustRGB map overlaid on Google Earth at 14:00 UTC on April 26, 2023.
Figure 30b: The DustRGB map at 14:00 UTC on April 26, 2023.
Figure 30c: The DustRGB map at 04:00 UTC on April 26, 2023.
Figure 30d: The DustRGB map at 10:00 UTC on April 26, 2023.
Figure 30e: The DustRGB map at 16:00 UTC on April 26, 2023.

Figure 31 – May 02, 2023

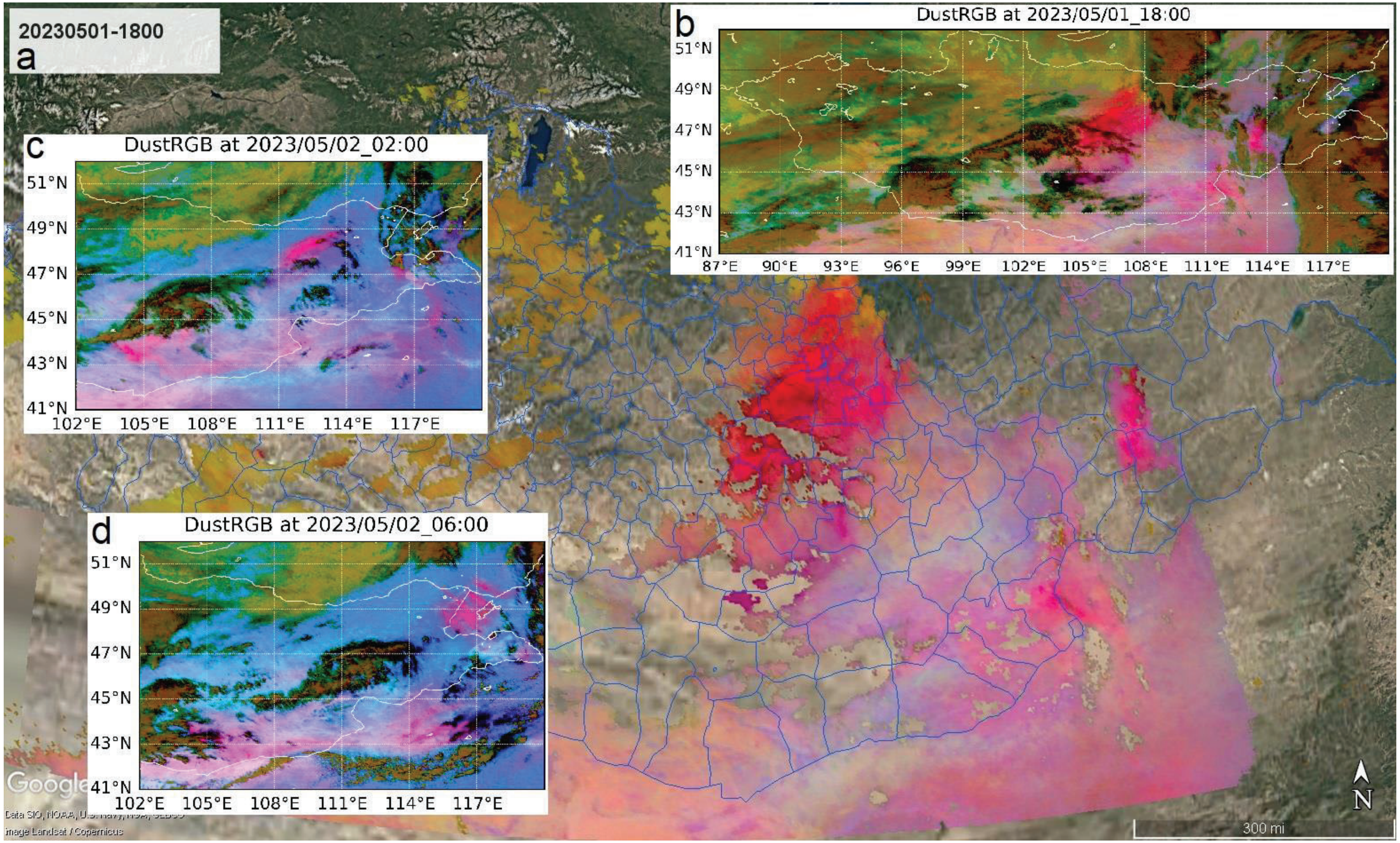

Introduction: A sequel to the dust storm of May 01, 2023. A dust plume crossed Ulaanbaatar, the capital city of Mongolia (Figure **31a**).

Figure 31a: The DustRGB map overlaid on Google Earth at 18:00 UTC on May 01, 2023.
Figure 31b: The DustRGB map at 18:00 UTC on May 01, 2023.
Figure 31c: The DustRGB map at 02:00 UTC on May 02, 2023.
Figure 31d: The DustRGB map at 06:00 UTC on May 02, 2023. The dust storm terminated around 06:00 UTC on May 2, 2023.

Figure 32 – May 04, 2023

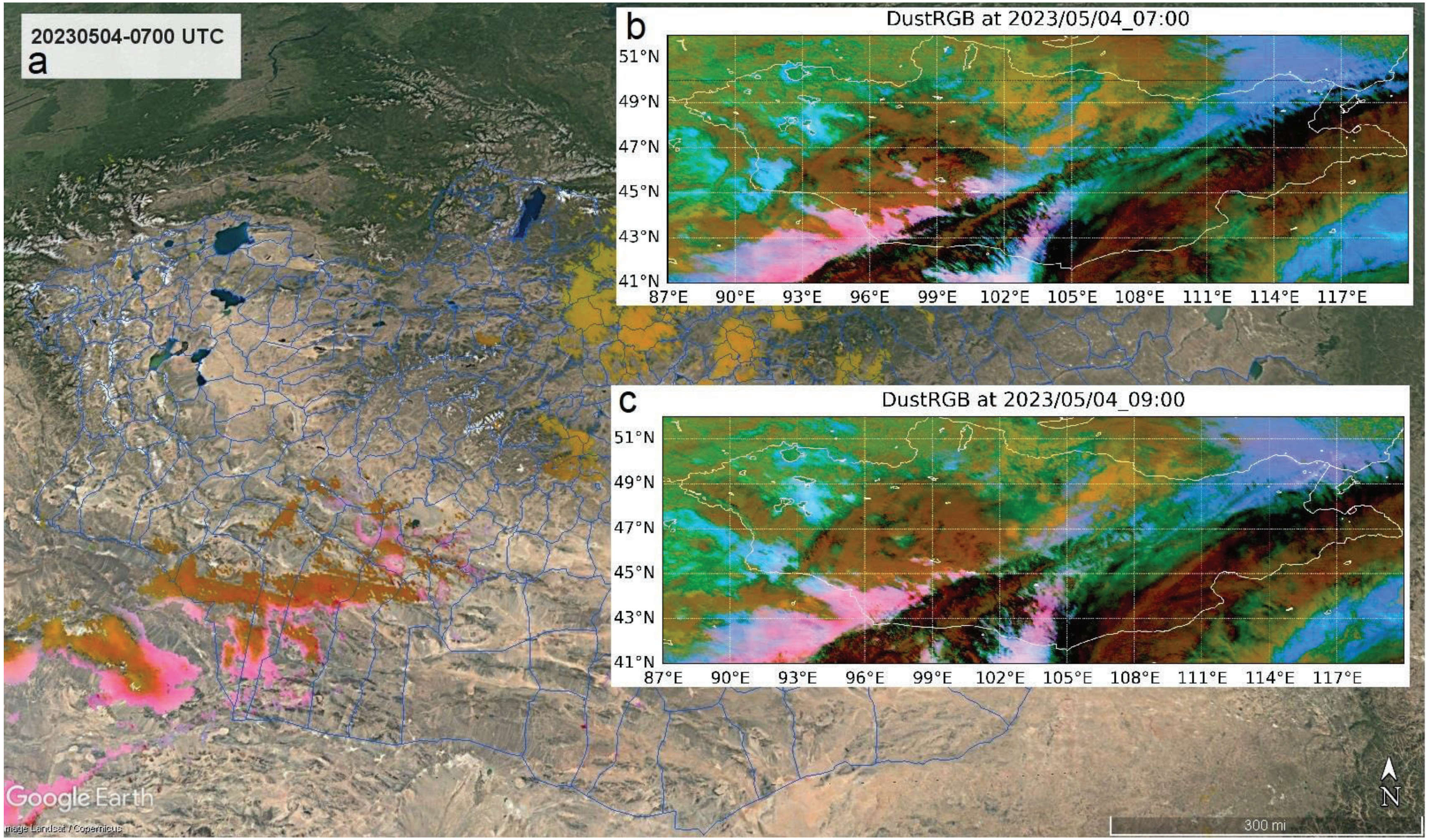

Introduction: A slight dust plume was observed over a part of the Gobi region.

Figure 32a: The DustRGB map overlaid on Google Earth at 07:00 UTC on May 04, 2023.
Figure 32b: The DustRGB map at 07:00 UTC on May 04, 2023.
Figure 32c: The DustRGB map at 09:00 UTC on May 04, 2023.

Post script: It cannot be ruled out that there are other dust hotspots below the cloud cover (Figures **32b** and **32c**).

Figure 33 – March 10, 2023

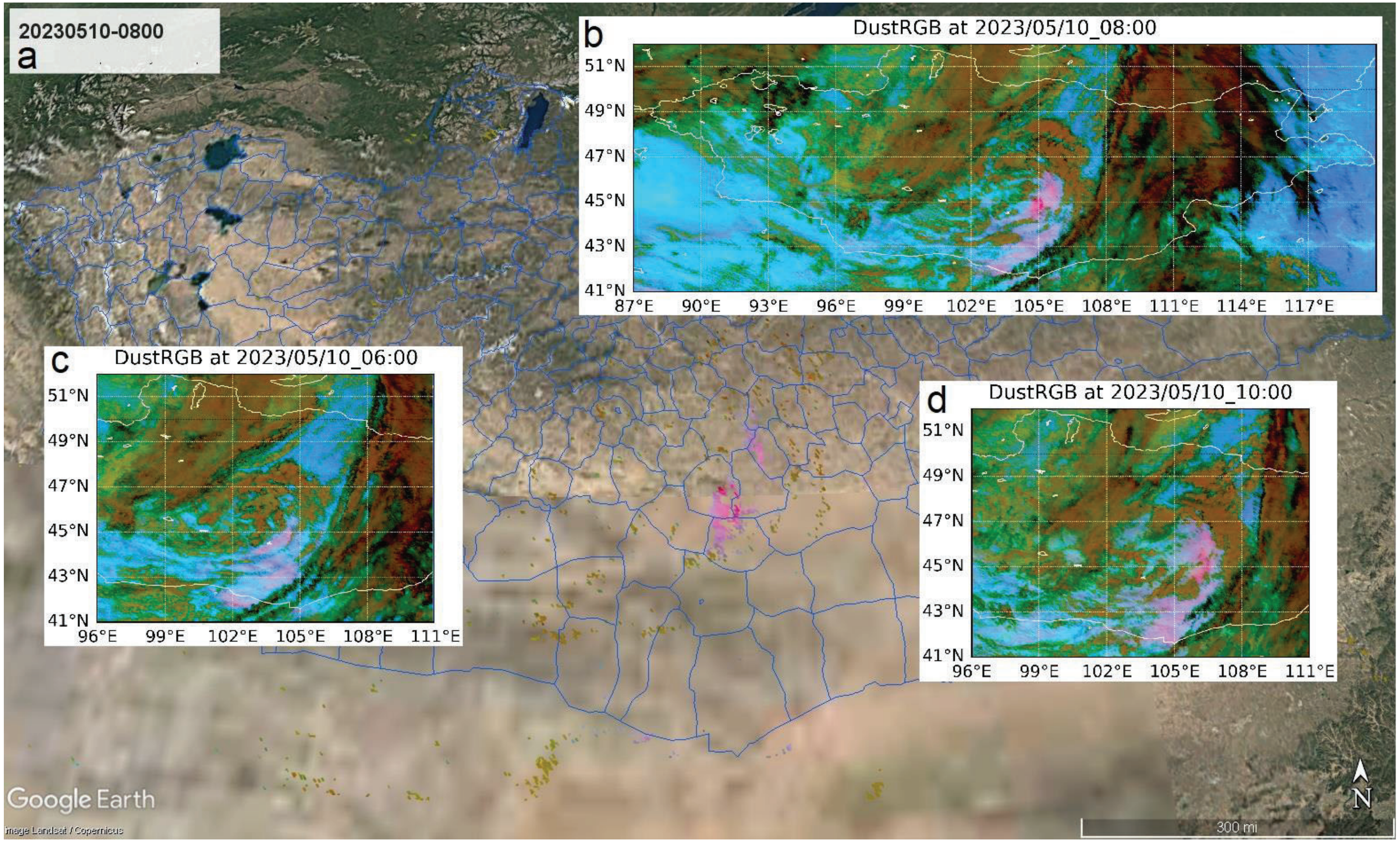

Introduction: A slight dust plume was observed over a part of the Gobi region. Around 06:00 UTC on May 10, 2023, dust dispersion was initially observed (Figure **33c**).

Figure 33a: The DustRGB map overlaid on Google Earth at 08:00 UTC on May 10, 2023.
Figure 33b: The DustRGB map at 08:00 UTC on May 10, 2023.
Figure 33c: The DustRGB map at 06:00 UTC on May 10, 2023.
Figure 33d: The DustRGB map at 10:00 UTC on May 10, 2023.

Post script: It cannot be ruled out that there are other dust hotspots below the cloud cover (Figures **33b**, **33c**, and **33d**).

Figure 34 – May 14, 2023

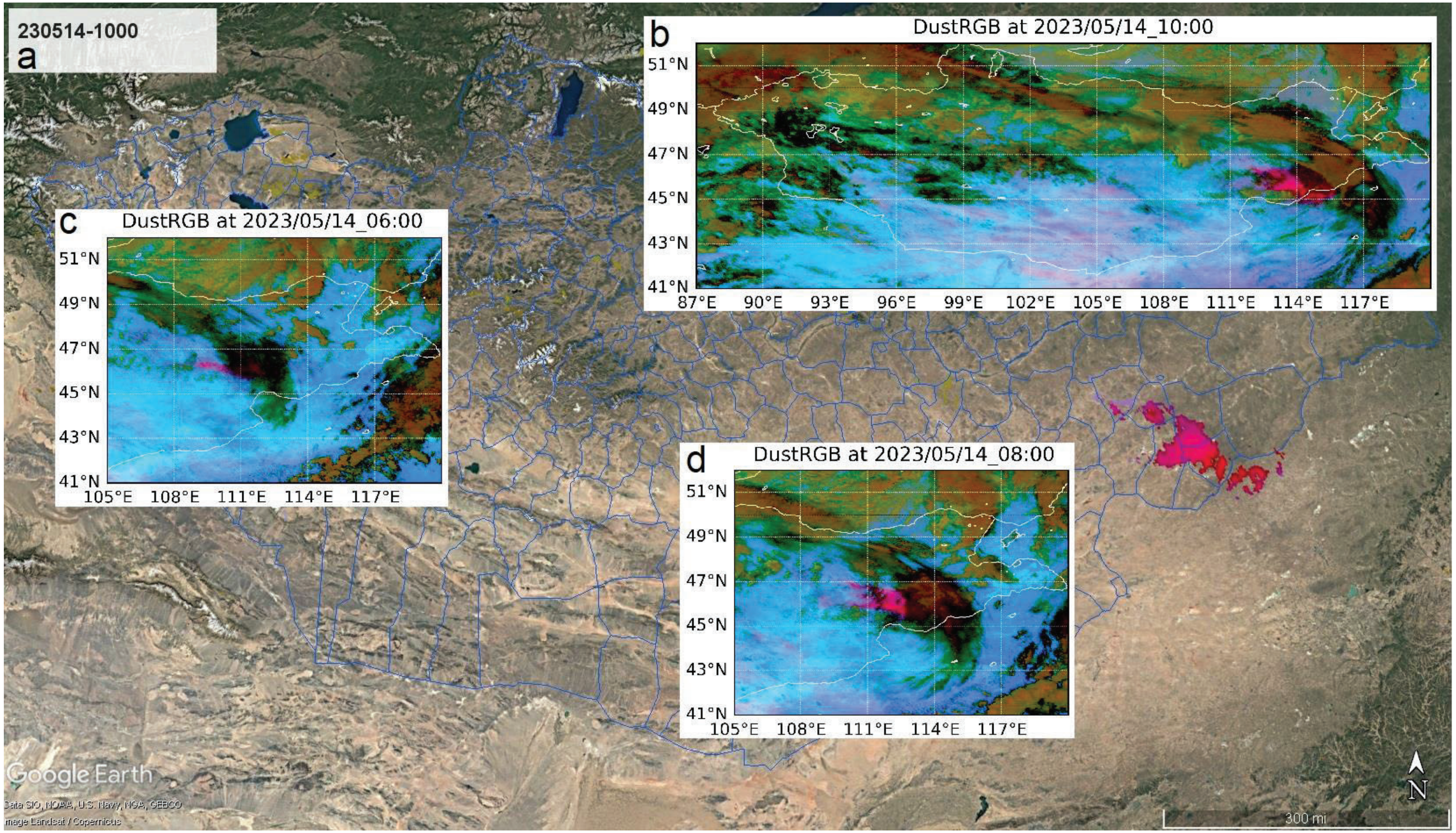

Introduction: A dust plume dispersed, heading to the east.

Figure 34a: The DustRGB map overlaid on Google Earth at 08:00 UTC on May 10, 2023.
Figure 34b: The DustRGB map at 08:00 UTC on May 10, 2023.
Figure 34c: The DustRGB map at 06:00 UTC on May 10, 2023.
Figure 34d: The DustRGB map at 10:00 UTC on May 10, 2023.

Post script: Because the DustRGB map overlaid on Google Earth was difficult to recognize, the initial location of the dust plume wasn't included in the map.

Figure 35 – May 15, 2023

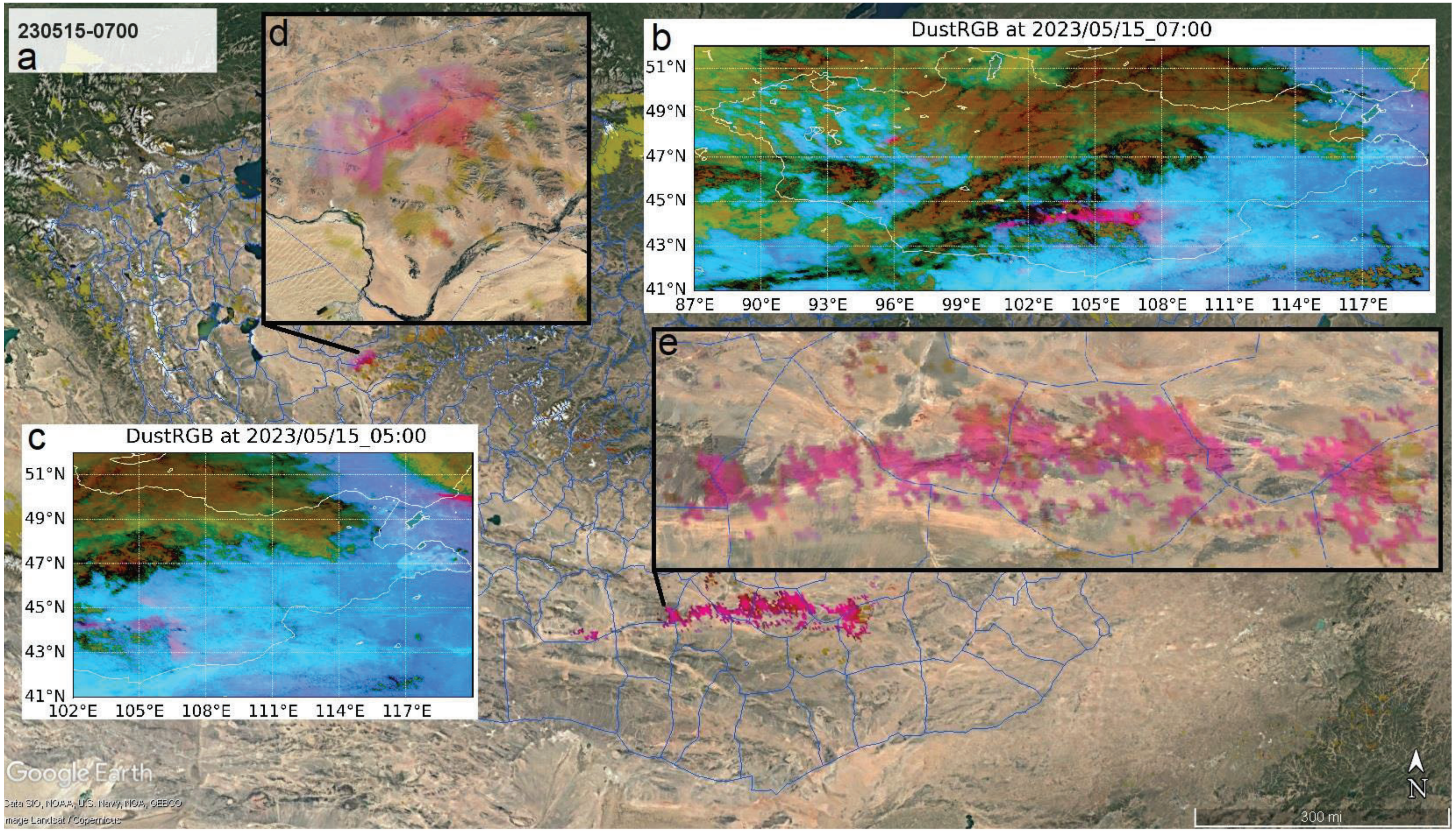

Introduction: A small dust plume and another dust plume along the latitude were detected.

Figure 35a: The DustRGB map overlaid on Google Earth at 07:00 UTC on May 15, 2023.
Figure 35b: The DustRGB map at 07:00 UTC on May 15, 2023.
Figure 35c: The DustRGB map at 05:00 UTC on May 15, 2023.
Figure 35d: A small dust plume on the north side of the Zavkhan River. This area has sand dunes.
Figure 35e: A dust plume near Ulaan Lake, which has been mostly dry in recent decades.

Post script: Because the DustRGB map overlaid on Google Earth was difficult to recognize, the initial location of the dust plume couldn't be included in the map.

Figure 36 – May 18, 2023

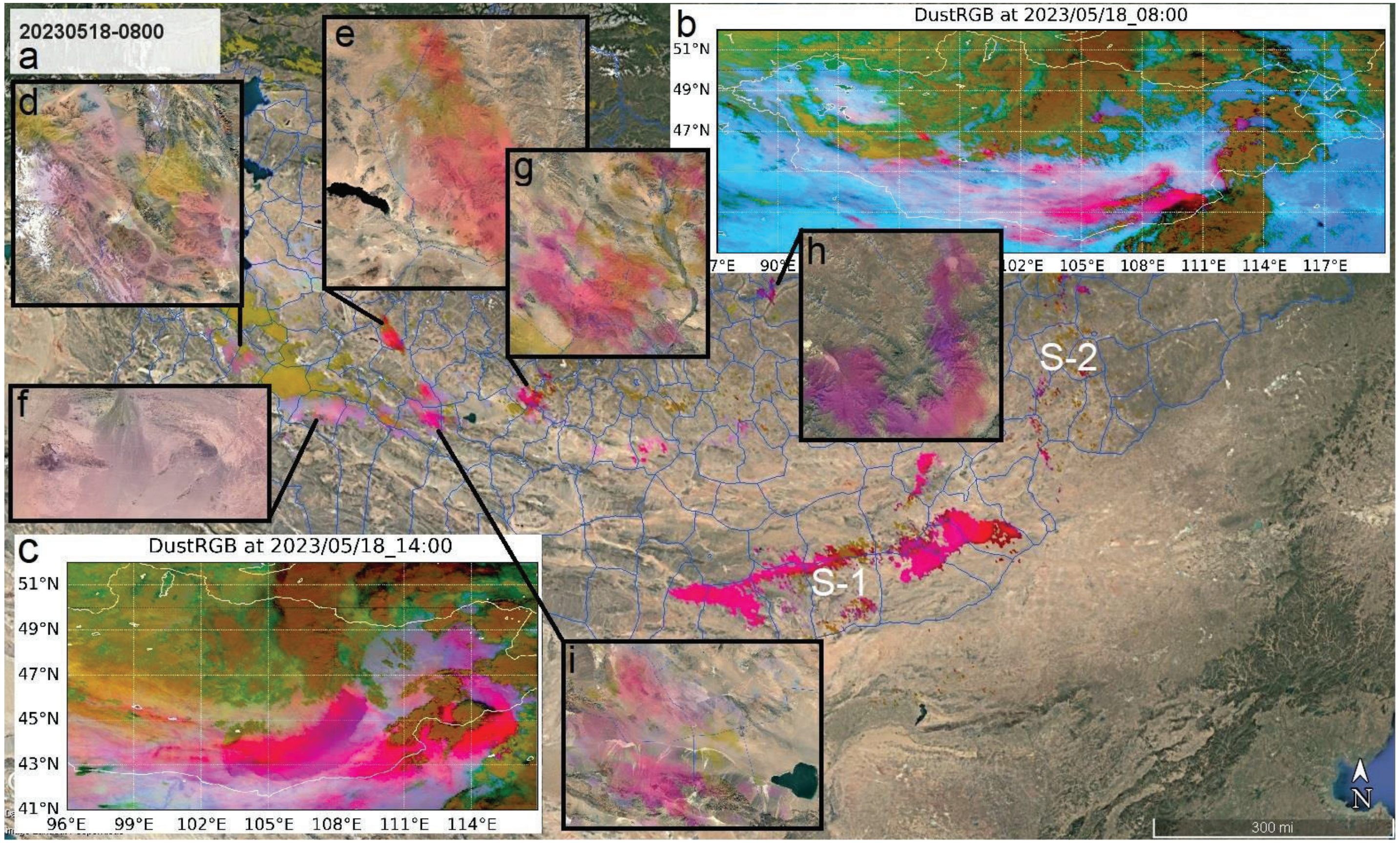

Introduction: Several dust hotspots were detected (Figure **36b**) and evolved into an intense dust storm in the southeast of the territory (Figure **36c**).

Figure 36a: The DustRGB map overlaid on Google Earth at 08:00 UTC on May 18, 2023.
Figure 36b: The DustRGB map at 08:00 UTC on May 18, 2023 and
Figure 36c: The DustRGB map at 14:00 UTC on May 18, 2023.
Figure 36d: Dust detection within the Altai Mountains.
Figure 36e: Dust detection on the north side of Gegeen Lake.
Figure 36f: Dust detection in the Altai Mountains. There is an iron ore mine called "Tayan Nuur."
Figure 36g: Dust detection in the southern part of the Khangai Mountains.
Figure 36h: Dust dispersion near Ulaanbaatar from cultivated land.
Figure 36i: Dust dispersion from the west side of Buuntsagaan Lake.

Post script: S-1 shows the dust disersion from Gobi region. **S-2** shows dust dispersion from steppe region, but dust plume was under cloud cover.

Figure 37 – May 19. 2023

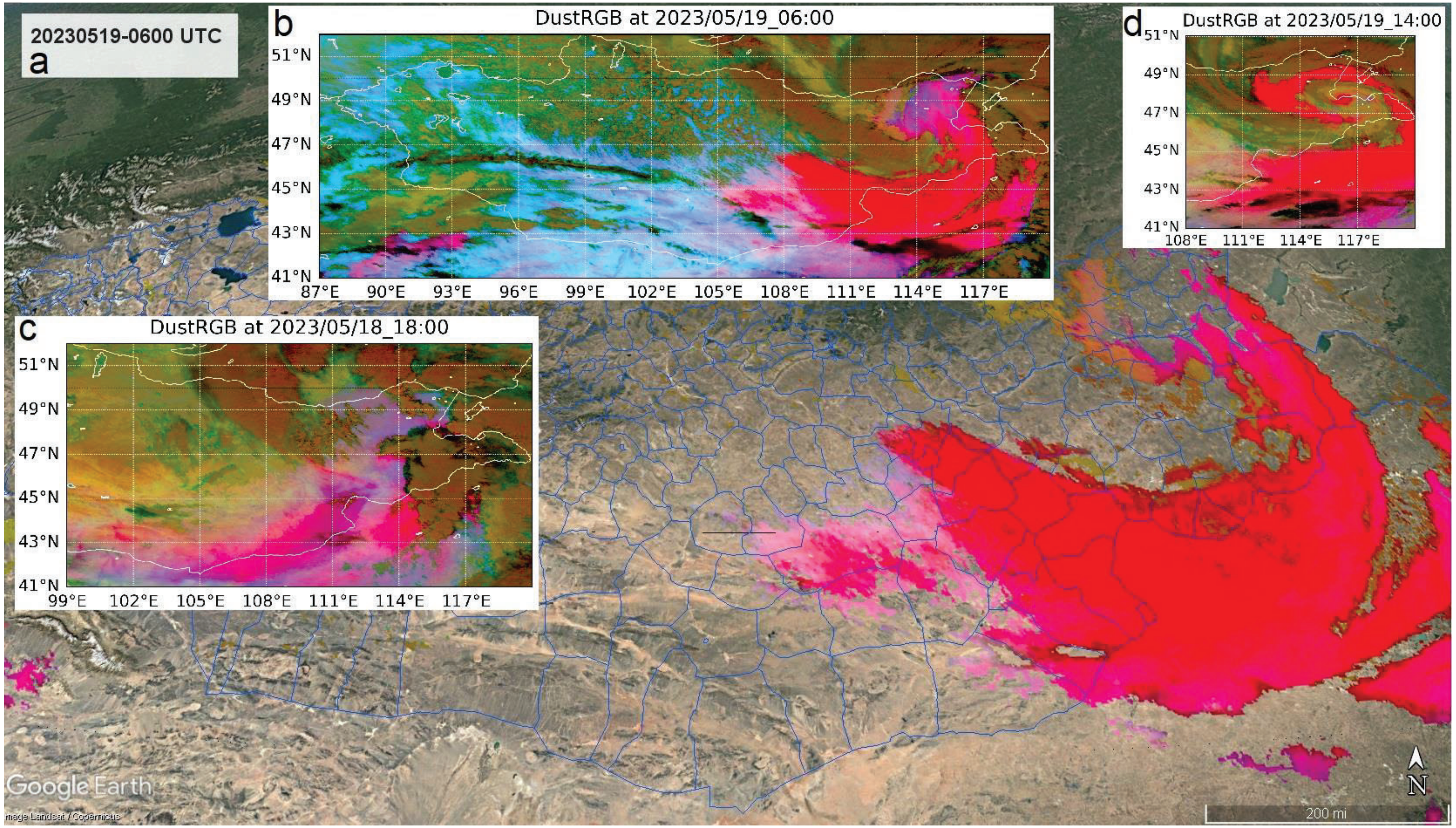

Introduction: The dust events on April 19, 2023, were the sequel to the previous storm on April 18, 2023 (Figure **37c**). An intense dust plume developed in the eastern part of the territory.

Figure 37a: The DustRGB map overlaid on Google Earth at 06:00 UTC on May 19, 2023.
Figure 37b: The DustRGB map at 06:00 UTC on May 19, 2023.
Figure 37c: The DustRGB map at 18:00 UTC on May 18, 2023.
Figure 37d: The DustRGB map at 14:00 UTC on May 19, 2023.

Post script: The dust plume appeared significantly intense and remained relatively stable, rotating anti-clockwise.

Figure 38 – May 31, 2023

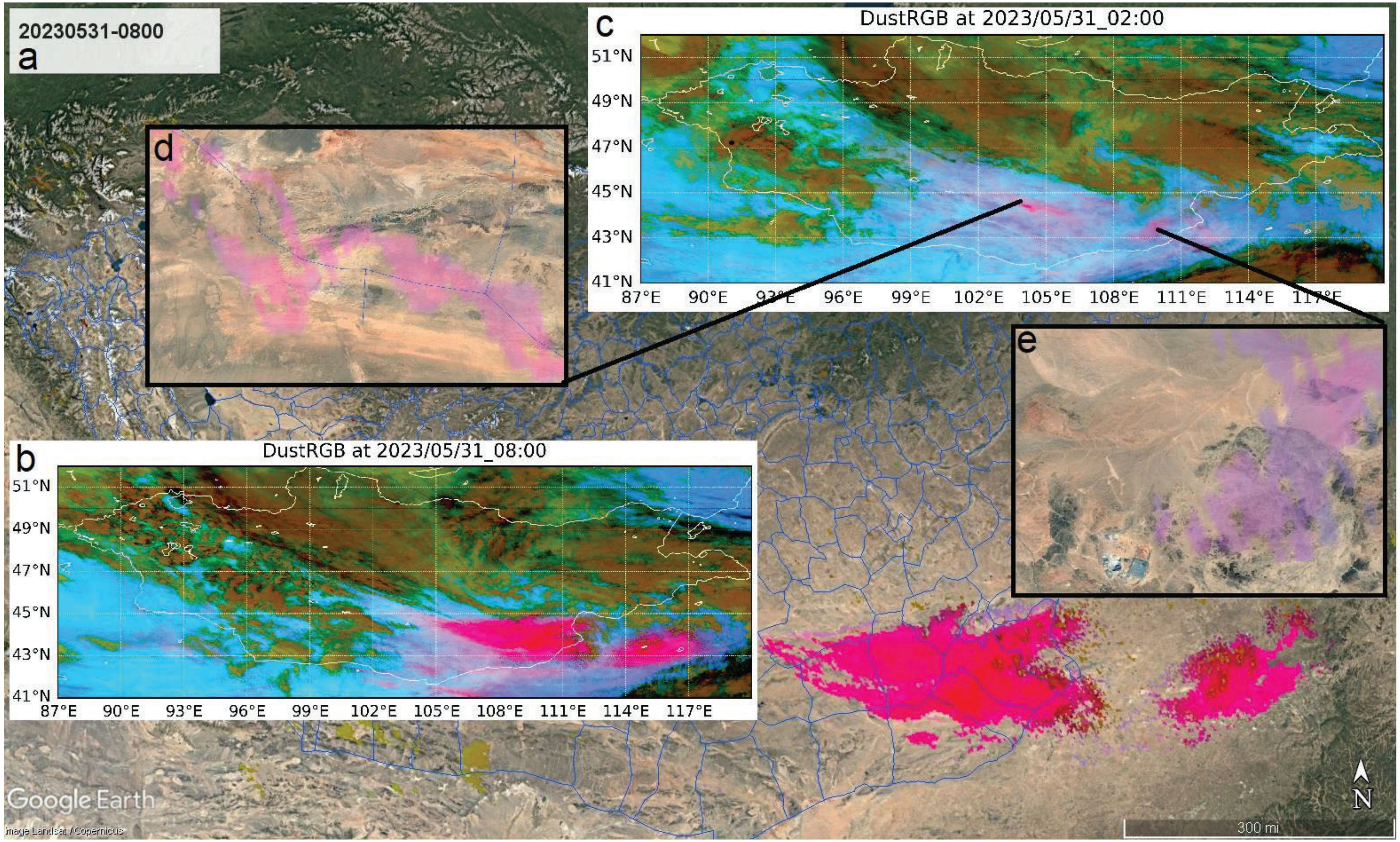

Introduction: An intense dust plume developed around 08:00 UTC on May 31, 2023 (Figure **38b**). Prior to that, two distinct plumes were detected in the Gobi region at 02:00 UTC on May 31, 2023 (Figure **38c**).

Figure 38a: The DustRGB map overlaid on Google Earth at 08:00 UTC on May 31, 2023.
Figure 38b: The DustRGB map at 08:00 UTC on May 31, 2023.
Figure 38c: The DustRGB map at 02:00 UTC on May 31, 2023.
Figure 38d: An intense dust plume near Ulaan Lake, which has been mostly dry in recent decades.
Figure 38e: Dust detection near "Oyu Tolgoi," one of the largest known copper and gold deposits in the world.

国際化推進共同研究概要

No.4

[採択番号] 24EA-4

タイト ル： Convective impact on clouds, composition, and dynamics of the upper troposphere and lower stratosphere

研究代表者： UEYAMA REI

所内世話人： EGUCHI Nawo

研究概要：深い対流は対流圏の境界層から上部対流圏/下部成層圏(UT/LS)へ短期間で空気を運び、下部成層圏の化学組成に影響を与える可能性がある。アジア夏季モンスーン(ASM) は、深い対流を介して UTLS の組成に影響を与えることで近年注目を集めています。このメカニズムに関する最近の観測活動であるthe Asian summer monsoon Chemical and CLimate Impact Project (ACCLIP)では、2022 年の北半球夏季に 2 つの航空機を使用して北西太平洋地域の ASM UTLS の組成をサンプリングしました。

この共同研究では、ラグランジュトラジェクトリモデルと対流雲の雲頂観測データを統合して、ACCLIP 航空機観測で採取した空気塊に寄与した ASM の対流輸送過程を診断しました。この診断手法は主要な ASM のサブシステムに関連する対流輸送の特性を調査するために適用され、寿命が数日から数か月に及ぶ時間スケールの場合、東アジア亜熱帯前線に沿った対流による輸送は、一般的に南アジア上の対流による輸送よりも多くの UTLS 汚染物質と関連していることが明らかになりました。

Convective impact on clouds, composition, and dynamics of the upper troposphere and lower stratosphere

Rei Ueyama (NASA Ames Research Center)

I. Abstract

Deep convection transports boundary layer air to the upper troposphere/lower stratosphere (UTLS) region over a short timescale and can influence the chemical composition of the lowermost stratosphere. The Asian Summer Monsoon (ASM) has garnered attention in recent years for its impacts on the composition of the UTLS via deep convection. A recent observational effort into this mechanism, the Asian summer monsoon Chemical and CLimate Impact Project (ACCLIP), sampled the composition of the ASM UTLS over the northwestern Pacific region during boreal summer 2022 using two airborne platforms. In this work, we integrate Lagrangian trajectory modeling with convective cloud top observations to diagnose ASM convective transport which contributed to ACCLIP airborne observations. This diagnostic is applied to explore the properties of convective transport associated with prominent ASM sub-systems, revealing that for species ranging in lifetime from days to months, transport from convection along the East Asia Subtropical Front was generally associated with more UTLS pollutants than transport from convection over South Asia. The presented diagnosis of convective transport contribution to ACCLIP airborne sampling indicates a key scientific success of the campaign and enables process studies of the climate interactions from the two ASM sub-systems.

II. Introduction

One of the important mechanisms of stratosphere and troposphere exchange is deep convection that detrains mass in the upper troposphere and lower stratosphere (UTLS). These convective storms are especially strong and frequent over the Asian and North American monsoon regions during boreal summer (ASM and NAM, respectively). Water vapor and boundary layer pollutants lofted by deep monsoon convection are typically trapped within the strong anticyclonic circulation in the UTLS and later dispersed throughout the global stratosphere, where they can have a significant impact on radiative and chemical processes, potentially including stratospheric ozone. Despite the importance of convection on UTLS composition, its global impact is not well quantified. A comprehensive knowledge of the relationships between convection, clouds, composition, and dynamics in the UTLS is urgently needed to evaluate and improve model simulations of the time-evolving convective impact on climate.

The implications on ASM UTLS composition in particular have inspired a wide range of observational efforts. These have included the deployment of both balloon-borne and airborne instruments for direct in situ sampling of the UTLS anticyclone's chemical and aerosol properties. A recent large-scale effort of this kind was the Asian summer monsoon Chemical and Climate Impact Project (ACCLIP; Pan et al., 2022, 2024), which used an array of airborne and ground-based measurements to sample the composition of the ASM UTLS anticyclone from over the western Pacific during boreal summer 2022. The primary goal of ACCLIP was to measure the chemical composition of the air mass transported to the UTLS by ASM deep convection, as well as its export to the surrounding regions. Given the airborne sampling was performed over the western Pacific region, transport of polluted air by ASM convection to the UTLS was not directly observed at the time and location of convection, but rather after the air masses were transported following large-scale quasi-horizontal flow. Analysis of ACCLIP airborne data for ASM process understanding thus benefits from a diagnostic of the deep convection locations and UTLS transport time scales that contributed to the sampled air masses.

In this work, we present a convective transport diagnostic for ACCLIP airborne sampling which is designed to connect individual flight segments with convective transport times and locations over Asia. This diagnostic confirms the critical success of ACCLIP at sampling ASM convective transport to the UTLS, and enables broader investigation of the ASM's impacts on atmospheric composition and climate.

III. Method/Data

Airborne sampling over the western Pacific region during ACCLIP was conducted using two research aircraft, the NSF NCAR Gulfstream V (GV) and the NASA WB-57, both operated from Osan Air Base in the Republic of Korea. An overview of the flight tracks is shown in Figure 1. The GV performed 14 research flights between 31 July and 31 August 2022. The final inbound GV transit leg (Guam to Osan) and the initial outbound GV transit leg (Osan to Anchorage) were both configured as full science flights to provide background contrast between the polluted ASM UTLS and the surrounding tropical and extratropical regions. The WB-57 performed 15 research flights from Osan between 2 August and 1 September 2022.

A distribution of deep convection occurrence during August 2022 (Figure 1a) shows frequent deep convection over South Asia (mainly along the Ganges River Plain in northern India) as well as oceanic convection over the Bay of Bengal and the tropical western Pacific. For the most part, deep convection was remote to the ACCLIP measurements, which underscores the value of estimating the contribution of convective transport to the airborne sampling. From a vertical perspective (Figures 1b and 1c), the GV mostly sampled the UT environment (150-250 hPa; 11-15 km; 350-370 K), while the WB-57 extensively sampled a higher-altitude layer which included the lower stratosphere (60-200 hPa; 13-19 km; 360-450 K) over a smaller horizontal range.

To diagnose the contribution of convective transport to ACCLIP airborne observations, we integrate trajectory modeling with satellite observations of convective cloud top altitudes. Specifically, we initiate backward trajectories every 60 seconds along each GV and WB-57 research flight track and calculate them backward in time for 30 days. Trajectories are calculated using the TRAJ3D model (Bowman, 1993; Bowman & Carrie, 2002; Bowman et al., 2013), with air parcel motion determined solely from the zonal, meridional, and vertical velocities provided as input. We configure the TRAJ3D model to use both analysis wind fields from the Global Forecasting System (GFS) as well as ERA5 (Hersbach et al., 2020) to explore the sensitivity of our results to the input wind fields. GFS wind fields are provided to TRAJ3D at 1° horizontal spacing every six hours, while ERA5 wind fields are provided at 0.25° horizontal spacing every hour. We configure TRAJ3D to represent vertical motion using the kinematic vertical velocity fields (pressure tendency ω in hPa s^{-1}) from the GFS and ERA5. We use a 30-minute time step in TRAJ3D, and air parcel positions are provided from the model every 3 hours.

We restrict backward trajectory initiations to aircraft positions above the 500 hPa pressure surface to focus on air masses influenced by deep convection. To account for inherent uncertainties in trajectory calculations, at each 60-second flight track interval 75 individual trajectories are initiated in a regular grid centered on the flight track position, with 5 trajectories spaced in longitude, 5 trajectories spaced in latitude, and 3 trajectories spaced in the vertical. The total grid dimensions are 0.1° in longitude, 0.1° in latitude, and 0.2 hPa in pressure.

Convective cloud top altitudes are provided at 3-hour intervals from satellite observations of brightness temperatures and rainfall rates using the method described by Pfister et al. (2022). The estimated uncertainty of the cloud top altitudes is 0.5-1.0 km over land and smaller over the ocean. This product is selected to ensure that the flight segments can be associated with an occurrence of active convection. At the first instance where a backward trajectory has a pressure altitude lower than that of a co-located convective cloud top, the location at convection and time from flight track to convection are recorded. These values are then "assigned" to the airborne chemical observations recorded at the time of trajectory initiation. For instruments with a sampling frequency less than 60 seconds (e.g., those that measure CO and SO_2), observations within the corresponding 60-second period are averaged. For instruments with a sampling frequency greater than 60 seconds (e.g., those that measure VOCs), the observation nearest the trajectory launch time is used. Trajectories which reach the lower boundary of the model (>1000 hPa) are automatically classified for convective transport at that location and time. Although there may not be active convection there, this simulated surface contact gives some "origin" information for the sampled air mass, which aligns conceptually with the goal of this work.

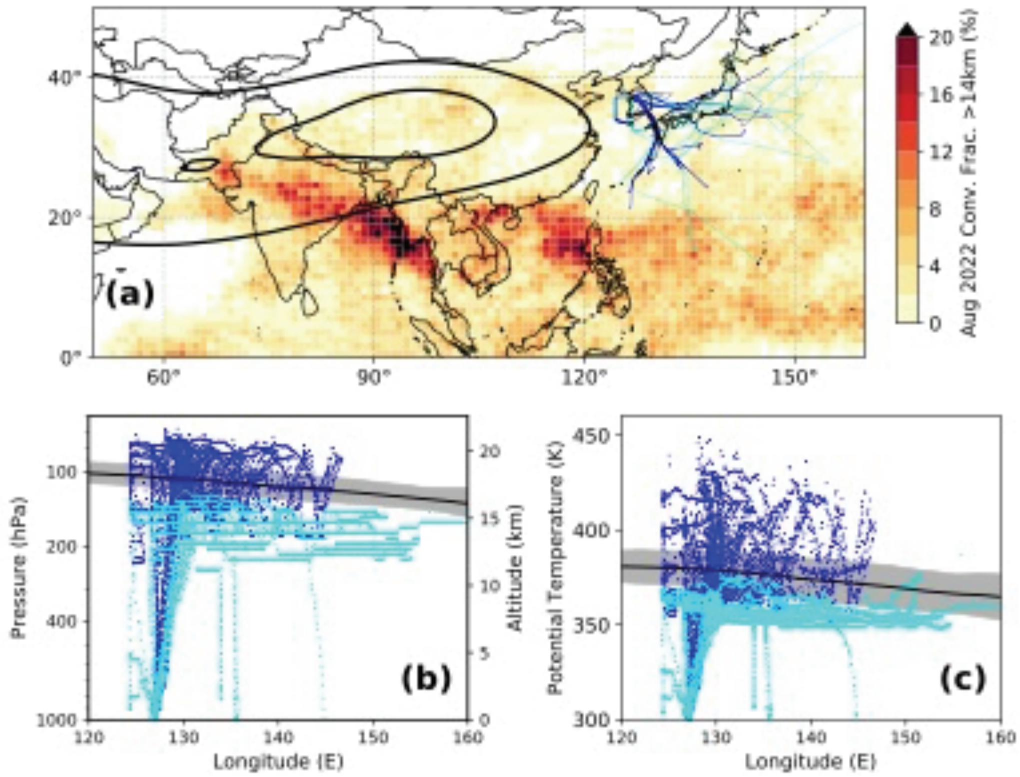

Figure 1: An overview of ACCLIP (2022) airborne sampling and the convective environment. Flight tracks from the NASA WB-57 are shown in blue and NSF NCAR GV flight tracks are shown in cyan. Panel (a) shows flight tracks overlain on a distribution of deep convective occurrence fraction, calculated as the fraction of August 2022 where a given location featured a convective cloud top altitude of at least 14 km. Convective cloud top altitudes are derived from satellite observations using the method described by Pfister et al. (2022). 150 hPa streamfunction contours of [1.0, 2.5]*10^7 m^2 s^{-1} are shown in black from the NCEP Climate Forecast System (CFS). Panel (b) shows flight tracks in pressure and altitude space, and panel (c) shows flight tracks in potential temperature space. In (b) and (c), the August 2022 mean lapse-rate tropopause from ERA5 reanalysis averaged from 20-40°N latitude is shown as a black line with gray shading denoting its standard deviation.

IV. Results

Distributions of the locations and the transit times from convection contributing to ACCLIP measurements from the introduced convective transport diagnostic are shown in Figure 2. The locations of convective transport over Asia (Figures 2a and 2c) are physically consistent with the behavior of prominent ASM sub-systems. Convective transport along the Ganges River Plain to the southwest of the Tibetan Plateau, mainly comprising Pakistan and northern India, is consistent with the location of the "Monsoon Trough". Convective transport encompassing parts of northern China and the Yellow Sea is consistent with the location of the East Asia Subtropical Front (EASF). Prior transport modeling studies have identified the southern flank of the Tibetan Plateau as a primary source for the air mass within the ASM UTLS anticyclone (e.g., Bergman et al., 2013; Vogel et al., 2015; Clemens et al., 2023). However, the sampling location over the western Pacific as well as a northward shift in the location of the EASF during August 2022 (Pan et al., 2024) enabled ACCLIP to prominently sample convective outflow from the EASF as well.

The chemical composition of convectively transported air from these two ASM subsystems to the UTLS over the western Pacific Ocean is expected to be distinct due to the different environmental forcings and contributing emissions. We explore this hypothesis by categorizing airborne measurements according to convective transport from these sub-systems using the domains defined in Figures 2a and 2c. We henceforth refer to these contributions with the shorthand "South Asian Summer Monsoon (SASM)" (in orange) and "East Asian Summer Monsoon (EASM)" (in red) for simplicity. We acknowledge that western Pacific convective outflow was sampled during ACCLIP as well, although this had a smaller contribution given that ACCLIP research flights were designed to target the eastward extension of the ASM UTLS anticyclone into the western Pacific region, rather than sampling local oceanic convection.

Distributions of transit time from SASM and EASM convection to ACCLIP airborne measurements are shown in Figures 2b and 2d. These distributions indicate that a considerable portion of ACCLIP sampling was of relatively fresh (less than ~2 day old) outflow from EASM convection. Longer transport times from SASM and EASM convection to the flight tracks (up to 30 days in the present analysis) show a contribution of confined air masses that spiral in the ASM UTLS anticyclone until they reach the aircraft position. Overall, ACCLIP sampled a larger contribution of convection from the EASM compared to the SASM within 30 days (see the legends in Figure 2b and 2d).

Comparison of the calculations using GFS analysis (Figure 2a-b) and ERA5 reanalysis (Figure 2c-d) wind fields indicates a qualitative similarity in their identification of EASM and SASM convection as prominently contributing to ACCLIP measurements. Quantitatively, ERA5 wind fields indicate a considerably larger contribution from convection within the prior 30 days (80.4%, compared to 58.6% for GFS wind fields). The ERA5 calculation especially indicates a greater contribution from SASM convection compared to the GFS calculation. In similar transport modeling work, ERA5 wind fields were shown to better represent vertical transport in a convection-dominated environment compared to the GFS, perhaps owing in part to the higher spatial resolution and hourly temporal availability of ERA5 which can reduce inherent under-sampling of convective-scale processes (Smith et al., 2021; Bowman et al., 2013).

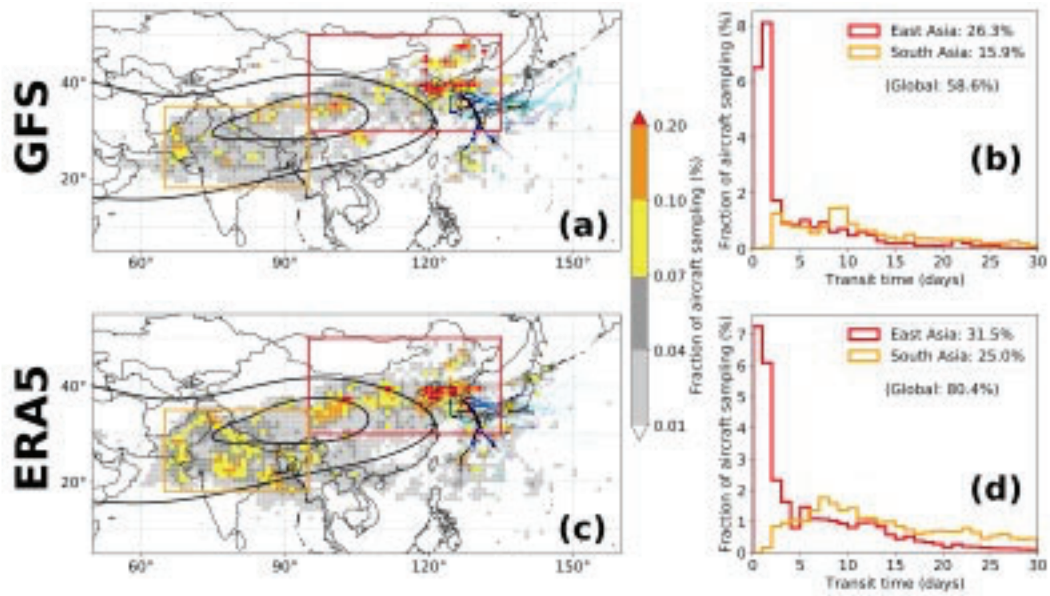

Figure 2: Overview of the locations and time scales of convective transport contributing to ACCLIP airborne sampling. Left panels show distributions of convective transport locations, with red and orange boxes indicating the selected EASM and SASM domains (respectively) considered in this study. Flight tracks and streamfunction contours are the same as in Figure 1a. Right panels show transit time distributions from convective outflow to airborne measurements categorized by EASM and SASM convection, with total contribution percentages printed on the legends. The top row shows results from GFS analysis wind fields, while the bottom row shows results from ERA5 reanalysis wind fields. All distributions are normalized to the total number of backward trajectories launched from the flight tracks.

Distributions of carbon monoxide (CO), dichloromethane (CH_2Cl_2), sulfur dioxide (SO_2), and toluene ($C_6H_5CH_3$) categorized by SASM and EASM convective transport are shown in Figure 3. These species are selected for this analysis due to their range of chemical lifetimes and their importance for understanding ASM impacts on global climate. Each of the selected trace gas species shows larger mixing ratios when transported from EASM convection compared to transport from SASM convection. The identification of CO mixing ratios in excess of 300 ppbv transported from EASM convection demonstrates the importance of convective transport from this region for impacting the composition of the ASM UTLS, which has been largely undiscovered by previous measurement efforts.

Dichloromethane (Figure 3b) is a dominant contributor of very short lived (VSL) organic chlorine, which has the potential to deplete stratospheric ozone. The ASM may facilitate injection of VSL chlorine into the stratosphere (WMO, 2022); enhanced VSL chlorine injection from EASM convection during ACCLIP was recently highlighted by Pan et al. (2024). SO_2 (Figure 3c) is a prominent precursor for the formation of sulfate aerosol, which may contribute to the composition of the Asian Tropopause Aerosol Layer (ATAL; e.g., Vernier et al., 2011) and subsequently impact climate through changes to radiative forcing (e.g. Fadnavis et al., 2024). The contribution of EASM convection to aerosol precursors in the UTLS is thus an important finding. Toluene (Figure 3d) is an anthropogenically sourced species with a relatively short lifetime (~2 days).

This species shows a considerable enhancement (~6 times higher) in EASM convective outflow compared to that of the SASM (Figure 3d, see legend). Due to its relatively short atmospheric lifetime, it is likely that chemical loss between SASM convection and the West Pacific UTLS contributes to this disparity.

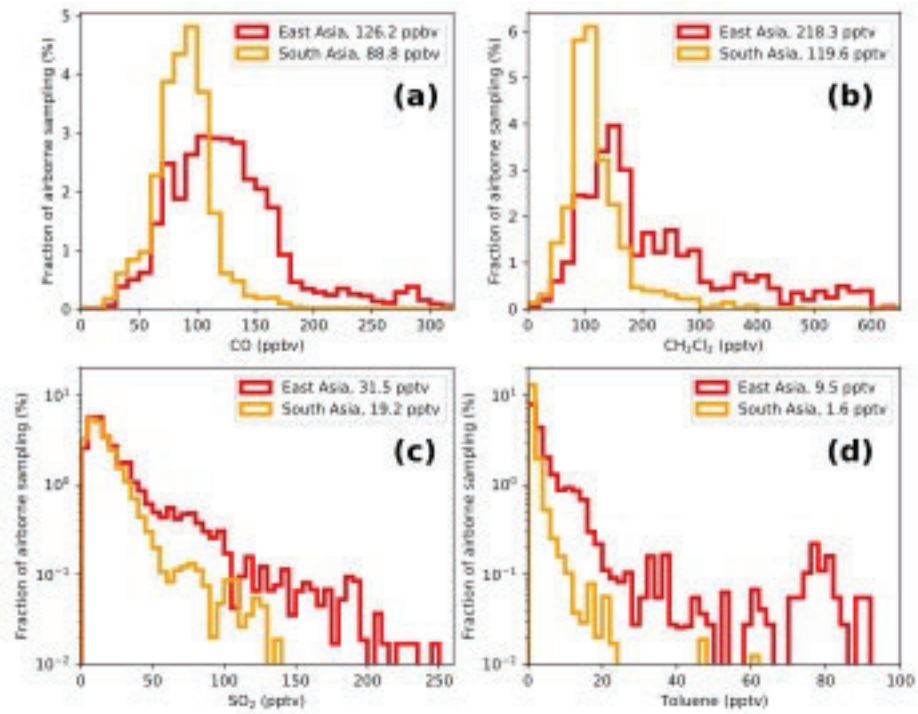

Figure 3: Distributions of selected trace gas species associated with (red) EASM and (orange) SASM convection, following the domains marked in Figure 2. Mean values of each distribution are given in the legends. Shown are (a) CO, (b) dichloromethane (CH_2Cl_2), (c) sulfur dioxide (SO_2) and (d) toluene ($C_6H_5CH_3$). Toluene sampling is from the GV aircraft only. Measurements of toluene that fall below the TOGA-TOF instrument's lower detection limit (0.1 pptv) are replaced with a value of half the detection limit (0.05 pptv). Note the log-scale y-axes on panels (c) and (d).

V. Conclusions

In this study, we developed a convective transport diagnostic for airborne in situ observations from the 2022 ACCLIP campaign, which are derived from a synthesis of Lagrangian trajectory modeling and satellite-based convective cloud top altitudes. This diagnostic enables individual flight track segments to be attributed to a specific location and time where convective transport to the UTLS occurred. Application of this diagnostic demonstrates a critical success for the campaign; while airborne sampling was conducted over the West Pacific, the diagnostic enables the contribution of ASM sub-systems to the overall ASM UTLS air mass export to be investigated. Analysis using the convective transport diagnostic showed that a considerable fraction of ACCLIP airborne sampling was of convective transport from the SASM and EASM (Figure 2). The identified importance of convective outflow from the EASM to the export of the ASM air mass represents a crucial step toward broadening the understanding of the ASM's role in global climate. Furthermore, transport originating from EASM convection is generally associated with larger pollutant concentrations compared to transport originating from SASM convection. This includes species with anthropogenic and industrial sources which range in chemical lifetime from days to months (Figures 3). These species are important for UTLS aerosol formation (e.g., SO_2) and injection of short-lived chlorine into the stratosphere (e.g., CH_2Cl_2; see also Pan et al., 2024).

In addition to the analyses presented here, the ACCLIP convective transport diagnostic continues to be used toward improved understanding of chemical and aerosol processes which comprise the ASM's role in global composition and climate. This includes the injection of very-short-lived chlorine substances into the stratosphere (Pan et al., 2024), analysis of the stratospheric sulfur budget (Gurganus et al., 2025), and analysis of black carbon removal in ASM convection (Berberich et al., 2025).

VI. References

Berberich, J., Jacoby, S. A., Michaioloudi, G., Schwarz, J. P., Viciani, S., D'Amato, F., et al. (2025). Observations of black carbon aerosol in monsoonal shedding events show extremely efficient wet removal. JGR, accepted.

Bergman, J. W., Fierli, F., Jensen, E. J., Honomichl, S., & Pan, L. L. (2013). Boundary layer sources for the Asian anticyclone: Regional contributions to a vertical conduit. Journal of Geophysical Research: Atmospheres, 118 (6), 2560–2575.

Bowman, K. P., Lin, J. C., Stohl, A., Draxler, R., Konopka, P., Andrews, A., & Brunner, D. (2013). Input data requirements for lagrangian trajectory models. Bulletin of the American Meteorological Society, 94 (7), 1051–1058.

Bowman, K. P., & Carrie, G. D. (2002). The mean-meridional transport circulation of the troposphere in an idealized GCM. Journal of the Atmospheric Sciences, 59 (9), 1502–1514.

Clemens, J., Vogel, B., Hoffmann, L., Griessbach, S., Thomas, N., Fadnavis, S., Ploeger, F. (2023). Identification of source regions of the Asian tropopause aerosol layer on the Indian subcontinent in August 2016. EGUsphere, 2023, 1–39.

Fadnavis, S., Sonbawne, S. M., Laakso, A., Ploeger, F., Rap, A., Heinold, B., MuÅNller, R. (2024). Long range transport of South and East Asian anthropogenic aerosols counteracting Arctic warming. NPJ Climate and Atmospheric Science, 7 (1), 101

Gurganus, C., Rollins, A., Waxman, E., Pan, L. L., Smith, W. P., Ueyama, R., Thornberry, T. (2025). Highlighting the impact of anthropogenic OCS emissions on the stratospheric sulfur budget with in-situ observations. JGR, in review.

Hersbach, H., Bell, B., Berrisford, P., Hirahara, S., HoraÅLnyi, A., Mun˜oz-Sabater, J., et al. (2020). The ERA5 global reanalysis. Quarterly Journal of the Royal Meteorological Society, 146 (730), 1999–2049.

Pan, L. L., Atlas, E. L., Honomichl, S. B., Smith, W. P., Kinnison, D. E., Solomon, S., et al. (2024). East Asian summer monsoon delivers large abundances of very short-lived organic chlorine substances to the lower stratosphere. Proceedings of the National Academy of Sciences, 121 (12), e2318716121.

Pan, L. L., Kinnison, D., Liang, Q., Chin, M., Santee, M. L., Flemming, J., et al. (2022). A multimodel investigation of Asian summer monsoon UTLS transport over the western Pacific. Journal of Geophysical Research: Atmospheres, 127 (24), e2022JD037511.

Pfister, L., Ueyama R., Jensen E., and Schoeberl, M., 2022: Deep convective cloud top altitudes at high temporal and spatial resolution, Earth and Space Science, 9, e2002EA002475. https://doi.org/10.1029/2022EA002475.

Smith, W., Pan, L., Honomichl, S., Chelpon, S., Ueyama, R., & Pfister, L. (2021). Diagnostics of convective transport over the tropical western Pacific from trajectory analyses. Journal of Geophysical Research: Atmospheres, 126 (17), e2020JD034341

Vernier, J.-P., Thomason, L., & Kar, J. (2011). CALIPSO detection of an Asian tropopause aerosol layer. Geophysical Research Letters, 38 (7).

Vogel, B., GuÅNnther, G., MuÅNller, R., Groo., J.-U., & Riese, M. (2015). Impact of different Asian source regions on the composition of the Asian monsoon anticyclone and of the extratropical lowermost stratosphere. Atmospheric chemistry and physics, 15 (23), 13699–13716

WMO. (2022). Scientific assessment of ozone depletion: 2022. GAW Report No. 681 278

VIII. Research meeting and discussion

International Joint Research Program 2024 allowed for sponsored travel by Rei Ueyama to attend the Meteorological Society of Japan Fall meeting and the 4th Asian Conference on Meteorology (ACM) which took place back-to-back in Tsukuba, Japan from November 12-21, 2024. She gave an oral presentation at ACM on November 19 titled “Convective transport to the UTLS over the Asian summer monsoon as observed during the 2022 ACCLIP airborne campaign”. She also a co-author on two of Dr. Kuniko Kodera’s posters at ACM titled “Role of deep ascending branch in the Hadley circulation and penetrating clouds in recent trends in tropospheric boreal summer” and “Role of very deep tropical convection in extreme weather in August 2022 through modulation of the Tibetan High”. She held research discussions with RIAM sponsor Professor Nawo Eguchi and Dr. Kodera during her 10-day visit. Dr. Ueyama and Professor Eguchi also visited JAXA and met with Mr. Ryohsuke Tamura, an engineer who is developing cloud microphysics instrumentation. Dr. Ueyama discussed the potential opportunity for no-cost participation in and contributions to a planned NASA airborne mission using high-altitude aircraft.

IX. Additional information

Rei Ueyama participated in the ACCLIP campaign as a Lead Meteorologist and Flight Planner.

X. Other members of the joint research team

Nawo Eguchi	RIAM, Kyushu University
Kunihiko Kodera	Meteorological Research Institute

国際化推進共同研究概要

No.5

[採択番号] 24EA-5

タイトル： Atmospheric Coupling Process from the troposphere to the thermosphere/ionosphere.

研究代表者： CULLENS Chihoko

所内世話人： EGUCHI Nawo

研究概要：大気重力波は大気下層のエネルギーや運動量を上層大気に運び、大循環を駆動している。また対流によって発生した重力波は中間圏や下部熱圏まで伝播し、さらに熱圏や電離圏まで伝播し、上層大気の風や電子密度に大きな乱れを引き起こします。そのため、重力波を介した対流圏、成層圏、中間圏の結合過程を理解することは重要です。

本稿では、台風によって発生した重力波の上層大気における影響を理解するため、衛星搭載のCloud Imaging and Particle Size (CIPS)とAtmospheric Infrared Sounder（AIRS）が観測した、2018年10月下旬に台風Yutuによって発生した重力波を解析した。それらによって、高度50～55kmと30～40kmの同心円状の重力波が観測され、高解像度のECMWF-IFSおよびECMWF再解析バージョン5（ERA5）とも、発生したタイミング、場所、波長がよく一致した。

Title: Atmospheric Coupling Process from the troposphere to the thermosphere/ionosphere

Chihoko Cullens, University of Colorado at Boulder / LASP

Gravity waves transport momentum and energy from the lower atmosphere to the upper atmosphere and drive atmospheric circulations. Convectively generated gravity waves can propagate up to the mesosphere and lower thermosphere, and even higher into the thermosphere and ionosphere, and cause large disturbances in winds and electron densities in the upper atmosphere (e.g., Vadas & Liu, 2013, Cullens et al., 2023). Therefore, it is important to understand coupling process between the troposphere/stratosphere to the thermosphere through gravity waves.

Our preliminary studies presented that the satellite-based Cloud Imaging and Particle Size (CIPS) instrument and Atmospheric Infrared Sounder (AIRS) observed concentric gravity waves generated by Typhoon Yutu in late October 2018 at altitudes of 50–55 and 30–40 km, respectively. These concentric gravity wave characteristics compared well with the high-resolution European Centre for Medium-Range Weather Forecasting Integrated Forecasting System (ECMWF-IFS) and ECMWF reanalysis v5 (ERA5). Both ECMWF-IFS with 9 km and ERA5 with 31 km horizontal resolution show concentric GWs at similar locations and timing as the AIRS and CIPS observations. The GW wavelengths are ∼225–236 km in ECMWF-IFS simulations, which compares well with the wavelength inferred from the observations. After validation of ECMWF GWs, 45 years of typhoon events are analyzed using ECMWF-IFS and ERA5 to obtain characteristics of concentric GWs in the Western Pacific regions. Through our proposed project, we have analyzed 45 years of reanalysis data and conducted statistical studies of relative importance of background wind conditions (gravity wave propagations) and strength of typhoons (gravity wave sources).

Figure 1 shows correlations between strength of typhoon and gravity wave momentum flux (GW-MF). There are negative correlations between minimum central pressure of typhoons and GW-MF at ~13-15 km altitudes; however, such correlations disappear above ~20 km. On the other hand, changes in background wind indicated by wind rotation and speed have negative correlations above ~20 km. These results suggest that influences of strength of typhoons are stronger up to ~15 km, then background winds that affect gravity wave propagation are more important above ~20 km for atmospheric coupling process. Our results were presented at AGU fall meeting in December 2024, and these results will be summarized and submitted to JGR-Atmosphere in 2025.

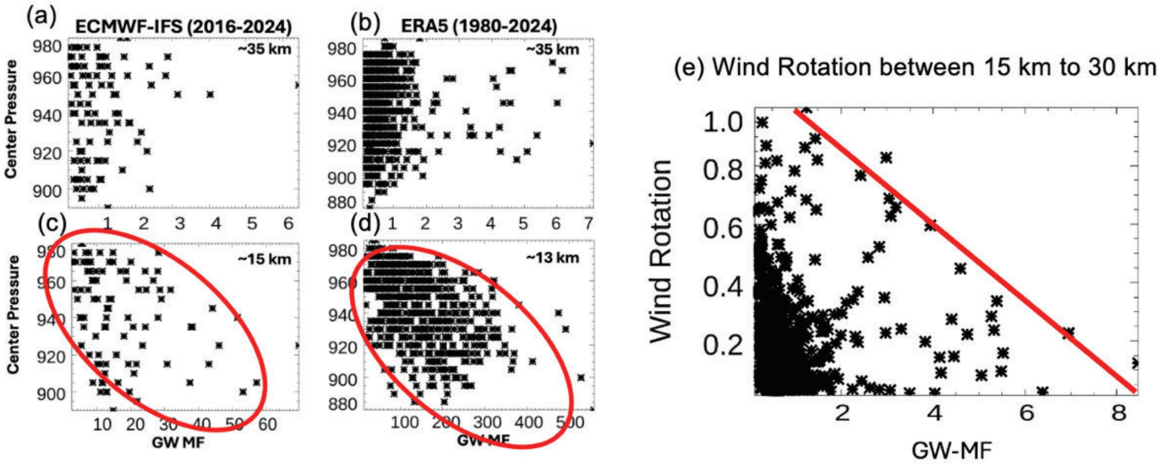

Figure 1. (a-d) correlations between GW momentum flux (GW-MF) and minimum central typhoon pressure with (a, c) ECMWF IFS data (9 km horizontal resolution) and (b, d) ERA 5 data (31 km horizontal resolution). (e) Correlations between GW-MF and wind rotation (an indicator for GW propagation probability).

国際化推進共同研究概要

No.6

[採択番号] 24EA-6

タイトル: Exploring new approaches in lidar remote sensing of cirrus clouds

研究代表者: VOELGER Peter

所内世話人: SATO Kaori

研究概要：Balloon-borne particle imagerによる氷晶雲特性の実測観測から、その生成条件の解析と、それらの観測データに基づいた氷粒子散乱特性の理論計算を実施し、衛星解析プロダクトの検証に応用した。

Research report
Grant No. 24EA-6
Title: Exploring New Approaches in Lidar Remote Sensing of Cirrus Clouds

Participants:

Peter Voelger, Gopika Gupta (Swedish Institute of Space Physics, IRF)
Janos Stenszky (Luleå University of Technology, LTU)
Kaori Sato, Hajime Okamoto (RIAM)
Tomoaki Nishizawa, Yoshitaka Jin (National Institute for Environmental Studies, NIES)

Background:

Lidar is one of the most common remote sensing instruments for investigating cirrus clouds. However, the great diversity of ice particles in cirrus clouds can result in very different backscatter signals from two clouds even though these clouds might appear to be similar. While this creates some challenges for the interpretation of measurement data, it can potentially also help in retrieving additional information. This project aimed at investigating what type of information potentially could be gathered. This was done by way of simulations, based on in-situ measurements of microphysics of ice particles in cirrus clouds.

Microphysics of cirrus clouds:

It is well known that characteristics of cirrus cloud particles depend on both local conditions and on the history of the cloud. Therefore, it is to be expected that properties of cirrus in polar regions differ from those in the midlatitudes and tropics. This has consequences for both lidar measurements and for the radiative budget of polar cirrus, which is an important property for climate studies. In-situ measurements, performed with LTU's balloon-borne particle imager B-ICI in northern Sweden, did indeed show differences, as the observed particles tend to be smaller and more compact than those in non-polar regions (Wolf et al., 2018). Data from several recent measurements with B-ICI have been analysed with the goal to define typical characterisations for different atmospheric conditions. This new data can help improving cirrus classification schemes for space-borne lidars, e.g. the scheme that has been developed at RIAM for interpreting data from CALIOP and ATLID, to incorporate regional differences in cirrus clouds.

Simulation of scattering properties of ice particles:

Once the microphysical characteristics of cirrus particles are described the scattering of light by individual ice particles can be calculated. While it is theoretically possible to consider all observed ice crystal shapes we can restrict simulations to several typical shapes, e.g. columns, bullets, rosettes, compacts, and agglomerates for the size range for which cirrus particles have been observed. Most of the simulations were done at IRF using a code developed by Macke et al. (1996). The advantage of that package is that it allows for simulations for non-perfect shapes. In this way impurities of ice crystals, which are common can be included, making results more realistic for atmospheric applications. Scattering characteristics for agglomerated particles were available from a database at RIAM, based on Ishimoto et al. (2012). One general characteristic of scattering on ice crystals in cirrus clouds is the dominance of forward scattering. The reason is the large size of the particles relative to the wavelength of the incident light. On the other hand, backscattering intensity and polarisation are strongly dependent on shape and size of the particles.

Simulation of lidar signals:

A consequence of the significant forward scattering is that multiply scattered photons can contribute to the lidar backscatter signal. Commonly used inversion methods ignore mutliple scattering (ms) and assume single scattering only. In the case of cirrus this leads to erroneous results. While the lidar equation including ms has no analytical solution it is possible to estimate the influence of ms with help of model simulations. Such simulations were performed with help of a Monte-Carlo model (Kerscher et al., 1995). Of particular interest was a lidar configuration that had been developed by NIES in recent years, a multiple-field-of-view lidar. Such a system allows recording backscatter signals with different ms contributions, i.e. the ms depending on the field-of-view. This approach opens new ways to utilise ms as an additional source of information. Simulations of lidar backscatter signals were been performed for various cloud configurations.

Activities:

Work packages were planned, coordinated, and distributed during web meetings with all involved parties. These meetings were organised every two to three months, depending on availability of the Co-Is. Results were distributed after they had been approved by the team that had produced them. To wrap up the project a visit to RIAM by one of the Swedish participants is planned for March 2025.

Outlook:

The grant enabled the start of a collaboration between the involved Swedish and Japanese institutions. One purpose of the planned visit to RIAM is to draft possibilities to summarise current results for publication. These results have also pointed us to follow-up questions which deserve more detailed investigation. *How* these questions can be addressed should be discussed after the conclusion of this project.

References:

- Ishimoto, H., K. Masuda, Y. Mano, N. Orikasa, and A. Uchiyama: Irregularly shaped ice aggregates in optical modeling of convectively generated ice clouds, JQSRT, 113, 632-643, doi:10.1016/jqsrt.2012.01.017, 2012.
- Kerscher, M., W. Krichbaumer, M. Noormohammadian, and U. G. Oppel: Polarized multiply scattered LIDAR signals, Opt. Rev., 2, 304-307, doi:10.1007/s10043-995-0304-7, 1995.
- Macke, A., J. Mueller, and E. Raschke: Single scattering properties of atmospheric ice crystals, J. Atm. Sci., 2813-2825, doi:10.1175/1520-0469(1996)053%3C2813:SSPOAI%3E2.0.CO;2, 1996.
- Wolf, V, T. Kuhn, M. Milz, P. Voelger, M. Krämer, and R. Christian: Arctic ice clouds over northern Sweden: microphysical properties studied with the balloon-borne ice cloud particle imager B-ICI, Atm. Chem. Phys., 18, 17371-17386, doi: 10.5194/acp-18-17371-2018, 2018.

国際化推進共同研究概要

No.7

［採択番号］ 24NU-1

タ イ ト ル ： Design of local heating on PANTA to drive inverse cascade of turbulence to MHD scale structure

研究代表者： YUN Gunsu

所内世話人： MOON Chanho

研究概 要：

本研究では、PANTA装置におけるプラズマ加熱および電流駆動手法として、電子サイクロトロン共鳴加熱（ECH）および直流バイアスを活用し、MHDスケールの構造形成を促進することを目指しました。電子温度変動の二次元可視化にはトモグラフィー技術を、電流駆動には電子銃を導入しました。さらに、磁場変動の計測には新たに開発した磁気プローブを使用しました。

また、国際的な連携強化を目的として、POSTECHと九州大学のプラズマ研究者間でワークショップを開催し、計測プローブの技術討論やプラズマ放電のデモンストレーションを実施しました。このような交流を通じて、今後の共同研究の発展が期待されます。

RIAM JOINT RESEARCH REPORT SUMMARY (English Form)

1. Research ID: 24NU-1

2. Research Title: Design of local heating on PANTA to drive inverse cascade of turbulence to MHD scale structure

3. Category: International

4. Applicant

Affiliation: POSTECH

Name: Gunsu Yun

5. RIAM Attendant: Moon, Chanho

6. Summary (150~200 words in Japanese or 100~150 words in English):

This research investigates plasma heating and current drive methods applicable to PANTA, focusing on electron cyclotron resonance heating (ECH) and DC biasing to facilitate the formation of MHD-scale structures through inverse cascade phenomena. The study plans to utilize tomography for 2D imaging of electron temperature fluctuations and an electron gun for current drive, though its installation is pending. A magnetic pickup coil is also under development to measure magnetic field fluctuations. Inspired by KSTAR experiments, where electron cyclotron current drive (ECCD) led to multiple flux tubes evolving into larger coherent structures, this research aims to explore similar processes in PANTA. Future work includes installing and testing the electron gun, deploying the magnetic pickup coil, and refining measurement techniques. Additionally, a workshop is planned to enhance collaboration between plasma researchers at POSTECH and Kyushu University, featuring discussions on diagnostic probes, hands-on tutorials, and a plasma discharge demonstration.

*) Submit either one of Japanese or English forms.

Design of local heating on PANTA to drive inverse cascade of turbulence to MHD scale structure

Affiliation: POSTECH
Applicant: Gunsu Yun

Abstract

This research investigates plasma heating and current drive methods applicable to PANTA, focusing on electron cyclotron resonance heating (ECH) and DC biasing, with the goal of designing and implementing an external heating system. Once equipped, the system will enable the study of inverse cascade phenomena, specifically the formation of large-scale structures from turbulent eddies as a novel pathway for MHD-scale structure formation.

To achieve this, we plan to utilize PANTA's existing tomography system for 2D imaging of electron temperature fluctuations over time, like the Electron Cyclotron Emission Imaging (ECEI) diagnostic used in KSTAR. The current drive is intended to be performed using an electron gun, though its installation is still pending. Additionally, a magnetic pickup coil probe is being designed for measuring magnetic field fluctuations.

As a preliminary study, we analyzed previous research conducted on KSTAR, where electron cyclotron current drive (ECCD) was observed to facilitate the formation of multiple flux tubes (MFTs) that evolved into larger coherent structures through energy transfer between Fourier harmonics, suggesting an inverse cascade process. This theoretical and experimental foundation will guide similar investigations in PANTA.

While the research presents valuable insights, certain limitations exist. The absence of an installed electron gun limits current drive experiments, and the magnetic pickup coil is still under design. Additionally, the resolution and range of the tomography system may impose constraints on data interpretation. Future research will address these challenges by implementing the necessary hardware and refining measurement techniques to further explore turbulence-driven large-scale structure formation in magnetized plasmas.

1. Purpose of the Research

This research aims to evaluate plasma heating and current drive methods suitable for PANTA, such as electron cyclotron resonance heating (ECH) and DC biasing, and subsequently design a heating system that can be implemented. By equipping PANTA with an external heating system, we intend to investigate inverse cascade phenomena—specifically, the formation of large-scale structures from turbulent eddies—as a novel pathway for MHD-scale structure formation.

2. Experimental Method

To observe MHD structures in PANTA, we plan to utilize the tomography system currently installed in the device, which enables 2D imaging of electron temperature fluctuations over time, similar to the Electron Cyclotron Emission Imaging (ECEI) diagnostic used in KSTAR. For current drive, we aim to use an electron gun; however, its installation is still pending. Additionally, to measure magnetic field fluctuations, we are designing and preparing to install a magnetic pickup coil probe.

2.1 Preliminary Study

As a preliminary study for implementing such experiments on PANTA, we have analyzed previous research on inverse cascade phenomena observed in KSTAR using electron cyclotron current drive (ECCD). The study by Dong-Kwon Kim et al. (2024) in *Nuclear Fusion* demonstrated that multiple flux tubes (MFTs) evolved into larger coherent structures through energy transfer between Fourier harmonics, suggesting an inverse cascade process. This provides a theoretical and experimental foundation for understanding similar large-scale structure formation in PANTA.

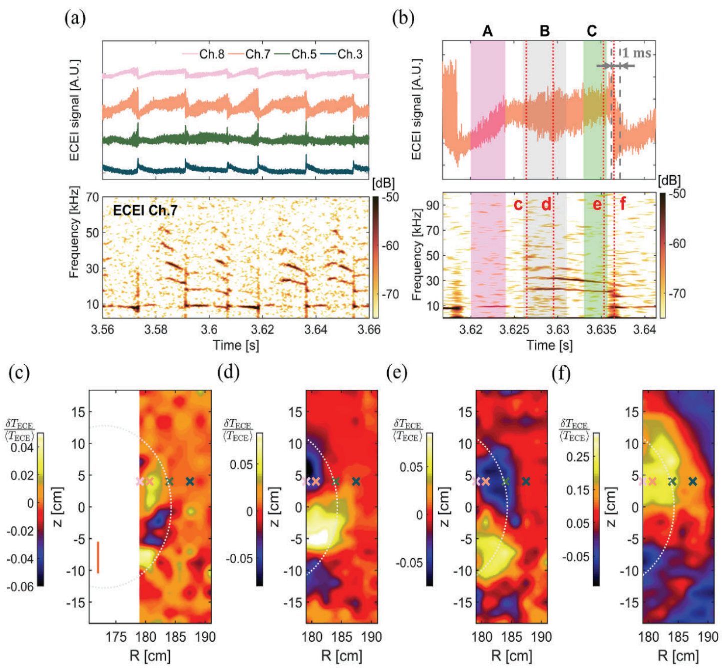

[1] Dong-Kwon Kim *et al*. Nucl. Fusion **64** 046004 (2024).

3. Conclusion

3.1 Significance of Results

The experimental findings provide insights into the formation of MHD-scale structures in PANTA and their comparison with inverse cascade phenomena observed in other devices like KSTAR. These results contribute to understanding turbulence-driven large-scale structure formation in magnetized plasmas.

3.2 Comparison with Previous Studies

Compared to KSTAR experiments that used ECEI to visualize electron temperature fluctuations, PANTA employs a tomography system, offering different observational perspectives. The planned implementation of an electron gun for current drive and magnetic pickup coils for fluctuation measurements will further enhance the study of plasma turbulence and structure formation.

3.3 Limitations of the Experiment

- The electron gun for current drive has not yet been installed, limiting the scope of current-driven plasma studies.
- The magnetic pickup coil is still in the design phase, preventing direct measurement of magnetic field fluctuations.
- The resolution and measurement range of the current tomography system may impose constraints on data interpretation.

3.4 Future Research Directions

- Installation and testing of the electron gun to study current drive effects in PANTA.
- Deployment of the magnetic pickup coil to measure and analyze magnetic field fluctuations.

Figure 1 Observed Inverse cascade phenomena in KSTAR [1]

- Further data collection and analysis to quantitatively evaluate inverse cascade phenomena.
- Exploration of additional heating methods, such as RF heating, to enhance control over plasma conditions.

[1] Dong-Kwon Kim *et al*. Nucl. Fusion **64** 046004 (2024).

POSTECH
POHANG UNIVERSITY OF SCIENCE AND TECHNOLOGY

九州大学
KYUSHU UNIVERSITY

The 1st POSTECH-Kyushu University Joint Workshop on Probe Diagnostics

7-9 January 2025

Venue: Room 109, Science Bldg. III (Department of Physics)
Room 102, Experiment Bldg. II (Division of Adv. Nuclear Eng.)
77 cheongam-ro, Pohang-si, Gyeongbuk, 37673, Korea

Host: Prof. Gunsu Yun (POSTECH)

✓ **7 Jan (Tue)**

Time	Session	Speaker
~ 17:00	Registration / Check-in to POSCO International Center	
17:00 – 18:00	Introduction to P4 Research Group & RAPID linear device	Gunsu Yun (POSTECH)
18:00 – 20:00	Welcome Dinner	Chanho Moon (Kyushu Univ.)
20: 00 ~	Adjourn	Youngdae Yoon (APCTP)

✓ **8 Jan (Wed)**

Morning session (9:00 – 12:00)

Time	Session	Speaker
9:00 – 9:30	Review of plasma sheath physics and diffusion theory	Gunsu YUN (POSTECH)
9:30 – 10:00	Operation principle of Langmuir probes	Chanho MOON (Kyushu Univ.)
10:00 – 10:30	Coffee break	
10:30 – 11:00	Operation principle of enthalpy probe	Sooseok CHOI (Jeju Nat. Univ.)

11:00 – 11:20	Working principle of electro-optic (EO) probe	Dongjune Lee (KRISS)
11:20 – 11:40	Introduction to the Magnetoplasma Dynamic Thruster (MPD)	Kil-Byoung CHAI (KAERI)
11:40 – 12:00	Magnetized microwave plasma experiments at RAPID	Kyungtae KIM (POSTECH)
12:00 – 13:30	Lunch break	

Afternoon session (14:00 – 17:00)

Time	Session	Speaker
14:00 - 16:00	Demonstration of plasma discharges at RAPID linear device	Hyeong-gu Kang (POSTECH)
16:00 – 16:30	Coffee break	
16:30 – 18:00	Hands-on tutorial of EO probe at RAPID	Yeonghoon Yun (East-photonics)
18:00 – 20:00	Workshop Dinner	Gunsu Yun (POSTECH)
20:00 ~	Adjourn	Seongbin Hong (POSTECH)

✓ **9 Jan (Thu)** at Pohang Accelerator Laboratory (PAL)

Time	Session	Speaker
10:00 – 11:00	Study Tour of PLS-II	Saehyun Bae (POSTECH)
11:00 – 12:00	Study Tour of XFEL (X-tray free electron Laser)	Dr. Taekyun Ha (PAL)
12:00 – 14:00	Lunch break	
14:00 – 16:00	Discussion on Joint research	Chanho Moon (Kyushu Univ.)
16:00 – 16:30	Closing	Gunsu Yun (POSTECH)

POSTECH P4

RIAM
Research Institute
for Applied Mechanics,
Kyushu University

5. Proceedings of the Workshop

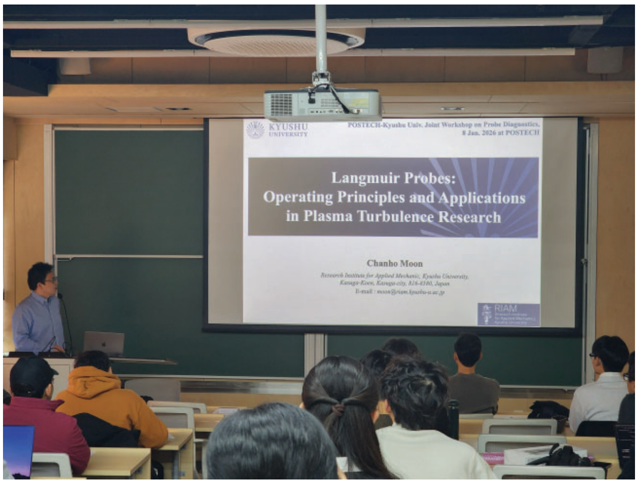

A workshop is planned to discuss the operating principles and physical analysis methods of various plasma diagnostic probes used in linear plasma devices, including the RAPID device at POSTECH and the PANTA device at Kyushu University.

Key sessions include:

- **Prof. Gunsu Yun (POSTECH)**: "Review of plasma sheath physics and diffusion theory"
- **Prof. Chanho Moon (Kyushu Univ.)**: "Operation principle of Langmuir probes"
- **Prof. Sooseok Choi (Jeju Nat. Univ.)**: "Operation principle of enthalpy probe"
- **Dr. Dongjune Lee (KRISS)**: "Working principle of electro-optic (EO) probe"
- **Dr. Kil-Byoung Chai (KAERI)**: "Introduction to the Magnetoplasma Dynamic Thruster (MPD)"

After the probe operation and physical analysis method sessions, a plasma discharge demonstration using various plasma sources on the RAPID device at POSTECH is planned. A hands-on tutorial will follow, where plasma properties will be measured using EO probes and Langmuir probes.

On the final day of the workshop, a tour of PLS-II and XFEL is scheduled.

Expected Outcomes

- Exchange of research activities and collaboration between POSTECH and Kyushu University on linear plasma devices and diagnostics.
- Hands-on experience with newly developed electro-optic probe systems and existing diagnostic tools, facilitating research collaboration.
- Encouraging participation from graduate and undergraduate students through preliminary sessions on plasma sheath physics and diffusion theory.
- Strengthening collaboration between plasma research and accelerator research through the scheduled accelerator facility tour.

国際化推進共同研究概要

No.8

[採択番号]　24NU-2

タイト ル： Generation and transport of runaway electrons in disruptions

研究代表者： Hurst Noah

所内世話人： NISHIZAWA Takashi

研究概 要：トカマク炉においてディスラプション時に発生する逃走電子は炉に深刻な損傷を与える可能性がある。そのため逃走電子に関わる物理を解明し、その発生を回避することはトカマク方式による核融合炉の実用化において最重要課題の１つである。本研究では九州大学のPLATOトカマク装置において高速カメラを用いて計測を行った。X線に起因すると考えられるノイズが観測され、PLATOトカマクにおいて逃走電子が生じている可能性が示唆された。Hurst氏の所属するWisconsin大学ではMST装置を用いて逃走電子に関する研究が推進されてきた。今後Wisconsin大学で開発された計測システムをPLATO装置に導入し、逃走電子の生成、抑制に関わるメカニズムの解明に取り組む予定である。

Generation and transport of runaway electrons in disruptions

University of Wisconsin, Madison Noah Hurst

Background and aim of research

Runaway electrons generated through disruptions have been seen as one of the most serious issues in a tokamak reactor. A sudden quench of the plasma current associated with a disruption creates a strong inductive electric field that accelerates some portion of electrons to relativistic velocities. These electrons are called runaway electrons (REs) and have damaged the first-wall materials in existing large tokamak experiments. In reactor-size tokamaks, it is predicted that REs may lead to intolerable damage. Therefore, understanding the physics involved in the RE generations and their transport has been an important area of research in the development of a tokamak reactor.

REs have been studied at the University of Wisconsin, Madison by using a toroidal plasma confinement device, Madison Symmetric Torus (MST). MST is capable of sustaining significant RE populations in a quasi-steady state by creating low-density tokamak plasmas. To measure the dynamics of REs, several sophisticated diagnostic systems, e.g. hard/soft x-ray detectors and magnetic measurements[1,2,3], have been developed. Drastic changes in the RE populations have been observed by these systems when resonant magnetic perturbation (RMP) is applied. However, due to the stabilization provided by a thick aluminum shell (5cm), disruptions are hardly made in MST. Thus, the behaviors of REs during disruptions cannot be studied in this device. In this proposal, REs associated with

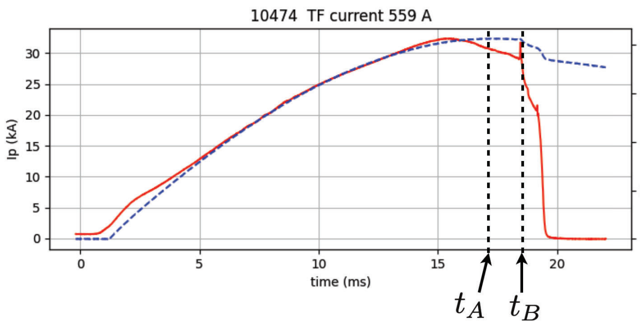

Figure 1 waveforms of the plasma current (red solid line) and the current in vertical field coils (blue dashed line).

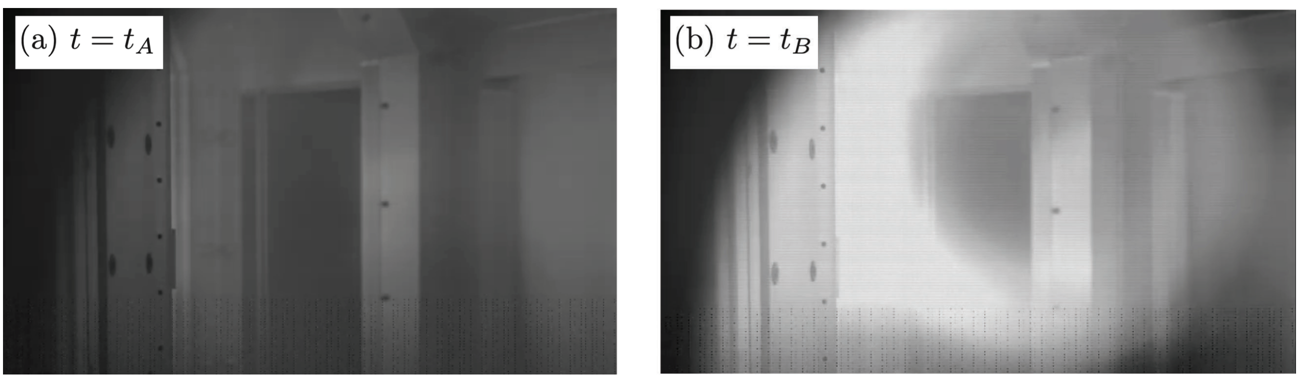

Figure 2 Snapshots of the discharge shown in Fig 1 right before (a) and during (b) the

disruptions will be studied by using PLATO at RIAM. By utilizing both MST and PLATO, the dynamics of REs can be thoroughly investigated.

Progress in 2024

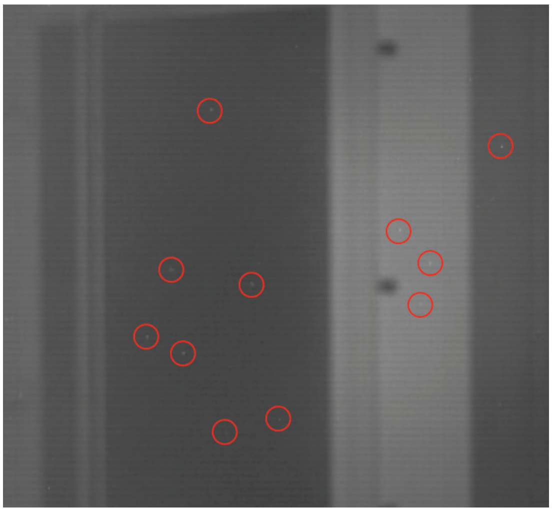

Figure 3 Noise in the fast camera signal during flattop

Due to family issues, a visit to Kyushu University was not made. Instead, I invited one of the collaborators in this project, Yuichi Kawachi to my institute to discuss plans for the study of REs at PLATO. Through discussions with Yuchi, I decided to analyze the videos of PLATO plasmas recorded by a fast camera first. A discharge shown in Fig 1 presents features that might indicate the presence of REs. At t_B the plasma disrupts. In this moment, a spike in the plasma current is seen. Snapshots of this discharge at t_A and t_B are shown in Fig. 2. Strong radiation in the visible wavelength range is observed at t_B. While recombination also contributes, REs can be the source of this radiation. This kind of pulse shape is hardly found at MST since the thick conducting vacuum vessel prevents sudden changes in the plasma current. In addition, Fig 3 indicates that REs might also be present during the flattop. In the red circles, pixels with high intensities are seen. This noise is thought to be caused by x-rays originating from REs.

Even though the fast camera provides interesting observations, more dedicated diagnostics are required to confirm the presence of REs in PLATO and study their dynamics. The fast x-ray system developed at University of Wisconsin[1] can be employed at PLATO to detect x-rays generated solely by REs. The RIAM advisor Takashi Nishizawa is going to be away from RIAM in 2025. Thus, we are planning to bring this system to PLATO in 2026.

References

[1] DuBois, Ami M., John David Lee, and Abdulgadar F. Almagri. "A high time resolution x-ray diagnostic on the Madison Symmetric Torus." *Review of Scientific Instruments* 86.7 (2015).

[2] Munaretto, Stefano, et al. "Generation and suppression of runaway electrons in MST tokamak plasmas." Nuclear Fusion 60.4 (2020): 046024.

[3] Delgado-Aparicio, L. F., et al. "Multi-energy reconstructions, central electron temperature measurements, and early detection of the birth and growth of runaway electrons using a versatile soft x-ray pinhole camera at MST." Review of Scientific Instruments 92.7 (2021).

国際化推進共同研究概要

No.9

[採択番号] 24NU-3

タイト ル： Advanced tokamak physics and integrated transport modelling

研究代表者： Na Yong-Su

所内世話人： MOON Chanho

研究概 要：

PANTAを用いてプラズマ乱流の理解を深めるためのいくつかの初期的な成果を示します。10チャンネルのプローブを回転させ、2つの密接に配置されたチャンネル間の位相差を測定することにより、過剰決定系の方程式を構築しました。この方程式系を解くことで、測定された交差位相を個別の波数成分に分解でき、これによりプラズマ乱流の線形特性を明らかにします。今後の研究では、非線形乱流の特徴解析と観測された変動の起源の特定に焦点を当てる予定です。

Wave vector decomposition on fluctuations in PANTA device

Yong-Su Na, Huiwon Chung, Chweeho Heo, Gyungjin Choi

Department of Nuclear Engineering, Seoul National University, Seoul 08826, Republic of Korea

Tokamak plasmas exhibit fluctuations arising from various instabilities. While these instabilities can have diverse origins, such as magnetohydrodynamic (MHD) or Alfvénic modes, the most fundamental driver of both transport and fluctuations is turbulence. However, the inherent toroidal geometry of tokamaks introduces significant complexity, making it challenging to comprehensively investigate the underlying physics of plasma turbulence. In this context, linear magnetic confinement devices have emerged as valuable tools, offering a simpler geometry that facilitates a more detailed exploration of turbulence-related phenomena. The Plasma Assembly for Nonlinear Turbulence Analysis (PANTA) is a prime example of a linear magnetic device. Specifically designed to investigate fundamental plasma turbulence physics, PANTA has been instrumental in enabling studies of turbulence phenomena that are challenging or impractical to conduct in tokamaks. Its simplified geometry and controlled experimental conditions provide a unique platform for advancing our understanding of plasma turbulence.

In this report, we present initial analysis results from experiments conducted on PANTA, a collaborative effort between the Department of Nuclear Engineering at Seoul National University and the Research Institute of Applied Mechanics at Kyushu University. The primary objective of this collaboration is to investigate fundamental plasma turbulence characteristics, particularly those occurring at the edge of confined plasma and in the scrape-off layer regions. While the plasma generated in PANTA marginally satisfies the conditions required for studying these phenomena, it is deemed suitable for the purposes of this collaboration.

Linear spectra of fluctuations are measured using the rotatable ten-channel Langmuir probe array (10LPA) on PANTA. This probe array is designed to rotate along the axial direction in the (r, θ, z) coordinate system, where the axial direction aligns with the magnetic field. The axial separation between adjacent probes is 3 mm, with each probe positioned to measure distinct radial locations, as illustrated in Fig. 1.

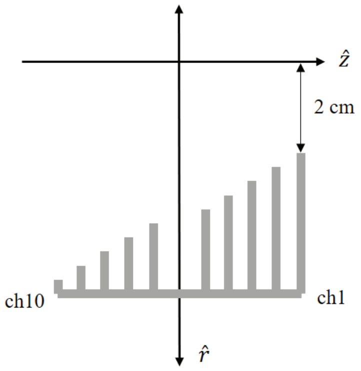

Fig. 1 Ten-channel probe array configuration

In the experiments, the magnetic field strength was held constant at 0.1 T, and the inlet gas species used was Argon. Plasma generation and heating were achieved using helicon waves. Electron density n_e profile, was reconstructed through voltage scans conducted with a separate Langmuir probe, which generated the characteristic I-V curves. To examine how plasma profiles respond to neutral gas pressure adjustments, we varied the neutral gas pressure P_{neut}, from 15 to 30 standard cubic centimeters per minute (sccm) in increments of 5 sccm. This allowed for a controlled parameter scan. The reconstructed plasma profiles for each P_{neut} are shown in Fig. 2, with error bars representing the standard deviations of values determined from I-V curve measurements across multiple trials.

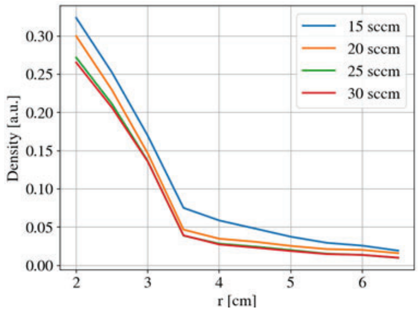

Fig. 2 Electron density profiles

As shown in Fig. 2, the steepest gradient of n_{e} is observed within a radial range of 2–3 cm. This region is predicted to host the majority of instabilities, such as drift waves, making it a key focus for our wave vector decomposition analysis. In a linear device where the poloidal plane is perpendicular to the axial magnetic field, poloidal harmonics are anticipated to play a significant role in driving turbulence. To investigate these harmonics, we analyze the cross-phase between two channels in the 10LPA array that are closest to the target radial range, enabling the extraction of individual wave vector components. However, a complicating factor arises due to the two channels measuring slightly different flux surfaces because of their physical separation. To address this issue, it is necessary to construct and solve a linear system. By rotating the 10LPA at an angle ψ_i, we formulate a linear system as follows:

$$\begin{pmatrix} R(\psi_0) & \Theta(\psi_0) & Z(\psi_0) \\ R(\psi_1) & \Theta(\psi_1) & Z(\psi_1) \\ \vdots & \vdots & \vdots \end{pmatrix} \begin{pmatrix} k_r \\ k_\theta \\ k_z \end{pmatrix} = \begin{pmatrix} \delta\phi_0 \\ \delta\phi_1 \\ \vdots \end{pmatrix}.$$

Here, $R(\psi_i)$, $\Theta(\psi_i)$, $Z(\psi_i)$ and $\mathrm{k_r}, k_\theta, k_z$ each represent displacement and the wave vector component in each direction, respectively. $\delta\phi_i$ refers to a cross-phase at each rotation. Rotating $10°$ per step, we configure an overdetermined system. By adopting least square method and singular value decomposition, the system can be solved to resolve each wave vector component as illustrated in Fig. 3.

Figure 3 illustrates that fluctuations with frequencies below 30 kHz exhibit nearly zero radial wavenumbers while showing a linear relationship between the wave number and frequency for both the poloidal and axial directions. The poloidal wave number increases as P_{neut} is raised, while the axial wave number remains constant. The origin of these fluctuations is still under investigation and will be addressed in the next phase of this collaborative study.

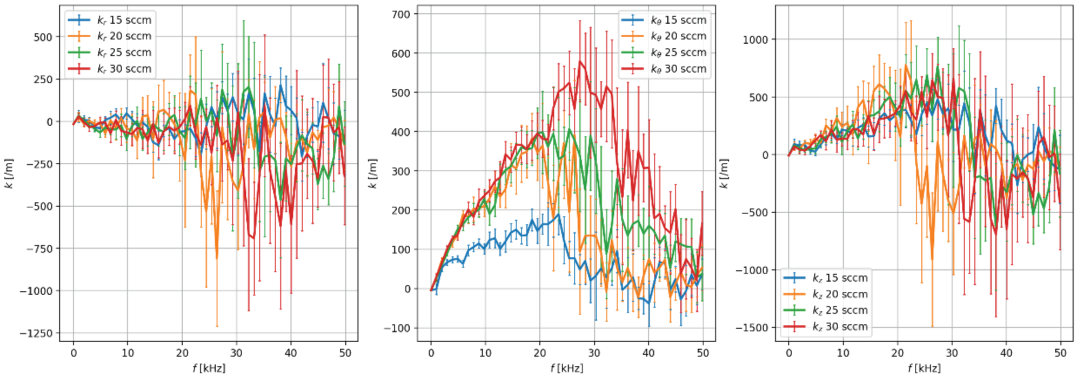

Fig. 3 Wave vector components in each direction

In conclusion, we present several preliminary findings to enhance the understanding of plasma turbulence using PANTA. By rotating 10LPA and measuring the phase difference between two closely spaced channels, an overdetermined system of equations was constructed. Solving this system allows us to decompose the measured cross-phase into individual wave vector components, which provides the linear characteristics of plasma turbulence. Future work will focus on analyzing nonlinear turbulence features and identifying the origins of the observed fluctuations.

2024 Nuclear Fusion Leading Technology Development Project Workshop

DATE

27th November 2024

INSTITUTION

Seoul National University (SNU), *Hanyang University (HYU)*, *Korea Atomic Energy Research Institute (KAERI), Ulsan National Institute of Science and Technology (UNIST)*, and *Kyushu University (KU)*

VENUE

31-301, 1 Gwanak-ro, Gwanak-gu, Seoul 08826, Republic of Korea

TIME TABLE

Time	Content	Presenter
09:30 – 10:00	Welcome address and introduction of researchers	Yong-Su Na (SNU)
10:00 – 11:00	Experimental research on the nonlinear dynamics of plasma turbulence in magnetize linear devices	Chanho Moon (KU)
11:00 – 12:00	Direct measurement of space potential and fluctuations by using the ball-pen probe in high-density linear helicon plasma	D. Di Matteo (KU)
12:00 – 13:30	Lunch break	
13:30 – 14:30	Development of a new concept of high temperature plasma heating and sustainment	Sangjin Park (SNU)
14:30 – 15:30	A development of a novel Fokker-Planck code for heating and current drive in high temperature tokamak plasmas	Yunho Jeong (HYU)
15:30 – 16:00	Coffee break	
16:00 – 17:00	A new core technology development of negative ion source and fast wave current drive for the extreme high temperature heating and stable sustainment of fusion plasmas	JongGab Jo & Kihyun Lee (KAERI)
17:00 – 18:00	Fundamental research on ECH/CD Gyrotron for steady-state tokamak operation	Jinho Lim (UNIST)

国際化推進共同研究概要

No.10

[採択番号]　24NU-4

タイトル： Investigation of thin film deposited by chemical vapor deposition using the 3-D tomographic system for advanced semiconductor application

研究代表者： CHUNG SEUNG-MIN

所内世話人： MOON Chanho

研究概要：

最近の3D X-pointメモリおよび原子層堆積（ALD）技術の進展により、半導体技術が大きく進化しました。PE-ALDでは、プラズマを利用して高速な堆積と広範な温度制御が可能で、低温下でもアモルファスカーボン膜の精密な制御が行えます。一方、熱ALDでは、より高いsp^3 C-C結合率を持つ滑らかな表面が得られ、オヴォニック閾値スイッチング（OTS）や相変化ランダムアクセスメモリ（PRAM）の用途に適しています。この技術の進展により、3Dメモリのビット密度向上や複雑な基板への対応が実現されています。

Investigation of thin film deposited by chemical vapor deposition using the 3-D tomographic system for advanced semiconductor application

Yonsei University

Seung-min Chung

Recent advancements in 3D X-point memory have been marked by notable industry achievements. Intel-Micron's successful development and mass production of stackable memory and SK-Hynix's innovative two-terminal selector—with a carbon layer engineered to enhance Ovonic Threshold Switch (OTS) reliability—demonstrate the rapid evolution of memory technologies. In particular, a study by A. Verdy showed that inserting a thin carbon layer between the TiN electrode and the OTS material significantly improved selector performance, achieving ultra-low leakage currents (10 pA) and remarkable endurance (10^9 cycles), thereby setting new benchmarks for back-end-of-line (BEOL) OTS selector technology. In parallel, while 3D X-point phase-change memory (PCM) promises ideal areal density, additional stacking inevitably increases the number of photolithography and process steps, raising production costs and lowering throughput. As device dimensions continue to shrink and substrate structures become more complex, the adoption of a 3D NAND-like architecture is emerging as a critical future direction for 3D X-point PCM. Such an architecture must not only improve areal bit density but also overcome the challenges associated with uniformly depositing electrode materials on intricate three-dimensional substrates.

Atomic Layer Deposition (ALD) has attracted considerable attention as a promising technique for fabricating nanomaterials on complex architectures. ALD enables the deposition of ultra-thin films with excellent uniformity, atomic-scale thickness control, high conformality, and low-temperature processing. The conventional ALD process involves four key steps: (1) precursor exposure that allows chemisorption onto the substrate, (2) purging of by-products with inert gases, (3) reactant exposure to enable chemical reactions with the chemisorbed precursors, and (4) a subsequent purging step to complete the cycle. Recent studies have explored the potential of ALD for carbon material synthesis. For example, Zhang et al. demonstrated the ALD growth of graphene layers using benzene precursors and hydrogen radicals, achieving controlled layer deposition at low temperatures. Although this process yielded high-quality graphene with improved layer control through the modulation of ALD cycles, the resulting films were neither uniformly monolayered nor scalable to large areas. To address these challenges, our study extends the application of ALD for carbon materials by demonstrating an amorphous carbon deposition process on tungsten (W) and SiO_2 substrates. A key innovation of our work is the comparative investigation of two ALD techniques: Plasma Enhanced ALD (PEALD) versus conventional thermal ALD. By systematically comparing the film properties and deposition dynamics on complex substrates, we aim to understand the advantages and limitations of each approach. PEALD, which utilizes plasma-generated reactive species, is anticipated to offer enhanced film conformality and quality at lower processing temperatures, potentially overcoming the limitations inherent to thermal ALD—especially for the integration of carbon layers in next-generation 3D memory architectures.

This study, therefore, not only extends ALD applications to more practical substrates but also provides a critical comparative analysis between PEALD and thermal ALD. The findings are expected to offer valuable insights for optimizing electrode deposition processes, thereby paving the way for future advancements in 3D X-point memory and related memory technologies.

Experient Method

The PE-ALD (Plasma-Enhanced Atomic Layer Deposition) chamber used for depositing amorphous carbon thin films is equipped with a showerhead-type injector and a capacitively coupled plasma (CCP) reactor. The sample stage, located at the center of the chamber, is heated to a maximum temperature of 600 °C. Prior to the deposition process, the substrate undergoes pre-treatment with O_2 plasma to remove byproducts and a CBr_4 exposure step to enhance the carbon growth rate. Each ALD cycle consists of four sequential steps: first, the hydroxylated SiO_2 and W substrates are exposed to CBr_4 precursors. Next, residual precursor molecules are purged using an inert Ar gas flow. Subsequently, the substrates are exposed to reactants, which may include hydrogen plasma gas (H_2+Ar), NH_3 gas, or H_2 gas, depending on the specific process (thermal ALD or PE-ALD). Finally, any byproducts and residual reactant gases are removed with an additional Ar gas purge. The CBr_4 precursor, sourced from Sigma-Aldrich, is vaporized at 60 °C. To maintain consistent CBr_4 flux and prevent condensation, the supply lines are continuously heated to approximately 70 °C. CBr_4 has a bond dissociation energy of 56.2 kcal/mol, which facilitates its decomposition and reaction during the deposition process. For the deposition process, thermal ALD employs NH_3 or H_2 as the reactant gas, while plasma-enhanced ALD (PE-ALD) uses a mixture of H_2 and Ar plasma. These conditions ensure precise control over the deposition of amorphous carbon films, achieving uniform and stable film growth on SiO_2 and W substrates.

Results & Discussion

The graphs illustrate the growth rate of amorphous carbon films deposited via PE-ALD and Thermal ALD across a temperature range of 150 to 400 °C. For PE-ALD, the ALD window lies between 200 and 250 °C, while the ALD window for Thermal ALD is observed between 250 and 300 °C. This difference arises because plasma provides higher reaction energy compared to purely thermal reactions, enhancing the chemisorption process. The growth rate data further support that the plasma-enhanced ALD process enables faster carbon film deposition. Sheet resistance measurements, obtained using a 4-point probe across various temperatures, show that at 250 °C, Thermal ALD produces films with lower sheet resistance than PE-ALD. This suggests that amorphous carbon films deposited through different processes exhibit distinct structural and electrical properties.

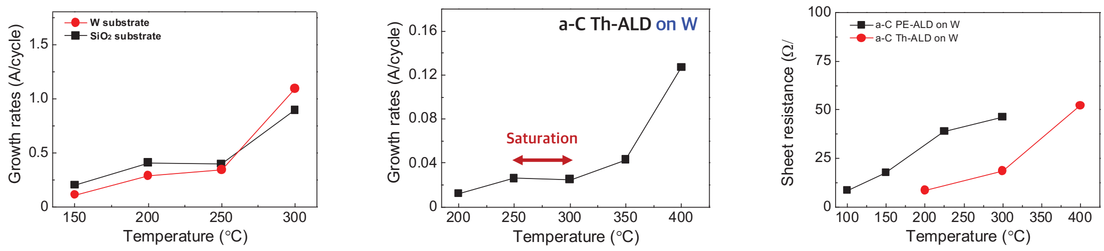

XPS spectra of the amorphous carbon films grown by PE-ALD and Thermal ALD reveal differences in bonding states. Films deposited via Thermal ALD exhibit the highest sp³ C–C bonding content at 71%, while PE-ALD films show the lowest sp³ content at 52%. These results indicate that Thermal ALD-grown amorphous carbon films contain a higher level of nanocrystalline sp³ carbon. Furthermore, the atomic percentage of bromine in the films, presented in the accompanying table, shows higher Br content in Thermal ALD films compared to PE-ALD films. This difference is attributed to the effect of plasma energy, which breaks Br ligands during the hydrogen plasma process in PE-ALD.

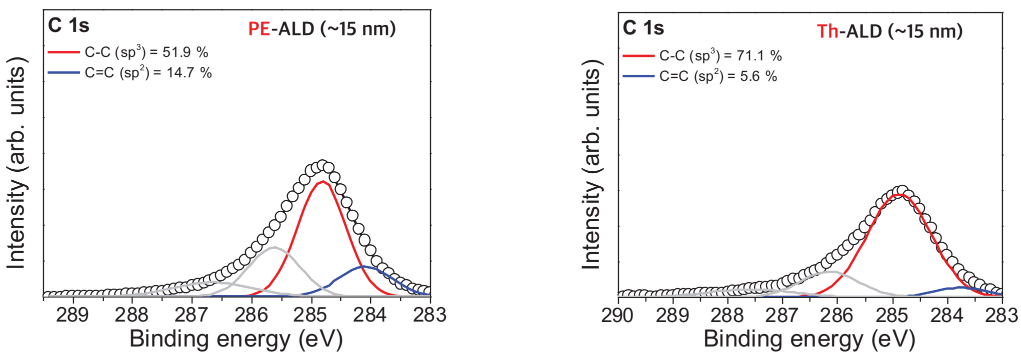

Conclusion

PE-ALD offers significant advantages in the deposition of amorphous carbon films, including faster growth rates, a broader ALD window at lower temperatures, and improved control over the deposition process. These benefits make PE-ALD an excellent choice for applications requiring high throughput and precise film deposition, particularly in advanced electronic devices. Additionally, its ability to achieve uniform films at lower processing temperatures highlights its potential for integrating amorphous carbon films into next-generation semiconductor technologies.

国際化推進共同研究概要

No.11

24NU-5

タ イ ト ル： Plasma start-up and sustainment in spherical tokamak configuration by RF

研究代表者： TAKASE Yuichi

所内世話人： 出射　浩

研究概要：
令和6年2月1、2日の2日間で国際 WS をハイブリッド形式で開催した。英国から 3 名、米国から 2 名、国内から多数の参加があった。QUEST 実験の最近の進展・検討に加え、国内外実験研究の検討・進展、新たな理論・シミュレーション解析などが議論された。英国から 3 件、米国から 2 件、国内で 8 件の研究成果発表があり、主に球状トカマクでの非誘導プラズマ電流立ち上げに関し、活発な議論があった。

Plasma start-up and sustainment in spherical tokamak configuration by RF

TAKASE Yuichi
(Tokamak Energy Ltd., United Kingdom)

An on-site/on-line hybrid workshop on "Plasma start-up and sustainment in spherical tokamak configuration by RF" will be held on 27th and 28th February at Advance Fusion Research Center in Research Institute for Applied Mechanics, Kyushu University. The proposed agenda is shown below. Lively in-depth discussions were held following each presentation.

Agenda

27th February AM

9:20 -9:30

Yuichi Takase / Hiroshi Idei

WS purpose and agenda

9:30 - 10:10

Yuichi Takase

Fusion Development at Tokamak Energy

10:10-10:50

Felicity Maiden （Invited）

Modelling Microwave Start-up in Spherical Tokamaks

10:50-11:20

Zhou Junyao

Plasma start-up using EBWCD on QUEST

11:20 - 12:00

Masayuki Ono

Dual utilization of X-I and O-I ECCD for fully solenoid-free operations for a fusion reactor

12:00-12:40

Hitoshi Tanaka

Control parameter mapping for formation of initial closed flux surfaces by ECH in LATE

12:40-13:30

Lunch

13:30-14:00

Hiroshi Idei

ECH Progress and Plans for QUEST

14:00-14:30

Makoto Hasegawa

Production and control of divertor configuration in QUEST

14:30-15:00

Takeshi Ido

Development of a heavy ion beam probe for turbulent transport studies in QUEST

15:00-15:10

Coffee Break

15:10-15:40

Yoshihiko Nagashima

Initial observation of interaction between kHz range turbulent fluctuations and MHz range fluctuations in the SOL region of the QUEST spherical tokamak

15:40-16:10

Ryuya Ikezoe

Proposal of RF plugging to solve divertor issues and the first step using toroidal local electrodes in a toroidal ECR slab plasma

16:10-16:50

Akira Ejiri

Parameter survey study on the Fusion by Advanced Superconducting Tokamak (FAST)

16:50-17:30

Aleksandra Alieva

Overview of the H&CD design for TE-FPP

Group Photo

28th February AM

9:30-10:10

Roger Raman

Recommended Three-Year CHI Plan on QUEST and Planned Experiments during Year-1

10:10-10:50

Atsushi Fukuyama

Recent progress of kinetic full wave analysis of EC waves in QUEST plasmas

10:50-11:20

Syunichi Shiraiwa

Recent application of Petra-M finite element framework for RF heating/current drive and space plasmas

11:20-12:00

Yusuke Kosuga

Role of Parallel Velocity Gradient (PVG) turbulence in spherical tokamaks

12:00-12:40

Shin Kubo

Toward the experimental and numerical estimation of the power flux of the electron Bernstein wave

12:40-13:30

Lunch

28th February PM

All suggested focus and output for this joint drafting session

Drafting of proposals for experiments, diagnosis, and analysis

Summary of Presentations

Yuichi Takase

okamak Energy (TE) is aiming for early commercialization of fusion energy by combining the advantages of the low aspect ratio (A) tokamak and high temperature superconductor (HTS) coils. In addition to achieving ion temperatures exceeding 100 million degrees K needed for fusion burn on ST40, we are developing technologies needed for fusion reactors. In HTS coil development, we are beginning tests of an HTS coil system in the spherical tokamak configuration (Demo4). Is addition to continuing fusion-relevant science and technology development, we are actively designing future devices, including a fusion neutron source and a fusion pilot plant. TE is involved in the FAST Project in Japan as an international design and technology partner. FAST is intended to demonstrate long-pulse fusion burn, power and particle exhaust solutions, fuel cycle, compact high-field magnet system, as well as development and testing of blanket modules for power conversion and tritium breeding, with the eventual goal of demonstrating electricity generation in the 2030s. Low-A tokamaks using HTS coils with $R_0 \sim 2$ m and $A \sim 2$ (FPL < 1 year) are being considered extensively. $B_{t0} \sim 3$ T and $I_p \sim 6$ MA can be achieved using the HTS technology developed at TE to produce 50-100 MW fusion power and ~ 0.5 MW/m^2 neutron wall loading for ~ 1000 sec. TE was awarded a design study of a Fusion Pilot Plant (FPP) for integrated test and validations of technologies, systems and processes required for commercial fusion energy deployment, under the U.S. Milestone Based Fusion Development Program. The FPP will demonstrate scalable net power in a fully integrated system. Parameters used as working assumption are: $R_0 = 4.25$ m, $A = 2$, $B_{t0} = 4.5$ T, and $I_p = 16$ MA. Novel I_p ramp-up and sustainment scenarios utilising RF power (EC and IC), bootstrap current, and induction by the CS and other poloidal field coils are being investigated.

Felicity Maiden (Invited)

Understanding the solenoid-free start-up of tokamaks is critical to successful power plant design. Start-up involves the plasma ionisation, initiation of a plasma current and current drive until closed flux surfaces are formed and the plasma is confined. This phase is different to the flat-top due to the open field lines, additional current drive mechanisms, inclusion of ionisation physics and low densities and temperatures. At present, most experimental tokamaks start-up with a central solenoid. However, solenoid-free microwave start-up has significant advantages for power plants as the microwaves can be used for current drive over the duration of the pulse and the technology is relatively robust to the harsh conditions. This is particularly attractive for spherical tokamaks like STEP with limited space in the centre column for a shielded solenoid. Nevertheless, start-up is not well understood. Previous work has interpreted experimental results to propose potential mechanisms for the formation of closed flux surfaces. However, there is currently no way to predict the time evolution of the current drive and plasma parameters. We have developed a novel Fokker-Planck solver Start-Up Modelling of Microwaves In Tokamaks (SUMMIT) to simulate microwave start-up in time. SUMMIT accounts for the changing field structure from open field lines, along which many particles are lost, to closed flux surfaces as well as particle sources due to ionisation, microwave diffusion, collisional diffusion and induction. This enables the interaction and relative importance of different current drive mechanisms and plasma parameters to be explored as the plasma evolves. Detailed comparisons with microwave start-up experiments performed on MAST have shown remarkable agreement and explained results not fully understood at the time. Particularly, the lost particles are found to play a crucial role in the current drive. This new understanding can be used to inform the design of future experiments and power plants.

Zhou Junyao

Experimental results of X-B mode conversion on HFS injection on QUEST to identify the effect of EBWCD and the reconstruction of current density profile in open flux surface (OFS) phase are reported. An incident antenna was located 0.17m above the equatorial plane of vacuum vessel to inject the X-mode ECW from HFS perpendicularly to the magnetic field. The ECW was expected to be converted to EBW at upper-hybrid resonance layer, then absorbed near the electron cyclotron resonance layer. A closed flux surface (CFS) was successfully formed by applying a magnetic configuration with n-index=0.35. The direction of EBWCD is decided by B_T and B_R directions. When the B_T direction was inversed from counter-clockwise (CCW) to clockwise (CW), the peak of measured magnetic flux ,which indicates the concentration of pressure driven current and equilibrium EBWCD, moved from top side to bottom side. The plasma current behaviour in OFS phase until CFS formed also changed from constant to ramp-up. For further investigation, the additional B_R was applied to adjust the absorption area for equilibrium and anti-equilibrium EBWCD. The results showed that plasma current grew faster with the increasing equilibrium area ratio. However, plasma failed to start up when the plasma mid-plane was too far away from the antenna or the ratio was smaller than 1. According to the plasma density by Thomson scattering, it was considered that ECW was reflected between the centre stack and L cut-off in high density. Then the L cut-off disappeared in low density and the ECW was converted into EBW at UHR layer and be absorbed near ECR layer. An improved current density profile model was used for reconstructing the current distribution in OFS phase. The results showed the location of plasma mid-plane indeed affected the EBWCD in opposite directions, and larger the equilibrium area ratio, larger the equilibrium current. The total EBWCD was estimated by the assumption of same pressure driven current under similar configurations. Then the EBWCD efficiency about 0.017A/W in OFS phase was obtained. These results indicate that EBWCD played a significant role in plasma start-up and can be improved by applying B_R to reduce the anti-equilibrium current.

Masayuki Ono

In the present work, we investigated this densification process where the plasma density is increased by a factor of 10 continuously from the low density X-I start-up regime to the high density O-I sustainment phase. A relevant question is can either X-I or O-I provide adequate ECCD as the plasma density is ramped up with a realistic power balance. The electrons have several power loss channels. In addition to the usual transport losses, there are radiative loses including synchrotron, bremsstrahlung and various impurity radiations. The radiative losses are relatively well understood, and can become excessive if the high Z impurity level is too high. In this exercise, we found an acceptable impurity level for lower Z carbon to be 2.5 %, for higher Z iron to be $2.5x10^{-}$

^{2} % and for very high Z tungsten to be 2.5 x 10^{-3} % which gives the Z-effective of ~ 2. Ions are heated through Coulomb collisions with hotter electrons. The ion temperature rise is balanced by the ion transport loss which could be close to ion neo-classical values as observed in the NSTX H-mode. The ions thus heated can produce fusion power if the 50:50 mixture of D-T is used. The resulting fusion alpha-heating power could reach ~ 100 MW level (or ~ 500 MW fusion power) at the sustainment density which together with the available ECH power could balance the electron power loss channels. The H-mode access appears to be possible with the available ECH plus the fusion a-heating power.

Hitoshi Tanaka

In order to find control parameter regions in which the toroidal plasma current increases and closed flux surfaces are formed, we produced a toroidal ECR plasma under a weak steady vertical field by changing the strength and decay index of the vertical field, the injection microwave power Pnet and hydrogen influx ΓH2. There is a minimum and a maximum value of the vertical magnetic field strength BvC at which a closed magnetic surface (CFS) is formed, and if the vertical magnetic field is too strong or too weak, a closed magnetic surface is not formed. As Pnet is increased, the area of formation of CFS expands toward higher BvC. It may be because the pressure-driven current increases even under strong BvC when Pnet is large, and the modification of poloidal field is enough for generation of CFP electrons. When Pnet is large and hydrogen influx is low, the discharge terminates in about several tens of msec. It may be because the electrons are much accelerated by ECH under low collisionality and the losses along field lines and by toroidal drift become significant. As ΓH2 is decreased, the area of formation of CFS expands and CFS becomes formed in the case of low Pnet. As decay index is increased, the area of formation of CFS expands toward higher BvC. It may be because larger mirror ratio for larger decay index cause higher population of trapped electrons which brings higher plasma pressure and precession current.

Hiroshi Idei

The 8.56 GHz system has mode selectivity on O- and X-mode. Non-inductive plasma ramp-up of relatively large-sized plasma is expected with on-axis bulk heating through significant single path absorption (> 15 % as a beam) in fundamental O-mode scenario. In X-mode scenario, efficient current ramp-up is expected due to up-shifted fundamental absorption at the inboard side in the low density. Fairly high (40-60 % as beams) were obtained at 0.5 - 4 x 10^{17} m^{-3} due to fundamental and 2^{nd} harmonic X-mode resonances. Since the electrons in wide energy range is in up-shifted 2^{nd} harmonic resonance near the axis, simultaneous achievement of high plasma current and high electron temperature is expected in the X-mode scenario. The transmission lines are adjusted for O-mode excitation. The 1.5 kA plasma current was ramped and sustained with 10 kW O-mode waves for 10 sec.

A new 28 GHz gyrotron system has been prepared. After coil adjustment, the gyrotron is set. To avoid stopping the experiments, 2 line system has been considered. The 2 line system would be effective for simultaneous achievement of high plasma current ramp-up and bulk electron heating with oblique and quasi-perpendicular injections. The 100 kA power supply is under development to conduct (inboard) fundamental and (on-axis) 2^{nd}

harmonic resonance experiments. The efficient plasma ramp-up with on-axis heating is expected (as presented in 2021).

Makoto Hasegawa

The research demonstrates that achieving a stable divertor configuration across various aspect ratios is possible. Further studies are required to analyze PF coil current waveforms and refine equilibrium calculations. Additionally, controlling the position of the divertor leg remains a challenge that requires further investigation. Lastly, improving vertical position control by enhancing feedback mechanisms and stabilizing effects from hot walls or vacuum vessels will be a key focus for future work. This study provides valuable insights into divertor configuration control, contributing to improved plasma confinement and overall fusion performance in spherical tokamaks.

Takeshi Ido

An HIBP is being installed for measuring the electrostatic and electromagnetic turbulences in QUEST. The required energy for the probe beam ranges from 15 to 50 keV for Cs+ at a magnetic field strength of 0.25 T. The 0.5T operation requires 60-200 keV, which will require significant modification of the beamline. The observable area covers the upper half of plasmas, and the HIBP can be applied to plasmas with the toroidal current of up to 150 kA　for 0.25 T operation (and to 300 kA for 0.5 T operation in future). The expected signal intensity is sufficient for turbulence measurement in the core region when the electron density is up to 1x1019 (m-3), which is higher than the cut-off density of ECH in the QUEST tokamak.

Yoshihiko Nagashima

In this presentation, preliminary results of scrape-off layer plasma measurements in QUEST using newly developed electrode system that can work as a limiter and a Langmuir probe.　Measured bulk electron temperature is about 10-20 eV and is consistent with preceding works in QUEST. In addition, during inboard poloidal null tokamak operations performed with 8.2 GHz or 28 GHz RF source, signs of correlations/interactions between low frequency floating potential spikes/fluctuations and MHz range fluctuations were detected using the electrode system.

Ryuya Ikezoe

RF plugging at divertor leg using local electrodes was proposed to solve the heat load problem of the divertor and to explore the control knob for the mixing ratio of fuel ion species. Expected innovative technologies are: ① Selective ion species plugging → A solution to the fuel dilution problem; ② SOL plasma confinement → SOL width expansion（reduction of heat load）→ development of new concept, stabilization, neutral particle control, etc.; ③ Suppression of backflow of impurity ions → The coexistence of detached diverters and core confinement; ④ Control of detached plasma → Optimization, Stabilization, Control. Towards the demonstration of scientific and technological feasibility: １. RF plugging using local electrodes in a toroidal system → A simple test has been started using an ECR slab plasma on QUEST; 24% reduction of ion flux was obtained at the initial test. 2. Suppression of impurity ions backflow and control of detached plasma → planned and partially started using a linear machine.

Akira Ejiri

FAST (Fusion by Advanced Superconducting Tokamak) is a project being proposed as a facility for R&D, testing, and to demonstrate integration of systems necessary for a Deuterium Tritium (DT) fusion energy reactor. The required specifications for FAST are: DT fusion power of 50-100 MW, neutron wall loading of 0.3-1 MW/m^2, discharge duration of about 1000 sec, full-power operation time of about 1000 hrs. Quasi 0-dimensional parameter survey using hybrid energy confinement times has been conducted to find a cost-effective design window. A compact low aspect ratio HTS tokamak with NBI can satisfy the requirements of FAST. A cost effective combination of n_{Wlmax} and P_{fus} are found. To satisfy the requirements $n_{Wlmax} > 0.65$ MW/m^2 and $P_{fus} > 70$ MW. An appropriate parameter set is $A \sim 2.3$, $R \sim 2$ m, $f_{\mathrm{GW}} \sim 0.5$, $\kappa \sim 2.3$, $P_{\mathrm{NBI}} \sim$ 50 MW, Device cost ~ $800M (w/o BOP and a first of kind costs). The plasma is NBI-driven one, and the normalized density and pressure are not so high.

Aleksandra Alieva

Tokamak Energy (TE) is developing a pre-conceptual design of the Fusion Pilot Plant (FPP) based on a spherical tokamak for the US Milestone-Based Fusion Development Program. The auxiliary heating and current drive (H&CD) system is being designed to support the fusion plasma parameters achievement and sustainment during the pulsed operation of the machine. A solely electron cyclotron (EC) based auxiliary H&CD system is being considered for the flat-top phase of proposed plasma scenarios. For the analysed scenarios current profiles consist of the auxiliary current and bootstrap one. Hence, for the non-inductive current drive during this phase, it is crucial to find the most efficient system layout in terms of EC current drive efficiency ζ. To do so, a parametric scan was done via ray-tracing modelling. This work presents the comparison of results obtained for three plasma designs, highlighting the main observed dependencies on a launcher setup, choice of frequency, and wave polarisation. It is shown that O mode polarisation provides high EC current drive efficiencies ζ among all plasma radii. Furthermore, a reliable current ramp-up phase is still being developed, exploring additional H&CD approaches that could be compatible with a FPP design.

Roger Raman

Full (or nearly full) non inductive current startup and current ramp up is yet to be demonstrated on any tokamak. With the recent successful demonstration of Transient CHI startup on QUEST using a reactor-relevant electrode configuration, combined with the capability for high power non-inductive current drive systems on QUEST, during the next two to three years, QUEST is well positioned to be the first device to demonstrate this major capability for the development of the ST concept. The three-year plan outlined below would permit QUEST to make significant progress towards achieving this significant goal thereby being the first device to influence the future path of the ST and Tokamak reactor development programs worldwide. Major elements of the plan are: Assess the maximum transient CHI generated closed flux current potential on QUEST;

Using a suitable high closed flux current discharge with low electron density, heat it using induction and ECH; Using the best discharges developed during YRs-1 and 2, ramp the current up using induction and then using a combination of non-inductive current drive methods conduct a first test of non-inductive current ramp-up of the CHI target plasma; Good wall conditions are needed to obtain low electron density, low resistivity plasmas for current ramp-up; Obtain between shot partial pressure data for gases and test hot-wall capability for CHI; Hydrogen GDC and Ti-gettering systems could be deployed for low cost and would enormously benefit CHI and other plasma operations on QUEST.

Atsushi Fukuyama

In order to describe kinetic response of electron cyclotron (EC) waves in inhomogeneous plasmas, integral forms of dielectric tensor have been introduced. For plasmas with Maxwellian velocity distribution functions, plasma dispersion kernel function (PDKF) and plasma gyro kernel function (PGKF) describes parallel and perpendicular motion of charged particles. The O-X-B mode conversion of EC waves in QUEST plasmas has been described in 1D and 2D models on horizontal plane. Extension to the analysis in poloidal cross section is under way.

Syunichi Shiraiwa

The plasma dielectric models used in the Petra-M finite element framework is discussed. Petra-M implements three dielectric models with different physics complexities. Cold plasma model has been applied in the wide variety of wave simulation problems, including fusion plasmas, space plasmas, and plasma thrusters. This model is also used in RF sheath calculations in NSTX-U and WEST using the entire 360 degree torus. Local-K plasma model is more recently development, which allows to use the dielectric response of Maxwellian plasmas. These two models both approximate the dielectric response as a local response. Therefore, the spatial dispersion and kinetic waves physics is not captured. To address this issue, we are also developing non-local dielectric model. Our approach is to utilize a rational approximation of uniform plasma dielectric tensor and to transform it to a vectorial dielectric response operator. The operator acts on the dielectric current, and therefore, the resultant equation becomes a couple partial differential equations for the electric field and the dielectric currents. Although started from a unform plasma theory, the resultant operator allows for computing the non-local dielectric response expressed as a convolution integral without explicitly forming an operator for the convolution. We discussed the derivation of dielectric operator and application to the 1D EBW mode conversion problems. Then, we discussed the application of 2D wave problem for the lower hybrid waves, ICRF minority heating, and O-X-B mode conversion. Simulation results are qualitatively reasonable and captures wave physics expected for each simulation problems. These results are promising, opening the possibility to extend a hot plasma wave simulation model in large complicated 3D problems in future.

Yusuke Kosuga

Parallel velocity gradient (PVG) driven turbulence arises from an instability driven by the inhomogeneity of a flow along the magnetic field. It has been argued that PVG can arise in toroidal plasmas, especially when there is a strong drive of parallel flows (or approximately, toroidal flow). These include, but not limited to, NBI driven plasmas, plasmas with a transport barrier, plasmas in the scrape off layer (SOL). This talk describes a physical picture behind PVG turbulence, based on the results obtained from experiments on PANTA and theoretical modeling. Linear analysis provides relevant mode features, including the threshold for excitation, asymmetric fluctuation spectrum in the axial mode number, large level of parallel velocity fluctuation, etc. These are used to identify the excitation of PVG in PANTA. Once PVG is excited, PVG results in the relaxation of parallel velocity profile, while the density profile is peaked. This coupled evolution can be described in a unified manner by using entropic evolution. PVG may be excited in spherical tokamaks, since equilibrium return flows in ST are strong in the high field side of the collisional edge plasmas. In particular, impurities can be typically in this regime, and the parallel flow shear associated with impurity flows can be a source of driving PVG turbulence in STs.

Shin Kubo

Scattering measurement is the powerful diagnostic method to measure the excited density fluctuation by the injected RF power. In particular, the electron Bernstein wave (EBW) is the electro-static and the density fluctuation is directly connected to the fluctuating electric field in the plasma. Since the wavelength of the EBW is the order of Larmor radius, high frequency in the range of 0.5-1 THz is required for the scattering source. HCN laser (337 μm/890 GHz) is now introduced in the QUEST for a scattering source and detection system is under construction. Optical vortex heating that might propagate over cutoff density is proposed and first trial was performed in the LHD without appreciable effect yet. The miter bend mirror to excite optical vortex will be optimized for the next chance. In both scattering and optical vortex propagation estimation, we are developing extended quasi optics code in which local para-axial approximation is used taking the first order wavenumber derivative of dielectric tensor.

Photos

国際化推進共同研究概要

No.12

[採択番号]　24NU-6

タイトル： Development of Core-SOL-Divertor model for simulating tokamak with impurities

研究代表者： WISITSORASAK

所内世話人： KASUYA Naohiro

研究概要：

トカマクプラズマにおける不純物輸送について統合的な解析を可能とするために、TASKコードへSOL・ダイバータ領域の効果を組み合わせるのが本研究の課題である。SOL・ダイバータ領域の密度・温度の動的な変化を解く計算モデルを構築しコード化した。そしてTASKコードへの組み込み作業を開始した。本年度は研究代表者が自己資金による訪問も含めて3回九大応力研を訪問し、研究打合せを通じて九大をはじめ多くの日本の核融合研究者との研究交流を行うことができた。

Development of Core-SOL-Divertor Model for Simulating Tokamak Plasmas with Impurities

Apiwat Wisitsorasak

Department of Physics, Faculty of Science,
King Mongkut's University of Technology Thonburi,
Bangkok, Thailand

1 Introduction

Impurities in tokamak plasma introduce several deleterious effects on the overall performance of the devices. A large amount of impurities can dilute the fuel and reduce the rate of fusion reactions. Furthermore, one of the most immediate effects is the loss of radiated power, which leads to lower plasma temperatures. For example, impurity ions such as oxygen and carbon, originating from the tokamak vessel, strongly cool the plasma near the edge. However, excessive edge cooling destabilizes the plasma and leads to plasma disruption, which can severely damage the wall and other structures [1]. On the other hand, metal ions from the plasma-facing components, such as tungsten, can travel farther from the edge and cause significant radiation in the core. This prevents the plasma from reaching a high enough temperature for ignition. Hence, the concentration of impurities should be minimized. For a tokamak with a divertor configuration, the impurities should be pumped away near the divertor; otherwise, they will accumulate in the vessel. Despite the downside effects of impurities, the radiation of plasma impurities nevertheless has some helpful consequences. Injection of noble gases such as argon or neon is intentionally used to increase radiation in the edge region of the plasma. A well-controlled amount of these seeded impurities helps to disperse the plasma power exhaust over wider surface areas and reduce the temperature in front of the plasma-facing components.

2 Model Equations

To dynamically model the SOL and divertor plasma, one may reduce the complexity of the problem by considering only the transport along a magnetic field line. Instead of using a 1D or 2D transport model, one can focus on the relevant physical quantities of the plasma at specific points along the field line. The simplest model is the so-called two-point model, which considers only two points: the upstream (or stagnation point) and the target point. However, the two-point model does not account for asymmetric transport. A five-point model was originally proposed by Hayashi-san to study thermoelectric instability. It can also be used to model the dynamic response of SOL-divertor plasma during an ELM crash, which may induce thermoelectric instability and large SOL currents [2]. The model also only considers the transport of hydrogenic species without explicitly including impurities. In this work, we first describe the five-point model. The impurity transport will be solved in the background of the hydrogenic species and will be introduced later in this section.

2.1 The Five-Point Model of Hydrogenic Species

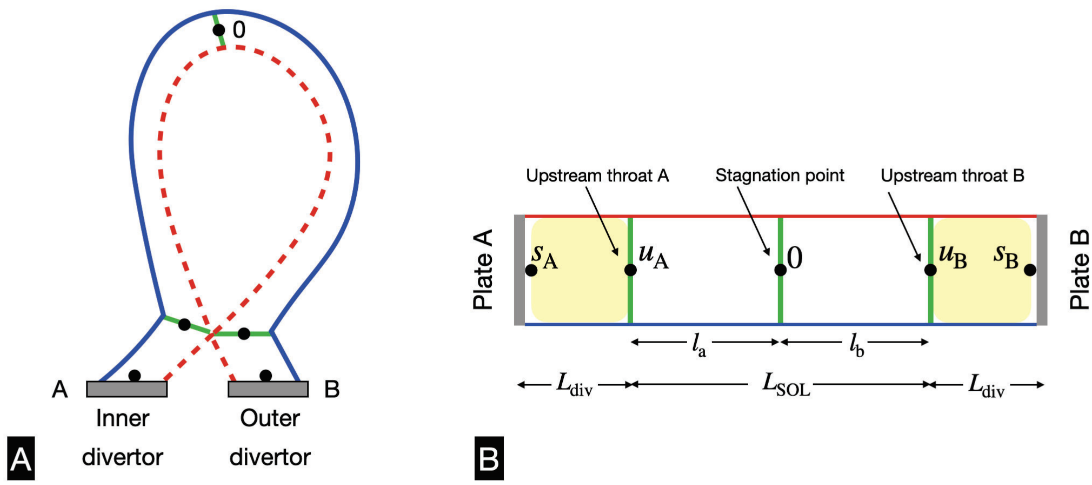

Figure 1: Schematic diagram showing the geometry of the five-point model which considers the transport along the magnetic field.

The geometry of the five-point model is shown in Figure 1. The model considers the flux tube closest to the separatrix in single-null or double-null plasmas. The flux tube is divided into four regions. The fluid equations are integrated and reduced to a set of nonlinear algebraic equations with physical variables at the five positions:

1. the stagnation point (0) where the parallel ion flow velocity equals to zero.
2. the upstream throats of the inner divertors (u_A)
3. the upstream throats of the throat divertors (u_B)
4. the sheath entrance of the inner divertors (s_A)
5. the sheath entrance of the outer divertors (s_B)

Here, the total length of the SOL is $L_{\mathrm{SOL}} = l_a + l_b$. The two divertor legs are assumed to have the same length (L_{div}).

2.1.1 Continuity Equation

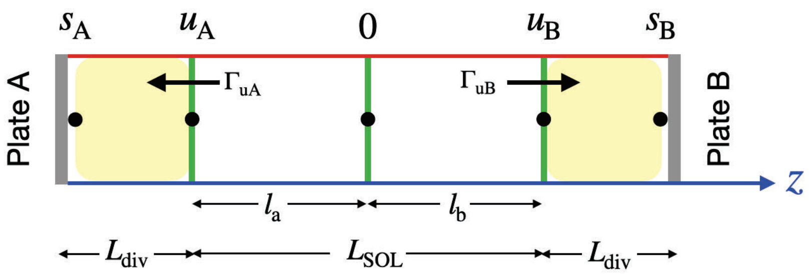

Figure 2: Geometry of the five-point model.

The magnetic field line in these regions can simply be straightened to describe the transport along the parallel direction (z), see Figure 2. The continuity equation is written as:

$$\frac{\partial n}{\partial t} + \frac{\partial \Gamma_z}{\partial z} = S, \tag{1}$$

where n is the particle density, Γ_z is the particle flux, and S is the particle source or sink term.

One can then integrated along the field line from the upstream throat A to the the upstream throat B:

$$\int_{z=-l_a}^{z=l_b} \frac{\partial n}{\partial t} \mathrm{d}z + \int_{z=-l_a}^{z=l_b} \frac{\partial \Gamma_z}{\partial z} \mathrm{d}z = \int_{z=-l_a}^{z=l_b} S \ \mathrm{d}z \tag{2}$$

$$L_{\mathrm{SOL}} \frac{\partial n_0}{\partial t} + (\Gamma_{\mathrm{uB}} + \Gamma_{\mathrm{uA}}) = S_0 L_{\mathrm{SOL}} \tag{3}$$

Rearranging the equation, we then found

$$\boxed{L_{\mathrm{SOL}} \frac{\mathrm{d}n_0}{\mathrm{d}t} = -\Gamma_{\mathrm{uB}} - \Gamma_{\mathrm{uA}} + S_0 L_{\mathrm{SOL}},} \tag{4}$$

where we assume that $L_{\mathrm{SOL}} \equiv l_a + l_b$ is the total length of the SOL. Γ_{uA} and Γ_{uB} are the particle flux along the field line towards the throats A and B, respectively. The particle source rate S_0 is due to the radial diffusion from the core into the SOL and is a function of radial particle flux Γ_r. The value of Γ_r is assumed to be uniform on the last closed flux surface. We can write $S_0 = \dfrac{\partial \Gamma_r}{\partial r} = \dfrac{\partial}{\partial r}\left(\dfrac{\Phi_{\mathrm{sep}}}{S_{\mathrm{sep}}}\right) \approx \dfrac{\Phi_{\mathrm{sep}}}{\lambda_r S_{\mathrm{sep}}}$, where S_{sep} is the the separatrix surface area, Φ_{sep} is the rate of the total particles from the core to the SOL, and λ_r is the characteristic width of the SOL. The values of $S_{\mathrm{sep}}, \Phi_{\mathrm{sep}}$, and λ_r must be provided as input variables.

Considering the continuity in the divertor region B, and integrating from $z = L_{\mathrm{SOL}}$ to $L_{\mathrm{SOL}} + L_{\mathrm{div}}$, it is found that

$$\int_{z=L_{\mathrm{SOL}}}^{z=L_{\mathrm{SOL}}+L_{\mathrm{div}}} \frac{\partial n}{\partial t} \mathrm{d}z + \int_{z=L_{\mathrm{SOL}}}^{z=L_{\mathrm{SOL}}+L_{\mathrm{div}}} \frac{\partial \Gamma_z}{\partial z} \mathrm{d}z = \int_{z=L_{\mathrm{SOL}}}^{z=L_{\mathrm{SOL}}+L_{\mathrm{div}}} S \ \mathrm{d}z \tag{5}$$

$$L_{\mathrm{div}} \frac{\partial n_{sB}}{\partial t} + (\Gamma_{\mathrm{sB}} - \Gamma_{\mathrm{uB}}) = S_B L_{\mathrm{div}} \tag{6}$$

Rearranging the equation, we then obtain

$$\boxed{L_{\mathrm{div}} \frac{\mathrm{d}n_{sB}}{\mathrm{d}t} = \Gamma_{uB} - \Gamma_{sB} + S_B L_{\mathrm{div}}.} \tag{7}$$

Likewise, considering the continuity equation on the other side of the divertor region, we obtain

$$\boxed{L_{\mathrm{div}} \frac{\mathrm{d}n_{sA}}{\mathrm{d}t} = \Gamma_{uA} - \Gamma_{sA} + S_A L_{\mathrm{div}}.} \tag{8}$$

Here, the particle source $S_{A,B}$ is computed from the particles reaching the divertor plate: $S_{A,B} =$

$\frac{\eta_r \Gamma_{sA,sB}}{L_{\mathrm{div}}}$, where η_r is the recycling coefficient. Γ_{sA} and Γ_{sB} are the particle fluxes at the sheath entrances A and B, respectively. They are given as $\Gamma_{\mathrm{sA,sB}} = n_{\mathrm{sA,sB}} C_{\mathrm{sA,sB}}$, where the sound speed $C_{\mathrm{sA,sB}} = \sqrt{\frac{T_e + 3T_i}{m_i}}$.

2.1.2 Parallel Momentum Equation

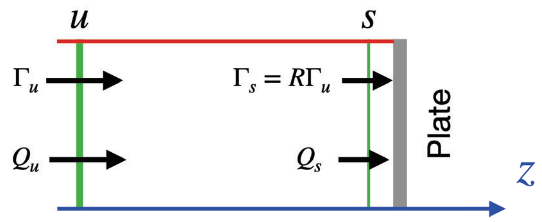

Figure 3: Geometry of the divertor.

The parallel momentum equation in the SOL and divertor regions is written as:

$$\frac{\partial}{\partial t}(m_i n v) + \frac{\partial}{\partial z}\left(P + m_i n v^2 - \eta \frac{\partial v}{\partial z}\right) = 0 \tag{9}$$

Integrating from $z = 0$ to $z = l_{\mathrm{b}} + L_{\mathrm{div}}$:

$$\underbrace{m_i \int_{z=0}^{z=l_b+L_{\mathrm{div}}} \frac{\partial}{\partial t}(nv)\ \mathrm{d}z}_{1} + \underbrace{\int_{z=0}^{z=l_b+L_{\mathrm{div}}} \frac{\partial}{\partial z}\left(P + m_i n v^2 - \eta \frac{\partial v}{\partial z}\right) \mathrm{d}z}_{2} = 0. \tag{10}$$

Consider the integration of the first term 1 and write $\Gamma = nv$:

$$m_i \int_0^{l_b+L_{\mathrm{div}}} \frac{\partial}{\partial t}(nv)\ \mathrm{d}z = m_i \left(\int_0^{l_b} \frac{\partial \Gamma}{\partial t}\ \mathrm{d}z + \int_{l_b}^{l_b+L_{\mathrm{div}}} \frac{\partial \Gamma}{\partial t}\right) \mathrm{d}z \tag{11}$$

$$= \frac{m_i l_b}{2} \frac{\partial \Gamma_{uB}}{\partial z} + \frac{m_i L_{\mathrm{div}}}{2} \left(\frac{\partial \Gamma_{uB}}{\partial t} + \frac{\partial \Gamma_{sB}}{\partial t}\right), \tag{12}$$

where we assume that $\partial\Gamma/\partial t$ linearly increases in each region, as we integrate along the z direction. For simplicity, one may approximate that the the flux at the divertor plate is proportional to the the flux at the divertor throat, i.e. $\Gamma_{sB} = R\Gamma_{uB}$, where R is the particle flux amplification factor.

Thus term 1 can be finally written as (from Eq.12):

$$
\begin{aligned}
1 = m_i \int_0^{l_b+L_{\text{div}}} \frac{\partial}{\partial t}(nv)\ \mathrm{d}z &= \frac{m_i l_b}{2}\frac{\partial \Gamma_{uB}}{\partial z} + \frac{m_i L_{\text{div}}}{2}\left(\frac{\partial \Gamma_{uB}}{\partial t} + R\frac{\partial \Gamma_{uB}}{\partial t}\right) && (13)\\
&= \frac{m_i}{2}\left(l_b + (1+R)L_{\text{div}}\right)\frac{\partial \Gamma_{uB}}{\partial t}. && (14)
\end{aligned}
$$

For the second term (2) of Eq.10, we can assume that the viscosity is negligible, i.e. $\eta \approx 0$:

$$
\begin{aligned}
2 &= \left(P + m_i n v^2\right)\Big|_0^{l_b+L_{\text{div}}} && (15)\\
&= \left(P|_{z=sB} - P|_{z=0}\right) + \left(m_i n v^2|_{z=sB} - m_i n v^2|_{z=0}\right) && (16)\\
&= n_{sB}\left(T_{e,sB} + T_{i,sB}\right) - n_0\left(T_{e,0} + T_{i,0}\right) + n_{sB}\left(T_{i,sB} + T_{e,sB}\right) && (17)\\
&= -n_0\left(T_{e,0} + T_{i,0}\right) + n_{sB}\left(2T_{e,sB} + (1+g)T_{i,sB}\right), && (18)
\end{aligned}
$$

where $m_i n v^2|_{z=0} = 0$ at the stagnation point. The term $m_i n v^2|_{sB} \approx m_i n C_s^2 = m_i n \cdot (gT_i + T_e)/m_i$, where g is the degrees of freedom. From Eq.10, we finally obtain:

$$
\boxed{\frac{m_i}{2}\left(l_b + (1+R_B)L_{\text{div}}\right)\frac{\mathrm{d}\Gamma_{uB}}{\mathrm{d}t} = n_0(T_{e,0} + T_{i,0}) - n_{sB}\left(2T_{e,sB} + (1+g)T_{i,sB}\right)} \tag{19}
$$

Likewise, we can write the parallel momentum in the other side of the SOL as:

$$
\boxed{\frac{m_i}{2}\left(l_a + (1+R_A)L_{\text{div}}\right)\frac{\mathrm{d}\Gamma_{uA}}{\mathrm{d}t} = n_0(T_{e,0} + T_{i,0}) - n_{sA}\left(2T_{e,sA} + (1+g)T_{i,sA}\right)} \tag{20}
$$

2.1.3 The Energy Transport Equation

The energy transport equation for the electrons is written as

$$
\frac{3}{2}\frac{\partial}{\partial t}(nT_e) + \frac{\partial Q_e}{\partial z} = -J\frac{\partial \phi}{\partial z} + W_{e,\text{SOL}}. \tag{21}
$$

Integrate the above equation from u_A to u_B, we then obtain

$$
\boxed{\frac{3}{2}\frac{\mathrm{d}n_0 T_{e0}}{\mathrm{d}t} = -Q_{e,uB} - Q_{e,uA} - J(\phi_{uB} - \phi_{uA}) + (W_{e0} + W_{e,eq,0})L_{\text{SOL}},} \tag{22}
$$

where W_{e0} is the energy source and depends on the heat flux from the core, $W_{e0} = \dfrac{Q_{e,\mathrm{sep}}}{\lambda_T \cdot S_{\mathrm{sep}}}$. The equipartition energy is given by $W_{e,\mathrm{eq},0} = \dfrac{3}{2} n_0 \dfrac{T_{i,0} - T_{e,0}}{\tau_{\mathrm{eq},0}}$

In the divertor region (from $z = u_B$ to s_B), the electron energy transport equation becomes:

$$\boxed{\frac{3}{2}\frac{\mathrm{d}n_{sB}T_{e,sB}}{\mathrm{d}t} = Q_{e,uB} - Q_{e,sB} - J(\phi_{uB} - \phi_{sB}) + (W_{e,B} + W_{e,\mathrm{eq},B})L_{\mathrm{SOL}}.} \tag{23}$$

Likewise, the equation in the other side of the divertor region can be written as:

$$\boxed{\frac{3}{2}\frac{\mathrm{d}n_{sA}T_{e,sA}}{\mathrm{d}t} = Q_{e,uA} - Q_{e,sA} - J(\phi_{uA} - \phi_{sA}) + (W_{e,A} + W_{e,\mathrm{eq},A})L_{\mathrm{SOL}}.} \tag{24}$$

In the same way, we can write it for the ions:

$$\boxed{\frac{3}{2}\frac{\mathrm{d}n_0T_{i0}}{\mathrm{d}t} = -Q_{i,uB} - Q_{i,uA} + (W_{i0} + W_{i,eq,0})L_{\mathrm{SOL}},} \tag{25}$$

where $W_{i0} = W_{e0}$, and $W_{i,\mathrm{eq},0} = -W_{e,\mathrm{eq},0}$. For the divertor region, we have

$$\boxed{\frac{3}{2}\frac{\mathrm{d}n_{sB}T_{i,sB}}{\mathrm{d}t} = Q_{i,uB} - Q_{i,sB} + (W_{i,B} + W_{i,\mathrm{eq},B})L_{\mathrm{SOL}},} \tag{26}$$

and

$$\boxed{\frac{3}{2}\frac{\mathrm{d}n_{sA}T_{i,sA}}{\mathrm{d}t} = Q_{i,uA} - Q_{i,sA} + (W_{i,A} + W_{i,\mathrm{eq},A})L_{\mathrm{SOL}}.} \tag{27}$$

The upstream heat flux including both conductive and convective fluxes is given by:

$$Q_{\mathrm{euA,B}} = Q_{j\mathrm{eff}} \pm \left(\frac{5}{2} + \alpha\right) T_{\mathrm{euA,B}} \frac{J}{e} + \frac{5}{2} T_{\mathrm{euA,B}} \Gamma_{\mathrm{uA,B}} \tag{28}$$

and

$$Q_{j\mathrm{uA,B}} = Q_{j\mathrm{eff}} + \frac{5}{2} T_{\mathrm{euA,B}} \Gamma_{\mathrm{uA,B}}, \tag{29}$$

where the subscript j denotes the electrons and ions.

2.2 Modelling of Impurity Production and Transport

2.2.1 Continuity Equations of Impurities

The dynamic five-point model can be extended to explicitly describe impurity production and transport in the tokamak edge region. This task can be achieved by considering the multi-fluid equations of impurity species. Upon considering an impurity species with atomic number $Z_{\max}$, the continuity equation of the jth charge state, $j = 1, ..., Z_{\max}$, can be written as [1, 3]:

$$\frac{\partial n_j}{\partial t} = -\frac{\partial n_j v_j}{\partial z} - \frac{\partial \Gamma_j^{\perp}}{\partial x} + n_{j-1}\alpha_{j-1} - n_j(\alpha_j + \beta_j) + n_{j+1}\beta_{j+1} + S, \tag{30}$$

where m_Z is the impurity mass, n_j is the impurity density of the jth charge state, v_j is the parallel component of velocity, u_j is the perpendicular component, $\alpha_j = n_e\langle\sigma v\rangle^j_{\text{ion}}$ and $\beta_j = n_e\langle\sigma v\rangle^j_{\text{rec}}$ are the ionization and recombination rate coefficients, respectively, v_H is the velocity of hydrogen species, and τ_j is the impurity-hydrogen collision time. S denotes the particle source rate. Note, in this section, that z is assumed to the direction along the field line, and x is the perpendicular (radial) direction. $\Gamma_j^{\perp}$ is the impurity flux from the core. For simplicity, we further assume the impurity temperature to be equal to the hydrogen temperature, i.e. $T_Z = T_i = T_H$, and the pressure $p_j = n_j T_H$.

For the typical plasma edge, the temperature is less than 100 eV, and the density is between 10^{18} and 10^{21} m^{-3}. The recombination of the impurity ions can be ignored. Neglecting the perpendicular fluxes and integrating equation 30 in the SOL region ($z = -l_a$ to $z = l_b$) yields:

$$\boxed{L_{\text{SOL}}\frac{dn_{j,0}}{dt} = -\Gamma_{j,\text{uB}} - \Gamma_{j,\text{uA}} + L_{\text{SOL}}\left(n_{j-1,0}\alpha_{j-1,0} - n_{j,0}\alpha_{j,0} + S_{j,0}\right),} \tag{31}$$

where $S_{j,0}$ is the impurity source rate.

One can also integrate equation 30 in the divertor regions ($z = u_{\text{A,B}}$ to $z = s_{\text{A,B}}$):

$$\boxed{L_{\text{div}}\frac{dn_{j,\text{sA}}}{dt} = \Gamma_{j,\text{uA}} - \Gamma_{j,\text{sA}} + L_{\text{div}}\left(n_{j-1,\text{sA}}\alpha_{j-1,\text{sA}} - n_{j,\text{sA}}\alpha_{j,\text{sA}} + S_{j,\text{sA}}\right),} \tag{32}$$

and

$$\boxed{L_{\mathrm{div}}\frac{dn_{j,\mathrm{sB}}}{dt}=\Gamma_{j,\mathrm{uB}}-\Gamma_{j,\mathrm{sB}}+L_{\mathrm{div}}\left(n_{j-1,\mathrm{sB}}\alpha_{j-1,\mathrm{sB}}-n_{j,\mathrm{sB}}\alpha_{j,\mathrm{sB}}+S_{j,\mathrm{sB}}\right).} \tag{33}$$

Here, the ionization rate coefficients α_j which is a function of the electron temperature can be taken from the Open Atomic Data and Analysis Structure (Open-ADAS), specifically from ADF07 (electron impact ionization coefficients), https://open.adas.ac.uk/adf07. Likewise the recombination rates can also be computed using Open-ADAS data.

2.2.2 The Parallel Momentums of Impurities

The momentum equation for impurities is written as:

$$\begin{aligned}\frac{\partial(m_Z n_j v_j)}{\partial t} &= -\frac{\partial(m_Z n_j v_j^2)}{\partial z}-\frac{\partial(m_Z n_j v_j u_j)}{\partial x}-\frac{\partial p_j}{\partial z}-m_Z n_j\left(\frac{v_H-v_j}{\tau_j}\right)\\ &\quad + m_Z\left[n_{j-1}v_{j-1}\alpha_{j-1}-n_j v_j(\alpha_j+\beta_j)-n_{j+1}v_{j+1}\beta_{j+1}\right],\end{aligned} \tag{34}$$

Integrate Equation 35 from $z=0$ to the divertor plate of each side, one obtains:

$$\begin{aligned}\underbrace{\int_0^{l_b+L_{\mathrm{div}}}\frac{\partial}{\partial t}(m_Z n_j v_j)\mathrm{d}z}_{\text{A}} &= \underbrace{-\int_0^{l_b+L_{\mathrm{div}}}\frac{\partial}{\partial z}\left(m_Z n_j v_j^2+P_j\right)\mathrm{d}z}_{\text{B}}\underbrace{-\int_0^{l_b+L_{\mathrm{div}}}\frac{\partial(m_Z n_j v_j u_j)}{\partial x}\mathrm{d}z}_{\text{C}}\\ &\quad \underbrace{-\int_0^{l_b+L_{\mathrm{div}}} m_Z n_j\left(\frac{v_H-v_j}{\tau_j}\right)\mathrm{d}z}_{\text{D}}\\ &\quad \underbrace{+\int_0^{l_b+L_{\mathrm{div}}} m_Z\left[n_{j-1}v_{j-1}\alpha_{j-1}-n_j v_j(\alpha_j+\beta_j)-n_{j+1}v_{j+1}\beta_{j+1}\right]\mathrm{d}z}_{\text{E}}\end{aligned} \tag{35}$$

Consider the first term on the left hand side (A):

$$\text{A} = \int_0^{l_b+L_{\mathrm{div}}}\frac{\partial}{\partial t}(m_Z n_j v_j)\mathrm{d}z = \frac{m_Z}{2}\left(l_b+(1+R_j)L_{\mathrm{div}}\right)\frac{d}{dz}\Gamma_{j,uB}. \tag{36}$$

note that this integration is similar to Equation 14. Consider term (B):

$$
\begin{aligned}
\text{(B)} &= \int_0^{l_b+L_{\text{div}}} \frac{\partial}{\partial z}\left(m_Z n_j v_j^2 + P_j\right) \mathrm{d}z && (37)\\
&= \left(m_z n_j v_j^2 + P_j\right)\Big|_0^{l_b+L_{\text{div}}} && (38)\\
&= \left(m_z n_j v_j^2\Big|_{l_b+L_{\text{div}}} - m_z n_j v_j^2\Big|_0\right) + \left(P_j\Big|_{l_b+L_{\text{div}}} - P_j\Big|_0\right) && (39)\\
&= n_{j,\text{sB}} T_{\text{H,sB}} + \left(n_{j,\text{sB}} T_{\text{H,sB}} - n_{j,0} T_{\text{H},0}\right) && (40)\\
&= -n_{j,0} T_{\text{th},0} + 2 n_{j,\text{sB}} T_{\text{H,sB}}, && (41)
\end{aligned}
$$

where we approximate that $\left|\frac{m_z n_j v_j^2}{n_j T_H}\right|\Big|_0 \approx \left|\frac{v_j}{v_j^{\text{H}}}\right| \ll 1$ with $v_j^{\text{H}} = \sqrt{\frac{T_{\text{H}}}{m_z}}$ [3].

The second term ((C)) on the right-hand side of Equation 35 is assumed to be negligible in this simple derivation. In more realistic model, this radial momentum diffusion term should be included if the information of the impurity flow from the region inside the LCFS is provided, i.e. $\Gamma_j^{\perp} = n_j u_j = -D_{\perp}^{j} \frac{\partial n_j}{\partial y}$.

Consider the third term ((D)):

$$
\begin{aligned}
\text{(D)} &= \int_0^{l_b+L_{\text{div}}} m_Z n_j \left(\frac{v_H - v_j}{\tau_j}\right) \mathrm{d}z && (42)\\
&= \int_0^{l_b} m_Z n_j \left(\frac{v_H - v_j}{\tau_j}\right) \mathrm{d}z + \int_{l_b}^{L_{\text{div}}} m_Z n_j \left(\frac{v_H - v_j}{\tau_j}\right) \mathrm{d}z && (43)
\end{aligned}
$$

Let us assume that $\tau_j \approx \tau$ for all impurities species j.

$$
\begin{aligned}
\text{(D)} &= \frac{m_z}{\tau}\left[\int_0^{l_b} n_j v_{\text{H}} \mathrm{d}z - \int_0^{l_b} n_j v_j \mathrm{d}z + \int_{l_b}^{L_{\text{div}}} n_j v_{\text{H}} \mathrm{d}z - \int_{l_b}^{L_{\text{div}}} n_j v_j \mathrm{d}z\right] && (44)\\
&= \frac{m_z}{\tau}\left[\frac{1}{2}\left(n_{j0} v_{\text{H}0} + n_{j,uB} v_{\text{H},uB}\right) - \frac{l_b}{2}\Gamma_{j,uB} + \frac{1}{2}\left(n_{j,uB} v_{\text{H},uB} + n_{j,sB} v_{\text{H},sB}\right)\right.\\
&\qquad \left. -\frac{L_{\text{div}}}{2}\left(\Gamma_{j,sB} + \Gamma_{j,uB}\right)\right] && (45)\\
&= \frac{m_z}{\tau}\left[\frac{n_{j0} v_{\text{H}0}}{2} + \frac{n_{j,sB} v_{\text{H},sB}}{2} + n_{j,uB} v_{\text{H},uB} + \frac{1}{2}\left(l_b + (1+R) L_{\text{div}}\right)\Gamma_{j,uB}\right] && (46)
\end{aligned}
$$

Consider the last term ((E)) of Equation 35. We can use the same trick by separating the integration into two interval, i.e. $\int_0^{l_b+L_{\text{div}}} \ldots \mathrm{d}z = \int_0^{l_b} \ldots \mathrm{d}z + \int_{l_b}^{L_{\text{div}}} \ldots \mathrm{d}z$ and assuming $\Gamma_{j,sB} =$

$R\Gamma_{j,uB}$, where R is the amplification flux factor. For example, integrating the first term of (E) will lead to

$$
\begin{aligned}
\text{(E1)} &= \int_0^{l_b+L_{\mathrm{div}}} m_z n_{j-1} v_{j-1} \alpha_{j-1} \mathrm{d}z && (47)\\
&= m_z \left[\int_0^{l_b} n_{j-1} v_{j-1} \alpha_{j-1} \mathrm{d}z + \int_{l_b}^{L_{\mathrm{div}}} n_{j-1} v_{j-1} \alpha_{j-1} \mathrm{d}z \right] && (48)\\
&= m_z \left[\frac{l_b}{2} \left(\underbrace{\alpha_{j-1,0}\Gamma_{j-1,0}}_{\approx 0} + \alpha_{j-1,uB}\Gamma_{j-1,uB} \right) + \frac{L_{\mathrm{div}}}{2} \left(\alpha_{j-1,uB}\Gamma_{j-1,uB} + \alpha_{j-1,sB}\Gamma_{j-1,sB} \right) \right] && (49)\\
&= m_z \left[\frac{l_b}{2} \alpha_{j-1,uB}\Gamma_{j-1,uB} + \frac{L_{\mathrm{div}}}{2} \left(\alpha_{j-1,uB}\Gamma_{j-1,uB} + R\alpha_{j-1,uB}\Gamma_{j-1,uB} \right) \right] && (50)\\
&= \frac{1}{2} \left(l_b + (1+R) L_{\mathrm{div}} \right) m_z \alpha_{j-1,uB}\Gamma_{j-1,uB} && (51)
\end{aligned}
$$

Thus the integration term of (E) can be written as

$$
\text{(E)} = m_z \left(l_\mathrm{b} + (R_j+1) L_{\mathrm{div}} \right) \left(\alpha_{j-1,\mathrm{uB}} \Gamma_{j-1,\mathrm{uB}} - \alpha_{j,\mathrm{uB}} \Gamma_{j,\mathrm{uB}} \right) \qquad (52)
$$

After integrating Equation 35, we finally obtain:

$$
\begin{aligned}
\frac{m_Z}{2} \left(l_\mathrm{b} + (R_j+1) L_{\mathrm{div}} \right) \frac{d\Gamma_{j,\mathrm{uB}}}{dt} &= n_{j,0} T_{\mathrm{H},0} - 2 n_{j,\mathrm{SB}} T_{\mathrm{H,SB}} \\
&+ \frac{m_Z}{\tau_j} \left[\frac{1}{2} n_{j,0} v_{\mathrm{H},0} + \frac{1}{2} n_{j,\mathrm{sB}} v_{\mathrm{H,sB}} + \frac{m_Z}{2} \left(l_\mathrm{b} + (R_j+1) L_{\mathrm{div}} \right) \Gamma_{j,\mathrm{uB}} \right] \\
&+ m_z \left(l_\mathrm{b} + (R_j+1) L_{\mathrm{div}} \right) \left(\alpha_{j-1,\mathrm{uB}} \Gamma_{j-1,\mathrm{uB}} - \alpha_{j,\mathrm{uB}} \Gamma_{j,\mathrm{uB}} \right). \qquad (53)
\end{aligned}
$$

The impurity-flux amplification factor is defined as $R_j \equiv \Gamma_{j,\mathrm{sB}}/\Gamma_{j,\mathrm{uB}}$. The other equation on the other side can be obtained by changing subscript uB to uA. In this analysis, the parallel velocity of the main ion v_H is unknowns, but it can be obtained by an appropriate model for the main-ion dynamics [1]. Likewise, we can write similar equation for the transport in the other side of the divertor by replacing the subscript uB to uA.

In order to close the system for the impurity density, we need an equation for the impurity neutrals n_0. For simplicity, the angular distribution of sputtered ions and the recombination processes will be neglected. Assuming that the impurity neutrals are emitted in the direction normal to the plate, we can write [3]:

$$v_0 \hat{n} \cdot \vec{\nabla} n_0 = -\alpha_0 n_0, \tag{54}$$

where $\hat{n}$ denote a normal vector. Integrating this equation yields

$$n_0 = n_{0p} e^{-z/\lambda_0}, \tag{55}$$

where $\lambda_0 = v_0/\alpha_0$ is the mean free path of the neutrals for ionization, and n_{0p} is the density at the target plate. Note that λ_0 is a weak function of a distance through the electron density, however, it is assumed, for sake of simplicity, to be constant.

The neutral flux at the plate can be obtained by requiring that the neutrals are emitted via sputtering processes:

$$\Gamma_{0p} = \left(Y_H \Gamma_{H,p} + \sum_{j=1}^{z_{\max}} Y_j \Gamma_{j,p} \right) \sin \Theta, \tag{56}$$

where $\Gamma_{H,p}$ is the hydrogen flux at the plate, Y_H is the sputtering yield from hydrogen, and Y_S is the self-sputtering yield [4]. For simplicity, the impurity neutrals are assumed to have thermal velocity $v_z = \sqrt{2T_{\text{neutral}}/m_Z}$. The impurity atoms are born with a constant temperature $T_{\text{neutral}} = 2$ eV. Once $\Gamma_{H,p}$ and $\Gamma_{j,p}$ are known, the neutral densities at the target plate and at a distance z can be determined.

Finally, in principle, the impurity density (n_j) and particle flux (Γ_j) of each charge state at each location along the SOL and divertor (equations 31 - 53) can be numerically determined by using standard numerical techniques such as the Runge-Kutta or Euler method.

3 Equation Summary

The transport equations of the hydrogenic species can be summarized as follows.

$$L_{\mathrm{SOL}}\frac{\mathrm{d}n_0}{\mathrm{d}t} = -\Gamma_{\mathrm{uB}} - \Gamma_{\mathrm{uA}} + S_0 L_{\mathrm{SOL}}, \tag{57}$$

$$L_{\mathrm{div}}\frac{\mathrm{d}n_{sB}}{\mathrm{d}t} = \Gamma_{uB} - \Gamma_{sB} + S_B L_{\mathrm{div}}, \tag{58}$$

$$L_{\mathrm{div}}\frac{\mathrm{d}n_{sA}}{\mathrm{d}t} = \Gamma_{uA} - \Gamma_{sA} + S_A L_{\mathrm{div}}, \tag{59}$$

$$\frac{m_i}{2}\left(l_b + (1+R_B)L_{\mathrm{div}}\right)\frac{\mathrm{d}\Gamma_{uB}}{\mathrm{d}t} = n_0(T_{e,0}+T_{i,0}) - n_{sB}\left(2T_{e,sB} + (1+g)T_{i,sB}\right), \tag{60}$$

$$\frac{m_i}{2}\left(l_a + (1+R_A)L_{\mathrm{div}}\right)\frac{\mathrm{d}\Gamma_{uA}}{\mathrm{d}t} = n_0(T_{e,0}+T_{i,0}) - n_{sA}\left(2T_{e,sA} + (1+g)T_{i,sA}\right), \tag{61}$$

$$\begin{aligned}\frac{3}{2}\frac{\mathrm{d}n_0 T_{e0}}{\mathrm{d}t} &= -Q_{e,uB} - Q_{e,uA} - J(\phi_{uB} - \phi_{uA}) \\ &\quad +(W_{e0} + W_{e,eq,0})L_{\mathrm{SOL}},\end{aligned} \tag{62}$$

$$\frac{3}{2}\frac{\mathrm{d}n_0 T_{i0}}{\mathrm{d}t} = -Q_{i,uB} - Q_{i,uA} + (W_{i0} + W_{i,eq,0})L_{\mathrm{SOL}}, \tag{63}$$

$$\begin{aligned}\frac{3}{2}\frac{\mathrm{d}n_{sB}T_{e,sB}}{\mathrm{d}t} &= Q_{e,uB} - Q_{e,sB} - J(\phi_{uB} - \phi_{sB}) \\ &\quad +(W_{e,B} + W_{e,\mathrm{eq},B})L_{\mathrm{SOL}},\end{aligned} \tag{64}$$

$$\begin{aligned}\frac{3}{2}\frac{\mathrm{d}n_{sA}T_{e,sA}}{\mathrm{d}t} &= Q_{e,uA} - Q_{e,sA} - J(\phi_{uA} - \phi_{sA}) \\ &\quad +(W_{e,A} + W_{e,\mathrm{eq},A})L_{\mathrm{SOL}},\end{aligned} \tag{65}$$

$$\frac{3}{2}\frac{\mathrm{d}n_{sB}T_{i,sB}}{\mathrm{d}t} = Q_{i,uB} - Q_{i,sB} + (W_{i,B} + W_{i,\mathrm{eq},B})L_{\mathrm{SOL}}, \tag{66}$$

$$\frac{3}{2}\frac{\mathrm{d}n_{sA}T_{i,sA}}{\mathrm{d}t} = Q_{i,uA} - Q_{i,sA} + (W_{i,A} + W_{i,\mathrm{eq},A})L_{\mathrm{SOL}}. \tag{67}$$

The equations for the impurity species are as follows: here, $j = 1, 2, 3, ..., z_{\max}$ denotes the ionization states.

$$
\begin{aligned}
L_{\mathrm{SOL}} \frac{\mathrm{d}n_{j,0}}{\mathrm{d}t} &= -\Gamma_{j,\mathrm{uB}} - \Gamma_{j,\mathrm{uA}} + L_{\mathrm{SOL}} \left(n_{j-1,0}\alpha_{j-1,0} - n_{j,0}\alpha_{j,0} \right), & (68) \\
L_{\mathrm{div}} \frac{\mathrm{d}n_{j,\mathrm{sA}}}{\mathrm{d}t} &= \Gamma_{j,\mathrm{uA}} - \Gamma_{j,\mathrm{sA}} + L_{\mathrm{div}} \left(n_{j-1,\mathrm{sA}}\alpha_{j-1,\mathrm{sA}} - n_{j,\mathrm{sA}}\alpha_{j,\mathrm{sA}} \right), & (69) \\
L_{\mathrm{div}} \frac{\mathrm{d}n_{j,\mathrm{sB}}}{\mathrm{d}t} &= \Gamma_{j,\mathrm{uB}} - \Gamma_{j,\mathrm{sB}} + L_{\mathrm{div}} \left(n_{j-1,\mathrm{sB}}\alpha_{j-1,\mathrm{sB}} - n_{j,\mathrm{sB}}\alpha_{j,\mathrm{sB}} \right), & (70) \\
\frac{m_Z}{2} \left(l_{\mathrm{b}} + (R_j + 1) L_{\mathrm{div}} \right) \frac{\mathrm{d}\Gamma_{j,\mathrm{uB}}}{\mathrm{d}t} &= n_{j,0} T_{\mathrm{H},0} - 2 n_{j,\mathrm{sB}} T_{\mathrm{H,SB}} & \\
&\quad + \frac{m_Z}{\tau_j} \left[\frac{1}{2} n_{j,0} v_{\mathrm{H},0} + \frac{1}{2} n_{j,\mathrm{sB}} v_{\mathrm{H,sB}} + \frac{m_Z}{2} \left(l_{\mathrm{b}} + (R_j + 1) L_{\mathrm{div}} \right) \Gamma_{j,\mathrm{uB}} \right] & \\
&\quad + m_z \left(l_{\mathrm{b}} + (R_j + 1) L_{\mathrm{div}} \right) \left(\alpha_{j-1,\mathrm{uB}} \Gamma_{j-1,\mathrm{uB}} - \alpha_{j,\mathrm{uB}} \Gamma_{j,\mathrm{uB}} \right), & (71) \\
\frac{m_Z}{2} \left(l_{\mathrm{b}} + (R_j + 1) L_{\mathrm{div}} \right) \frac{\mathrm{d}\Gamma_{j,\mathrm{uA}}}{\mathrm{d}t} &= n_{j,0} T_{\mathrm{H},0} - 2 n_{j,\mathrm{sA}} T_{\mathrm{H,sA}} & \\
&\quad + \frac{m_Z}{\tau_j} \left[\frac{1}{2} n_{j,0} v_{\mathrm{H},0} + \frac{1}{2} n_{j,\mathrm{sA}} v_{\mathrm{H,sA}} + \frac{m_Z}{2} \left(l_{\mathrm{b}} + (R_j + 1) L_{\mathrm{div}} \right) \Gamma_{j,\mathrm{uA}} \right] & \\
&\quad + m_z \left(l_{\mathrm{b}} + (R_j + 1) L_{\mathrm{div}} \right) \left(\alpha_{j-1,\mathrm{uA}} \Gamma_{j-1,\mathrm{uA}} - \alpha_{j,\mathrm{uA}} \Gamma_{j,\mathrm{uA}} \right). & (72)
\end{aligned}
$$

4 Algorithm

The impurity transport model can be coupled with the original five-point model to predict the densities and temperatures of both hydrogenic and impurity species. This combined model shall be named the SOL module. The SOL module can then be integrated into the main plasma simulation for the core region as follows (see Figure 4):

- At each time step, the main simulation numerically solves the plasma dynamics in the core

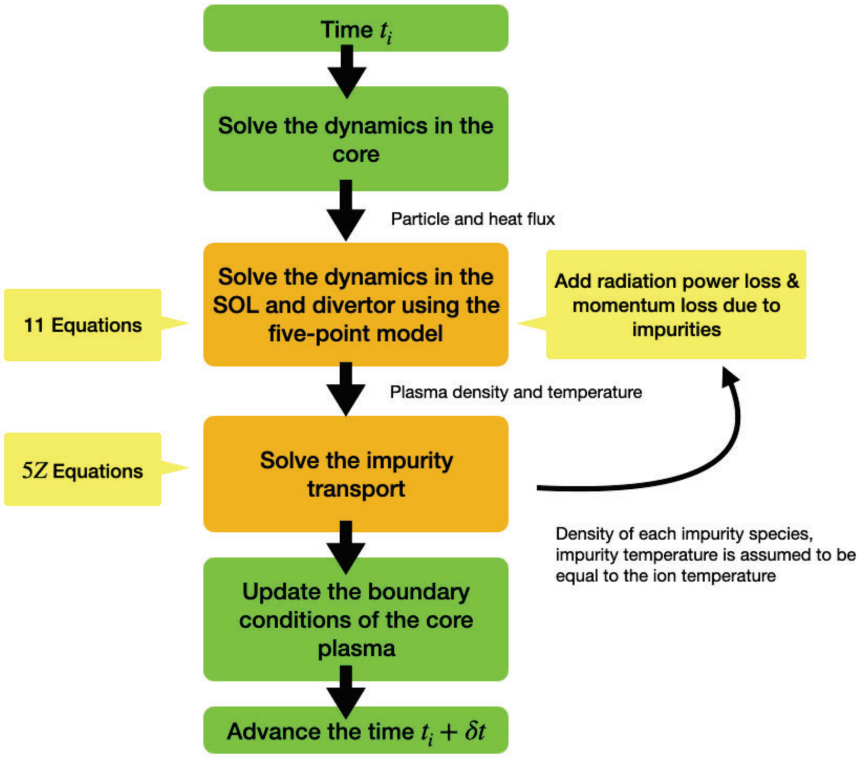

Figure 4: Algorithm for solving the extended five-point model.

and provides the particle and heat fluxes to the SOL module.

- In the SOL module, the original five-point model is first solved using the classical Runge-Kutta method (RK4), yielding the densities and temperatures at specific points along the field line.

- Assuming that the impurity ions share the same temperature as the main ions, the impurity transport model is then solved to determine the densities of the impurity species.

- These impurity densities are returned to the core simulation, updating the boundary conditions for the next time step.

5 Preliminary Results

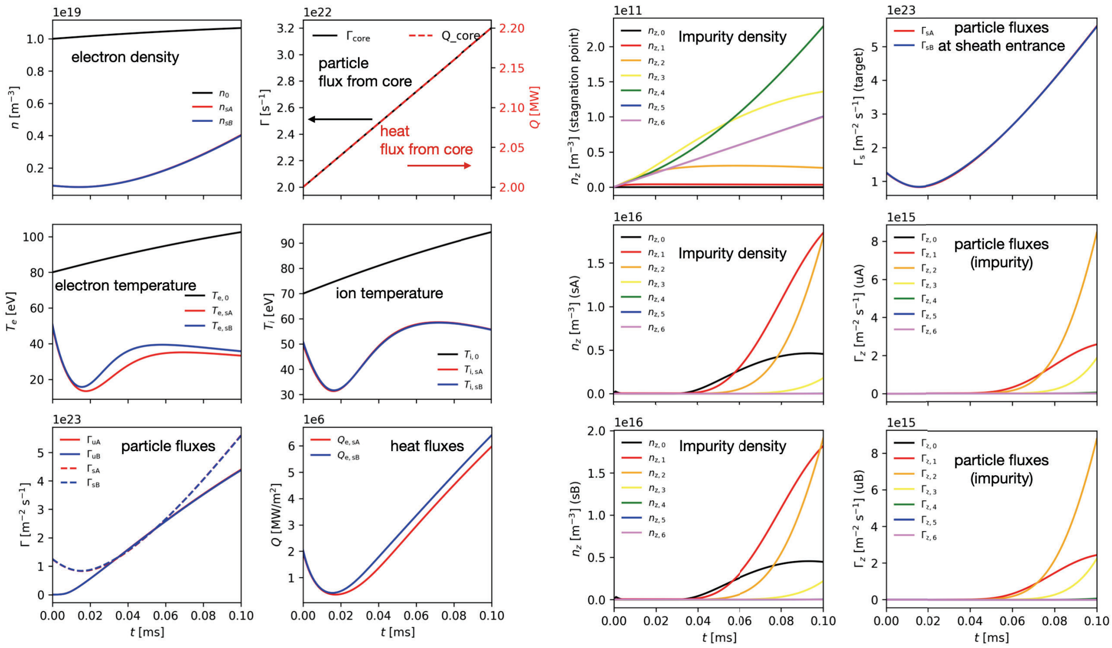

Figure 5: Case 1: Low particle and heat fluxes. The figures show the time evolution of the plasma densities (n_0, n_{sA}, n_{sB}), temperatures (T_{e0}, T_{i0}, $T_{e,sA}$, $T_{e,sB}$, $T_{i,sA}$, $T_{i,sB}$), particle and heat fluxes (Γ_{uA}, Γ_{uB}, Γ_{sA}, Γ_{sB}), and impurity densities of different charge states (n_j) at different locations.

In the present work, we have developed a computer code using Fortran programming to solve the dynamical equations for the densities and temperatures in the core, the scrape-off layer (SOL), and the divertor regions, as described in the previous section. This model requires the geometry of the SOL and divertor regions, the particle flux from the core, and the heat flux from the core as input information. The user must also specify the type of main plasma ions and impurity species.

To demonstrate the usability of the code, we have assumed that the characteristic lengths of the SOL and divertor regions are $L_{\mathrm{SOL}} = 100$ m and $L_{\mathrm{div}} = 4$ m, respectively. Protons are assumed to be the main plasma ions, and carbon is assumed to be the impurity species. We further assume that the particle flux from the core linearly increases from 2.0×10^{22} s^{-1} to 3.2×10^{22} s^{-1} within 0.1 ms, and the heat flux similarly increases from 2.0 MW to 2.2 MW within 0.1 ms. Figure 5 illustrates the electron densities, electron temperatures, ion temperatures, particle fluxes, heat fluxes, impurity densities, and impurity particle fluxes at each location.

In Figure 6, similar plots are shown, but higher values of the particle and heat fluxes are

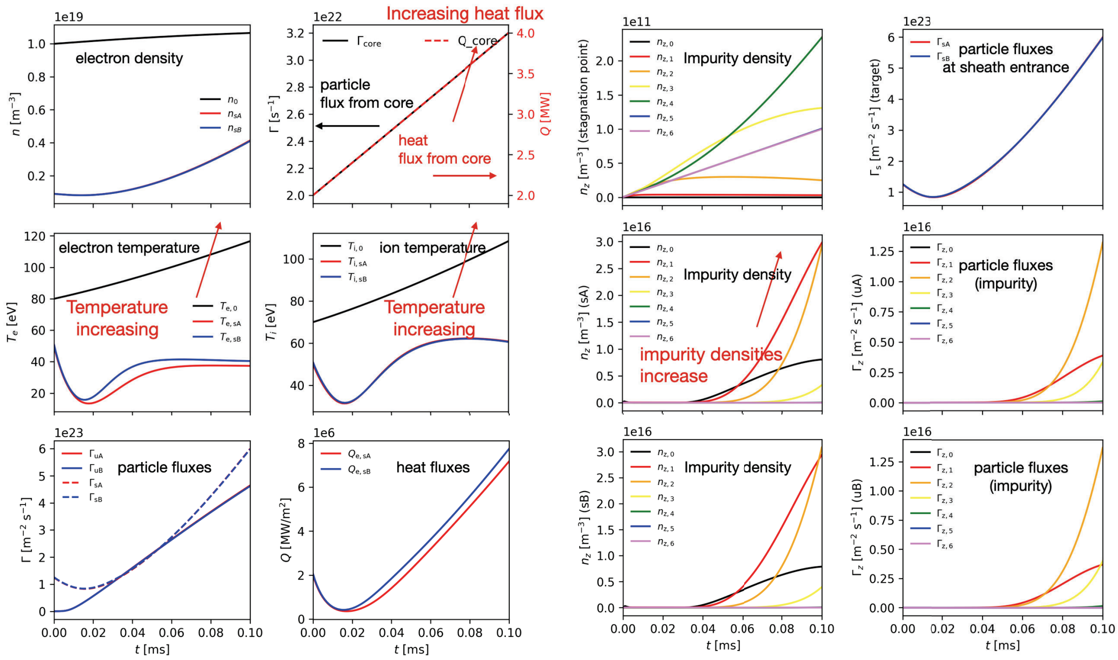

Figure 6: Case 2: High particle and heat fluxes. The figures show the time evolution of the plasma densities (n_0, n_{sA}, n_{sB}), temperatures (T_{e0}, T_{i0}, $T_{e,sA}$, $T_{e,sB}$, $T_{i,sA}$, $T_{i,sB}$), particle and heat fluxes (Γ_{uA}, Γ_{uB}, Γ_{sA}, Γ_{sB}), and impurity densities of different charge states (n_j) at different locations.

assumed. It is found that the densities and temperatures of the main plasma ion species increase. The impurity densities also rise due to the higher sputtering yield.

6 Summary and Future Work

We have successfully extended the five-point model to include the effects of impurities in the SOL regions. The model consists of 11 + 5Z dynamical equations, which can be numerically solved using the classic Runge-Kutta method. The model requires geometric information of the SOL and divertor regions, as well as the types of the main plasma ions and impurities, and their initial values as input. A Fortran program has been developed to simulate the dynamics of the plasma in the SOL and divertor regions based on this model. It allows us to compute the evolution of the densities and temperatures at each location along the SOL and divertor regions. Note that this model assumes that the impurities have the same temperature as the main plasma ions.

In future work, we plan to extend the model to simulate the SOL plasma in the detached regime, where high recycling fluxes occur near the divertor targets. To couple the extended 5-point model to the transport calculations in the core region, we will implement a new module for the TASK code, namely TASK/SOL, which is based on this model. Validation of the model with experimental data or other simulation codes will be conducted.

References

[1] P. C. Stangeby *et al.*, *The plasma boundary of magnetic fusion devices*, vol. 224. Institute of Physics Publishing Bristol, 2000.

[2] N. Hayashi, T. Takizuka, and M. Hosokawa, "Modeling of dynamic response of sol-divertor plasmas to an elm crash," *Journal of nuclear materials*, vol. 363, pp. 1044–1049, 2007.

[3] R. Zagorski and F. Romanelli, "Modelling of impurity production and transport in the scrape-off layer of a high density limiter tokamak," *Nuclear fusion*, vol. 36, no. 7, p. 853, 1996.

[4] N. Matsunami, Y. Yamamura, Y. Itikawa, N. Itoh, Y. Kazumata, S. Miyagawa, K. Morita, R. Shimizu, and H. Tawara, "Energy dependence of the ion-induced sputtering yields of monatomic solids," *Atomic data and nuclear data tables*, vol. 31, no. 1, pp. 1–80, 1984.

国際化推進共同研究概要

No.13

[採択番号]　24NU-7

タイトル： Joint study of calorimetric measurement of heat load and power balance estimation and measurement and simulation of energetic electrons loss in steady state operation (SSO) plasmas on QUEST and EAST

研究代表者： LIU Haiqing

所内世話人： HANADA Kazuaki

研究概 要：パワーバランスについての中国の超伝導装置EASTとQUESTの共同研究。EASTは最近、高性能プラズマであるHモードを1000秒間維持する世界的にも価値の高い実験に成功している。パワーバランスは長時間運転が可能な装置でないと計測が困難であり、九大は計測の点で実績があり、この共同研究は常に世界でトップクラスの実績を保っている。EASTでの計測では90%を超えるパワーの計測ができている。これは100%の計測を行ったTRIAM-1Mの結果に次ぐ精度である。

また、熱負荷分布が磁場配位で変わることから、最適な磁場配位の探索にも着手した。PPPLで開発されたHEATコードを用いた磁場配位による熱負荷分布の計算とAIの一つであるDNNを用いて制御にも使用可能な計算速度で必要なPFコイル電流を計算する手法の開発を行った。

本件に関する発表は以下のとおりである。

１． IAEA-TM on SSO K.Hanada et al, Oct.2024 at Vienna（Extended oral:重要な講演に対して発表時間を長く割り当てる。IAEAで開催される会議では招待講演はないためExtended Oralは招待講演相当）

（様式 11・拠点）

RESEARCH REPORT

Date: FEB 14 2025

Visiting scientists: (name) **Haiqing LIU**

(position) **Professor**

(university / institute) **Institute of Plasma Physics,**

Chinese Academy of Sciences

Host scientist: (name) **Kazuaki Hanada**

(position) **Professor**

(university / institute) **Kyushu University**

Research period: (from) April 1 2024 (to) March 31 2025

Research subject: Joint study of calorimetric measurement of heat load and power balance estimation and measurement and simulation of energetic electrons loss in steady state operation(SSO) plasma on QUEST and EAST

Introduction

The ability to sustain long-pulse steady-state plasma operation is a fundamental requirement for realizing commercial fusion energy in the near future. Both the QUEST and EAST tokamaks possess the capability to sustain plasma long-pulse steady-state operation, making them invaluable experimental platforms for advancing related research. One of this year's primary collaborative research efforts focuses on deepening the understanding of power balance in long-pulse steady-state plasmas. The research emphasizes two key aspects: (1) utilizing diagnostic data combined with code simulations to calculate the heat load on non-water-cooled plasma-facing components (PFCs), ultimately achieving over 90% measurement of injected power during long-pulse discharges on EAST; and (2) performing a power balance analysis and comparison of long-pulse I-mode discharge #106915 and H-mode discharge #122254 on EAST, based on detailed heat load data.

Another major collaborative research project this year is 'Prediction of PF Coil Currents from Plasma Configuration Based on Deep Neural Networks', explores the integration of artificial intelligence with experiment plasma configuration control. The recent experimental objective of QUEST is plasma discharge with a divertor configuration, and this study aims to support that goal. By employing deep neural networks (DNN), a relationship is established between the plasma configuration parameters and the currents of individual PF coils. This approach enables the rapid determination of the required PF coil currents for a target configuration during experiments, making it a promising tool for configuration control in fusion devices.
I plan to visit QUEST building from March 13rd to March 20th, I will make some detailed discussions with Prof. Hanada and other RIAM colleagues.

Recent results in 2024-2025

The calorimetric diagnostic measures the heat load on PFCs during discharges by detecting the temperature of the PFC cooling water. This method avoids indirect measurement, providing accurate and reliable heat load data, making it a critical diagnostic system for power balance research. However, during the 1056 s discharge #106915, the cooling water temperature curves obtained from the calorimetric diagnostic became complex. This complexity arises because, in the EAST device, the cooling water flows in a closed loop, and the cooling tower cannot cool the water temperature back to its initial value after just one cycle. Therefore, when the discharge duration exceeds the cooling water circulation time, the heat carried by the water flowing out of EAST during the second cycle includes the total heat from cooling the PFC in the second cycle, as well as part of the heat from cooling in the first cycle. This situation complicates the cooling water analysis. To address this issue, a two-step correction method has been proposed: time calibration and data calibration.
After data correction, calorimetric diagnostic data can be used for heat load analysis in kilosecond-scale discharges. However, for non-water-cooled PFCs, the calorimetric method cannot be applied for heat load measurements. Instead, the Heat flux Engineering Analysis Toolkit (HEAT) code is utilized to simulate the heat flux and radiation on these PFCs, enabling the estimation of heat loads. By combining calorimetric diagnostics with code simulations, approximately 90% of the injected power can be measured, which is an important achievement in EAST. Figure 1 shows the distribution of PFC modules

in EAST, where only module F is non-water-cooled. Figure 2 presents the radiation distribution across various PFCs obtained using the HEAT simulation. Table 1 provides a comparison of power balance for discharge #106915 and #122254. The total radiation was measured using bolometer diagnostics. It can be observed that for both discharges, the proportion of heat loads on the upper and lower divertors to the injected power is approximately the same, around 70%. However, the radiation percentage in H-mode is roughly twice that in I-mode. A more detailed power balance analysis is currently underway.

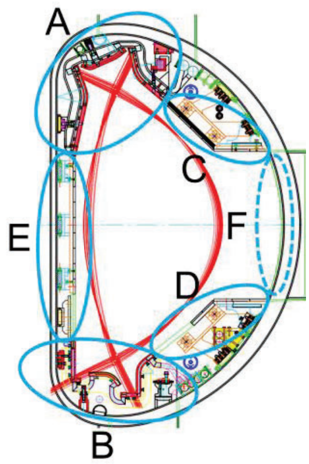

Figure 1. The distribution of PFC modules in EAST.

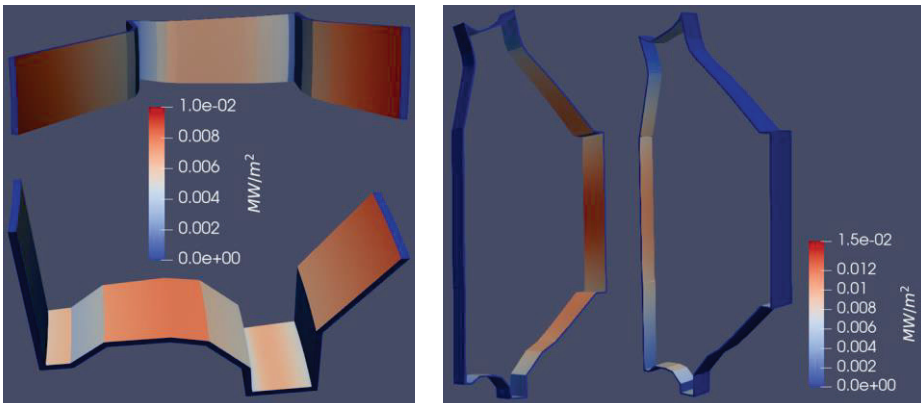

Figure 2. The radiation distribution across different PFCs simulated by the HEAT code.

Table 1. The power balance analysis between discharge #106915 and #122254.

Shot number	106915	122254
Mode	I	H
The heat load and proportion on the following PFCs (MW)		
Module A	0.38 (28.30 %)	0.51 (18.45 %)
Module B	0.57 (41.98 %)	1.38 (49.75 %)
Module CDE	0.19 (13.95 %)	0.53 (19.04 %)
Main limiter	Unmeasured	0.01 (0.33 %)

Radiation on Module F (simulation)	0.04 (3.58 %)	0.16 (5.82 %)
Total injected energy (MJ)	1428.34	1130.77
Radiation	11.36 %	20.68 %
All known energy	87.80 %	93.39 %

A tokamak confines plasma using magnetic fields. Optimizing the plasma magnetic configuration is critical for enhancing plasma performance and stability. The plasma configuration is primarily governed by a set of poloidal field (PF) coils, making it essential to determine the current settings for each PF coil (I_{PF}) based on the target plasma configuration prior to the experiment. In this study, we developed a DNN model capable of accurately and efficiently predicting I_{PF} set for a given target plasma configuration. The dataset for the model were QUEST various equilibrium, which generated using a newly developed equilibrium calculation code. Comprehensive testing and evaluation revealed highly satisfactory performance of this model. Additionally, fine-tuning the $I_{PF\ 35\text{-}1}$ can further reduced the strike point error. Figure 3 presents an example of good diverter configuration prediction. It can be observed that the predicted configuration aligns well with the original configuration.

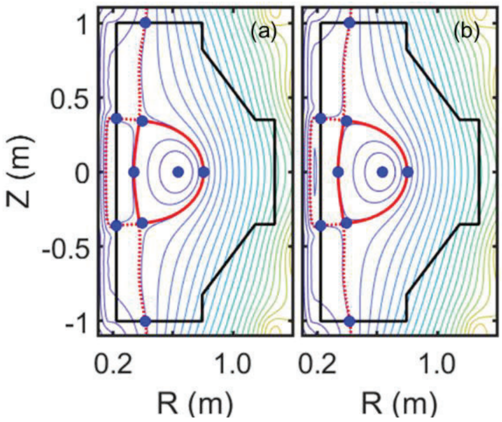

Figure 3. An example of good prediction. (a) the original configuration, (b) the predicted configuration.

Discussions

This year's collaborative research continued to focus on the long-pulse steady-state operation of plasmas and achieved significant results in two parts: (a) combining calorimetric diagnostic data with code simulations to achieve about 90% of the injected power measurement during EAST discharges, (b) conducting detailed power balance analysis of long-pulse I-mode and H-mode discharges. These studies contribute substantially to advancing the long-pulse steady-state operation of plasmas.

This research was conducted by Dr. Wang Yunfei, with whom I engaged in numerous productive discussions. This work marks the first successful measurement of approximately 90% of the injected power on EAST, which holds great importance for analyzing the deposition locations of injected energy, mitigating localized heat loads, optimizing discharge heating schemes, and conducting in-depth power balance studies. The calorimetric diagnostic data correction method proposed in this research enables the effective use of calorimetric diagnostics for heat load analyses in kilosecond-scale discharges. The findings lay a solid foundation for the long-pulse steady-state operation of future fusion devices. Furthermore, the detailed comparative analysis of power balance in long-pulse I-mode and H-mode discharges provides critical insights into exploring confinement modes suitable for future fusion devices. Additionally, we explored the integration of machine learning into the field of fusion research, yielding promising results. This part of the study was also performed by Dr. Wang Yunfei. This study introduces a comprehensive methodology for predicting the I_{PF} set required for achieving a target plasma configuration, leveraging a deep neural network (DNN). The process involves constructing a plasma configuration dataset using equilibrium calculation codes, optimizing the PF coil arrangement, and developing a DNN-based prediction model. The proposed DNN model utilizes configuration feature points as input and outputs the corresponding I_{PF} set necessary to realize the desired configuration. This approach is entirely code-driven and device-independent, making it particularly advantageous for the design and validation of PF coils and plasma configurations before device construction. Currently, the model is limited to predicting I_{PF} sets for up-down symmetric configurations. Future work will focus on expanding the dataset to include configurations such as single-null divertors, enhancing the model's applicability. Compared to traditional methods, the DNN model offers significantly faster computation and has the potential to be integrated into plasma control systems. This integration could enable direct control of plasma configurations, replacing the conventional indirect control methods reliant on I_{PF} sets. During the coming visit stay, I will have more detailed discussions with Prof. Hanada and Prof. Ido under this international joint research frame. And we will make new co-proposals in the next EAST experimental campaign. We will continue to study the power balance (particle balance) estimation in steady state operation (SSO) plasmas on QUEST and EAST.

Acknowledgement and comments:

Work supported by the international joint research at the Joint Usage of Research Centers for Applied Mechanics for 2024. We hope that the international joint research at the Joint Usage of Research Centers for Applied Mechanics could continue to enhance China-Japan cooperation on fusion plasma research in the future.

Co-publication list of the joint usage / research in 2024-2025:

N/A

(Signature)________________________

(Name in print) Haiqing Liu

国際化推進共同研究概要

No.14

[採択番号]　24NU-8

タイト ル： Functional dependency of phase transitions on the heating frequency of a helicon discharge

研究代表者： FAHRENKAMP Nils

所内世話人： MOON Chanho

研究概 要：

PANTAデータの再解析とヘリコン波がプラズマモード遷移に与える影響の初期評価により、研究が進展し、RF周波数と磁場強度に対する臨界密度の理解が深まりました。今後の実験に向けた基盤が整いました。新しい計測機器の導入により、RIAMとの共同研究が進展し、ヘリコン波の伝播に関する理論モデルの検証や放電モードの物理理解が進みます。今後は、ドイツの直線装置VINETAの診断機器を強化し、ヘリコンプラズマの生成とその応用に関する研究をさらに進めていきます。

Functional dependency of phase transitions on the heating frequency of a helicon discharge (1_24NU-8)

N. Fahrenkamp
Institute of Physics, University of Greifswald,
Felix-Hausdorff-Str.6, 17489 Greifswald, Germany

I. AIM

The primary objective of this report is to extend the analysis of our previous PANTA experiments and to integrate new insights into helicon plasma behavior with the upcoming experimental enhancements on VINETA. In 2023, our work at RIAM on the PANTA device established a detailed picture of plasma flow patterns, mode transitions, and the influence of radio-frequency (RF) heating on plasma density, see the report of 2023. The high ionization rates of helicon discharges and their heating mechanism are not understood to this day. A key piece to this understanding is the dispersion relation of the propagating wave. Effects of the dispersion relation also relate to a rarely studied parameter of the wave, its frequency. The existence of a critical magnetic field B_c as postulated by Kwak et al. [1] was the research topic of Stefan Knauer in 2023. Going beyond the work of Kwak we furthermore look for a dependency of B_c on the heating frequency f_{rf}. PANTA allows us to study the influence of the f_{rf} on a helicon discharge, which is and will not be possible for us in our helicon plasma device VINETA in Greifswald. In addition to the dependence of B_c on f_{rf}, another topic of open research is the question in which way phase transitions of the discharge modes depend on f_{rf}, too. To increase the insight of the scientific community into these topics we measured plasma discharges at PANTA with varying magnetic fields, pressures, heating powers and heating frequencies to derive a dependency for the mode transitions in 2023.The current study revisits these findings by refining the power-law dependencies observed in the E, H, and W operational modes and by examining the interplay between RF frequency and magnetic field strength. Additionally, preparations are underway to incorporate advanced diagnostic equipment into the VINETA experiment at Greifswald — a development made possible through our continued collaboration with RIAM. This equipment, arriving in February together with guest from RIAM with the support of our grant, is expected to significantly enhance our ability to compare and contrast plasma phenomena between the two devices.

II. SCIENTIFIC CREDENTIALS, THE E-H-W MODE TRANSITIONS

Helicon plasmas are known to exhibit three distinct modes of operation: the capacitive mode (E-mode), the inductive mode (H-mode), and the helicon-wave sustained mode (W-mode) with very high densities. In [2] critical densities are proposed, observed with a double loop antenna ($m = 0$). The transition between E and H-modes should occur when the skin depth δ is equal to the half radius of the Pyrex tube [3]. Similarly a minimum density depending on the magnetic field strength is necessary to observe the first longitudinal helicon-wave mode. At higher magnetic field strength the critical density for the H-W transition is higher and at higher f_{rf} the critical density for the H-W transition is lower [4]. This relation is linear in theory, but somewhat less pronounced in experiments. Our previous investigations on PANTA revealed that, under low-power conditions, the plasma operates in the E-mode with a square-root dependence on absorbed RF power, whereas at higher powers the W-mode emerges, marked by a pronounced step in the density profile. In the 2023 report, these transitions were quantified by fitting the central plasma density using power laws and Gaussian profiles, providing a robust framework to estimate the critical densities at the mode transitions. The extended analysis further demonstrates that the transition between these modes is strongly influenced by both the RF driving frequency and the applied magnetic field. In particular, our preliminary findings indicate that higher RF frequencies lead to a reduction in the critical density required for the transition into the W-mode. Moreover, the relationship between the magnetic field strength and plasma density is not strictly linear; rather, a non-monotonic behavior is observed near the lower hybrid resonance, suggesting a complex interplay between wave dispersion and plasma confinement.

III. EXPERIMENTAL SETUP

The experiments conducted in 2023 utilized the PANTA device [5], a linear magnetized plasma apparatus with a length of approximately 4.05 m and a diameter of 45 cm. A homogeneous axial magnetic field of up to 150 mT is generated by Helmholtz coils, and the plasma is initiated using a double loop helicon source with a typical cylindrical radius of 5 cm. Langmuir probe diagnostics and additional probe measurements (floating potential, ion saturation current) were employed to acquire detailed measurements of the plasma density and flow patterns. These measurements allowed for the identification of the distinct E-, H-, and W-mode regimes and the determination of the critical densities associated with each transition.

For 2024, while no new data could be acquired from Japan, our analytical efforts have been redirected towards an in-depth reanalysis of the 2023 dataset. In parallel, significant upgrades are being planned for the VINETA experiment at Greifswald. VINETA operates on similar principles to PANTA, and the arrival of new diagnostic instrument — brought by our RIAM colleagues — will facilitate comparative studies, see figure 1.

FIG. 1: New Components brought by our RIAM colleagues. Consisting of ceramic tubing, metal probe materials, screw-drivers, soldering equipment, and cables and connectors

The enhanced setup on VINETA will allow us to extend the parameter scans to include a broader range of magnetic fields, gas pressures and RF powers thereby providing an opportunity to test the universality of the helicon dispersion relation and to further explore mode transition dynamics.

IV. RESULTS

The reanalysis of the 2023 PANTA data has yielded several significant insights. Detailed examinations of the central plasma density as a function of absorbed RF power confirm the presence of three distinct discharge modes, see figure 2.

In the low-power E-mode, the density scales approximately with the square root of the RF power [6]. For the H-mode density increases linearly with rf power [7] while in the high-power W-mode, a step-like increase in density is evident. Fitting the data with power-law models has refined our estimates of the critical densities at the H-W transition [2], revealing that these thresholds are strongly modulated by both the RF frequency and the magnetic field strength.

Furthermore, our extended analysis, see figures 3 and 4 indicates that increasing the RF driving frequency tends to lower the critical density required for a transition into the W-mode. This behavior can be attributed to the effect of helicon-wave dispersion, where higher frequencies enhance the efficiency of energy coupling into the plasma. Additionally, the observed non-monotonic behavior of plasma density near the lower hybrid resonance—where the electron temperature and transport dynamics undergo notable changes—further supports the hypothesis that resonant phenomena play a key role in the mode transition process.

The forthcoming integration of new diagnostic tools into VINETA is expected to complement these

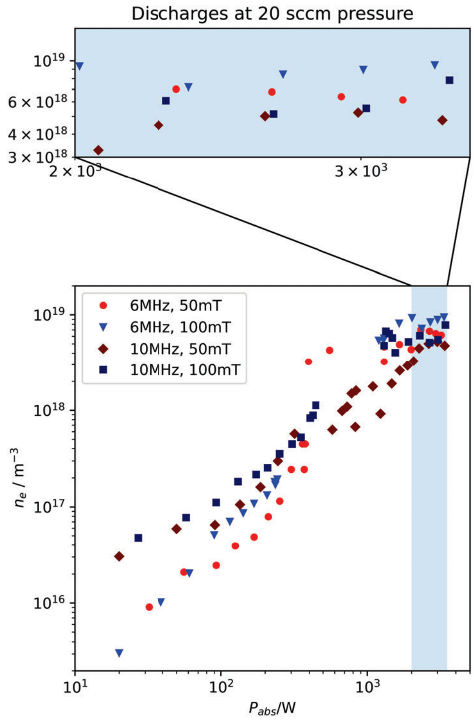

FIG. 2: Central density vs. absorbed power at two different magnetic field strengths and heating frequencies. The background pressure was 0.2 Pa.

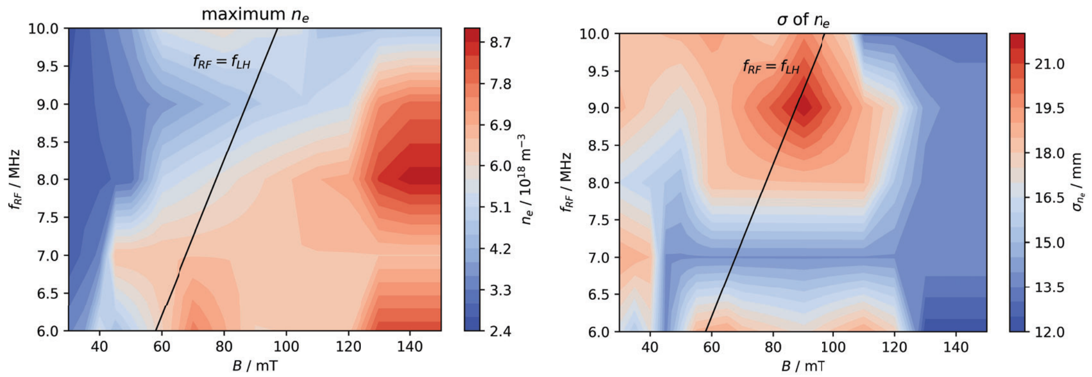

FIG. 3: The maximum plasma density in the center of the discharge and the width of the fitted radial distribution over magnetic field strength. The displayed line represents the lower hybrid resonance for varying magnetic field strength

findings. By enabling measurements and extending the range of operational parameters, the VINETA upgrades will allow us to systematically investigate the similarities and differences between the plasma behavior in PANTA and VINETA. This comparative approach is anticipated to provide deeper insights into cross-field transport, turbulence characteristics, and the overall stability of helicon discharges.

V. CONCLUSION

Although the planned 2024 trip to Japan was not realized, our research has advanced significantly through the comprehensive reanalysis of the 2023 PANTA data and the preliminary evaluation of helicon-wave effects on plasma mode transitions. The refined understanding of the critical density dependencies on RF frequency and magnetic field strength lays a solid foundation for future experimental investigations. The upcoming arrival of new diagnostic equipment at the VINETA facility represents a crucial step

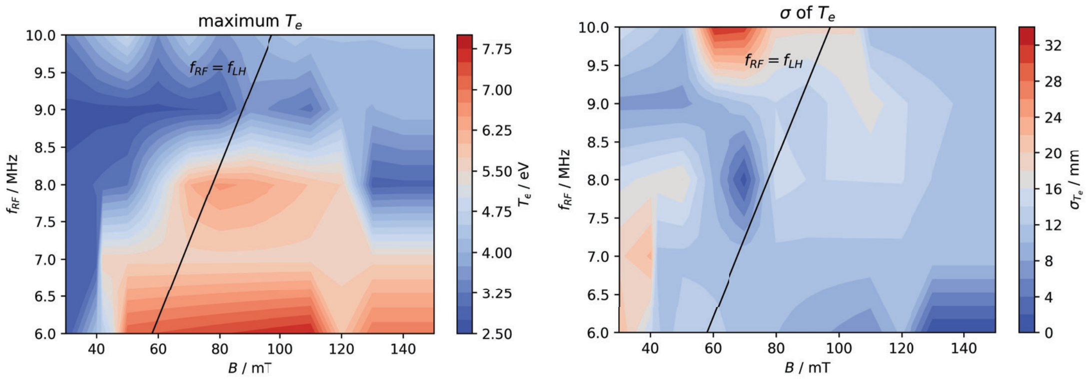

FIG. 4: The maximum electron temperature in the center of the discharge and the width of the fitted radial distribution over magnetic field strength. The displayed line represents the lower hybrid resonance for varying magnetic field strength

forward in our collaborative efforts with RIAM. With enhanced measurement capabilities, we are poised to expand our experimental possibilities, validate theoretical models of helicon wave propagation, and further elucidate the underlying physics governing the E, H, and W discharge modes.

Our future work will focus on integrating the upgraded VINETA diagnostics with continued comparative studies, ultimately advancing the scientific community's understanding of helicon plasma generation and its practical applications in industrial and space propulsion systems.

[1] J. G. Kwak, H. D. Choi, H. I. Bak, S. Cho, J. G. Bak, and S. K. Kim, Physics of Plasmas **4**, 1463 (1997).

[2] V. Kaeppelin, M. Carrère, and J. B. Faure, Review of Scientific Instruments **72**, 4377 (2001), ISSN 0034-6748, https://pubs.aip.org/aip/rsi/article-pdf/72/12/4377/19295379/4377_1_online.pdf, URL `https://doi.org/10.1063/1.1419228`.

[3] C. M. Franck, O. Grulke, and T. Klinger, Physics of Plasmas **10**, 323 (2003).

[4] K. P. Shamrai, Plasma Sources Science and Technology **7**, 499 (1998), URL `https://dx.doi.org/10.1088/0963-0252/7/4/008`.

[5] T. Yamada, S.-I. Itoh, T. Maruta, N. Kasuya, S. Shinohara, Y. Nagashima, M. Yagi, K. Terasawa, S. Inagaki, Y. Kawai, et al., Plasma and Fusion Research **3**, 044 (2008).

[6] A. W. Degeling, C. Jung, R. Boswell, and A. Ellingboe, Physics of Plasmas **3**, 2788 (1996).

[7] J. Hopwood, C. Guarnieri, S. Whitehair, and J. Cuomo, J. Vac. Sci. Technol. A **11**, 152 (1993).

国際化推進共同研究概要

No.15

［採択番号］　24NU-9

タイト ル： Slug dynamics at transitional drift-wave turbulence

研究代表者： MANZ Peter

所内世話人： MOON Chanho

研究概 要：

本研究では、層流から乱流への遷移に関する流体力学的概念を基に、磁化プラズマにおけるドリフト波乱流の遷移過程を調査した。特に、大振幅構造の相関時間の解析を通じて、プラズマにおける準コヒーレントモードの振る舞いを明らかにし、遷移的乱流の特徴を検討した。さらに、単純な幾何学系における流体とプラズマの類似性を比較し、磁化プラズマ乱流の理解を深めることを目的とする。

Slug dynamics at transitional drift-wave turbulence (No.1 _24NU-9)

Peter Manz , Institute of Physics, University of Greifswald, Germany

Primary member of the join research team is Prof. Chanho Moon

Aim: The existence of a critical point of an underlying non-equilibrium continuous phase transition is indicated by small changes in the control parameter leading to large changes in the correlation times. The long-term development of the transitional regime of drift-wave turbulence is studied in a magnetized plasma column by means of the conditional average technique to search for divergent behaviour in correlation.

Background: In fluid dynamics, the process in which a laminar flow becomes turbulent is referred to as the laminar-turbulent transition and the flow to as transitional flow. Structures of large amplitude are given particular emphasis in transitional flows. These are turbulent areas spatially separated from areas of laminar flow. In pipe flows, large amplitude structures are called puffs. Puffs can split into two parts, which is called puff splitting [1]. The puff splitting process has been related to direct percolation theory [2], which is an universality class of non-equilibrium continuous phase transitions. At even higher Reynolds numbers, the turbulent patches tend to grow and spread in space instead of just moving or splitting. These growing regions of turbulence are called slugs [3, 4].

Turbulence is responsible for the majority of particle and heat loss in magnetically confined fusion plasmas. Magnetically confined high-temperature plasmas are usually in the state of developed turbulence. Due to the reduced turbulence level, improved confinement regimes in magnetically confined fusion plasmas could be assigned to transitional regimes [5]. In these confinement regimes, the turbulence is often dominated by quasi-coherent modes, a signature of transitional turbulence, as explained later. Mechanisms that can be transferred from transitional flows in neutral fluids to magnetized plasmas could then be relevant for understanding the dynamics in these regimes. The transition to a turbulent state can be studied in laboratory-scale low-temperature linear plasma experiments [6–9]. Here, drift waves and drift-wave turbulence occurs [10, 11]. Drift wave turbulence is the simplest case of turbulence in magnetized plasmas [12, 13]. Drift waves can sustain themselves and suppress other initially stronger linear instabilities of another type [14, 15].

Non-equilibrium continuous phase transitions are also called critical phenomena due to their association with a critical point. The most essential characteristic of a critical point is the divergence of the correlation length when approaching the critical point. Particularly interesting in this respect are indications of a divergent behavior of correlation times and lengths. At low mag netic field strength, drift-waves are excited, but these do not interact strongly with each other, the system can still be described quasi-linearly. This regime is therefore called the quasi-linear regime. Increasing the magnetic field strength in the low-temperature magnetized plasma, the dynamics become first more coherent in agreement to the Landau-Ruelle-Takens scenario [6, 8]. In the so-called mode-locked regime, a quasi-coherent mode occurs [7, 8]. The quasi-coherent mode is a nonlinear mode [8]. It is characterized by a high spatiotemporal symmetry, it appears particularly stable and long-living, also already known at PANTA as the solitary wave [16]. In the phase-locked regime, the coherence is highest. Increasing the control parameter, the system transits into the so-called weak turbulent regime. The quasi-coherent mode is destabilized by the occasional occurrence of phase defects [6, 17]. These defects have a relatively short lifetime of the order of the period duration of the dominant mode and lead to the broadening of the spectrum around the dominant peaks [6]. When the phase defects occur more often, the spatiotemporal symmetry gets lost, the dynamics gets less coherent and the weak turbulent state develops [6].

Correlation times of large-amplitude coherent structures can be studied in magnetized plasma by means of the conditional averaging technique [23]. Conditional averaging has been used in linear devices [24–32] in small laboratory toroidal devices [33–37] or in the edge of toroidal fusion experiments as well. In particular, large-scale coherent structures show similarities in linear devices and in the edge regions in fusion experiments [38]. The aim of this work is, as a first step, to compare the structures between systems of simple geometry, i.e. between neutral fluids in pipe flows and magnetized plasmas in linear devices such as PANTA.

Experiments: Experiments have been carried out in the linear magnetized plasma experiment PANTA [11] of a length of 4.0m and a diameter of 45 cm. For the pipe flow the Reynolds number is the control parameter. But the viscosity in plasmas is negligibly low, thus, the Reynolds number is not relevant here. Drift-waves are driven unstable by electron-ion collisions in the presence of a density gradient. In helicon heated plasmas, like in PANTA, the magnetic field strength B can be utilized as a control parameter [7–9]. A homogeneous axial magnetic field (at 70, 80 mT) is generated by a set of coils. In this range of magnetic field strength, in PANTA the phase-locked regime occurs [16], i.e. the regime between the quasi-linear and the weakly turbulent regime. Here, we expect the strongest changes in correlation time with respect to changes in the control parameter. The plasma is heated by a double loop helicon source with a diameter of 10 cm at one end of the device. The heating power was 3 kW. The rf frequency was 9 MHz. At the other end the plasma terminates at a stainless steel end-plate. The working gas was argon at a neutral gas pressure of 0.6 Pa. A discharge lasts 500 ms, whereby only the time of saturated quasi-stationary turbulence is analyzed here. That is about 400 ms.

Fluctuations have been measured by a 64-channel Langmuir probe array [39] which is installed at an axial distance of z = 1.885m away from the source. The Langmuir probes made of tungsten wire with a diameter of 0.8mm and length of 3mm are aligned on a circle of radius r = 4 cm. The azimuthal distance between the probes is 3.9mm. The probe tips measured alternating ion saturation current Isat and floating potential fluctuations, which are usually considered to be a good approximation for plasma density and potential fluctuations, respectively. Here, only the data from the tips measuring Isat is shown. The distance between two Isat tips is 7.8mm. The data is recorded with a sampling frequency of 1 MHz.

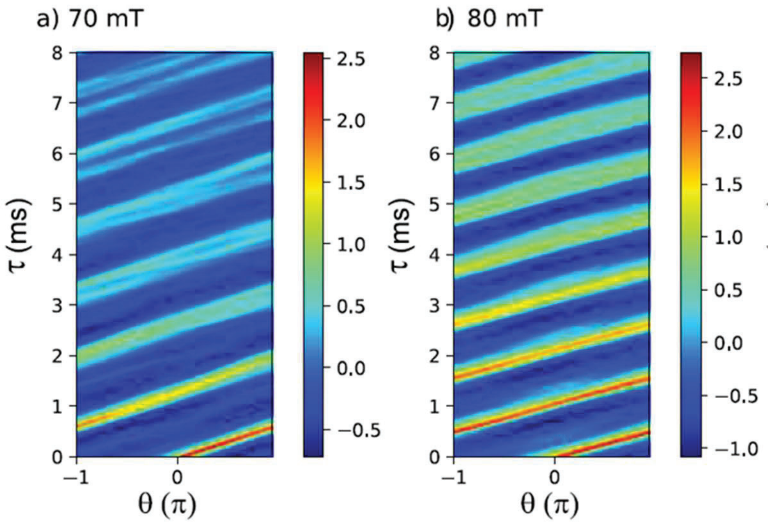

Figure 1 Conditional averaged dynamics of coherent density perturbations Isat/σ shown color-coded at a) B = 70, b) B = 80

Results: Figure 1a shows the conditional averaged dynamics of ion saturation current fluctuations for a discharge at B = 70 mT. At τ = 0, a strongly localized structure appears at the reference position (θ = 0). Since this is an increase in pressure, the term blob is used in the context of magnetized plasmas. In the pipe flow context, this corresponds to a puff. When considering only the reference probe (θ = 0), the e-folding time of the struc ture is already reached after τ = 50 µs. Usually this correlation time is regarded as the lifetime. The drift wave propagates in the electron diamagnetic direction along the probe array, resulting in the helical structure in Fig. 1a. The propagation velocity is about v $\approx$ 188 m/s. A correlation length ξ = vτ can be assigned to the correlation time τ via the propagation velocity v, in this case this corresponds to ξ = 94 mm. This is usually compared to the hybrid Lamor radius ρ_s. The characteristic size of drift waves is around k $\rho_s \sim 1$. At B = 70 mT, $\rho_s \approx$ 13 mm, hence this correlation length fulfills the expectations of drift waves. However, this time has little to do with the lifetime, but is determined by the size of the structure and the propagation induced Doppler shift. The lifetime as the time of persistence is significantly longer. The coherent structure runs around azimuthally several times, while its amplitude decreases continuously over time. If the persistence time is to be determined, the time along the propagation direction should be considered. Following the structure, the e-folding time is reached at τ = 2.35 ms. That is a factor of 50 larger than the single probe estimate and extremely long-lasting. Near the laminar-turbulent transition in the pipe flow, puff decay and splitting have time scales that are of order 107 advective time units [1]. This is also utterly long-lasting. Translated into a correlation length, this corresponds to ξ = 44.2 cm (34 ρ_s or 5 typical drift wavelengths) exceeding the typical azimuthal system length of 2πr = 25 cm. That is a very long azimuthal correlation length.

In a different representation, the comparison to the pipe flow becomes somewhat more obvious. The time averaged angular velocity v of the coherent structure has been estimated and then a transformation into the co-moving coordinate system $\theta' = \theta - v\tau/r$ has been per-formed. The system is now viewed from the perspective of an observer moving at a constant v. The helical structures appearing in Fig. 1 are thus tilted and appear straightened in Fig. 2.

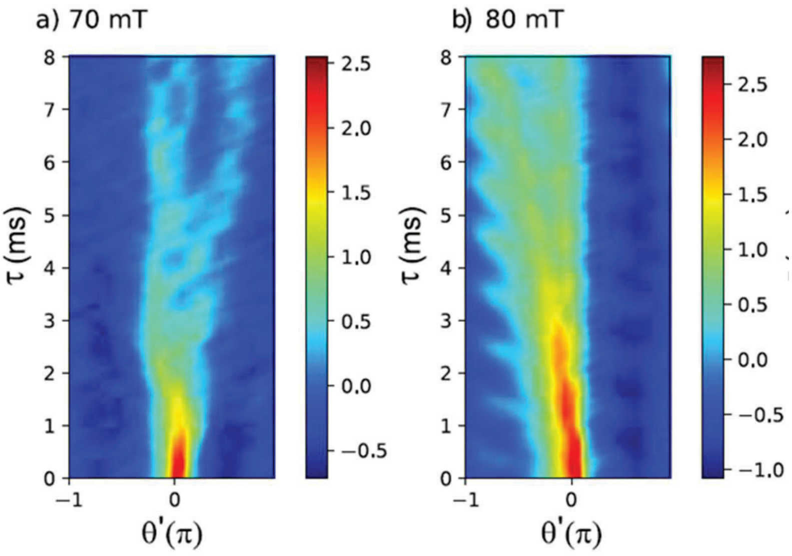

Figure 2 Conditional averaged dynamics of coherent density perturbations Isat/σ shown color-coded at a) B = 70, b) B = 80 mT in a co-moving frame of reference.

From around the e-folding time (τ > 2.35 ms), the leading edge of the puff becomes more and more disturbed. One can recognize the emission of small-scale streaky protuberances similar to the pipe flow[40]. If these streaky perturbation sufficiently separates from the parent puff, it seeds a new puff. Detachment from the parent puff originates from a reduction of turbulence amplitude [40]. This is important for the development of the gap between the parent puff and the new seeded puff. The gap is clearly visible in Figs. 1a and 2a around τ ~ 3 ms. The puff splits into two structures. However, most of these small perturbations fail at nucleating a new puff. Also this new puff is quickly damped out. This occurs at amplitudes between 0.5 and 0.8 far above the significance level of 0.16. If the structure is regarded as a wave, one can also speak of phase defects. Phase defects and puff splitting appear to be similar phenomena. The conditional averaged splitting time (τ ~ 3ms) is of the same order of magnitude as the conditional averaged decay time (τ = 2.35 ms), but exceeds it. This should be the phase in which turbulence cannot sustain itself, and turbulence should die out. That is what is happening in the following. At around τ~4 ms, the parent puff splits again. This then occurs from time to time and the structure is fragmented into multiple filaments progressively yielding trains of puffs. The amplitude continues to decrease. At some point, the detailed behavior on long time scales has to be considered to be no longer statistically significant.

Figs. 1b and 2b show even more long-lasting structures with a slightly increased magnetic field to B = 80 mT ($\rho_s \approx$ 11.4 mm). The drift wave propagates somewhat faster at v ≈ 230 m/s. The e-folding time at the reference probe is 96 µs (corresponding to ξ = 22 cm or three typical drift-wave wavelengths). Following the structure along the Langmuir probe array in the co-moving frame of reference, the e-folding time is 5 ms. The corresponding azimuthal correlation length is about 1.15 m (about 16 typical drift-wave wavelengths). This abrupt change in correlation times and lengths in response to a small change in the control parameter (here B) can certainly not be understood by change in the linear dynamics and is a clear sign of the existence of a critical point. Around the same time ($\tau \approx$ 4–5 ms) the structure splits. Conditional averaged splitting time and lifetime are roughly similar. Therefore, this discharge is close to the crossover point between dominant decay to splitting, which is the critical point for the transition to self-sustained turbulence in pipe flows.

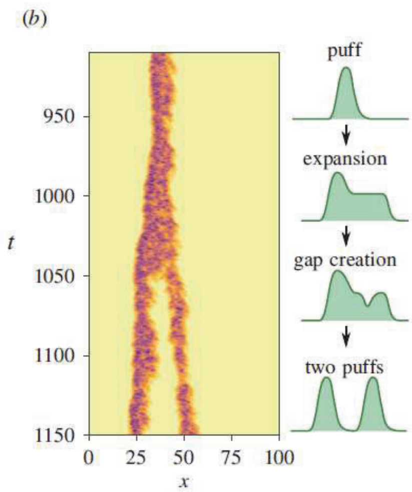

Figure 3 slug-gap-split mechanism from Frishman and Grafke [41]

Small-scale streaky perturbations at the front are absent. Splitting seems to follow a different dynamic. What else is different? The particular feature in this discharge is that the structure expands much more than for the B = 70 mT case. In pipe flow, slugs are expanding regions of fluctuations. Slugs expand because the front and back edge of the slug propagate with different velocities. In the pipe flow, these velocities are more different for higher Reynolds numbers and the slugs expand more strongly. The structure shown in Figs. 1b and 2b is expanding and therefore shows similarities to a slug. Frishman and Grafke [41] proposed a two-stage process called the slug-gap-split mechanism. In the first stage, fluctuations drive a slug. This can be observed here up to $\tau < 4$ ms. In the second stage, when the slug is wide enough, a laminar pocket forms within the core ($\tau \approx 4$–5 ms), separating it into two parts, each of which evolves its own puff or slug. A local decrease of turbulence down to a threshold value is responsible for the creation of a laminar gap. A further decrease of turbulence level should widen the gap. With time the fluctuation level drops and with it the gap develops and widens. Fig. 2b is strongly reminiscent of Fig. 1b in Ref. [41], shown here as Fig.3.

Turbulent structures in pipe flows and magnetized plasmas are perhaps more similar than one might think.

References

[1] K. Avila, D. Moxey, A. de Lozar, M. Avila, D. Barkley, Science 333, 192 (2011).

[2] G. Lemoult, L. Shi, K. Avila, et al., Nat. Phys. 12, 254–258 (2016).

[3] D. Barkley, B. Song, V. Mukund, et al., Nature 526,550–553 (2015).

[4] X.Wang, H.-Y. Shih, and N. Goldenfeld, Phys. Rev. Lett. 129, 034501 (2022).

[5] P. Manz et al., Nuclear Fusion 57, 086022 (2017).

[6] T. Klinger, A. Latten, A. Piel, G. Bonhomme, T. Pierre, and T. Dudok de Wit, Phys. Rev. Lett. 79, 3913 (1997).

[7] M. J. Burin, G. R. Tynan, G. Y. Antar, N. A. Crocker, and C. Holland, Physics of Plasmas 12, 052320 (2005).

[8] P. Manz, M. Xu, S. C. Thakur, and G. R. Tynan, Plasma Physics and Controlled Fusion 53, 095001 (2011).

[9] S. C. Thakur et al., Plasma Sources Science and Technology 23, 044006 (2014).

[10] F. Brochard, E. Gravier, and G. Bonhomme, Physics of Plasmas 12, 062104 (2005).

[11] T. Yamada et al., Plasma and Fusion Research 3, 044 (2008).

[12] A. Hasegawa and M. Wakatani, Phys.Rev.Lett. 50, 682 (1983).

[13] M. Wakatani and A. Hasegawa, Phys. Fluids 27, 611 (1984).

[14] B. D. Scott, Physics of Fluids B: Plasma Physics 4, 2468 (1992).

[15] P. Manz, et al., Plasma Physics and Controlled Fusion 60, 085002 (2018).

[16] T. Kobayashi et al., Plasma and Fusion Research 12, 1401019 (2017).

[17] O. Grulke and T. Klinger, New Journal of Physics 4, 67 (2002).

[18] C. Schröder, T. Klinger, D. Block, A. Piel, G. Bonhomme, and V. Naulin, Phys. Rev. Lett. 86, 5711 (2001).

[19] F. Brochard, G. Bonhomme, E. Gravier, S. Oldenbürger, and M. Philipp, Physics of Plasmas 13, 052509 (2006).

[20] C. Brandt, O. Grulke, and T. Klinger, Plasma Physics and Controlled Fusion 52, 055009 (2010).

[21] C. Brandt, O. Grulke, and T. Klinger, Physics of Plasmas 17, 032304 (2010).

[22] J. Kühnen, B. Song, D. Scarselli, N. B. Budanur, M. Riedl, A. P. Willis, M. Avila, and B. Hof, Nature Physics 14, 386 (2018).

[23] H. Johnsen, H. L. P´ecseli, and J. Trulsen, The Physics of Fluids 30, 2239 (1987).

[24] O. Grulke, T. Klinger, and A. Piel, Physics of Plasmas 6, 788 (1999).

[25] T. Windisch, O. Grulke, and T. Klinger, Physics of Plasmas 13, 122303 (2006).

[26] T. A. Carter, Physics of Plasmas 13, 010701 (2006).

[27] P. Manz et al. , Phys. Rev. Lett. 107, 195004 (2011).

[28] T. Windisch, O. Grulke, V. Naulin, and T. Klinger, Plasma Physics and Controlled Fusion 53, 124036 (2011).

[29] J. E. Maggs and G. J. Morales, Plasma Physics and Controlled Fusion 54, 124041 (2012).

[30] F. Kin et al. , Physics of Plasmas 25, 062304 (2018).

[31] H. Tanaka et al. Plasma Physics and Controlled Fusion 62, 075011 (2020).

32] T.-K. Kobayashi et al., Plasma Physics and Controlled Fusion 63, 032001 (2021).

[33] A. Fredriksen, C. Riccardi, L. Cartegni, and H. Pecseli, Plasma Physics and Controlled Fusion 45, 721 (2003).

[34 R. Barni and C. Riccardi, Plasma Physics and Controlled Fusion 51, 085010 (2009).

[35] T. Happel, F. Greiner, N. Mahdizadeh, B. Nold, M. Ramisch, and U. Stroth, Phys. Rev. Lett. 102, 255001 (2009).

[36] C. Theiler et al., Physics of Plasmas 15, 042303 (2008).

[37] B. Nold et al. Physics of Plasmas 21, 102304 (2014).

[38] G. Y. Antar et al. Phys. Rev. Lett. 87, 065001 (2001).

[39] T. Yamada et al., Review of Scientific Instruments 78, 123501 (2007).

[40] M. Shimizu, P.Manneville, Y. Duguet, and G. Kawahara, Fluid Dynamics Research 46, 061403 (2014).

[41] A. Frishman and T. Grafke, Proc. R. Soc. A. 478, 20220218 (2022).

国際化推進共同研究概要

No.16

[採択番号] 24NU-10

タイトル： Joint study of long pulse high beta discharges and related egde turbulence transport in steady state operation (SSO) plasmas on QUEST and EAST

研究代表者： GAO Xiang

所内世話人： HANADA Kazuaki

研究概要：高性能プラズマの定常運転にとって定期的な不純物やヘリウム灰の掃き出しは重要である。Edge Localized Mode(ELM)は、高性能プラズマであるHモードではしばしば観測される不安定性で、閉じ込め性能をわずかに劣化させるが上記の不要物の掃き出し効果のために利用することが想定されている。ITERではＥＬＭｙ　Ｈモードが標準運転として採用されている。一方、さらに性能の良い閉じ込めモードとして内部輸送障壁（ITB）を有するプラズマがあげられる。中国の超伝導トカマクEASTではELMで発生した熱・粒子がプラズマコア側に伝搬し、ＩＴＢを崩壊させる現象を初めて観測した。この現象には周辺部の鋸歯状振動が関わっていることは確認されたが詳しい原因はわかっていない。この現象は高性能プラズマの定常維持にとって重要な発見になる可能性があるため今後も詳細解明を行っていく予定である。

関連する共著発表

(1) X.Gao et al., "ELM penetration and ITB collapse in EAST hybrid discharges", 43rd ITPA-PEP meeting, Princeton, USA, April 23-26, 2024

(2) X.Gao et al., "ELM penetration in ITB plasma on EAST tokamak", 19TH INTERNATIONAL WORKSHOP ON H-MODE PHYSICS AND TRANSPORT BARRIERS, Mito, Ibaraki, Japan, September 24-27, 2024

（様式 11・拠点）

RESEARCH REPORT

Date: FEB 14 2025

Visiting scientists: (name) Xiang Gao

(position) Professor

(university / institute) Institute of Plasma Physics,

Chinese Academy of Sciences

Host scientist: (name) Kazuaki Hanada

(position) Professor

(university / institute) Kyushu University

Research period: (from) April 1 2024 (to) March 31 2025

Research subject: **Joint study of long pulse high beta discharges and related edge turbulence transport in steady state operation (SSO) plasmas on QUEST and EAST**

Introduction

Steady state operation (SSO) of tokamak plasma is one of the basic requirements for future fusion reactors. Long pulse high beta operation is one of important missions for ITER. Joint study long pulse high beta discharges in SSO plasma research field on QUEST and EAST is strongly supporting ITER experiment from both experience and theory. In 2024, we focus on the ELM penetration in ITB plasma on EAST tokamak and some potential comparison with similar phenomenon with QUEST device.
I plan to visit QUEST building from March 13rd to March 20th, I will make some detailed discussions with Prof. Hanada and other RIAM colleagues.

New results in 2024-2025

The penetration of edge localized mode (ELM) into internal transport barrier (ITB) plasma has been studied on the EAST tokamak with flat central safety factor profile q(0) ~ 1 recently. The experiment indicates that when the ELM inward penetration radius reaches to the ITB foot region, a significant influence on the ITB plasma is manifested, leading to the shrinking or collapse of the ITB on the EAST tokamak. Observations suggest that the onset of large ELM penetration, which extremely reduces the pedestal temperature and density, can trigger the collapse of the ITB, by means with the off-axis sawtooth on EAST tokamak. The off-axis sawtooth events contribute to a further decrement in the core stored energy after a bigger ELM crashes in the pedestal region. The reversal surface of the off-axis sawtooth is situated around the ITB foot. The delay time between ELM penetration reached to ITB foot and the followed off-axis sawtooth collapse is about 2~3 ms. It is also found that the shrinking and expanding of ITB is related with the net heating power. The mechanism of ITB collapse from ELM penetration to the off-axis sawtooth triggered is not clear yet. It also found that the shrinking and expanding of ITB is correlated with the net heating power. Further studies in simulation are needed, and the boundary and pedestal integration module for the BOUT++ code is under development.

Acknowledgement and comments:

Work supported by the international joint research at the Joint Usage of Research Centers for Applied Mechanics for 2024. I would like to thank our host, Professor K. Hanada. We hope that the international joint research at the Joint Usage of Research Centers for Applied Mechanics could continue to enhance China-Japan cooperation on fusion plasma research in the future.

My Co-Publications in 2024-2025:

(1) X.Gao et al., "ELM penetration and ITB collapse in EAST hybrid discharges", 43rd ITPA-PEP meeting, Princeton, USA, April 23-26, 2024
(2) X.Gao et al., "ELM penetration in ITB plasma on EAST tokamak", 19TH INTERNATIONAL WORKSHOP ON H-MODE PHYSICS AND TRANSPORT BARRIERS, Mito, Ibaraki, Japan, September 24-27, 2024

(Signature)______________________________

(Name in print) Xiang Gao

国際化推進共同研究概要

No.17

[採択番号] 24NU-11

タイト ル： Turbulence characteristics beyond the critical magnetic field of a helicon discharge with reagrd to the heating frequency

研究代表者： KNAUER Stefan

所内世話人： MOON Chanho

研究概 要：

本研究では、ヘリコン放電の高い電離率と加熱機構の解明を目的とし、特に伝搬波の分散関係と加熱周波数の影響を調査した。PANTA装置を用いた実験により、臨界磁場の存在を確認し、それが加熱周波数に依存することを示した。また、放電の相転移も加熱周波数に依存することが明らかとなった。さらに、九州大学の研究者がGreifswald施設を訪問し、VINETA実験の構築に貢献するなど、国際共同研究を深化させた。

Turbulence characteristics beyond the critical magnetic field of a helicon discharge with regard to the heating frequency

KNAUER, stefan; University of Greifswald, Physics department; Researcher
Grant number 24NU-11

Abstract

The high ionization rates of helicon discharges and their heating mechanism are not understood to this day. A key piece to this understanding is the dispersion relation of the propagating wave. Effects of the dispersion relation also relate to a rarely studied parameter of the wave, its frequency. The influence of the heating frequency on the critical magnetic field, where the discharges is expected to exhibit increased turbulence is investigated in this research.

Purpose

Last year we successfully confirmed the existence of a critical magnetic field B_c, postulated by Kwak et al. [1] at PANTA [2]. Going beyond the work of Kwak we furthermore demonstrated a dependency of B_c on the heating frequency f_H. PANTA allows us to study the influence of the f_H on a helicon discharge, which is a unique feature of PANTA. In addition to the dependence of B_c on f_H we furthermore demonstrated that also phase transitions of the discharge are dependent on f_H too. The results are very promising and are currently prepared to be published. Further developments on this subject can be found in the report by Nils Fahrenkamp grant number 1-24NU-8. Additionally we deepened our collaboration by having a visit of Prof Moon from KYUSHU Unv at the Greifswald facility. His comprehensive knowledge of linear plasma devices and years of experiences with PANTA are a great help to set up our experiment VINETA.

Methods & Results

The PANTA (fig1) experiment consists of a NAGOYA-III antenna, an approximately 4m long and 45cm in diameter vacuum vessel, 17 coils to create the magnetic field see fig. 1.

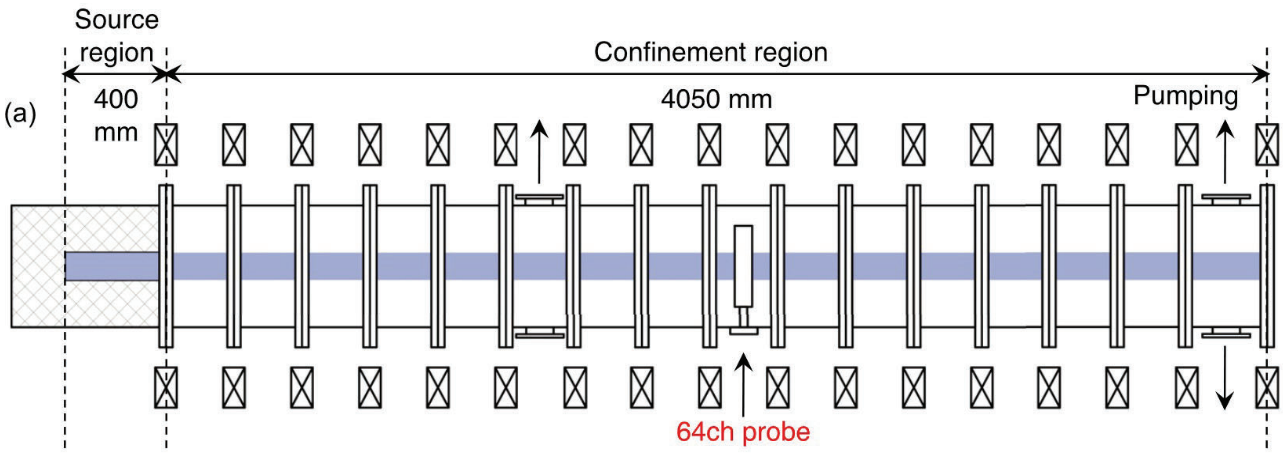

Figure 1: Scheme of the PANTA experiment. Source at the left, termination plate at the right. Crossed boxes indicate field coils. The utilized probe array is placed approximately in the center.

A very comparable set up is about to go into operation in Greifswald. Operational parameters are very similar to the PANTA experiment. VINETA is approximately 5m long and 0.4m in diameter. It has up to 6kW heating power at 13.56MHz and a magnetic field strength of up to 80mT. Putting both experiments into operation will allow us to compare results and exchange equipment, especially probe set ups. Prof Moon is an expert in probe operation and we look forward to profit from him. He will assist us in planning the operation of VINETA and the set up e.g. of measurement systems and data handling. He can pass his experience on and tell us about failures to avoid. Those would be the first steps of setting up our laboratory. Prof Moon has further knowledge about complex systems e.g. Thompson scattering systems and can give advice on how and when to implement such systems. Furthermore we set up a spark discharge/spheromac cannon experiment in Greifswald, maybe a similar system can be employed in PANTA. In the project with grant number 22_NU_0 we studied solitons and their dependence on temperature profiles. This can continued by the usage of ball pen probes, which Prof Moon has already used at PANTA and kindly provided us with sketches, plans and materials. Both experiments recently developed B_dot probes to study wave heating in their devices. By visiting us Prof Moon can compare our design with PANTAS. To further spark ideas and discussion we additionally invited Dr. Alf Köhn-Seemann, who can meet Prof Moon personally at this unique opportunity. Dr. Alf Köhn-Seemann is an expert in wave propagation simulations and has interest in working with the PANTA device. The preparations underway to incorporate advanced diagnostic equipment into the VINETA experiment at Greifswald is a development made possible through our continued collaboration with RIAM. Prof Moon and his equipment arriving in February together with guest from RIAM with the support of our grant, is expected to significantly enhance our ability to compare and contrast plasma phenomena between the two devices.

Fig 2: Discharge power supply that might be an inspiration for the spark injector at PANTA


Fig 3: equipment granted by Prof Moon to help kick off the measurements at VINETA.

Equipment shown fig.3 arrived just today, by an assistant of Prof Moon. We are very grateful for his continued assistance and the opportunity to collaborate with RIAM.

Fig 4: VINETA experiment in Greifswald to compare results with PANTA

[1] J. G. Kwak, H. D. Choi, H. I. Bak, S. Cho, J. G. Bak, and S. K. Kim, Physics of Plasmas 4, 1463 (1997).

[2] T. Yamada, S.-I. Itoh, T. Maruta, N. Kasuya, S. Shinohara, Y. Nagashima, M. Yagi, K. Terasawa, S. Inagaki, Y. Kawai, et al., Plasma and Fusion Research3, 044 (2008).

国際化推進共同研究概要

No. 18

24NU-12

タ イ ト ル： High power mm wave transmission line technology for advanced fusion devices

研究代表者： LECHTE Carsten

所内世話人： 出射　浩

研 究 概 要： 大電力ミリ波によるプラズマの不安定性抑制に向けた高速スイッチシステムの開発を進めている。これまで起きていた大電力試験時のアーキングを抑制するため、昨年度にインストールした新たな共振器ミラー６枚、ミリ波吸収フレームを用い、高電力試験を行なった。新たなアプローチ・エージング運転でアーキング頻度が抑制され、昨年度、低電力試験で得られていた良好な動作を高電力試験で達成した。高電力試験で必要なドリフトする動作周波数に応じた制御に成功し、安定した動作を実現した。

Report of international collaboration 2024NU-12 between RIAM and IGVP in FY2024: High power mm wave transmission line technology for advanced fusion devices

Mr. Dr. Carsten Lechte

Introduction: The MQIV diplexer developed at IGVP is a fast switch, power combiner, and mode filter for megawatt power 170 GHz millimeter waves using a Fabry-Perot resonator in a compact box design that is vacuum capable and can be directly interfaced with the 63.5 mm ITER ECRH waveguides which are available at QST. The device has 2 input and 2 output ports, which are connected as shown in Fig. 1. Our technical partners at TNO in the Netherlands have designed and built a fast mechanical tuning control unit for the device that is also vacuum-compatible.

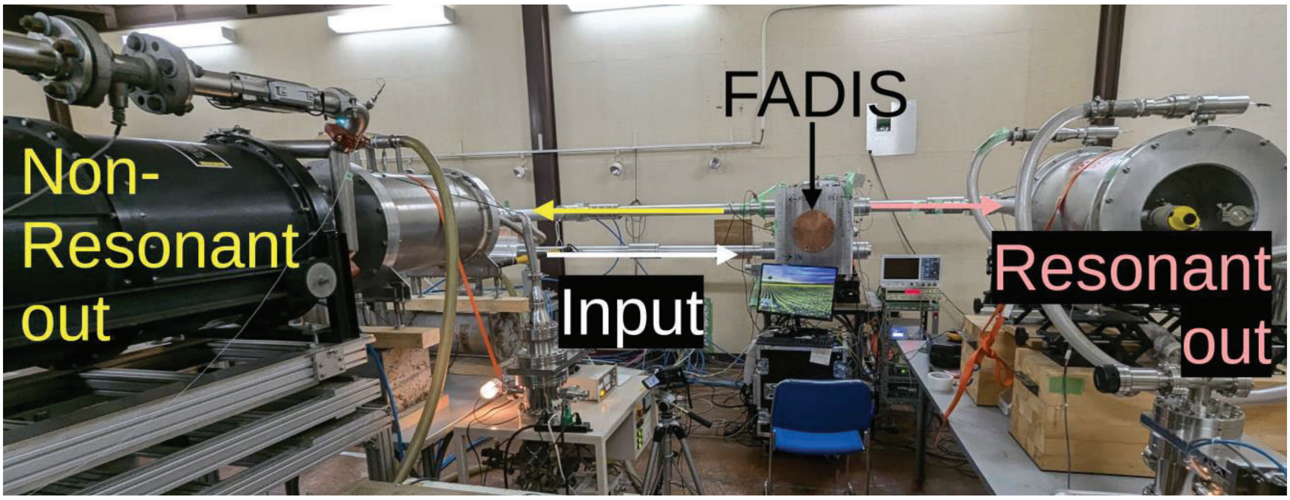

Fig 1: Diplexer integration into the test stand at QST. The input power is provided by a gyrotron. Both outputs are terminated by water-cooled dummy loads.

Previous high-power tests have demonstrated the switching capability of the device, but also highlighted problems with arcing and stray radiation. Both are believed to have been fully addressed in 2023.

After preparations in February 2024, high power tests at QST were performed in October 2024.

Arc mitigation: The mirror surfaces had been put into a “known-good” state with a galvanically deposited copper layer on the 4 surfaces of the main resonator, which were then re-machined back to the design shape. However, continuous low-level arcing was observed during all high-power tests.

Mechanical switching control: The promise of the fast mechanical tuning is to make the resonant frequency of the diplexer follow the gyrotron frequency evolution, and to compensate for any thermal detuning of the device. Fig. 2 shows the measured output frequency of the gyrotron source. The frequency changes by about 40 MHz. For comparison, the resonance of the diplexer is about 20 MHz wide, which makes it necessary to shift the resonance frequency of the diplexer in real-time. This is achieved by moving one of the resonator mirrors by fractions of a millimeter, thereby changing the length of the beam path in the resonator.
The requirements for tuning are less stringent if the goal is to keep the output in the non-resonant port all the time, since the distance between resonances is several 100 MHz.

Results: Fig. 3 shows a 5 second pulse of 200 kW with mechanical tuning to follow the frequency chirp of the input and putting ideally 100% of the power into only the resonant output. The pulse length was only limited by the temperature rise of the uncooled diplexer mirror surfaces.
The real-time frequency measurement shown in Fig 3 (bottom) is used for feed-forward control of the mirror position, shown in Fig 3 (top).
As can be seen in Fig. 3 (middle), the power fraction going into the resonant output is >90% except in the first second. The two signals are not on the same scale, so they do not add up to a constant. Furthermore, the power signals are quite noisy, which is why they are not at the moment used for feedback.
Throughout the pulse, a level of arcing was observed on the coupling gratings by means of a camera looking through one of six plexiglas viewports. The light level was steady and increased when the diplexer was in resonance. After the campaign, the mirror surfaces were inspected and superficial traces of the arcing were found.

Summary: Successful high-power tests of the diplexer were performed at QST. Full mechanical control was sustained for a 5s pulse with varying frequency, during which the power was kept in the resonant output port.

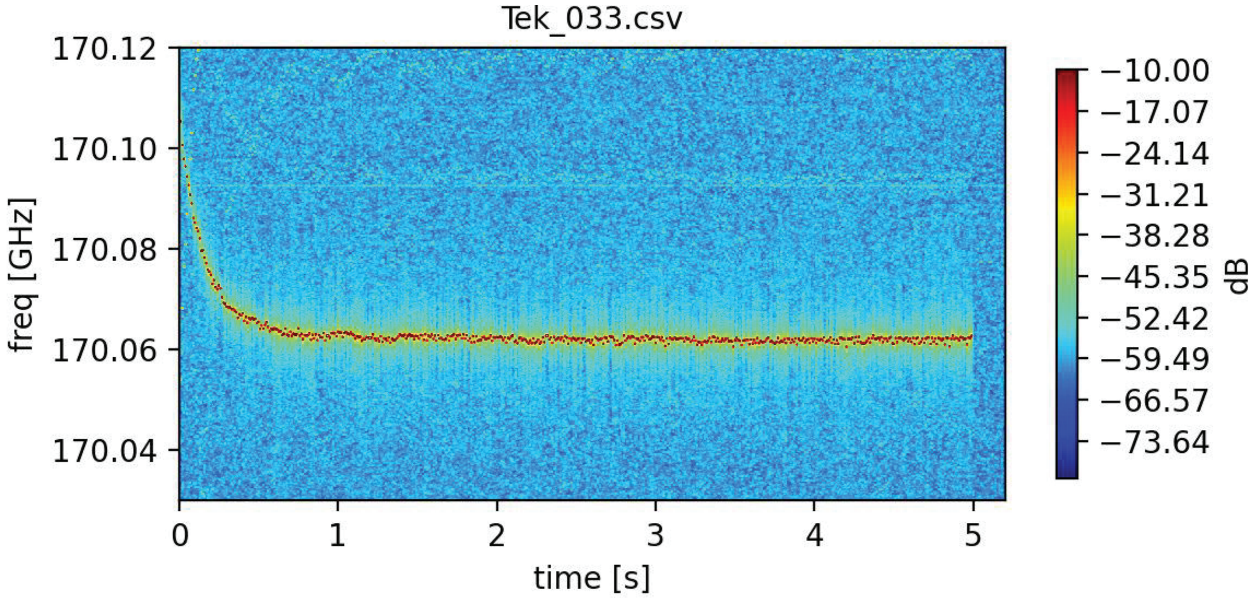

Fig. 2: Frequency spectrogram of the gyrotron output. After about 1s, thermal equilibrium of the resonant cavity is reached and the frequency stablizes.

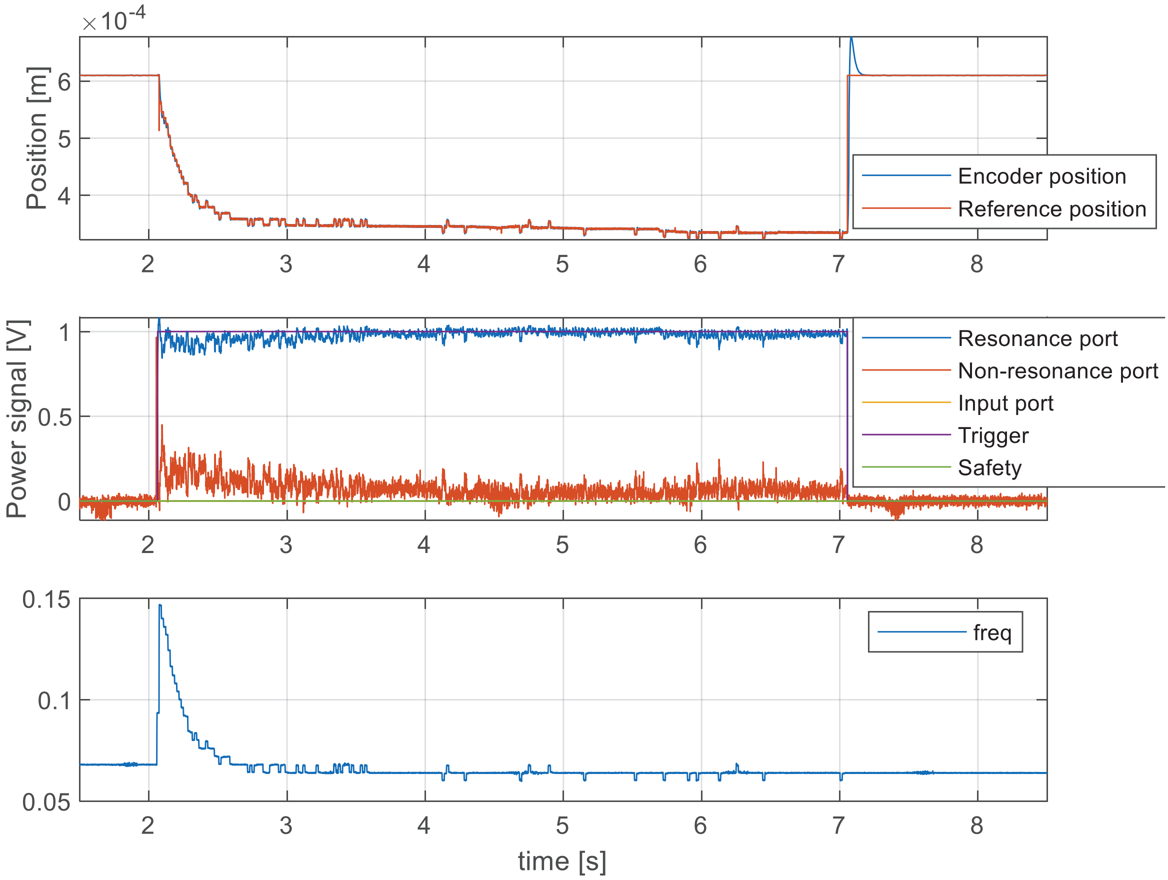

Fig. 3: The 5s shot with power going into the resonant output. Top: Position of the tuning mirror, middle: power fraction in resonant and non-resonant port, bottom: measured frequency signal used for feed-forward.

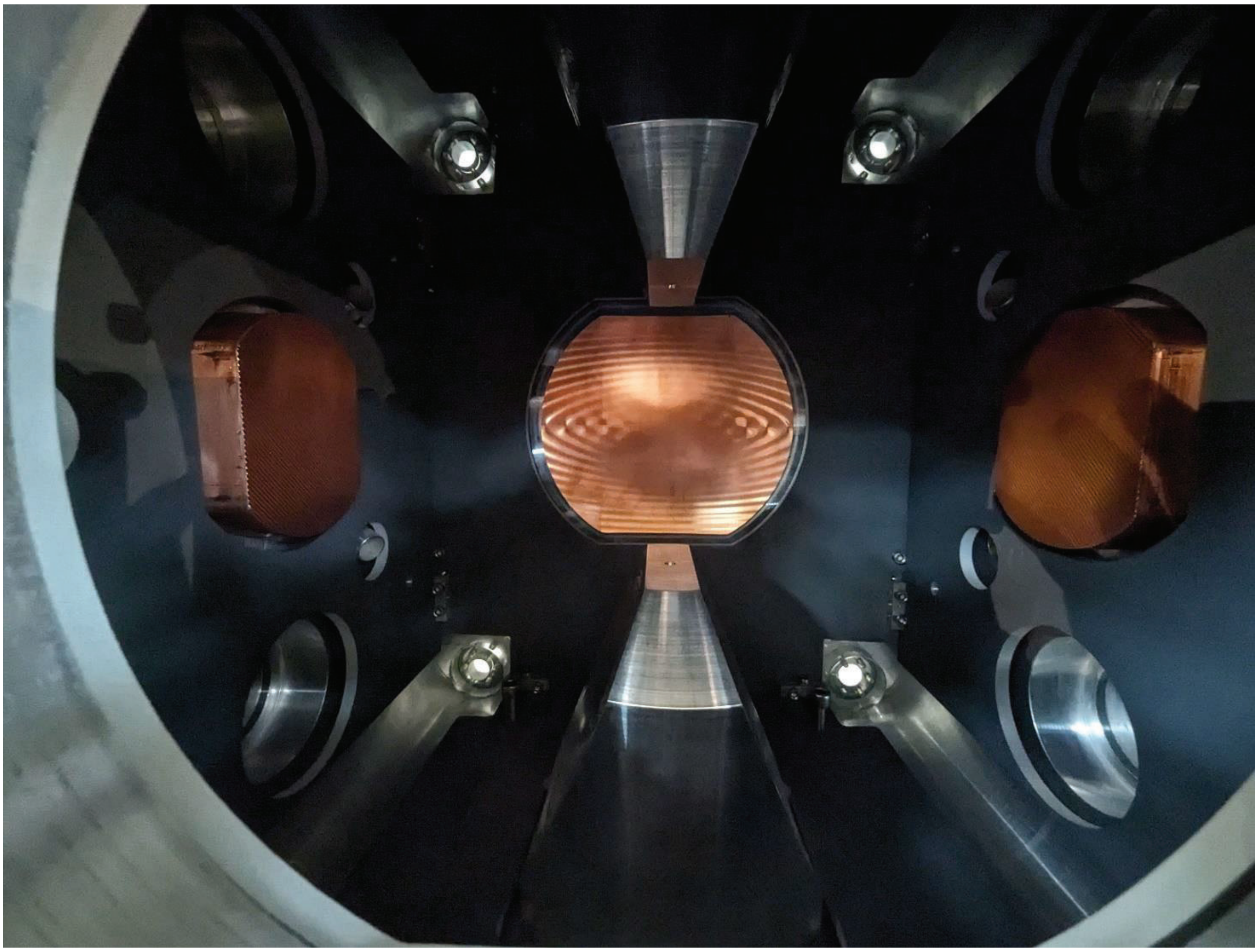

Fig. 4: The inside of the diplexer, viewed through the hole of the fixed resonator mirror, which was removed.

国際化推進共同研究概要

No.19

[採択番号]　24NU-13

タイトル：PLATO Tokamak startup experiments utilizing flux ropes

研究代表者：Park, JongYoon

所内世話人：MOON Chanho

研究概要：

本研究では、磁化プラズマカラム（フラックスロープ）を利用して、PLATOトカマク内でプラズマ電流を駆動することを目的としている。そのために、VESTやPEGASUSで使用されているアークプラズマガンを設計し、RIAM 2023国際共同研究により開発を完了した。2024年の研究では、PLATOの電源系統の保守や真空システムの不備により設置ができなかったが、最適な設置位置の検討と磁場計算を実施した。その結果、2カ所の設置候補を選定し、PLATOのコイル配置を基にVESTの磁場計算コードを用いた磁場解析を行った。

PLATO Tokamak startup experiments utilizing flux ropes

JongYoon Park (Seoul National University, Seoul, South Korea)

In plasma physics, a magnetized plasma column is referred to as a flux rope. This simple plasma structure is commonly observed on the Sun [1] and is widely utilized in plasma physics research, spanning from fundamental studies on ideal instabilities [2] to fusion research [3]. This study aims to employ flux ropes to initiate and drive plasma currents in the PLATO tokamak. To achieve this, a device capable of generating flux ropes with various plasma parameters (such as current, voltage, density, and temperature) under different external conditions (vacuum or plasma) within PLATO in a stable manner is required. To address this need, I designed an arc plasma gun [5] similar to those used in VEST at Seoul National University and PEGASUS at the University of Wisconsin [6]. The development of this arc plasma gun was successfully completed in 2023 through the RIAM 2023 International Joint Research program. This year, the primary objective is to install the arc plasma gun inside PLATO and commission it under various magnetic field configurations. The final goal is to utilize the arc plasma gun to drive plasma currents.

Figure 1. (Left) Developed plasma gun for PLATO during 2023 RIAM international joint research, (Right) Me and the gun delivered to PLATO team

Research Activities

Unfortunately, during the 2024 joint research year, the first step of the research plan—the installation of the arc plasma gun inside PLATO—could not be carried out due to the maintenance of the power system for the magnetic field and the absence of a vacuum system in PLATO. Instead, discussions were held regarding the optimal locations for the arc plasma gun. Following this, based on the operational results of the arc plasma gun at VEST and the similarities in coil configuration, the initial magnetic field calculations were conducted.

The most promising locations for the arc plasma gun were selected based on feasible operational scenarios in PLATO. The possible operations include: 1)Pre-ionization: Arc seed plasma for ohmic discharge, 2) Non-inductive current drive: Helicity injection, 3) Combined operation: Integration with ohmic heating.

Two locations capable of supporting all three operational modes were chosen, as shown in Fig. 2. The first location is #1 Lower-Corner at (R, Z) = (0.67, -0.41), and the second is #2 Lower-Mid at (R, Z) = (0.87, -0.32). It should be noted that depending on the magnetic field strength and direction, these locations may be adjusted to Upper-Corner or Upper-Mid positions. Additionally, the gun holder was designed and developed by the PLATO team in collaboration with me, as illustrated in Fig. 3.

Subsequently, magnetic field calculations were performed using the VEST field calculation code, which is written in MATLAB. As previously mentioned, the calculation locations and configurations were determined by scaling PLATO's coil locations in reference to VEST. For instance, the actual outer PF coil position in PLATO closely resembles that of VEST, making it feasible to perform field calculations. The results are presented in Fig. 4. The selected magnetic field configuration corresponds to a successfully operated scenario for DC helicity injection in VEST (Shot #35964).

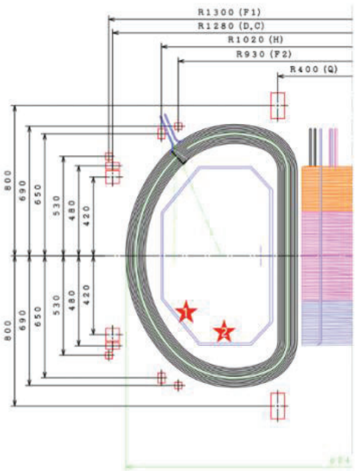

Figure 2. Two possible locations of arc plasma gun **Figure 3. Developed Gun Holder for PLATO**

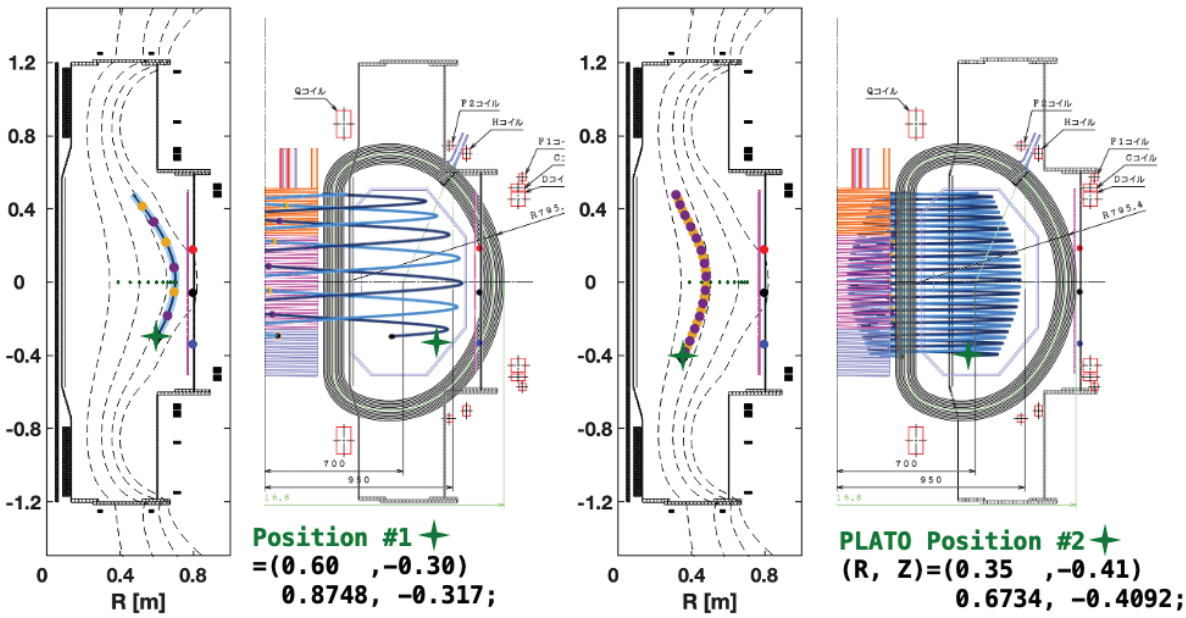

Figure 4. The field following calculation for (Left) Location #1, (Right) Location #2.

Discussion

The magnetic field profiles for the two selected locations have been successfully calculated for PLATO. The results indicate that both seed plasma generation and startup for Ohmic operation are feasible in PLATO. The field-following results presented in Fig. 4 are highly promising, particularly in terms of the formation of the current sheet.

However, the placement of the plasma gun cannot be determined solely based on calculations, as it will have significant implications for future applications. Therefore, experimental validation is required. One key difference between VEST and PLATO is the device size; VEST, as a spherical torus, has a shorter major radius. Since the operation of the plasma gun is highly dependent on its positioning, unlike in VEST, the gun in PLATO will be placed near the outer wall. Consequently, the precise selection of the gun's location and the configuration of vacuum magnetic fields will be critical tasks for the next phase of research.

Reference

[1] Kronberg P P 2002 Intergalactic magnetic fields Phys. Today 55 40–1

[2] Furno, I., et al. "Current-driven rotating-kink mode in a plasma column with a non-line-tied free end." Physical review letters97.1 (2006): 015002.

[3] Park, Jong Yoon, et al. "Identification of kink instability in 3D helical flux ropes at VEST." Physics of Plasmas 29.5 (2022).

[4] Hwang, Yong-Seok. Studies of non-inductive current drive in the CDX-U tokamak. Princeton University, 1993.

[5] Fiksel, G., et al. "High current plasma electron emitter." Plasma sources science and technology 5.1 (1996): 78.

[6] Hinson, Edward Thomas, et al. "Impedance of an intense plasma-cathode electron source for tokamak startup." Physics of Plasmas 23.5 (2016).

国際化推進共同研究概要

No.20

[採択番号] 24NU-14

タイト ル： Kinetic flux rope formation and relaxation on PANTA

研究代表者： YOON Young Dae

所内世話人： MOON Chanho

研究概 要：

本研究では、九州大学とAsia Pacific Center for Theoretical PhysicsのYoung Dae Yoon博士との共同研究活動について報告する。2025年1月7日から9日には、Yoon教授がPOSTECHで開催されたワークショップに参加し、診断技術に関する発表と活発な議論を行った。また、1月20日から26日には九州大学を訪問し、PANTAおよびQUESTの見学を実施した。さらに、PANTAにおけるレーザー誘起蛍光診断の可能性を調査し、レーザーのファイバーカップリングと集光光学系の設置が次のステップとして進められる予定である。

Kinetic flux rope formation and relaxation on PANTA

Young Dae Yoon, Asia Pacific Center for Theoretical Physics

This report details activities conducted between Kyushu University and Dr. Young Dae Yoon of Asia Pacific Center for Theoretical Physics. There have been two main research activities, namely the participation in POSTECH-Kyushu Joint Workshop, and Dr. Yoon's visit to Kyushu University to probe the possibility of reviving the laser-induced fluorescence diagnostics on PANTA.

1. Dr. Yoon participated in the POSTECH-Kyushu University Joint Workshop on Probe Diagnostics, held at POSTECH during 7-9 January 2025. This workshop involved several talks regarding diagnostics methods, including talks by Drs. Gunsu Yun of POSTECH, Chanho Moon of Kyushu University, Sooseok Choi of Jeju National University, and Kil-Byoung Chai of Korea Atomic Energy Research Institute. Some other participants included Dr. Andreas Bierwage of QST and Dr. Gyunjin Choi of KAIST. Fruitful discussions were had, including opportunities for collaboration.

2. Dr. Yoon also visited Kyushu University during the 20-26, January, 2025. He toured various devices such as PANTA and QUEST. He also examined the laser-induced fluorescence diagnostics on PANTA and operated the laser up until fiber coupling. Next steps would be to fiber-couple the laser and set up collection optics for the diagnostic to be fully functional.

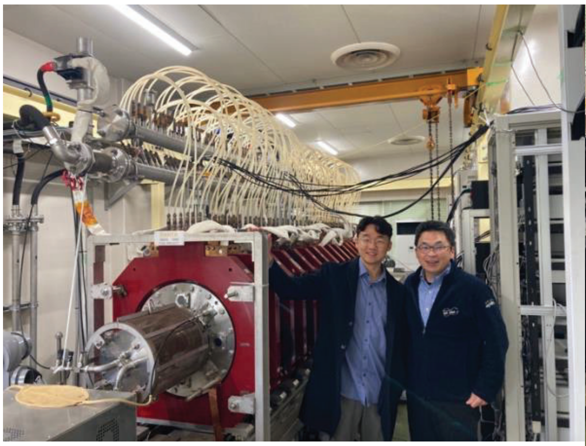

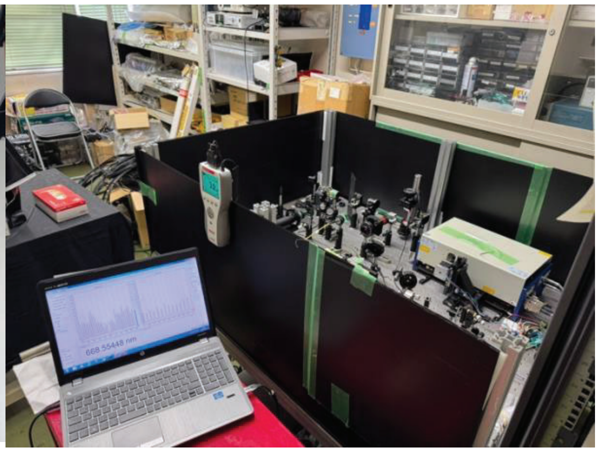

国際化推進共同研究概要

No. 21

[採択番号]　24NU-15

タイト ル： Three-dimensional electromagnetic particle-in-cell simulation for the instabilities in the magnetized plasmas

研究代表者： LEE　Hae June

所内世話人： MOON Chanho

研究概 要：

本研究では、PANTA装置を用いた実験とシミュレーションの比較により、磁化プラズマにおける輸送現象や乱流の特性を解析する。ラングミュアプローブアレイ、ボールペンプローブ、トムソン散乱、トモグラフィーなどの多様な診断手法を駆使し、プラズマ密度・温度・電位の時空間変動を詳細に測定する。得られた実験データを数値シミュレーションと照合することで、不安定性の発生メカニズムやプラズマダイナミクスの理解を深めることを目的とする。

Three-dimensional electromagnetic particle-in-cell simulation for the instabilities in the magnetized plasmas

Haejune Lee, Hanshin Cheong

Department of Electrical Engineering, Pusan National University, Busan 609-735, Korea

1) Introduction

Plasma parameters (i.e, electron temperatuere, plasma density, plasma potential, larmor radius etc..)are most important factor for plamsa physics and charged particle dynamics in magnetically confined plasmas. PANTA device provides an optimized experimental environment with linear cylindrical geometry of magnetized plasma and multiple diagnostics to study the plasma physics. For example, plasma density flcutuation and turbulence as plasma shear effect and ETG mode are generated in linear plamsa device by magnetic field(axial B-field). So, plasma diagnostics already investigated using Langmuir probe array, Ball-pen probe, Tomson scatter, Tomography and so many other electrical devices. These measuring instruments are very powerful tools for studying plasma dynamics and plasma turbulence in a steady state. Simulations are a powerful tool for studying the causes of perturbations or turbulence in a plasma through real-time charged particle dynamics that change with a very small time step. Overall, we will compare the results of the experiments and simulations to understand the instability and plasma dynamics inside the actual magnetised plasma.

2) Method

First of all, our goal is to implement the geometry and source of the cylindrical plasma device in the simulation domain. To solve the numerical error problem of the simulation that occurs near r = 0 in the cylindrical coordinate system, the entire system uses the Cartesian coordinate system. In order to implement the effect of the curved surface of the actual device in the simulation, geometry was implemented using the Ghost Fluid Method (GFM) technique[1]. Next, the magnetic field was set to a constant in the z-direction. This is because, although there is actually a slight error, the Helmholtz coil method is used to obtain a nearly uniform value. The plasma in the source part is a form of helicon plasma using a magnetic field, and the implementation of this part is technically quite difficult, so we first assumed that the particles (electrons and ions) would have a Gaussian distribution in the axial direction and proceeded with the simulation. The Maxwell velocity distribution was also used for the velocity distribution. In order to reflect the actual plasma entering the chamber, the flux and density distribution of electrons and ions in all the spaces where the source and the vacuum chamber part of the PANTA are connected are required. Therefore, we will discuss this little more with Professor. Chan-ho Moon. The inner wall of the chamber is ground, so particles that hit the boundary surface outside the simulation area ($r \geq 7.5$cm) are removed using a method to prevent the plasma density from increasing infinitely.

3) Result

To compare whether the data from the PIC simulation is similar to the experimental results from the PANTA device, we needed plasma data measured by the probe. We conducted the experiment based on the understanding of the probe analysis system, ballpoint pen probe, and probe array that Professor. Chan-ho Moon taught us last time. Figure 1 shows the values for the PANTA experiment measured by HanShin Cheong.

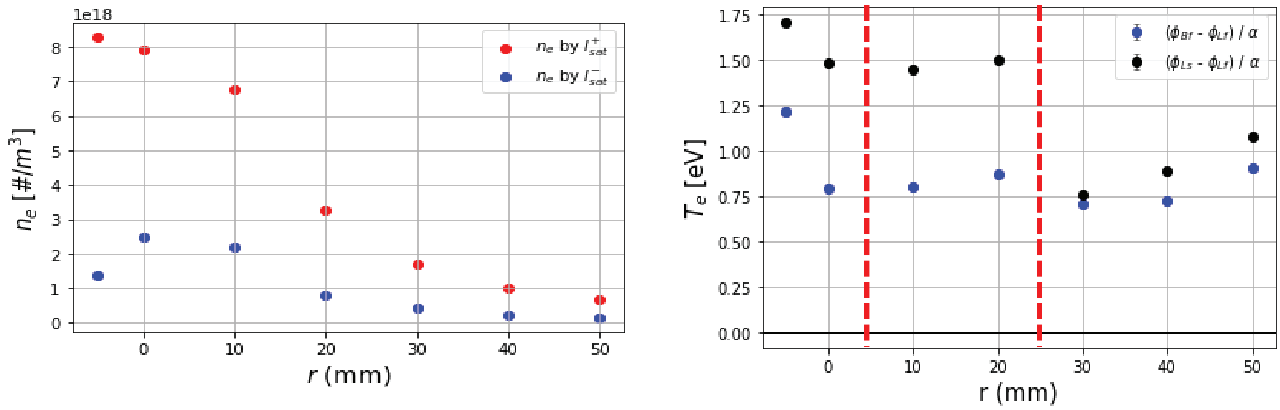

Fig.1 Result of plasma density profile by Ball-pen probe(left) and electron temperature by Ball-pen probe(right).

Figure 1 shows the plasma parameters, electron and ion densities, and electron temperatures measured with the Ballpen probe. The density of electrons shows a slightly different trend than that of ions, with the relatively lighter electrons showing a hall-profile rather than a Gaussian distribution at the center compared to ions. This can be expected to be due to the induced electric and magnetic fields inside the plasma, which drive electrons outward near the center and inward near r=1-2 cm, resulting in density peaks in regions other than the center, which are affected by shear.

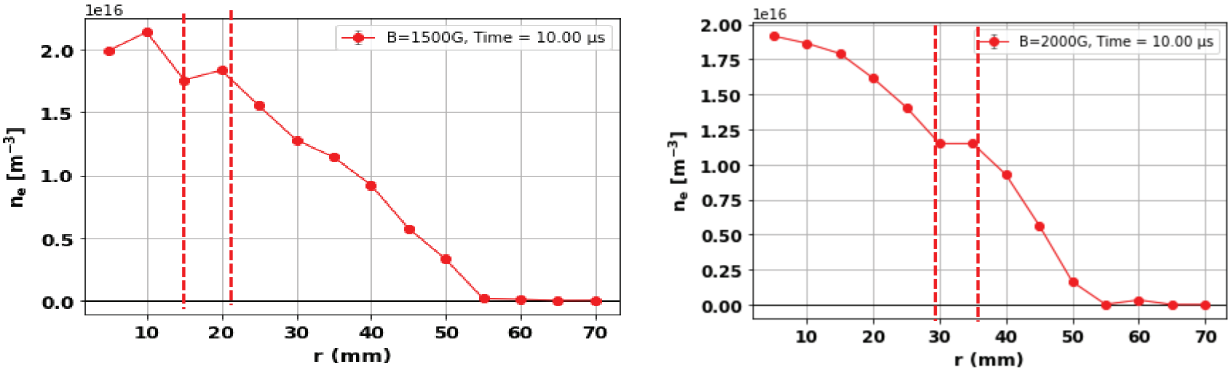

Fig.2 Result of *r*-direction plasma density profile by PIC simulation, B = *1500*G (left) and B = *2000*G (right).

The results of the simulation also show similar results. In Fig.2 , the stronger the magnetic field, the more the region where the density deviates from the normal Gaussian distribution is pushed outward, but it is located in a region similar to that shown in the experimental results. It is necessary to compare the data values by conducting experiments with density distribution in the r-direction from various angles and at a slightly finer interval to see whether the shear effect affects the formation of plasma density by reducing the speed of the **E**x**B** drift affected by the strength of the magnetic field.

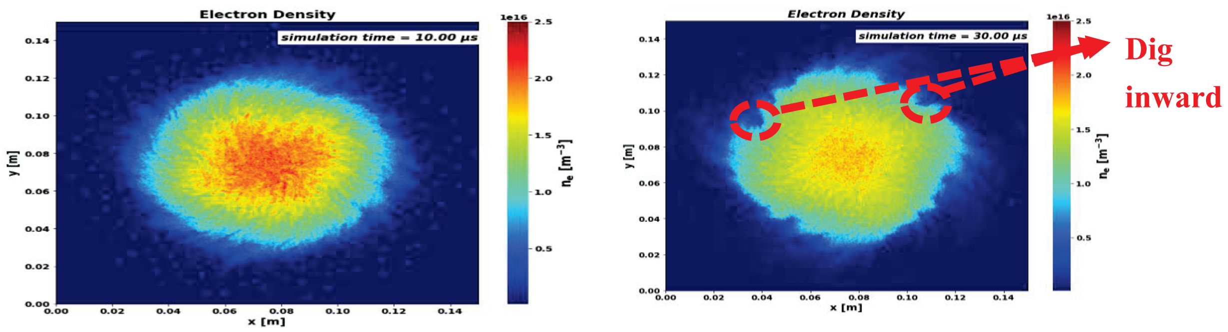

Fig.3 Result of *x-y* domain plasma density distribution by PIC simulation

As is well known, the distribution of plasma density due to the magnetic field is shown as rotating clockwise. This indicates that the results of the simulation are somewhat reliable. However, it is necessary to further study the effect of the density distribution shown in Figure 3 on the depressed area.

4) Future work

In the future, we plan to conduct international joint research with Kyushu University's RIAM to study the nonlinear turbulent characteristics and plasma dynamics of helicon plasma using the PANTA device. In addition This study was conducted in a 2-D simulation, but in the future, the scope will be expanded to include 3-D simulations to see the effects in the z-direction. Ultimately, we plan to simulate the environment as close as possible to the device by implementing a plasma source using the plasma flux value entering the PANTA vacuum chamber. After that, we will study the shear effect and turbulent characteristics through changes in the plasma potential and electromagnetic field values calculated from the simulation, and continue to study the causes of plasma turbulence in linear devices and plasma dynamics through comparisons with the papers previously published by Professor. Chan-ho Moon.

References.

[1] H. Park, Y. Sakiyama and H. J. Lee, "Two-dimensional particle-in-cell simulation of electron heating effect in multiple hollow cathode trenches with curved boundary," Frontiers in Physics, vol. 11, pp. 1137994(2023)

国際化推進共同研究概要

No.22

[採択番号] 24NU-16

タイトル： Theoretical modeling and verification of slug dynamics in proxy SOL plasmas in PANTA

研究代表者： CHOI Gyungjin

所内世話人： MOON Chanho

研究概要：

本研究では、韓国・ソウル大学（SNU）と九州大学応用力学研究所（RIAM）による国際共同研究を通じて、SOL（スクレイプオフ層）乱流の解析的理論の実験的検証を目指した。トカマクSOLプラズマとPANTAプラズマの流入特性に着目し、パイプ流との類似性を活用して理論モデルを構築した。特に、SOL領域が乱流の限界安定性付近にあることを考慮し、パイプ流の運動方程式モデルがトカマクSOLおよびPANTAプラズマに適用可能であることを示した。

Theoretical modeling of slug dynamics in proxy SOL plasmas

Gyungjin Choi

Department of Nuclear Engineering, Seoul National University, Seoul 08826, Republic of Korea

SOL turbulence physics is a topic of emerging interest in both science and engineering points of view, as recently addressed advanced tokamak operation scenarios contain turbulent pedestals. The finite level of turbulence at the turbulent pedestal spreads out to the SOL region, and thus significantly increases radial heat diffusion, resulting in wider SOL width and divertor heat flux distribution. However, while experimental and simulation studies on SOL turbulence have been done continuously, analytic theory developments for SOL turbulence are rare. Therefore, we conducted joint international research between SNU and RIAM toward the final goal of experimental validation of developed analytic theory using the linear plasma device PANTA.

Our strategy is to extensively utilize an analogy among tokamak SOL plasma, PANTA plasma, and pipe flow, all of which shared the property of streaming inflow. In addition, the SOL region is usually not far from the marginal stability of turbulence, either subcritical or supercritical. This is like the case of pipe flow, where we routinely observe puff and slug structures that are symptoms of near-turbulence-marginality. Specifically, we realized that the momentum equation model for the pipe flow can be readily applied to tokamak SOL and PANTA plasmas.

$$\frac{\partial q}{\partial t} + U(u)\frac{\partial q}{\partial x} = V(q,u) + D\frac{\partial^2 q}{\partial x^2} + A\xi q, \qquad \frac{\partial u}{\partial t} + u\frac{\partial u}{\partial x} = W(q,u) + \nu\frac{\partial^2 u}{\partial x^2},$$

where q is the turbulence intensity, u is the mean flow velocity, ξ is the normalized stochastic noise and D and ν are the collisional diffusivity and viscosity. The issue is how to determine the turbulence spreading speed $U(u)$ and the potentials $V(q,u)$ and $W(q,u)$. We find that the simplest theoretical modeling for these is $U(u) = u - \xi$, $V(q,u) = q[r - (r+\delta)(q-1)^2]$ and $W(q,u) = W_0(U_0 - u) + W_1(U_1 - u)q$.

Then, to examine the model in real world for an iterative model development, we performed plasma experiments and diagnosed turbulence in PANTA. The k- and ω-spectra of turbulent fluctuation have been obtained where the information of turbulence wave velocity is contained, utilizing rotatable ten-channel Langmuir probe array.

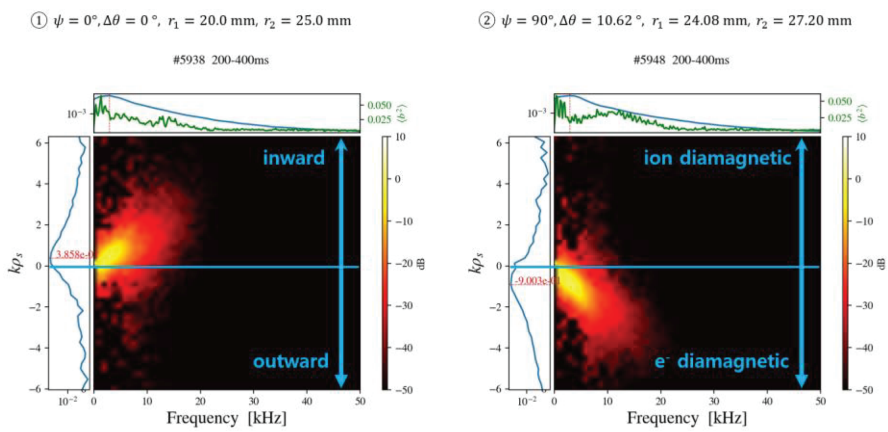

In the future collaboration, we are going to compare the drift wave propagation and turbulence spreading using the current model and the PANTA data, and improve theoretical model based on this experimental data analysis.

国際化推進共同研究概要

No.23

[採択番号] 24RE-1

タイトル： Steps to Digital Twins and Real-time Monitoring for floating offshore wind turbines

研究代表者： HU Zhiqiang

所内世話人： HU Changhong

研究概 要：

浮体式洋上風車のデジタル・ツインとリアルタイム・モニタリング技術の実現を目指して国際化推進共同研究プロジェクトを立ち上げ、今年度は初年度で、予定通り実施した。特に、浮体式洋上風車の動特性解析モデルの重要な要素である、浮体式洋上風車の係留システムの数学的モデリングに関する調査について成果を上げた。2024年11月25～27日に九州大学西新プラザにおいて開催された、所内世話人HUが主催した第1回アジア太平洋洋上風力発電技術会議に、「Time-Domain Integrated Analysis of Multi-Segment Mooring Systems for Floating Offshore Wind Turbines」のタイトルで共同利用成果を発表した。

Report for 2024 RIAM International Joint Research Project

[24RE-1]

Steps to Digital Twins and Real-time Monitoring for floating offshore wind turbines

Zhiqiang Hu
Marine, Offshore and Subsea Technology, School of Engineering, Newcastle University, UK

This collaborative research project between RIAM at Kyushu University and the Marine, Offshore, and Subsea Technology Group at Newcastle University was launched in 2024. Its goal is to develop technology for real-time monitoring of floating offshore wind turbines. The research outcomes are expected to offer a promising solution for the offshore wind industry by significantly reducing operation and maintenance costs and enhancing the feasibility of future offshore wind farms.

The research originated from the novel concept of SADA, initially proposed by Zhiqiang Hu's team at Newcastle University in 2020. The fundamentals of SADA and an engineering case study were introduced at the RIAM Symposium in 2021 and 2022, respectively. This project extends the SADA method to a further application stage by integrating a scouring model into the *DARwind* code, the core component of the SADA methodology. Additionally, the use of AI is planned to enhance the accuracy of predictions.

In 2024, the research team also completed an investigation into the mathematical modeling of the mooring system for floating offshore wind turbines, a critical component of the dynamic analysis model for FOWTs. Based on the research outcomes of the mooring system model, a paper was submitted to the APCOW 2024 conference organized by Kyushu University in Fukuoka.

Starting in 2024, Zhiqiang Hu led his research team at Newcastle University in developing a digital twin system for the monitoring and maintenance of floating offshore wind turbines (FOWTs). This research aims to address the challenges of reducing operation and maintenance costs while advancing digital twin technology for the offshore wind industry. The collaborative research outcomes achieved in 2024 are summarized below.

1) The 1st Asia-Pacific Conference on Offshore Wind Technology (APCOW 2024) was hosted by Kyushu University in November 2024. Mr. Jihuai Yang, a PhD student supervised by Zhiqiang Hu at Newcastle University, presented on the topic "Time-Domain Integrated Analysis of Multi-Segment Mooring Systems for Floating Offshore Wind Turbines." This paper showcased the latest research conducted by Jihuai Yang on mooring system modeling for FOWTs. The research was financially supported by the RIAM research project and co-authored with Prof. Changhong Hu of Kyushu University. Additionally, Zhiqiang Hu also attended the conference, chaired a session, and had part of his travel and accommodation costs covered by the project funding.

2) In 2024, the collaborative research focused on enhancing the efficiency and feasibility of the AI-based SADA method, a foundational element for developing a digital twin system for offshore wind turbine monitoring and operation. The SADA method was tested in combination with a wind-assisted propulsion model to validate energy-saving and CO_2 reduction capabilities. The AI training work has been completed, and significant research outcomes have been achieved. These findings will be included in a collaborative paper planned for submission to the ICSOS 2025 conference.

3) Based on the 2024 research, a collaborative conference paper titled "Time-Domain Integrated Analysis of Multi-Segment Mooring Systems for Floating Offshore Wind Turbines" was written and presented at the 1st APCOW 2024 conference. Furthermore, this conference paper will be expanded into a journal article, with plans to submit it to the Journal of Ocean Engineering in 2025.

In 2025, this collaborative research project will progress to the next stage, with a focus on establishing a digital twin system for the operation and maintenance (O&M) of offshore wind turbines. A key priority will be the enhancement of the SADA system, with particular emphasis on the deployment of neural layers, which will be of critical importance to its development.

国際化推進共同研究概要

No.24

[採択番号] 24RE-2

タイトル: Diffusion characteristics of dopants in GaN for enhanced III-nitride semiconductor technology

研究代表者: KEMPISTY Pawel

所内世話人: KUSABA akira

研究概要:

SiはGaNのn型ドーパントとして広く使用されている。その拡散挙動を解明するため、第一原理計算による拡散障壁の評価を行なった。フォノン計算によると、高温条件下でも障壁の低下は限定的であり、拡散は困難である結果を得た。この計算結果は、Siイオン注入後の高圧アニール実験において、Siの拡散が観測されなかったという最近の研究結果と一致している。また、ベイズ最適化による半導体構造探索の研究も進めた。この計算アプローチは、より複雑な欠陥構造(ドーパント-空孔配置)の研究に役立つと期待される。

Diffusion characteristics of dopants in GaN for enhanced III-nitride semiconductor technology

Pawel Kempisty, Institute of High Pressure Physics PAS

In 2024, our collaboration within the International Joint Research Program focused on two main topics. The first was the development of an atomic configuration optimization method and its validation using two-dimensional materials. This method is also expected to be applicable for optimizing dopant atomic configurations in GaN. The second was the investigation of the microscopic mechanism of donor dopant migration in GaN using first-principles calculations.

[TOPIC-1]

Objective: Hexagonal boron-carbon-nitride (h-BCN) is a graphene-like material where the atomic configuration strongly affects its bandgap. Understanding and optimizing stable configurations is essential for electronic applications. This study combines first-principles calculations with Bayesian optimization (BO) to efficiently explore energetically favorable atomic arrangements.

Methodology: A major challenge is the combinatorial explosion of possible configurations. To address this, a neighbor-atom encoding scheme was introduced, incorporating local atomic environments to enhance BO's search efficiency. Density Functional Theory (DFT) calculations were used to evaluate the stability of sampled structures, and band dispersion calculations were performed to analyze electronic properties.

Results & Discussion: Two stable stripe-like configurations were identified. The zigzag structure had a bandgap of 1.95 eV, while the armchair structure exhibited 1.05 eV, demonstrating the strong dependence of electronic properties on atomic arrangement. Principal Component Analysis (PCA) confirmed that BO efficiently captured structural features, optimizing the search space. This approach provides a scalable framework for exploring 2D materials with machine-learning-driven design.

[TOPIC-2]

Objective: Despite the widespread use of silicon as an n-type dopant in GaN, its diffusion behavior remains poorly understood, with experimental studies reporting conflicting results. Theoretical investigations on Si diffusion are scarce, particularly regarding vacancy-mediated mechanisms and crystallographic orientation effects, necessitating a detailed first-principles analysis to clarify the dominant diffusion pathways and reconcile experimental discrepancies.

Methodology: The study employs density functional theory (DFT) to model vacancy-mediated diffusion of Si in GaN. The Nudged Elastic Band (NEB) method was used to determine the minimum energy path (MEP) and migration energy barrier with high precision. Additionally, phonon calculations were performed to provide deeper insight into thermal effects. Next, a detailed estimation of the diffusion coefficient of Si in GaN for different crystallographic orientations was made, based on the principles of microscopic transition state theory, which describes atomic jumps between lattice sites.

Results & Discussion: The study confirms that Si diffusion in GaN should be negligible under typical conditions, as the energy barriers for this process are relatively high. For vacancy-mediated migration along

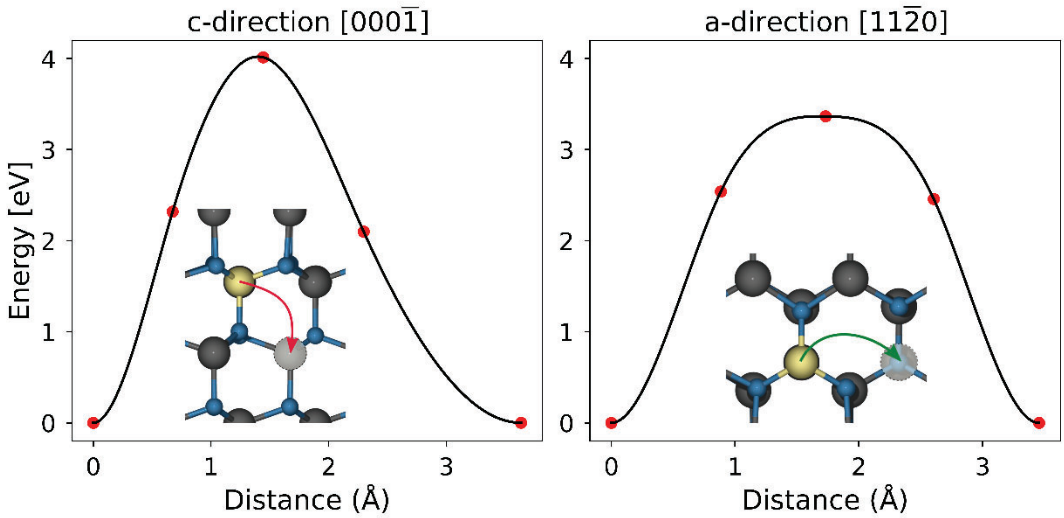

Figure 1. Energy barriers for Si atom vacancy-mediated migration in the metal sublattice of GaN

the a-direction, the energy barrier is slightly lower than that for the c-direction, e.g., 3.4 eV vs. 4.0 eV, respectively, as shown in Fig. 1. Phonon calculations indicate that these barriers slightly decrease at high temperatures, but by no more than 0.3 eV. Therefore, even considering a high vacancy concentration (e.g., 10^{18} cm^{-3}) required for this process, the diffusion coefficient is expected to be very low - specifically, lower than 10^{-14} cm^2/s for temperatures below 1500°C. Other diffusion schemes yield even lower diffusion coefficients, as the migration energy barriers are significantly higher. For example, in the direct Si-Ga swap mechanism, the barrier height exceeds 12 eV. This theoretical description of diffusion is fully consistent with recent findings from UHPA annealing experiments following Si ion implantation into GaN, where no silicon diffusion beyond the implantation region was detected.

Measurable effects of participation in the programme

List of publications:

[1] K. Kawka, P. Kempisty, K. Sakowski, S. Krukowski, M. Bockowski, D. Bowler, A. Kusaba; *J. Appl. Phys.* **135**, 225302 (2024).

[2] Y. Kangawa, A. Kusaba, T.Kawamura, P. Kempisty, K. Ishisone, M. Boero; *Cryst. Growth Des.* 25, 3, 740-746 (2025)

[3] T. Hara, A. Kusaba, Y. Kangawa, T. Kuboyama, D. Bowler, K. Kawka, P. Kempisty; arXiv:2411.04758 [cond-mat.mtrl-sci].

国際化推進共同研究概要

No.25

[採択番号]　24RE-3

タイトル：Comparative Study on Wave Energy Gathering Performance of Parabolic Breakwaters Based on HAMS Model and Boussinesq Equation Model

研究代表者：GAO JUNLIANG

所内世話人：劉　盈溢

研究概要：港湾周辺における波力エネルギーの活用が注目されている。港内に周期的な潜堤を配置することで、港湾保護と波力エネルギーの集積が可能となり、エネルギー変換効率の向上が期待される。なお、港湾周辺海域は、強い非線形波動条件と変化する海底地形が特徴である。本研究では、数値実験を通じて、港内の波場に対する潜堤の遮蔽効果および港外における波力エネルギー集積性能を解析し、波力エネルギーの効率的利用に資する知見の獲得を目指す。

掲載論文：

[1] Gao, J.L., Hou, L.H., Liu, Y.Y. & Shi, H.B (2024). Influences of Bragg reflection on harbor resonance triggered by irregular wave groups. Ocean Engineering, 305, 117941.

[2] Song, Z.W., Mi, C.L., Zhou, Z.B., Gao, J.L. & Liu, Y.Y (2024). Two-dimensional viscous study of coupled nonlinear fluid resonances in two narrow gaps. Physics of Fluids, 36, 103112.

[3] Gao, J.L., Mi, C.L., Song, Z.W. & Liu, Y.Y (2024). Transient gap resonance between two closely-spaced boxes triggered by nonlinear focused wave groups. Ocean Engineering, 305, 117938.

[4] Gong, S.K., Gao, J.L., Song, Z.W., Shi, H.B & Liu, Y.Y (2024). Hydrodynamics of fluid resonance in a narrow gap between two boxes with different breadths. Ocean Engineering, 311, 118986.

Introduction

The process of extracting wave energy typically involves three stages (Zhang et al., 2013). The first stage involves the wave energy converter, which captures the wave energy and maintains its motion. The second stage consists of an intermediate conversion device, which transforms the kinetic energy absorbed by the wave converter into usable mechanical energy. The third stage is the power generation system, where mechanical energy is converted into electrical energy by a generator.

Although significant progress has been made in wave energy extraction over the past few decades, along with promising prospects for its application, challenges remain, particularly in terms of the relatively low conversion efficiency. As a result, considerable efforts have been made to improve the conversion efficiency, both mechanically and electrically. Various specialized mechanical devices have been designed and tested in preliminary trials.

However, the potential for increasing wave energy density in coastal areas for wave power generation has often been overlooked, since traditional thinking assumes that wave height in these areas is naturally determined. Consequently, most efforts have focused on identifying sea areas with high wave energy density and enhancing the conversion efficiency of wave energy devices. Paradoxically, the sea areas with the highest wave energy densities are typically located far from the coast, making it costly to install the necessary power transmission infrastructure. In contrast, shallow coastal regions, which are closer to shore, tend to have lower wave energy densities than deeper offshore areas.

Since the 1980s, extensive studies have been conducted on the water surface waves scattered by periodically changing seabed topography, among which the most concerning phenomenon is the so-called "Bragg resonant reflection" of the water surface waves (e.g., Davies (1982); Ding et al. (2024); Liu and Cho (1993); Mahmoudof and Takami (2022); Ni and Teng (2021); Peng et al. (2019)). When the wavelength of the water surface waves is about twice that of the periodically changing seabed topography, most of the incident wave energy would be reflected by the periodically changing topography, and hence, the wave energy transmitted into the coastline would remarkably decline and the the wave energy at the offshore would remarkably increase (Liu et al., 2023; Xu et al., 2023).

In this study, the coupling interactions between the periodic seabed topography, the harbor, and incident irregular wave groups were investigated for the first time. The periodic seabed topography in this article is mimicked by sinusoidal bars that have been commonly used in the investigations of the Bragg resonant reflection phenomenon (e.g., Fang et al. (2024a, 2024b); Mei et al. (1988); Peng et al. (2019)). Both the shielding effect of periodical submerged embankments on the wave field inside the harbor and the wave energy reflection/gathering performance of periodical submerged breakwaters for the incident irregular waves outside the harbor were discussed.

Methodology

Governing equations

All numerical simulations in this paper are implemented by adopting a fully nonlinear Boussinesq-type model, FUNWAVE 2.0, developed at the University of Delaware by Kirby et al. (2003). The finite difference scheme is utilized to discretize and solve a set of fully nonlinear Boussinesq equations proposed by Wei et al. (1995), and a moving reference level, as performed in Kennedy et al. (2001), is also introduced in this model. This numerical model has been extensively utilized to simulate wave propagations, transformations, and evolutions from the offshore to the coastal zones in coastal/offshore engineering and oceanography communities.

The control equations of the numerical model can be formulated as

$$\eta_t + \nabla \cdot \mathbf{M} = 0, \tag{1}$$

and

$$\mathbf{u}_{\alpha t} + (\mathbf{u}_\alpha \cdot \nabla)\mathbf{u}_\alpha + g\nabla\eta + \mathbf{V}_1 + \mathbf{V}_2 = 0, \tag{2}$$

where

$$\begin{aligned}\mathbf{M} = {} & (h+\eta)\mathbf{u}_\alpha + (h+\eta)\cdot\left[\frac{z_\alpha^2}{2} - \frac{1}{6}(h^2 - h\eta + \eta^2)\right]\nabla(\nabla\cdot\mathbf{u}_\alpha) + \\ & (h+\eta)\left[z_\alpha + \frac{1}{2}(h-\eta)\right]\nabla\left[\nabla\cdot(h\mathbf{u}_\alpha)\right],\end{aligned} \tag{3}$$

$$\mathbf{V}_1 = \frac{z_\alpha^2}{2}\nabla(\nabla\cdot\mathbf{u}_{\alpha t}) + z_\alpha\nabla\left[\nabla\cdot(h\mathbf{u}_{\alpha t})\right] - \nabla\left[\frac{1}{2}\eta^2\nabla\cdot\mathbf{u}_{\alpha t} + \eta\nabla\cdot(h\mathbf{u}_{\alpha t})\right], \tag{4}$$

$$\begin{aligned}\mathbf{V}_2 = {} & \nabla\left[(z_\alpha - \eta)(\mathbf{u}_\alpha\cdot\nabla)(\nabla\cdot(h\mathbf{u}_\alpha)) + \frac{1}{2}(z_\alpha^2 - \eta^2)(\mathbf{u}_\alpha\cdot\nabla)(\nabla\cdot\mathbf{u}_\alpha)\right] + \\ & \frac{1}{2}\nabla\left[(\nabla\cdot(h\mathbf{u}_\alpha) + \eta\nabla\cdot\mathbf{u}_\alpha)^2\right].\end{aligned} \tag{5}$$

η, h, and t in the above equations refer to the free water surface elevation, water depth, and time. g refers to the acceleration due to the gravity. $\mathbf{u}_\alpha$ refers to the horizontal velocity vector at a reference elevation $z_\alpha=\alpha h$ with $\alpha=-0.531$. $\nabla=(\partial/\partial x, \partial/\partial y)$ represents the horizontal gradient vector. The subscript "t" represents the first-order time partial derivative of various variables.

The wave-generation method proposed by Chawla and Kirby (2000) is adopted to make the desired regular or irregular waves. Sponge layers with sufficient widths are deployed at the ambient boundaries of the numerical wave flume to dissipate outgoing waves with various directions and frequencies effectively. With significant enhancements in both the wave dispersion and the wave nonlinearity, the FUNWAVE 2.0 model has been proven to simulate the propagation and transformation of the water waves from the offshore area to the coast zone robustly and accurately (Bruno et al., 2009; Kirby et al., 2003).

Numerical wave flume

The numerical wave flume adopted in the present research is illustrated in Fig. 1. As stated earlier, the elongated rectangular harbor has plane dimensions of l=20 m × b=2 m. A Cartesian coordinate system (o, x, y, z) is defined in the wave flume. Its origin is arranged at the still water level (SWL) and the middle of the harbor entrance, with the z-axis measured upwards. The positive x-axial direction is consistent with the propagation direction of the incident wave groups. Because the incident irregular wave groups in the nine groups have pretty different spatial scales (see Table 1), the length of the computational domain outside the harbor is not set to a constant. However, each group is set to $12L_p$ to save computing resources. However, the width of the computational domain for each group is always set to 20 m. For the grid size along the x-axial direction, a uniform size of Δx=0.10 m is utilized inside the harbor. In contrast, it gradually rises outside the harbor from Δx=0.10 m at the harbor entrance to $\Delta x \approx 0.025L_p$ in the sponge layers. For the grid size along the y-axial direction, a uniform size of Δy=0.20 m is adopted inside and outside the harbor. For each group, the total simulated time is set to $280T_p$, and the time step of Δt=0.02 s is utilized. Fifty-one wave gauges (i.e., G_1-G_{51}) are arranged along the central line of the harbor equidistantly, and the distance between any adjacent gauges is 0.4 m. G_1 and G_{51} are deployed at the backwall and the entrance, respectively.

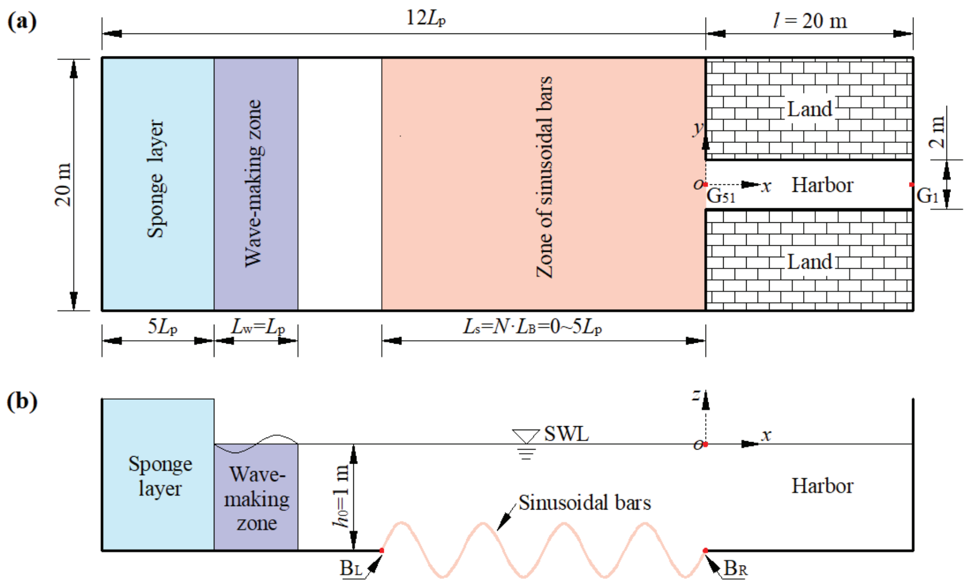

Fig. 1. Numerical wave flume adopted in the current study: (a) the top view, (b) the front view along the central line of the tank (taking the bars with N=4 as an example).

Table 1. Specific parameters of the incident irregular waves and the sinusoidal bars adopted in the simulations

Group	Parameters of incident waves					Parameters of sinusoidal bars		
	f_p (Hz)	T_p (s)	γ	L_p (m)	H_s (m)	N	D/h_0	$2L_B/L_p$
A1	0.180	5.56	1.3	17.02	0.06	0, 2, 4, 6, 8	0.1, 0.2, 0.3, 0.4	0.75−1.25
A2	0.180	5.56	3.3	17.02	0.06	0, 2, 4, 6, 8	0.1, 0.2, 0.3, 0.4	0.75−1.25
A3	0.180	5.56	10	17.02	0.06	0, 2, 4, 6, 8	0.1, 0.2, 0.3, 0.4	0.75−1.25
B1	0.249	4.02	1.3	12.05	0.06	0, 2, 4, 6, 8	0.1, 0.2, 0.3, 0.4	0.75−1.25
B2	0.249	4.02	3.3	12.05	0.06	0, 2, 4, 6, 8	0.1, 0.2, 0.3, 0.4	0.75−1.25
B3	0.249	4.02	10	12.05	0.06	0, 2, 4, 6, 8	0.1, 0.2, 0.3, 0.4	0.75−1.25
C1	0.313	3.19	1.3	9.35	0.06	0, 2, 4, 6, 8	0.1, 0.2, 0.3, 0.4	0.75−1.25
C2	0.313	3.19	3.3	9.35	0.06	0, 2, 4, 6, 8	0.1, 0.2, 0.3, 0.4	0.75−1.25
C3	0.313	3.19	10	9.35	0.06	0, 2, 4, 6, 8	0.1, 0.2, 0.3, 0.4	0.75−1.25

Results

Fig. 2 presents the time series of the free water surface elevations at gauge G_1 for the no-bar topography (i.e., N=0) and the sinusoidal bar topography with N=4, D/h_0=0.4 and $2L_B/L_p$=1.0 in all the nine groups. There are three phenomena that can be easily observed from this figure. Firstly, the wave height at gauge G_1 for the sinusoidal bar topography with N=4, D/h_0=0.4, and $2L_B/L_p$=1.0 is shown to be lower to varying degrees than the corresponding one for the no-bar topography (i.e., N=0) in all the nine groups considered. Secondly, the degree of decline in the wave height due to the existence of the sinusoidal bar topography outside the harbor entrance in Groups B1–B3 is the most significant when compared with that in the other six groups. Thirdly, as the spectral bandwidth parameter, γ, increases, the degree of decline in the wave height seems to increase monotonically. This phenomenon is reflected more evidently in Groups A1–A3 and Groups B1–B3.

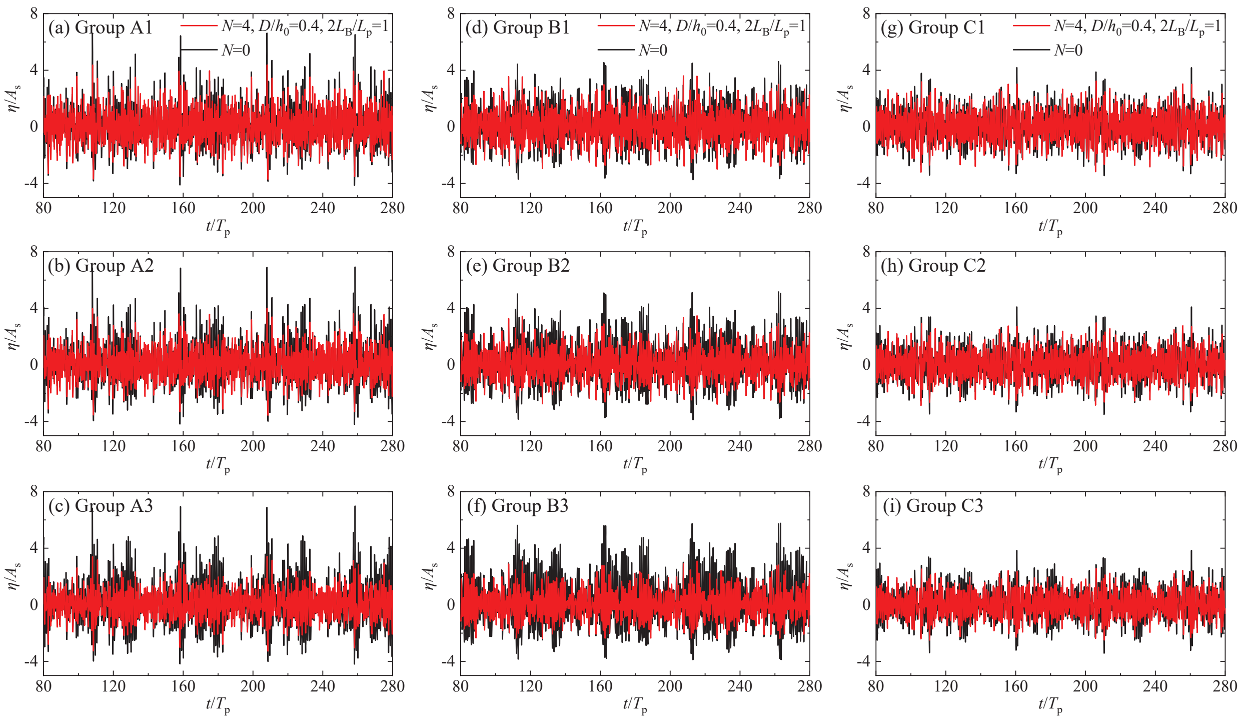

Fig. 2. Comparisons of the time series of the free water surface elevations at gauge G_1 for the no-bar topography (i.e., N=0) and those for the sinusoidal bar topography with N=4, D/h_0=0.4, and $2L_B/L_p$=1.0 in all the nine groups.

To quantitatively describe the phenomena shown in Fig. 2, the time series of the free water surface elevations at gauge G_1 during the last $200T_p$ (i.e., t=$80T_p$–$280T_p$) for the no-bar topography (i.e., N=0) and those for the sinusoidal bar topography with N=4, D/h_0=0.4 and $2L_B/L_p$=1.0 are further analyzed by using the discrete Fourier transform techniques. Fig. 3 illustrates the comparisons of the amplitude spectra for the time series of the free water surface elevations at gauge G_1 for all the cases shown in Fig. 2. Considering that only the lowest six resonant modes have a relatively significant amplification factor of the wave height (F_a > 1.5) and that only the lowest few resonant modes, under normal conditions, have significantly adverse impacts on the dock inundation and the safety of the ships moored in natural harbors (Maravelakis et al., 2021; Yan et al., 2023; Zheng et al., 2022), this article only focuses on the influence of the sinusoidal bars outside the harbor entrance on the lowest six modes. Higher resonant modes (including the seventh and the higher modes) are not considered for the data analyses.

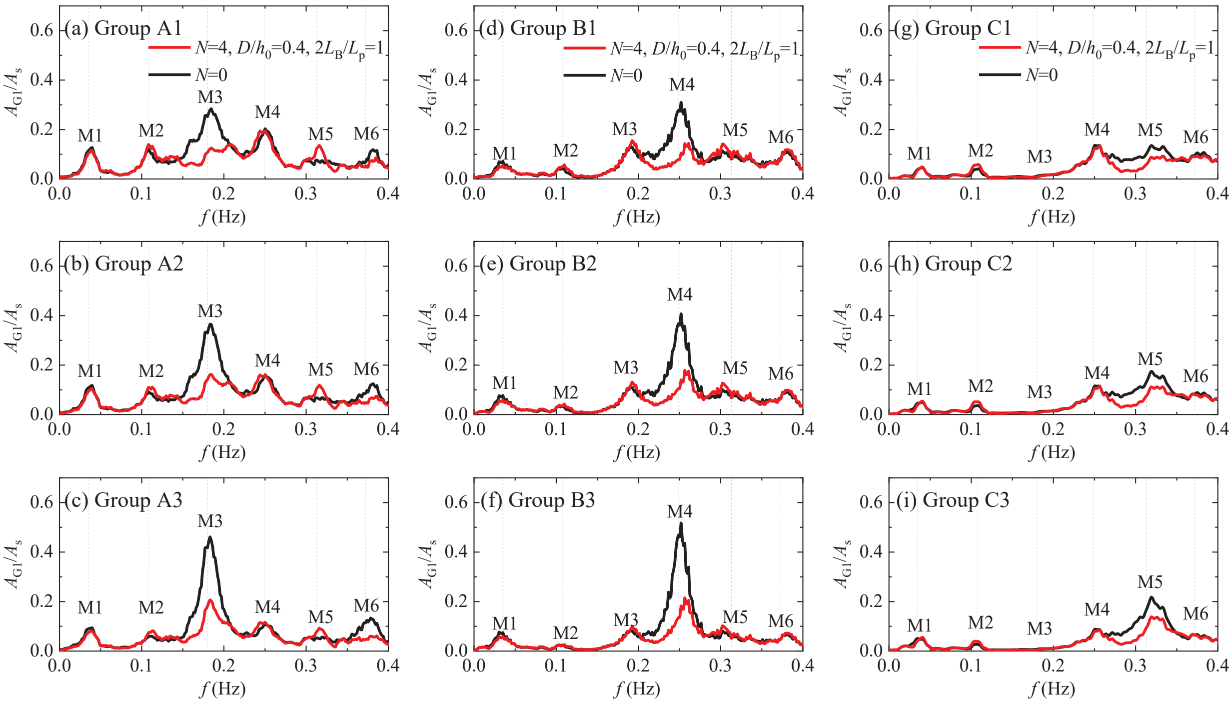

Fig. 3. Comparisons of the amplitude spectra for the time series of the free water surface elevations at gauge G_1 for all the cases in Fig. 2. The symbol "Mi" (i=1–6) marks out the i-th resonant mode.

Two phenomena can be observed in Fig. 3. Firstly, in each group, besides the main resonant mode, the other secondary resonant modes are also triggered to varying degrees because of the nonlinear wave-wave interactions, no matter whether the sinusoidal bars are deployed or not. Secondly, in all the nine groups, the main resonant modes are always the most significantly suppressed when the Bragg resonant reflection occurs over the patch of the bars. While for the other five secondary modes, some of them are mitigated (e.g., M6 in Groups A1–A3 and M1 in Groups B1–B3), and some are enhanced (e.g., M5 in Groups A1–A3 and M2 in Groups C1–C3) to varying degrees.

Fig. 4 further compares the modal shapes of the lowest six modes simulated by the numerical model and the ones predicted by the linear analytical solution of Mei (1983) for Groups A1–A3 under the two conditions of the no-bar topography (i.e., N=0) and the bar topography with N=4, D/h_0=0.4 and $2L_B/L_p$=1.0. It is also confirmed that under both topographical conditions, all the lowest six resonant modes are indeed triggered by the incident irregular wave trains, which is reflected in the phenomenon that all their modal shapes measured in the simulations are well consistent with those predicted by the analytical solution. In addition, the main resonant mode (i.e., Mode 3) in Fig. 4d–f can be visually found to be significantly suppressed by the Bragg resonance phenomenon occurring over the bar topography with N=4, D/h_0=0.4, and $2L_B/L_p$=1.0 as well.

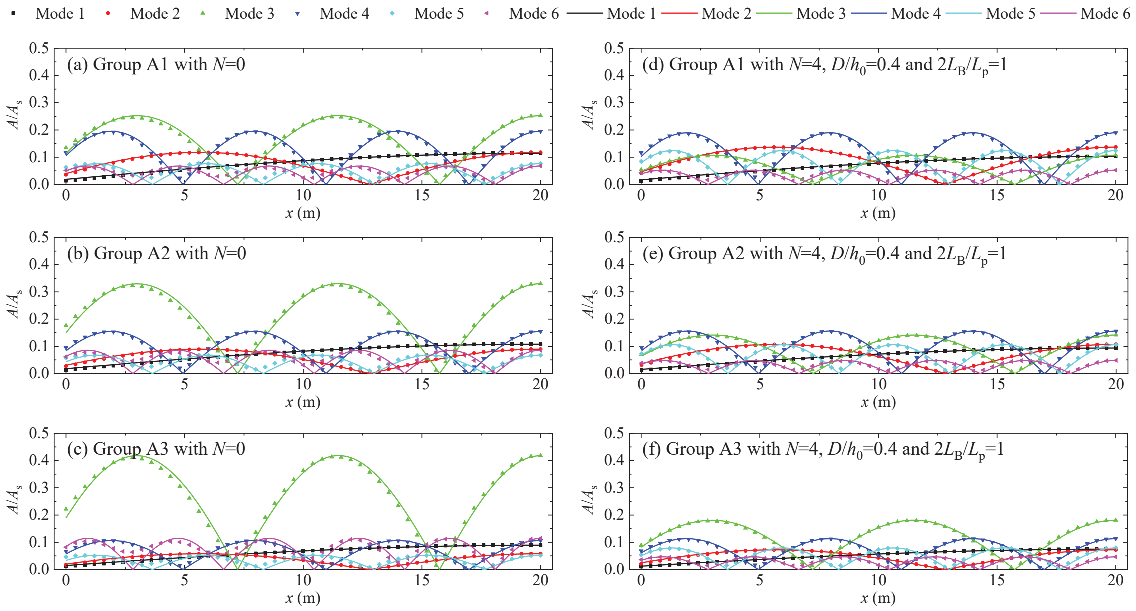

Fig. 4. Comparisons between the simulated modal shapes of the lowest six modes by the numerical model and the theoretical ones predicted by Mei (1983) for Groups A1–A3. (a)–(c) and (d)–(f) correspond to the no-bar topography (i.e., N=0) and the bar topography with N=4, D/h_0=0.4 and $2L_B/L_p$=1.0.

To further quantify both the effect of the sinusoidal bars on each resonant mode and the overall impact on the lowest six modes, the following two parameters are defined:

$$R_i = \frac{A_{G1}(i)}{A_{G1}^*(i)} \times 100\% \quad (i = 1-6) \tag{6}$$

and

$$R_W = \sqrt{\int_{f_L}^{f_H} S(f)df \Big/ \int_{f_L}^{f_H} S^*(f)df}\ , \tag{7}$$

where $A_{G1}^*(i)$ and $A_{G1}(i)$ denote the response amplitude of the i-th mode at gauge G1 for the no-bar topography (i.e., N=0) and that for the sinusoidal bar topography, respectively; $S^*(f)$ and $S(f)$ denote the wave energy density spectrum at gauge G_1 for the no-bar topography and that for the sinusoidal bar topography, respectively. f_L=0 and f_H=0.4 Hz denote the integration's lower and upper-frequency boundaries, respectively. Hereinafter, for ease of narration, R_i and R_W are called "the mitigation factor of the i-th mode" and "the overall mitigation factor of the lowest six modes", respectively. Obviously, a value of R_i closer to 0 indicates a higher mitigation degree for the i-th mode, and a value of R_W closer to 0 represents a higher mitigation degree for the lowest six modes as a whole (or in other words, the whole resonance of the harbor).

Table 2 lists the specific values of both R_i (i=1–6) and R_W for all the nine cases with the bar topography of N=4, D/h_0=0.4, and $2L_B/L_p$=1.0 shown in Fig. 2. Majority of phenomena presented in the above three figures (i.e., Figs. 7–9) are quantitatively embodied in this table. These phenomena include: (1) the main resonant modes are always the most significantly depressed compared to the other five secondary modes; (2) for the five secondary modes, some are mitigated (i.e., R_i < 100%), and some are enhanced (i.e., R_i > 100%) to varying degrees, which depends on the main resonant mode; (3) when the Bragg resonant reflection occurs for the fourth resonant mode, the mitigation effects on both the main resonant mode and the whole resonance of the harbor are the most significant compared to those when the Bragg resonant reflection appears for the third and the fifth main modes; and (4) the mitigation effect of Bragg reflection on the whole resonance of the harbor becomes increasingly significant as the spectral bandwidth parameter, γ, rises, regardless of the main resonant mode.

Table 2. Specific values of both the mitigation factor of the i-th mode, R_i (i=1–6), and the overall mitigation factor, R_W, for all the nine cases with the bar topography of N=4, D/h_0=0.4, and $2L_B/L_p$=1.0 shown in Fig. 2. The bold data correspond to the mitigation factor of the main resonant mode in each case.

Group	Ratios (%)						
	R_1	R_2	R_3	R_4	R_5	R_6	R_W
A1	89.78	116.20	**42.47**	97.15	162.79	77.54	80.09
A2	86.95	119.80	**42.82**	100.86	156.83	56.27	70.21
A3	83.61	124.81	**43.28**	106.50	151.02	40.76	58.95
B1	76.77	119.38	97.40	**28.48**	103.20	94.45	75.92
B2	76.86	110.19	94.77	**28.68**	102.96	96.55	64.84
B3	78.47	93.31	92.19	**28.99**	102.56	98.59	54.20
C1	91.45	143.84	74.01	91.40	**58.11**	93.21	82.77
C2	86.67	144.67	67.98	91.01	**57.05**	95.84	77.99
C3	83.56	145.23	58.49	89.83	**56.31**	100.22	72.36

References

Bruno, D., Serio, F.D., Mossa, M., 2009. The FUNWAVE model application and its validation using laboratory data. Coastal Engineering 56 (7), 773-787.

Chawla, A., Kirby, J.T., 2000. A source function method for generation of waves on currents in Boussinesq models Applied Ocean Research 22 (2), 75-83.

Davies, A.D., 1982. The reflection of wave energy by undulations on the seabed. Dynamics of Atmospheres and Oceans 6, 207-232.

Ding, Y., Liu, H.-W., Lin, P., 2024. Quantitative Expression of the Modified Bragg's Law for Bragg resonances of water waves excited by five types of artificial bars Physics of Fluids 36, 047130.

Fang, H., Tang, L., Lin, P., 2024a. Bragg scattering of nonlinear surface waves by sinusoidal sandbars. Journal of Fluid Mechanics 979, A13.

Fang, H., Tang, L., Lin, P., 2024b. Theoretical study on the downshift of class II Bragg resonance. Physics of Fluids 36, 017103.

Kennedy, A.B., Kirby, J.T., Chen, Q., Dalrymple, R.A., 2001. Boussinesq-type equations with improved nonlinear performance. Wave Motion 33, 225-243.

Kirby, J.T., Long, W., Shi, F., 2003. Funwave 2.0 Fully Nonlinear Boussinesq Wave Model On Curvilinear Coordinates. Report No. CACR-02-xx. Center for Applied Coastal Research, Dept. of Civil & Environmental Engineering, University of Delaware, Newark, Delaware.

Liu, H.-W., Xiong, W., Xie, J.-J., 2023. A new law of Class I Bragg resonance for linear long waves over arrays of parabolic trenches or rectified cosinoidal trenches. Ocean Engineering 281, 114973.
Liu, P.L.-F., Cho, Y.-S., 1993. Bragg reflection of infragravity waves by sandbars. Journal of Geophysical Research 98 (C12), 22733-22741.
Mahmoudof, S.M., Takami, M.L., 2022. Numerical study of coastal wave profiles at the sandy beaches of Nowshahr (Southern Caspian Sea). Oceanologia 64 (3), 457-472.
Maravelakis, N., Kalligeris, N., Lynett, P.J., Skanavis, V.L., Synolakis, C.E., 2021. Wave overtopping due to harbour resonance. Coastal Engineering 169, 103973.
Mei, C.C., 1983. The Applied Dynamics of Ocean Surface Waves. Wiley, New York.
Mei, C.C., Hara, T., Naciri, M., 1988. Note on Bragg scattering of water waves by parallel bars on the seabed. Journal of Fluid Mechanics 186, 147 - 162.
Ni, Y.-L., Teng, B., 2021. Bragg resonant reflection of water waves by a Bragg breakwater with porous trapezoidal bars on a sloping permeable seabed. Applied Ocean Research 114, 102770.
Peng, J., Tao, A., Liu, Y., Zheng, J., Zhang, J., Wang, R., 2019. A laboratory study of class III Bragg resonance of gravity surface waves by periodic beds. Physics of Fluids 31, 067110.
Wei, G., Kirby, J.T., Grilli, S.T., Subramanya, R., 1995. A fully nonlinear Boussinesq model for surface waves. Part 1. Highly nonlinear unsteady waves. Journal of Fluid Mechanics 294, 71-92.
Xu, J., Chen, L., Ning, D., Zhao, M., 2023. Resonance of water waves propagating over a uniform and a graded line array of rectified submerged cosinoidal bars. Applied Ocean Research 134, 103531.
Yan, M., Zheng, Z., Sun, Z., Ma, X., Dong, G., 2023. Numerical evaluation of the tension mooring effects on the hydrodynamic response of moored ships under harbor oscillations. Ocean Engineering 288, 116127.
Zhang, J., Yu, H.T., Chen, Q., Hu, M.Q., 2013. Dynamic characteristics and experiment analysis of a single phase permanent magnet linear generator for wave energy conversion. Transactions of China Electrotechnical Society 28 (7), 110–116 (in Chinese).
Zheng, Z., Ma, X., Yan, M., Ma, Y., Dong, G., 2022. Hydrodynamic response of moored ships to seismic-induced harbor oscillations. Coastal Engineering 176, 104147.

国際化推進共同研究概要

No.26

[採択番号]　24RE-4

タイトル：　High-Fidelity Aeroelasticity Simulation of Offshore Wind Turbine in Complex Offshore Environment

研究代表者：　LIU Cheng

所内世話人：　HU Changhong

研究概要：

本国際化推進共同研究について、共同研究・研究集会とも予定通り実施した。共同研究について、浮体式洋上風車に関する次世帯CFD手法の研究や、風車の空力弾性解析手法の開発などが行われ、関連の研究成果は９編の学術論文に纏められ投稿された。研究集会について、2024年11月25～27日に九州大学西新プラザにおいて開催された、所内世話人HUが主催した第1回アジア太平洋洋上風力発電技術会議に合流して、LIU Cheng先生を始め、上海交通大学から多くの研究者が参加し、浮体式洋上風車技術の開発や、関連の数値シミュレーション手法の開発などに関して講演と研究討議を行った。

Final Report: High-Fidelity Aeroelasticity Simulation of Offshore Wind Turbine in Complex Offshore Environment

Research Institute for Applied Mechanics, Kyushu University

Collaborative Research Project (2024)

---

1. Introduction

This report summarizes the progress and achievements of the collaborative research project *"High-Fidelity Aeroelasticity Simulation of Offshore Wind Turbine (OffWT) in Complex Offshore Environment"* conducted in 2024 under the Joint Usage/Collaborative Research Program at Kyushu University's Research Institute for Applied Mechanics (RIAM). The project aimed to address the challenges of nonlinear coupled dynamic responses in offshore wind turbines (OffWTs) under complex environmental interactions involving wind, waves, and currents. Key objectives included advancing numerical methodologies for multiphysics simulations, investigating wave-turbine interactions, and understanding the impact of turbulent wakes and bubble dynamics on turbine stability and power output.

Collaboration between Shanghai Jiao Tong University (SJTU) and RIAM, initiated in 2021, has been further strengthened through this project. Over the past year (2024), nine SCI-indexed papers were published, focusing on numerical methods for multiphase flows, wave-breaking mechanisms, bubble dynamics, and droplet formation. These contributions advance the foundational knowledge required for designing robust OffWTs in real ocean environments.

---

2. Research Objectives and Methodologies

The project employed high-fidelity numerical simulations combined with adaptive mesh refinement (AMR), interface-capturing techniques, and advanced turbulence models to investigate:

- **Wave-breaking dynamics** under wind and surface tension effects.
- **Bubble entrainment and collapse** in turbulent flows and their impact on pressure loads.
- **Multiphase interactions** (air-water, bubbles, droplets) in breaking waves.
- **Numerical framework development** for large-density-ratio flows and coarse/fine interface treatments.

Key methodologies included:

- **Adaptive Mesh Refinement (AMR)** for resolving multiscale phenomena efficiently.
- **Interface compression techniques** and **mass-momentum consistent schemes** for sharp interface representation.
- **High-order numerical schemes** (e.g., WENO, THINC) to minimize numerical dissipation.
- **Bubble/droplet detection algorithms** for statistical analysis of size, velocity, and spatial distributions.

---

3. Major Achievements

3.1 Advancements in Numerical Methods

1. **Robust Interface Treatment for Adaptive Meshes**
    - Developed a pressure compensation method and jump model to handle gravity and surface tension across coarse/fine mesh interfaces (*Paper 1*). This reduced unnecessary mesh refinement near free surfaces while maintaining accuracy comparable to uniform meshes.
    - Introduced a **volume-of-fluid (VOF)-based flux computation method** for large-density-ratio flows, enabling robust simulations of droplet breakup in high shear flows (*Paper 9*).
2. **Periodic Boundary Condition for Bubbly Flows**
    - Proposed a novel treatment for vertical periodic channels with gravity, enabling simulations of microbubble swarms in industrial applications (*Paper 8*).

3.2 Wave Dynamics and Breaking Mechanisms

1. **Wind-Driven Wave Breaking**
    - Identified critical conditions for wave breaking using dimensionless parameters (Bond number, Reynolds number) and derived a predictive equation for breaking onset (*Paper 2*). Demonstrated that surface tension suppresses plunging breaking but enhances capillary-driven energy dissipation.
2. **Plunging Breaker Characteristics**
    - Revealed four primary mechanisms of spray droplet formation and quantified bubble/droplet size distributions (power-law scaling) in breaking waves (*Paper 5*).
    - Analyzed the role of vortices in bubble fragmentation and turbulent flow initiation during bubble rise (*Paper 7*).

3.3 Bubble Dynamics and Collapse

1. **Toroidal Bubble Collapse**
    - Discovered that shock waves from collapsing toroidal bubbles focus along the torus axis, generating pressure peaks three times higher than spherical bubbles (*Paper 4*). This finding supports buoyancy material design for deep-sea submersibles.
2. **Bubble Cluster Collapse**
    - Demonstrated that spatial distribution and bubble count dominate pressure loads during cluster collapse, with minimal impact from wall proximity (*Paper 6*).

3.4 Vortex-Interface Interactions

- Classified four wave patterns (plunging/depression breakers, capillary waves) induced by decaying Lamb–Oseen vortices and mapped their regimes using Weber and Reynolds numbers (*Paper 3*).

---

4. Collaborative Outcomes and Knowledge Exchange

- **Publications**: Nine SCI papers were published in 2024, building on seven prior collaborative works since 2021.
- **Research Integration**: The project integrated expertise from SJTU (wave mechanics, bubble dynamics) and RIAM (adaptive mesh, compressible flows).
- **Workshops/Seminars**: Hosted joint workshops on renewable energy and offshore engineering, fostering interdisciplinary discussions.

---

5. Conclusion and Future Directions

The project successfully advanced numerical frameworks for simulating offshore wind turbine environments, providing critical insights into wave-breaking physics, bubble dynamics, and multiphase turbulence. Key outcomes include predictive models for wave breaking, bubble collapse, and droplet formation, which inform OffWT design and operational stability.

Future work will focus on:

- Extending 3D simulations to incorporate aeroelastic turbine blade responses.
- Experimental validation of bubble/droplet statistics in wave tanks.
- Integrating machine learning for real-time load prediction in turbulent offshore environments.

This collaboration underscores the importance of international partnerships in addressing global renewable energy challenges.

6. Publication List

[1]. Liu, C., Hu, Y., Gao, R., & Hu, C. (2025). Robust treatment for the coarse/fine interface of adaptive mesh in the simulation of two-phase flow. *Journal of Computational Physics*, *520*, 113485.

[2]. Chai, B., Liu, C., Hu, Y., Zhang, P., Xing, B., & Hu, C. (2024). Critical condition for wind-driven wave breaking with the effect of surface tension. *Ocean Engineering*, *311*, 118913.

[3]. Liu, C., Hu, Y., Xing, B., & Hu, C. (2024). Numerical investigation of the interaction between an interface and a decaying Lamb–Oseen vortex. *Physics of Fluids*, *36*(7).

[4]. Liu, C., Yang, X., Li, J., Hu, Y., Zhao, M., & Hu, C. (2024). Investigations on the shock wave induced by collapse of a toroidal bubble. *Physical Review E*, *110*(1), 015103.

[5]. Hu, Y., Liu, C., Yang, X., & Hu, C. (2024). Numerical investigation of the plunging breaker under various wave slopes: Characteristics of spray droplets and air entrainment. *Ocean Engineering*, *303*, 117635.

[6]. Yang, X., Liu, C., Hu, Y., Zhao, M., & Hu, C. (2024). Shock wave induced by the collapse of a bubble cluster with each bubble distributed randomly. *Ocean Engineering*, *300*, 117362.

[7]. Liu, C., Hu, Y., Yang, X., & Hu, C. (2024). Numerical study of bubble rise in plunging breaking waves. *Physics of Fluids*, *36*(5).

[8]. Gao, R., Liu, C., Hu, Y., & Hu, C. (2024). Numerical simulations of bubbly flows in a vertical periodic channel. *International Journal of Multiphase Flow*, *175*, 104816.

[9]. Liu, C., Gao, R., Chai, B., & Hu, C. (2024). A volume of fluid based method for consistent flux computation in large-density ratio two-phase flows and its application in investigating droplet bag breakup behavior. *Physics of Fluids*, *36*(1).

Submitted by: [Cheng Liu]
Affiliation: School of Ocean and Civil Engineering, Shanghai Jiao Tong University, Shanghai 200240, China

Date: [2025/2/10]

国際化推進共同研究概要

No. 27

［採択番号］　24RE-5

タイトル：　Fully coupled modeling of integrated floating energy systems consisting of wind and tidal turbines

研究代表者：　YANG, Yang

所内世話人：　劉　盈溢

研究概要：　本プロジェクトでは、流体力学解析ソフトウェア AQWA を基に、DLL を用いて空力・サーボ・弾性解析機能を追加し、完全連成数値解析ツールを開発した。また、AeroDyn プログラムを統合して潮流タービンの性能を評価した。異なる荷重条件におけるタービン設置位置の影響を検討した結果、潮流タービンの導入により IFES モデルの発電量が大幅に向上することが確認された。さらに、タービンの設置位置がモデル性能に大きく影響するため、効率的で安定した風力・潮流ハイブリッドシステムには最適化が必要であることが示唆された。本プロジェクトでは、5 本の論文を発表し、APCOW2024 国際会議に参加した。

掲載論文：

[1] Ding, J., Yin, J., Yang, Y., Yu, J., Bashir, M., Li, S., Li, C. (2025). Effects of WEC design parameters on fully coupled responses of a Barge-type wind-wave-integrated floating energy system. Journal of Marine Engineering & Technology, 1-14.

[2] Yin, J., Ding, J., Yang, Y., Yu, J., Ma, L., Xie, W., Nie, D., Bashir, M., Liu, Q., Li, C., Li, S. (2025). Wave-induced motion prediction of a deepwater floating offshore wind turbine platform based on Bi-LSTM. Ocean Engineering, 315, 119836.

[3] Zhang, Z., Yang, Y., Qin, Z., Bashir, M., Cao, Y., Yu, J., Liu, Q., Li, C., Li, S. (2024). Investigation of dynamic stall models on the aeroelastic responses of a floating offshore wind turbine. Renewable Energy, 237, 121778.

[4] Ding, J., Yang, Y., Yu, J., Bashir, M., Ma, L., Li, C., Li, S. (2024). Fully coupled dynamic responses of barge-type integrated floating wind-wave energy systems with different WEC layouts. Ocean Engineering, 313, 119453.

[5] Ding, J., Shi, Z., Yin, J., Yang, Y., Yu, J., Liu Y., Bashir, M., Li, C., Chen, S. (2025). Dynamic analysis of a wind-wave integrated floating energy system supported by barge-type platform. China Ocean Engineering, Accepted.

Purpose

This project aims to:

(1) Develop a fully coupled model for dynamic response prediction of wind-current and wind-wave integrated floating energy systems.

(2) Investigate the WEC and tidal turbine layout effects on the dynamic behavior of the IFES concepts.

Numerical modelling method

The coupled analysis framework of the IFES concept is developed by integrating the aero-servo-elastic model with AQWA through a dynamic link library (DLL). The capabilities of predicting aero-servo-elastic responses of the wind turbine and the hydrodynamic loads on the tidal turbines are implemented within the DLL that can be invoked by AQWA when performing a time-domain analysis. Fig. 1 presents a flowchart of the fully analysis framework of the IFES concept. Noting that the numerical simulation of the IFES subjected to wind, wave and current loadings is performed in AQWA. In each time step of the time domain analysis, the DLL will be invoked to predict the aerodynamic loads on the wind turbine and hydrodynamic loads on the rotating rotor of the tidal turbines under the influence of platform motions. t is apparent that the platform responses obtained using the AQWA solver are influenced by the responses of the wind turbine and tidal turbines predicted in the DLL, and vice versa. Based on the assumption of small rotations of the platform, the relative inflow current speed $U_{\mathrm{curr,rel}}$ is corrected as follows:

$$U_{\mathrm{curr,rel}} = U_{\mathrm{curr}} - U_{\mathrm{ptfm,surge}} - (Z_{\mathrm{tidal}} - Z_{\mathrm{ptfm}})U_{\mathrm{ptfm,pitch}} + (Y_{\mathrm{tidal}} - Y_{\mathrm{ptfm}})U_{\mathrm{ptfm,yaw}} \tag{1}$$

where U_{curr} is the defined inflow current speed at the tidal hub depth. $U_{\mathrm{ptfm,surge}}$, $U_{\mathrm{ptfm,pitch}}$ and $U_{\mathrm{ptfm,yaw}}$ are the surge, pitch and yaw velocities of the platform, respectively. Z_{tidal} and Z_{ptfm} are the vertical coordinates of the CMs of the tidal turbine and platform, respectively. Y_{tidal} and Y_{ptfm} are the lateral coordinates of the CMs of the tidal turbine and platform, respectively.

It is noted that the results directly produced by the AQWA solver and DLL are referred to different coordinate systems. More specifically, the tower-base loads are referred to the platform's local coordinate system that moves with the platform. The external force applied at the platform's CM is referred to the inertial coordinate system fixed in the origin of [0, 0, 0]. More details regarding the coupled modelling between AQWA and FAST can be found in the previous studies of the authors.

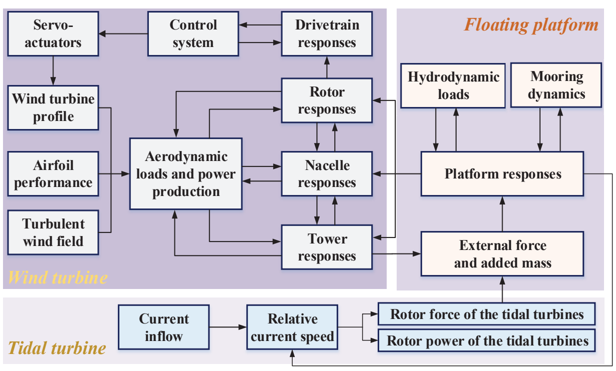

Fig. 1: Flowchart of the fully coupled model

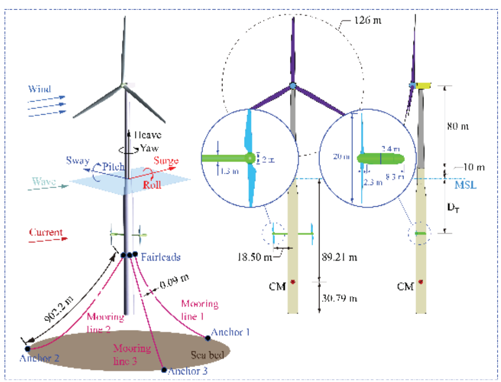

Fig. 2: Schematic diagram of the IFES

Experimental results and discussions

The IFES concept shown in Fig. 2 consists of a 5 MW wind turbine developed by the National Renewable Energy Laboratory (NREL) and two tidal turbines designed by the Sandia National Laboratory (SNL). The IFES concepts are examined for the load cases (LC) defined in Table1.

Table 1: Load case definition

ID of the load cases	Wind speed (m/s)	Significant Wave Height (m)	Peak Spectral Period (s)	Current Speed at MSL(m/s)	Probability
LC1	3.0	1.089	8.569	0.610	2.337%
LC2	4.0	1.108	8.496	0.650	3.569%
LC3	5.0	1.146	8.392	0.680	4.125%
LC4	6.0	1.198	8.264	0.730	5.555%
LC5	7.0	1.269	8.103	0.920	6.976%
LC6	8.0	1.359	7.923	1.060	7.776%
LC7	9.0	1.478	7.724	1.220	8.236%
LC8	10.0	1.617	7.569	1.310	7.657%
LC9	11.0	1.779	7.451	1.460	6.996%
LC10	12.0	1.954	7.443	1.520	6.766%
LC11	13.0	2.144	7.457	1.660	6.320%
LC12	14.0	2.350	7.508	1.700	5.986%
LC13	15.0	2.573	7.629	1.810	5.243%
LC14	16.0	2.808	7.810	2.010	4.699%
LC15	17.0	3.062	8.047	2.120	4.171%
LC16	18.0	3.361	8.294	2.230	3.236%
LC17	19.0	3.645	8.549	2.420	2.889%
LC18	20.0	3.860	8.796	2.510	2.125%
LC19	21.0	4.081	9.042	2.660	1.825%
LC20	22.0	4.335	9.288	2.710	1.145%
LC21	23.0	4.610	9.534	2.810	0.998%
LC22	24.0	4.905	9.779	2.860	0.715%
LC23	25.0	5.216	10.025	2.980	0.658%

The mean value and standard deviation of the power produced by the wind turbine and tidal turbines of each examined IFES model are calculated based on the results between 2500 s and 4500 s. Fig. 3 and Fig. 4 present the generator power of the whole system and the tidal turbines, respectively. As observed from Fig. 3, the total power of each IFES model is higher than that of the FOWT for each examined load case. The whole system's output power is increased by the tidal turbines as expected. Especially for LC17~LC23 in which the current speeds are higher than the rated speed of the tidal turbine, the two tidal turbines add 1.1 MW capacity to the whole system by producing the rated power. It is also found that the five IFES models have a similar average total power production in these load cases, although IFES1 has a relatively larger standard deviation. Since the tidal turbines of IFES1 are installed at -26.5 m depth that is the farthest to the CM of the spar platform. The platform pitch motion produces the largest variation to the relative speed of the tidal turbines. As a result, the power fluctuation of IFES1 is larger as observed. It is noted that the power productions of all the IFES models are very close within LC1~LC4. The reason to this observation is a bit different from that of the results in LC17~LC23. In LC1~LC4, the wind speeds are lower than 8m/s. The pitch motion induced by the aerodynamic loads is not severe. The surge speed of the tidal turbines due to the platform pitch motion are insignificant compared to its absolute inflow current speed. Consequently, the installation position of tidal turbines has a weak influence on the total power production.

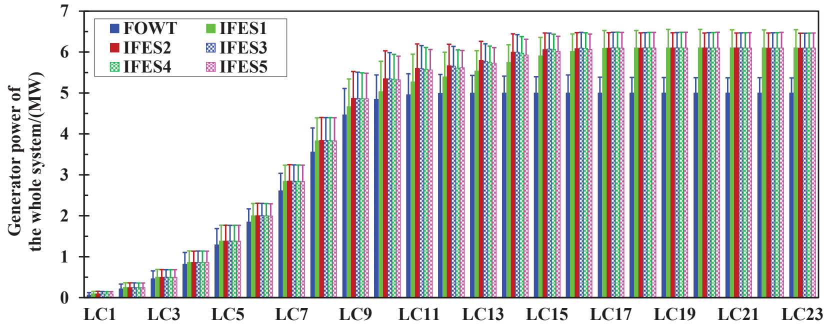

Fig. 3: Generator power of the whole system including the wind turbine and tidal turbines

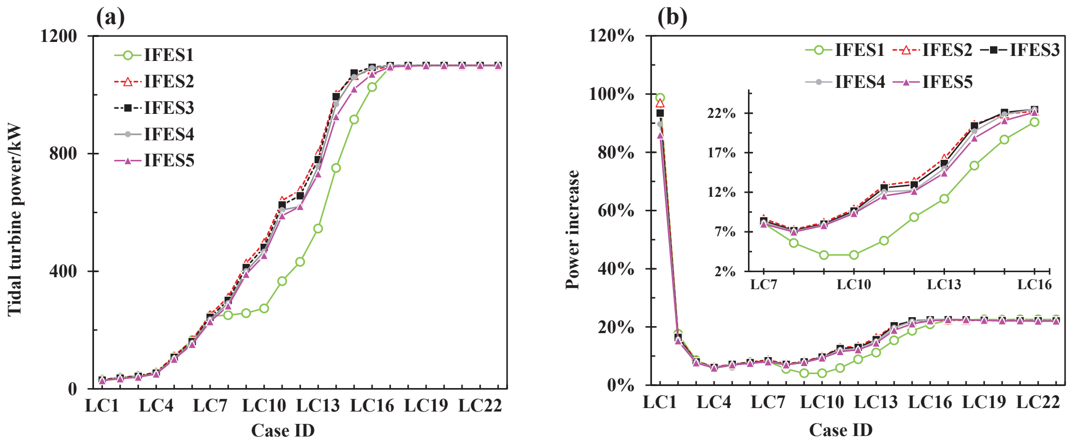

Fig. 4: Generator power of the tidal turbines of each examined IFES model. (a) Power of the tidal turbines power; (b) Increase rate of power

Fig. 5 presents the mean pitch motion of all the models and the pitch increase rate of the IFES models. Platform pitch of the IFES models is significantly influenced by the installation position of the tidal turbines as confirmed by the obvious differences observed from Fig. 5. Similar to tower-base bending moment, the pitch motions of IFES1 and IFES2 are increased while the pitch motions of IFES4 and IFES5 are reduced if comparing to the results of the FOWT. This is mainly because of the installation position of the tidal turbines. For the IFES1 and IFES2 models, the tidal turbines generate a positive bending moment together with the aerodynamic loads resulting in a larger pitch motion. However, the tidal turbines of IFES4 and IFES5 are installed below the system's CM. The hydrodynamic thrust of the tidal turbines produces a bending moment reverse to the aerodynamic bending moment. As shown in Fig. 5(b), the mean pitch motion of IFES1 is increased by as large as 78.2% under LC16. The average increase rate over the examined load cases is 37.3% for IFES1. While the reduction in mean pitch motion of IFES5 achieves 56.4% under LC14 and the average reduction over all the load cases is 35.3%.

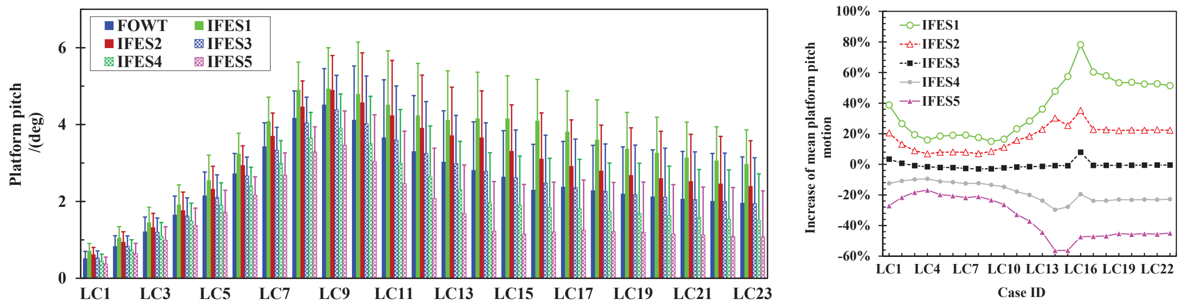

(a) Statistics of platform pitch of all the models (b) Increase rate of mean value

Fig. 5: Mean pitch motion of all the models and the pitch increase rate of the IFES models compared to the FOWT

As per the results presented in the previous section, it is found that the dynamic responses of the IFES models are significantly influenced by the tidal turbines under LC14. In addition, the extreme high/low values are achieved at LC14 for most IFES modes. The phenomenon implies that the coupling between the wind turbine and the substructure that includes the platform and tidal turbines is very complicated. Therefore, the dynamic responses of all the IFES models under LC14 are presented to explain how the tidal turbines affect the whole system's dynamic behavior. Fig. 6 presents the total power and tower-base bending moment of the IFES models and the FOWT under LC14.

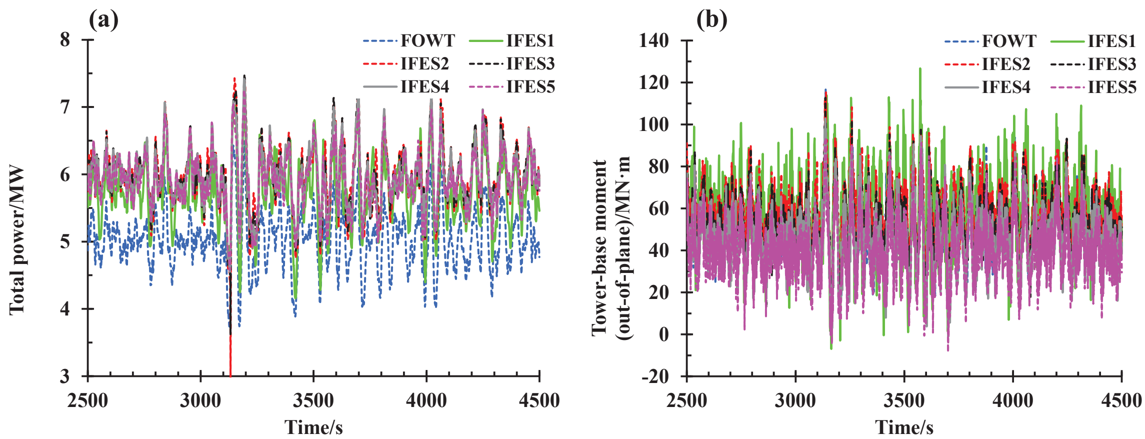

Fig. 6: The time domain dynamic responses of the IFES models and FOWT: (a) Total power of the whole system; (b) Tower-base bending moment.

List of publications

[1] Ding, J., Yin, J., Yang, Y., Yu, J., Bashir, M., Li, S., & Li, C. (2025). Effects of WEC design parameters on fully coupled responses of a Barge-type wind-wave-integrated floating energy system. *Journal of Marine*

Engineering & Technology, 1-14.

[2] Yin, J., Ding, J., Yang, Y., Yu, J., Ma, L., Xie, W., ... & Li, S. (2025). Wave-induced motion prediction of a deepwater floating offshore wind turbine platform based on Bi-LSTM. *Ocean Engineering*, *315*, 119836.

[3] Zhang, Z., Yang, Y., Qin, Z., Bashir, M., Cao, Y., Yu, J., ... & Li, S. (2024). Investigation of dynamic stall models on the aeroelastic responses of a floating offshore wind turbine. *Renewable Energy*, *237*, 121778.

[4] Ding, J., Yang, Y., Yu, J., Bashir, M., Ma, L., Li, C., & Li, S. (2024). Fully coupled dynamic responses of barge-type integrated floating wind-wave energy systems with different WEC layouts. *Ocean Engineering*, *313*, 119453.

[5] Ding, J., Shi, Z., Yin, J., Yang, Y., Yu, J., Liu Y., Bashir, M., Li, C., & Chen, S. (2025). Dynamic analysis of a wind-wave integrated floating energy system supported by barge-type platform. *China Ocean Engineering*, Accepted.

国際化推進共同研究概要

No.28

[採択番号] 24RE-6

タイトル: Hydrodynamic study on wave energy harvesting technique using floating liquid tank

研究代表者: ZHANG, Chongwei

所内世話人: 劉 盈溢

研究概要: 海洋エネルギー変換装置の生存性は、依然として大きな課題である。これらの装置における流体力学的応答の解析は、構造の最適化やエネルギー変換効率の向上、さらには浮体構造の安全性強化に不可欠である。本研究では、ブイ型波力エネルギー変換装置の流体力学的性能を実験的に調査した。その結果、複数自由度条件下では、単一自由度条件下と比較して浮体の相対変位や作用力、さらに軸に作用するトルクや回転速度の振幅が増大することが明らかとなった。加えて、液体タンクを用いた浮体式風力タービンの運動制御について数値シミュレーションを実施した結果、液体タンクは浮体基盤の最大ピッチ振幅を最大26%削減する効果があることが確認された。この効果は、様々な波浪条件下において一貫して認められた。

掲載論文:

[1] Zhang, C., Li, D., Ding, Z., Liu, Y., Cao, F., & Ning, D. (2024). Wave energy converter with multiple degrees of freedom for sustainable repurposing of decommissioned offshore platforms: An experimental study. Applied Energy, 376, 124204.

24RE-6

タ イ ト ル:　Hydrodynamic study on wave energy harvesting technique using floating liquid tank.

ZHANG, Chongwei

所内世話人:　劉 盈溢

Introduction

Marine energy is a type of renewable energy that offers several advantages, including no land occupation, widespread resource distribution, significant development potential, sustainability, and environmental friendliness. As such, it has become an essential component of global renewable energy development. Under the action of wind and wave loads, marine renewable energy devices experience significant oscillations. It is crucial to clearly understand the hydrodynamic performance of these structures and implement effective vibration suppression measures. One approach to controlling the motion of floating wind turbines is to utilize liquid tanks. Tuned liquid column damper (TLCD) is a classical vibration control technique that has been successfully used in high-rise buildings. Lee et al [1] was probably the first study that introduced TLCD to suppress the motion of floating platforms. Subsequently, Lee and Juang [2], Borg et al [3], Feizian et al [4], and Yu et al [5] examined the motion-reduction effects of the conventional U-shaped TLCD on various floating foundation types, including the tension-leg, semi-submersible, SPAR-type, and barge-type foundations, respectively. Understanding the complex interaction mechanisms between wave-induced rocking, floating platforms, and ocean waves is critical to optimizing tank geometry and maximizing the safety of Marine structures. However, a practical floating foundation normally has multiple vertical motion planes in various directions under combined action of wind and waves. As a modified solution, various concepts of multiple tuned liquid column dampers (MTLCDs) are proposed to control the motion in multiple directions. Meanwhile, the hydrodynamic performance and power generation efficiency of multi-degree-of-freedom oscillating float-type wave energy generator are evaluated. Previous research, experiments conducted by Zhang et al. [6] showed that a multi-axis WEC produced more power than did a single-axis WEC. Sergiienko et al. [7] compared the performances of floating and fully submerged point absorbers and found advantages for a fully submerged buoy with multiple motion modes. Numerical simulations conducted by Shi et al. [8] showed that increasing the number of multi-degree-of-freedoms (DOFs) improved the energy capture efficiency of a WEC across a wider frequency range. Al Shami et al. [9] investigated the effects of DOFs on a point-absorber WEC and found that increasing the number of DOFs significantly enhanced its average power capture. In Wang et al. [10], sea trials of a multi-DOF WEC showed a 32.76% higher time-averaged electrical power output compared to the single-DOF case.

In this study, an alternative concept of MTLCD is to be proposed to suppress the wave-induced motion of a semi-submersible floating wind turbine. An integrated numerical model of the MTLCD and floating foundation will be established using STAR-CCM+. Effects of the MTLCD on the motion responses of the floating foundation are to be investigated. At the same time, the hydrodynamic performance and energy capture efficiency of multi-degree-of-freedom wave energy device are studied by physical model tests.

Methodology

Numerical wave tank

An integrated numerical model of the MTLCD and floating foundation is established using STAR-CCM+. As shown in Fig. 1, the numerical wave tank has a length of 2200 m and a water depth of 100 m. Symmetric boundary conditions are implemented on the front and rear boundaries. The wall condition is defined on the sea bed. The left and upper boundaries are set as velocity inlet boundaries, and the right boundary is designated as the outlet boundary. The platform is located 1100 m from the left boundary, 70 m from the front boundary, and 50m above the bottom boundary. Wave forcing zones of 1.5 times wavelength long are employed at both the left and right boundary of the tank to prevent wave reflections. Aerodynamic loads on the structure are ignored.

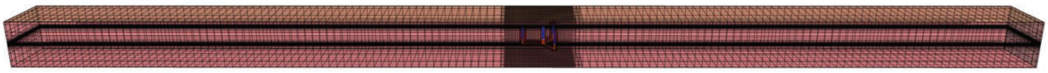

(a)

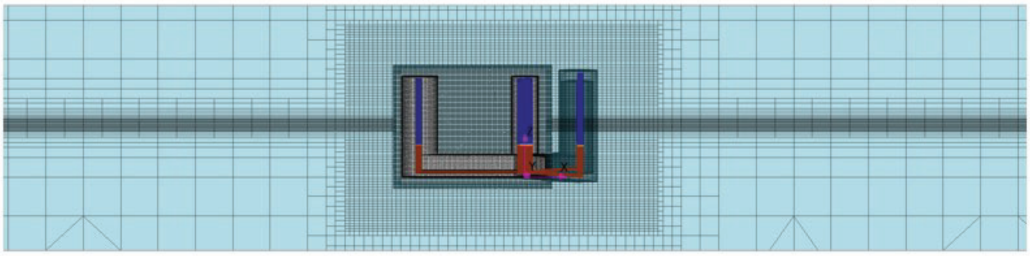

(b)

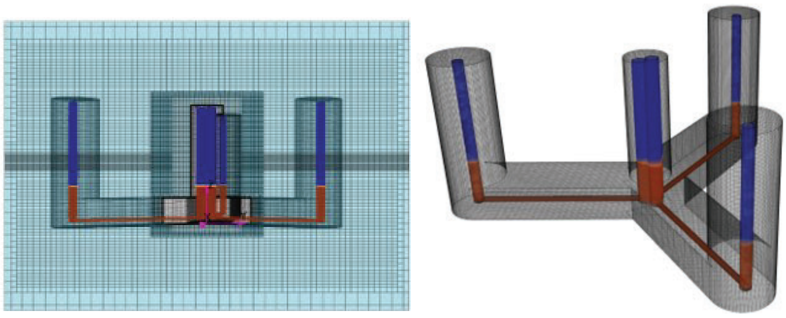

(a) (b)

Figure 1. (a) Mesh of computational domain; (b) front view of local mesh refinement; (c) side view of local mesh refinement; and (d) suface mesh of floating foundation.

The inlet velocity on left boundary is set based on the fifth-order Stokes wave theory. The velocity components of water particles are

$$u_x = \frac{\partial \Phi}{\partial x} = c\sum_{n=1}^{5} n\lambda_n \cosh nk(z+d)\cos n(kx-\omega t) \tag{1}$$

$$u_z = \frac{\partial \Phi}{\partial z} = c\sum_{n=1}^{5} n\lambda_n \cosh nk(z+d)\cos n(kx-\omega t) \tag{2}$$

where c represents the wave velocity, k the wave number, x the horizontal coordinate in the direction of wave propagation, z the vertical coordinate, d the water depth, ω the angular frequency, and ux and uz the velocity components of the water particles. The wave number is related to the wavelength λn through k =2π/ λn.

The fluid in the computational domain is assumed to be incompressible and viscous. The governing equations are given as

$$\nabla \cdot \boldsymbol{u}=0 \tag{3}$$

$$\frac{\partial \boldsymbol{u}}{\partial t}+(\boldsymbol{u}\cdot\nabla)\boldsymbol{u}=-\nabla p+\frac{1}{Re}\nabla^2\boldsymbol{u} \tag{4}$$

where ρ denotes the fluid's density, u the fluid's velocity, p the pressure, and Re the Reynolds number. The SST k-ω turbulent model is implemented. This model incorporates a modified turbulent viscosity formulation to account for the transport effects produced by turbulent shear stresses, thereby enhancing accuracy and reliability compared to the standard k-ω model across a broad range of flow conditions. The treatment of the wall employs a comprehensive y+ wall treatment strategy. The dynamic fluid-body interaction (DFBI) model is implicitly coupled with the unsteady RANS solver to deal with the six-degree-of-freedom motion of the floating foundation.

An overlapping grid technique is used to discretize the computational domain. The computational domain is composed of a background grid and an overlapping grid. A data transfer interface is established between two grids. Both the background and the overlapping grids are unstructured, with hexahedral mesh elements. The grids surrounding the platform and near the water surface are refined.

The Volume of Fluid (VOF) method is used to track the air-water interface. The interface is described by the phase volume fraction αi

$$\alpha_i=\frac{V_i}{V} \tag{5}$$

where Vi is the volume of the fluid phase in the i-th cell, and V the volume of the mesh cell. With αi = 0 and αi = 1, the cell is fully occupied by air and water, respectively. The air-water interface can be found in a cell with 0 < αi < 1.

Set-ups of wave-tank testing

The tank was 60.0 m long, 4.0 m wide, and 2.5 m deep and had a piston-type wave maker at one end and a 4.0 m-long damping beach at the other end. The water depth was set as H = 1.62 m. Fig. 2 shows the scaled prototype in the wave tank without and with water after installation. The buoy was initially in the middle of the tank, 26 m from the wave maker. The free floating buoy was initially upright at its predetermined draught. Fig. 8 shows the physical model of the buoy and suspension system. Seven wave conditions were considered in the wave-tank experiments, with the wave period T ranging from 1.6 s to 4.0 s. The wave height was constant at 0.250 m. The wave amplitude A = 0.125 m was taken for nondimensionalization. Wave gauges were used to monitor the wave amplitude in the tank.

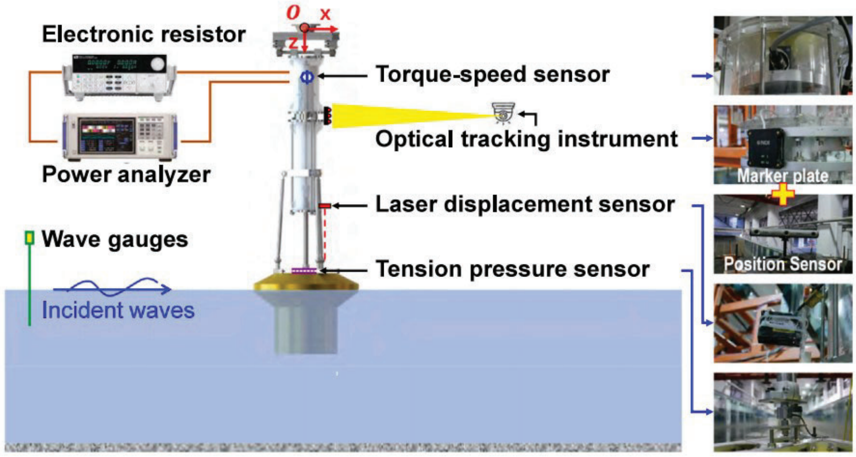

Fig. 2. Deployment of measurement system for MD-WEC model in wave-tank experiments

Results

Effects of MTLCD on pitch motion

Figure 3 compares histories of the pitch motion of a floating foundation with and without the MTLCD system in seven different wave conditions. In the case of T = 25 s, the floating foundation experiences a motion resonance in the pitch degree of freedom, and the maximum pitch amplitude is about 3.78°. With the MTLCD system, the maximum pitch amplitude is reduced to 2.8°, indicating a suppression effect of approximately 25.93%. Around the resonance condition, the suppression effect at T = 27 s is approximately 16.13%, and that at T = 23 s is approximately 25.46%. As the wave condition deviates from the resonance period, the suppressive effect of the MTLCD on the pitch motion reduces.

Figure 4 further compares the maximum pitch amplitudes of the floating foundation with and without MTLCD. The MTLCD effectively suppresses the pitch amplitude of the floating foundation in wave conditions of T =21s to 29s. Pronounced suppression effect can be observed in large-period wave conditions. As the wave period diverges from the natural period of the MTLCD, its suppression effect decreases gradually.

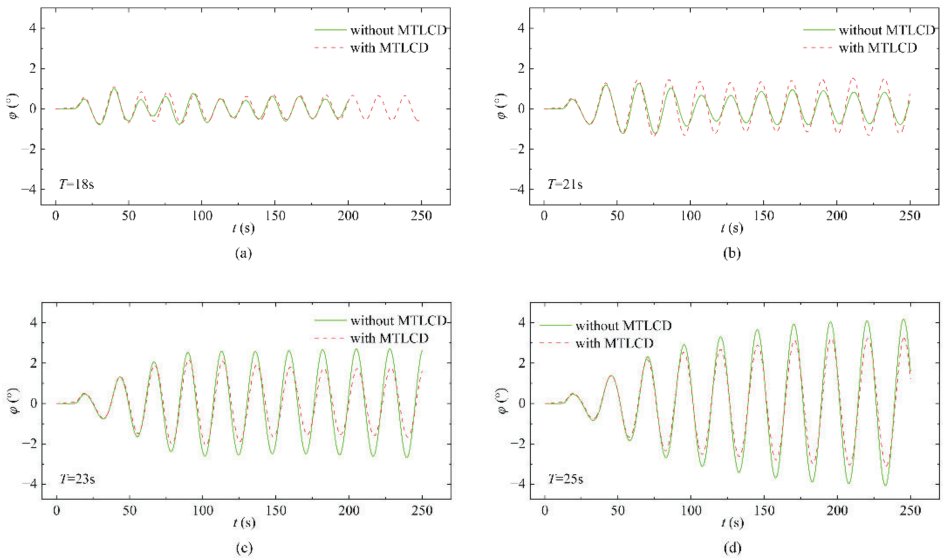

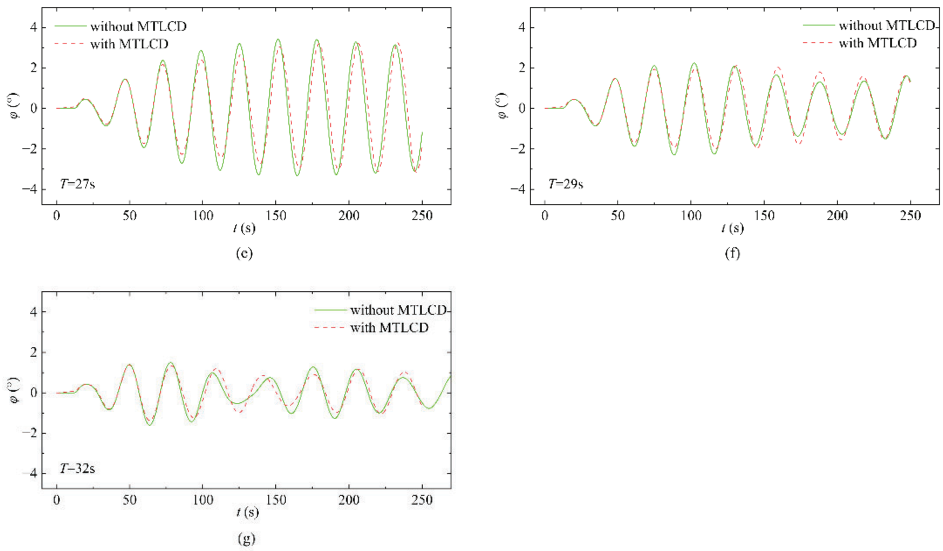

Fig 3. Histories of pitch motion of floating foundation with and without MTLCD

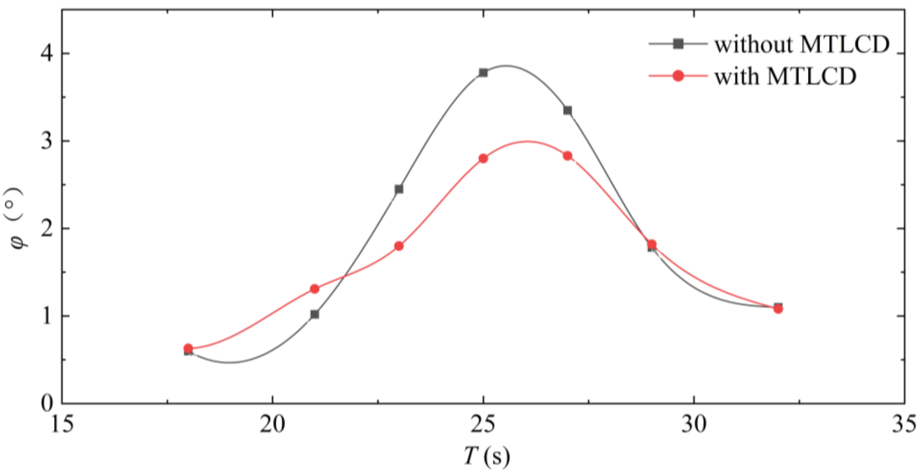

Fig 4. Comparison of maximum pitch amplitudes of floating foundation with and without MTLCD.

Kinematic and dynamic properties in energy absorption stage

Fig. 5(a) shows the wave-frequency component in the steady phase of the RH and force histories. The amplitude of either the RH displacement or the force of the buoy in the single-DOF case is always smaller than that in the multi-DOF case. Between T = 1.6 s and 2.8 s, the amplitude of the RH displacement for a multi-DOF buoy is almost twice that for the single-DOF case. In longer waves with period from T = 3.2 s to 4.0 s, the amplitude difference of the RH displacement between the single-DOF and multi-DOF cases decreases gradually. In terms of the force of the buoy acting on the drive tube, the amplitude in the single-DOF case briefly has an increasing trend with respect to the wave period, while that in the multi-DOF case reaches its peak at T = 2.0 s and then decreases steadily. Therefore, the MD-WEC device has special advantages in shorter-wave conditions in terms of the RH displacement and the force of the buoy.

According to the spectral analysis, the double-wave-frequency component dominates the histories of the torque and rotational velocity, which applies to both the single-DOF and multi-DOF cases. Fig. 5(b) compares the double-wave-frequency, component of these torque and rotational velocity histories. In either case, the pattern of the torque amplitude versus the wave period is similar to that of the rotational velocity. In wave conditions between $T = 2.0$ s and 3.2 s, the amplitudes of both the torque and rotational velocity of the shaft are evidently greater in the multi-DOF case. At $T = 2.0$ s, the torque and rotational velocity amplitude in the single-DOF case are only half and one-third of those in the multi-DOF case, respectively. During the parametric oscillation at $T = 3.6$ s, the $2f0$ component of the torque and rotational velocity has a smaller amplitude in the multi-DOF case.

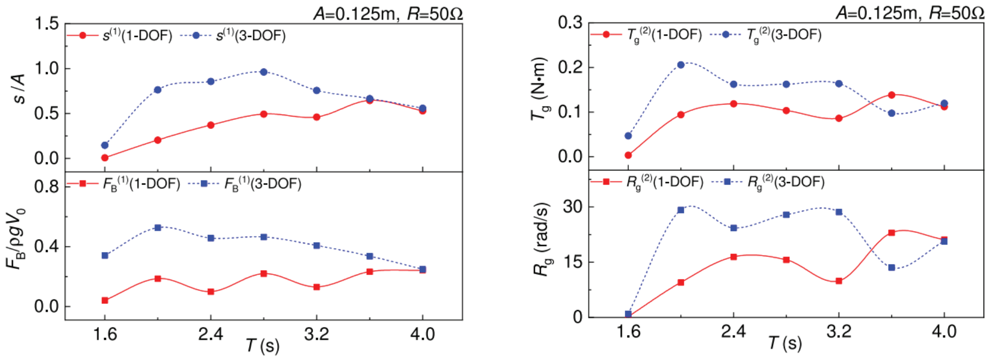

Fig. 5. (a) Wave-frequency (i.e., $f0$) component of RH displacement and force histories of buoy in single-DOF and multi-DOF cases. (b) Double-wave-frequency (i.e., $2f0$) component of torque and rotational velocity histories of output shaft of MMR gearbox in single-DOF and multi-DOF cases.

References

[1] Lee, H. H., Wong, S. H., & Lee, R. S. (2006). Response mitigation on the offshore floating platform system with tuned liquid column damper. Ocean engineering, 33(8-9), 1118-1142.

[2] Lee, H. H., & Juang, H. H. (2012). Experimental study on the vibration mitigation of offshore tension leg platform system with UWTLCD. Smart Structures and Systems, 9(1), 71-104.

[3] Borg, M., Utrera Ortigado, E., Collu, M., & Brennan, F. P. (2013, February). Passive damping systems for floating vertical axis wind turbines analysis. In European wind energy Conference (pp. 3-7).

[4] Feizian, H. R., Shafieefar, M., & Panahi, R. (2020). Application of tuned liquid column damper for motion reduction of semisubmersible platforms. International Journal Of Coastal, Offshore And Environmental Engineering (ijcoe), 5(2), 23-40.

[5] Yu, W., & Cheng, P. W. (2020, October). Verification of a passive tuned liquid multi-column damper for floating wind turbine. In ISOPE International Ocean and Polar Engineering Conference (pp. ISOPE-I). ISOPE.

[6] Zhang, D., George, A., Wang, Y., Gu, X., Li, W., & Chen, Y. (2015). Wave tank experiments on the power capture of a multi-axis wave energy converter. Journal of Marine Science and Technology, 20, 520-529.

[7] Sergiienko, N., Ding, B., Cazzolato, B., & Arjomandi, M. (2016). Performance comparison of the floating and fully submerged point absorber wave energy converters..

[8] Shi, H. , Huang, S. , & Cao, F. . (2019). Hydrodynamic performance and power absorption of a multi-freedom buoy wave energy device. Ocean Engineering, 172(JAN.15), 541-549..

[9] Al Shami, E., Wang, X., & Ji, X. (2019). A study of the effects of increasing the degrees of freedom of a point-absorber wave energy converter on its harvesting performance. Mechanical Systems and Signal Processing, 133, 106281.

[10] Wang, L., Lin, J., Li, H., Jiang, J., Wu, S., & Lu, G. (2024). Achieving efficient power generation for an enclosed drifting buoy by multi-DOF wave energy harvesting. Ocean Engineering, 305, 117834..

国際化推進共同研究概要

No. 29

［採択番号］ 24RE-7

タイトル： Modeling the hydrodynamics of the oscillating water column wave energy converter (OWC) device in real sea conditions

研究代表者： TRIVEDI, Kshma

所内世話人： 劉　盈溢

研究概要：本研究は、海流の存在下において起伏のある海底上に設置された振動水柱型波力エネルギー変換装置（OWC - WEC）の流体力学的挙動を数学的にモデル化することを目的とする。古典的な線形波浪 - 構造理論を組み込んだ2次元デカルト座標系内で数学的問題を検討し、対応する境界値問題を解くために境界要素法を採用した。入射波や海流のパラメータ、並びにOWC装置および起伏海底の構造的パラメータに基づき、振動水柱装置の正面障壁に作用する水平波力および効率に関する解析を行った。さらに、時間領域での解析により、順流および逆流の影響を考慮した各時点での自由表面振幅の変化を明示した。結果として、海流の存在に起因する「ドップラーシフト」効果が、効率および波力曲線の共振パターンに著しい影響を与えることが示された。特に、海流速度の増加に伴い、共振周波数はより大きな入射波数において発生することが確認された。

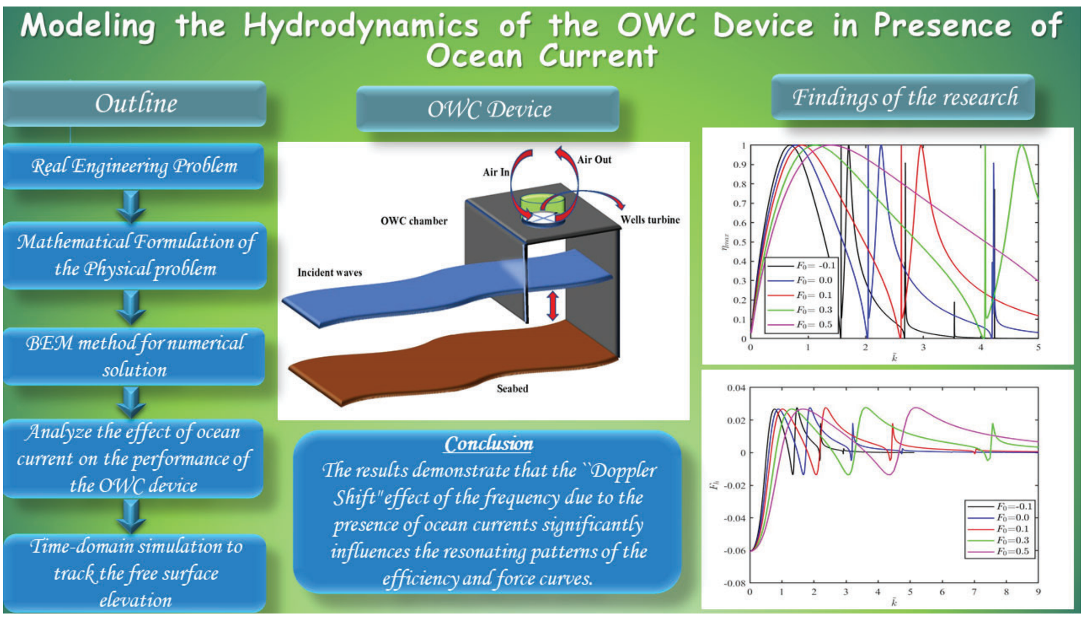

24RE-7

タ　イ　ト　ル：　Modeling the hydrodynamics of the oscillating water column wave energy converter (OWC) device in real sea conditions

研究代表者：　TRIVEDI, KSHMA

所内世話人：　劉　盈溢

Introduction:

Carbon emissions and environmental damage such as the greenhouse effect, acid precipitation, and stratospheric ozone depletion are primarily attributable to the consumption of non-renewable energy sources, like oil, coal, and natural gases, etc., in the development of products and facilities. Due to the significant advantages such as non-depletable, ubiquitous, and minimal environmental impact, renewable energy sources provide "greener" alternatives to handle these environmental degradations (see [1]-[3]). Of all the different types of renewable energy sources, wave energy is recognized as the most promising source of energy for a sustainable future world as the ocean covers the 71 of the earth's surface. The development of Wave Energy Converters (WECs) is characterized by a wide variety of concepts and designs aimed at harnessing wave energy. Based on their working principle, the WEC system is classified mainly into three categories: (i) Oscillating water column, (ii) Wave activated bodies, and (iii) Overtopping devices (see [4]-[7] for details). In addition, the aforementioned wave energy converters are further classified based on their different locations, namely nearshore or offshore, moored in a floating position or in a submerged position ([4], [5], [7]). Among all the wave energy converter devices, the OWC-WEC devices emerged as a significant breakthrough during the early nineteenth century, often recognized as the first generation of devices. The OWC device consists of an open-end box comprised of concrete or steel that is partially submerged in the ocean and the Wells turbine, which is located at the top of the OWC device chamber. In the presence of incident waves, pressure oscillations arise in the water column located inside the chamber. The internal pressure fluctuation within the enclosed chamber compels the air above the interior free surface to pass through the turbine, ultimately propelling the electrical generator to generate power ([8]). In order to create an effective wave energy converter device based on a rigid body model, significant theoretical and technological advancements have been performed ([10]-[12]).

In realistic marine environment, the development of ocean currents is based on the transfer of mass, momentum, and energy via the irregular smaller scale motions of certain kinds. Further, the tidal motion and wave breaking generate the currents in coastal areas with velocities of the order 10-100 cm/s. The natural phenomenon of wave-current interaction significantly impacts wave properties, such as wavelength, wave period, phase velocity, and group velocity. Consequently, this interaction leads to a transformation in the structural load experienced by all kinds of marine structures. Moreover, it is important to emphasize that ocean currents play significant roles in influencing both the speed and direction of waves ([13] - [15]). The power associated with the ocean current in the form of kinetic energy has an important foreseeable potential for electricity supply (see [15] - [16]). Due to such inherent properties, ocean currents can positively impact wave energy devices in several ways. They can increase the relative velocity of water, enhancing energy capture and stabilising wave patterns, leading to more consistent and efficient energy conversion. Currents also extend the operational range of devices, enabling them to perform effectively across various wave conditions and assist in optimal positioning by aligning devices with incoming waves. Additionally, currents can mitigate wave reflection and diffraction, further improving energy capture (see [17]).

In light of the OWC device's advantages, ocean currents can significantly enhance the hydrodynamic performance of the OWC devices by increasing air pressure variation for better turbine efficiency, improving energy capture through amplified water motion, and stabilizing the device against extreme conditions.

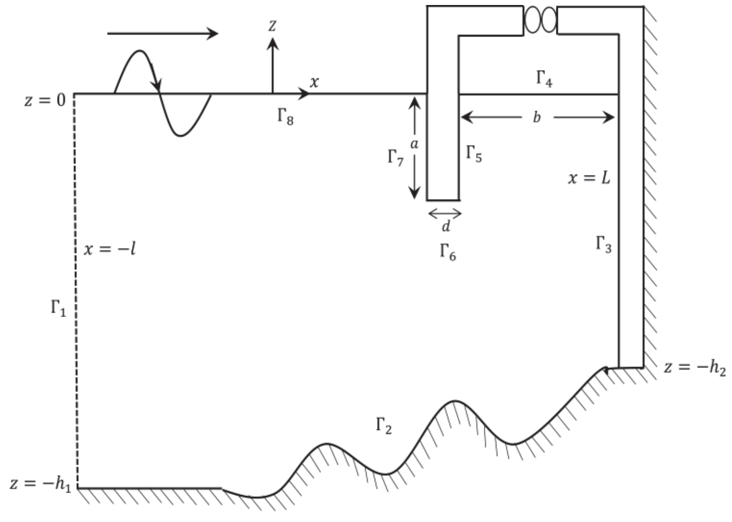

Fig:1 Vertical cross-section of the OWC device placed over the undulated seabed

Solution Methodology:

The procedure for converting BVP into system of integral equations is provided using the following flow chart:

The free space Green's function associated with the Laplace equation takes the form

$$G(x,z;\ \xi,\eta) = \frac{1}{2\pi}\ln r, \quad r = \sqrt{(x-\xi)^2 + (z-\eta)^2}$$

Applying Green's second identity to the velocity potentials and the aforementioned Green's function, the following Fredholm integral equation is obtained associated with the OWC device

$$\frac{c}{2\pi}\varphi^{S,R}(\xi,\eta) = \int_\Gamma \left(\varphi^{S,R}(x,z)\frac{\partial G}{\partial n}(x,z;\xi,\eta) - G(x,z;\xi,\eta)\frac{\partial \varphi^{S,R}}{\partial n}(x,z) \right) d\Gamma(x,z)$$

where $c = \pi$ for smooth boundaries. It is to be noted that for the free space Green's function, all the boundary conditions will be utilized in the aforementioned integral equations. However, for the free surface Green's function, only the undulated bottom bed, rear wall and the internal free surface boundary conditions will be utilized in the integral equations.

In both the processes, two Fredholm integral equations will be obtained: one for the scattered velocity potential and the other for the radiated velocity potential.

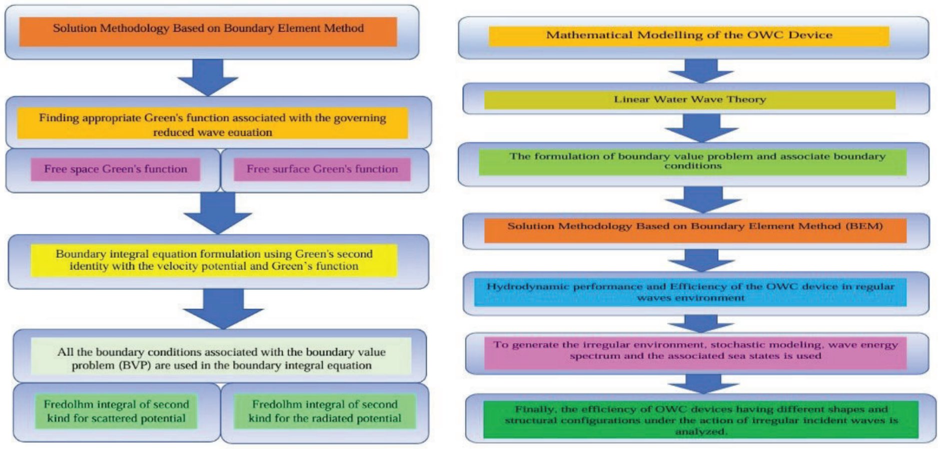

Fig:2. (a) Solution Methodology Based on BEM, and (b) working mechanism of the OWC device.

Results:

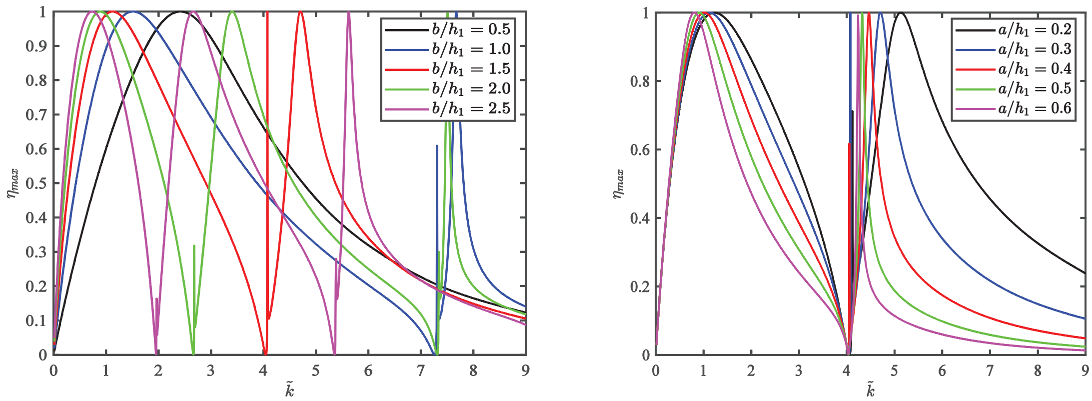

Fig: 2 Variation of η_{max} as a function of incident wave number $\tilde{k}$ for various (a) chamber width b/h_1, and (a) front wall's draft a/h_1in the presence of ocean current with $F_0 = 0.3$.

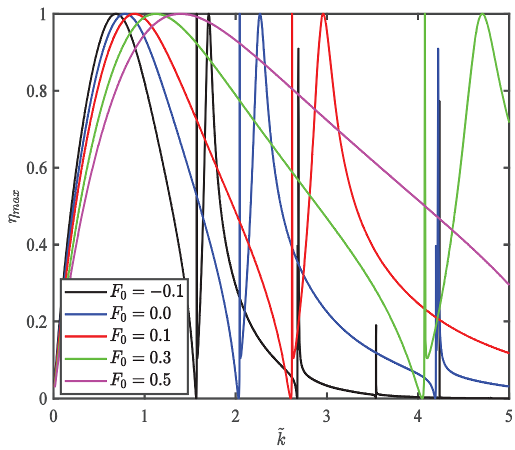

Fig:3. Variation of η_{max} vs $\tilde{k}$ for different $F_0 = 0.3$.

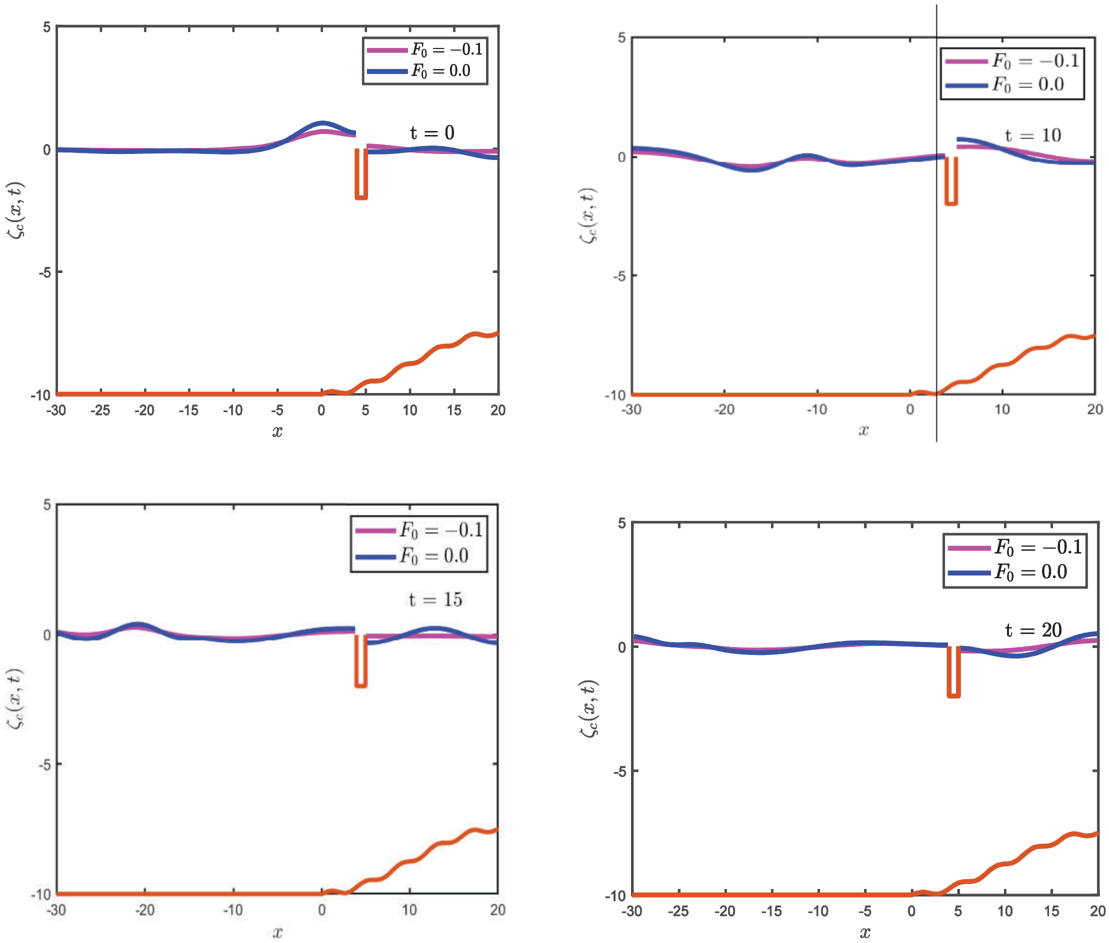

Fig: 4. Variation of free surface elevation $\zeta_c(x, t)$ with $F_0 = 0.3$ in the presence of an OWC device for different time (a) $t = 0\ sec$ (b) $t = 10$ sec, (c) $t = 15$ sec, and (d) $t = 20$ sec.

Conclusions:

In the current project, the hydrodynamic performance of an OWC-WEC device situated above an undulated sea bottom, subjected to the influence of ocean currents. To investigate the same, the examination is carried out in the context of the frequency and time-domain, respectively. The constant BEM is employed to address the corresponding BVP. Comprehensive derivations are presented for several factors pertaining to the assessment of the performance of the OWC device. These parameters include the radiation conductance and susceptance coefficients, as well as the volume fluxes related to the scattered potentials and the hydrodynamic efficiency. The present study has yielded the following conclusions:

- The occurrence of resonance in the efficiency curve is noted to be more prominent for lower values of the incident wavenumber when the chamber width and submergence depth are increased.
- In addition, the number of resonating peaks exhibits an increase in magnitude when the values of ocean current decrease, and the amplitude of the resonating peaks gradually declines for increasing values of wavenumber.
- It is found that the OWC-WEC device can effectively capture and store wave energy over prolonged durations. Furthermore, for higher magnitudes of following ocean current

velocities, the amplitude of $\zeta_c(x,t)$ is higher. However, for opposing current, the amplitude of $\zeta_c(x,t)$ is reduced due to the wave-blocking phenomenon, preventing wave propagation for higher magnitudes of opposing current velocities.

References:

[1] El-Farra NH, Christofides PD. Special issue on "control and optimization of renewable energy systems". Renewable Energy. 2017;100(100):1-2.

[2] Dincer I. Renewable energy and sustainable development: a crucial review. Renewable and sustainable energy reviews. 2000; 4(2):157-75.

[3] Gross R, Leach M, Bauen A. Progress in renewable energy. Environment international. 2003;29(1):105-22.

[4] Pecher A, Kofoed JP. Handbook of ocean wave energy. Springer Nature; 2017.

[5] Falc˜ao AF. Wave energy utilization: A review of the technologies. Renewable and sustainable energy reviews. 2010 ;14(3):899-918.

[6] Zhang Y, Zhao Y, Sun W, Li J. Ocean wave energy converters: Technical principle, device realization, and performance evaluation. Renewable and Sustainable Energy Reviews. 2021;141:110764.

[7] Ravindran M, Raju VS. Ocean energy. Proceedings of the Indian National Science Academy. 2015;81(4):983-91.

[8] Heath TV. A review of oscillating water columns. Philosophical Transactions of the Royal Society A: Mathematical, Physical and Engineering Sciences. 2012; 370(1959):235-45.

[9] Koley S, Trivedi K. Mathematical modeling of oscillating water column wave energy converter devices over the undulated sea bed. Engineering Analysis with Boundary Elements. 2020;117:26-40.

[10] Falnes J, McIver P. Surface wave interactions with systems of oscillating bodies and pressure distributions. Applied Ocean Research. 1985;7(4):225-34.

[11] Evans DV. The oscillating water column wave-energy device. IMA Journal of Applied Mathematics. 1978;22(4):423-33.

[12] Evans DV. Wave-power absorption by systems of oscillating surface pressure distributions. Journal of Fluid Mechanics. 1982;114:481-99.

[13] Phillips OM. The dynamics of the upper ocean, cambridge univ. press. New York, ´Etats-unis. 1966.

[14] Rey V, Capobianco R, Dulou C. Wave scattering by a submerged plate in presence of a steady uniform current. Coastal Engineering. 2002;47(1):27-34.

[15] Neumann G. Ocean currents. Elsevier; 2014.

[16] Chen JH, Chiu FC, Hsin CY, Tsai JF. Hydrodynamic consideration in ocean current turbine design. Journal of Hydrodynamics. 2016;28(6):1037-42.

[17] Bahaj AS. Generating electricity from the oceans. Renewable and Sustainable Energy Reviews. 2011;15(7):3399-416.